Title
Testing Self-Interacting Dark Matter with Spiral and Early-Type Galaxies

Author
Ren, Tao

Publication Date
2019

UNIVERSITY OF CALIFORNIA
RIVERSIDE

Testing Self-Interacting Dark Matter with Spiral and Early-Type Galaxies

A Dissertation submitted in partial satisfaction
of the requirements for the degree of

Doctor of Philosophy

in

Physics

by

Tao Ren

September 2019

Dissertation Committee:

Dr. Hai-Bo Yu, Chairperson
Dr. Philip Tanedo
Dr. Yanou Cui

The Dissertation of Tao Ren is approved:

Committee Chairperson

University of California, Riverside

Acknowledgments

First of all, I would like to thank my advisor, Dr. Hai-Bo Yu, for his help and guidance over the past five years. I also thank Dr. Philip Tanedo and Dr. Yanou Cui for serving as the committee members of my qualifying oral exam and thesis defense.

Furthermore, I would like to thank my collaborators, Dr. Anna Kwa and Dr. Manoj Kaplinghat from UC Irvine, and former postdocs Dr. Ayuki Kamada and Dr. Ran Huo for valuable discussions. I am also grateful to many other professors, graduate student friends and staff members for their help in life and work. In addition, positive feedbacks from undergraduate students on my teaching efforts are another encouragement to me.

Finally, I express my deepest gratitude to my family for unconditional love and support.

To my parents and grandparents.

ABSTRACT OF THE DISSERTATION

Testing Self-Interacting Dark Matter with Spiral and Early-Type Galaxies

by

Tao Ren

Doctor of Philosophy, Graduate Program in Physics
University of California, Riverside, September 2019
Dr. Hai-Bo Yu, Chairperson

In this dissertation, we explore the possibility of using a novel dark matter model, i.e., self-interacting dark matter (SIDM), to address the challenges that the traditional cold dark matter (CDM) paradigm has in explaining observations on galactic scales. For example, in spiral galaxies, galactic rotation curves exhibit a diverse behavior in the inner regions, while obeying an organizing principle, i.e., they can be approximately described by a radial acceleration relation. However, current CDM simulations can not offer a satisfactory explanation for both of them simultaneously. Additionally, in early-type galaxies (ETGs), the smallness of dark matter fractions within their effective radii indicates no signs of adiabatic contraction processes predicted by CDM simulations, and the nearly isothermal total density profiles featured with small scatters within large radii are also beyond naive expectations.

We apply the SIDM model to study kinematics and dynamics of these two main types of galactic systems. For spiral galaxies, we analyze the rotation curve data from the SPARC sample, and explicitly demonstrate that both the diversity and uniformity are naturally reproduced in a hierarchical structure formation model with the addition of dark matter self-interactions. Meanwhile, other properties such as the concentrations of dark matter halos, the stellar mass-to-light ratio distribution etc. are well consistent with observations and theoretical considerations. We also compare the SIDM results with those from hydrodynamical CDM simulations with strong baryonic feedback, and highlight the importance of the diverse baryon profiles in fitting to the rotation curves. For ETGs, we model the SIDM halos and baryon profiles with data from the SL2S sample. The total density profiles are close to the isothermal style and the inferred dark matter fractions match well with the data derived from strong lensing and stellar kinematics.

We show that SIDM can provide an economical explanation to the observations of spiral galaxies and ETGs, while being consistent with CDM predictions on large scales. Our results provide compelling arguments in favor of the idea that the inner halos of galaxies are thermalized due to dark matter self-interactions.

Contents

List of Figures

List of Tables

Chapter 1

Background

1.1 The Origin of Dark Matter

The modern hypothesis of dark matter (DM) originates from the observed anomalies among astrophysical systems during the 1930s. While studying the dynamics of the Coma cluster of galaxies, Fritz Zwicky first noticed the inconsistency between the observed line-of-sight velocities of galaxies in the Coma cluster and the cluster mass inferred from the observed luminosity [13, 14]. The large line-of-sight velocities indicated that the galaxies were moving too fast to be bound by the inferred mass. Besides the observations of clusters, rotation curves of spiral galaxies illustrated another controversy. Light distributions of spiral galaxies are usually bright in their centers and gradually become dim to the edges [15]. If their masses follow the light, one can expect Keplerian declines at large radii of rotation curves. However, the observed ones kept high velocity values until their edges of visible regions rather than expected declines [16]. These anomalies imply there exists additional and invisible matter (hence, DM) in galaxies and clusters of galaxies.

The examination of spiral galaxies' stability offered one new piece of theoretical evidence for the existence of DM in galaxies. Jeremiah Ostriker and James Peebles found the instability of stellar component-only disk galaxies using N-body simulations [17]. The star particles in the simulated disks initially distributed in a round shape regularly and the disk structure was supported mainly by circular motions. As one such system evolved under the gravitational interactions, the shape of the round disk began to change, the motion of star particles became more random, and the system was more like a pressure-supported one in the end [17, 18, 19]. However, observed spiral galaxies, such as the Milky Way, are largely rotation supported but much more stable than those in the simulations. In order to stabilize the system, several solutions were discussed [17]. The most plausible one is that the disk is not the only component in the galaxy and it is embedded in a large massive DM halo.

The measurements of extended rotation curves within and beyond optical disks serve as another solid evidence for DM from observations. During the 1970s, a number of observations about galactic rotation curves were reported [20, 21, 22, 23, 24, 25]. All of them pointed to the same conclusion that the flatness of rotation curves is common for spiral galaxies. They showed the rotation curves maintain unexpected high rotation velocities beyond the edges of their optical disks. One interpretation for this could be that the stellar components in their outer region become dimmer but the mass-to-light ratio (M/L) values are increasing dramatically, which is obviously unreasonable. If the stability issue of stellar disks is considered simultaneously, the existence of DM is a more reasonable explanation for the discrepancy between expected and observed rotation curves.

1.2 The Cold Dark Matter Paradigm

Observations of large scale structures of the Universe offer further supporting evidence for the existence of DM. The structure formation of the large scale Universe starts after the decoupling between the cosmological background radiation (CMB) photons and baryons [26]. However, the baryon density fluctuations inferred from the CMB anisotropy are too small to evolve and form the current observed large scale structure of the Universe from this cosmological moment of CMB [27, 28]. This strongly suggests there exists another kind of matter (DM) that decoupled from baryons and photons long time before CMB and started structure formations earlier [29].

The relic neutrinos are first chosen to be the DM, however they can't explain the structure formation completely. Neutrinos were moving close to the speed of light (hence, known as hot DM) when they decoupled from the photons after the Big Bang. Their free streaming would smooth out density fluctuations on a scale which evolve to superclusters nowadays after the expansion of the Universe [29]. In such a scenario, the structure formation started from large astrophysical systems, e.g., superclusters, and galaxies formed later due to fragmentations. Nevertheless, this top-down picture indicates galaxies will form relatively late around $z \approx 2$ which is contradict to the observation of high redshift galaxies [30]. With such difficulties in the hot DM framework, Peebles and others proposed an opposite theory, i.e., the cold DM (CDM) framework [31, 32, 33]. Different from the hot DM, CDM particles were moving much slower when they decoupled from photons. This feature makes the density fluctuations on small scales remained and a bottom-up structure formation picture follows. N-body simulations show in the CDM framework, galaxies can form much earlier than $z = 2$ [30]. Further observations confirmed the success of CDM on explaining the large scale structure of the Universe [34].

Because of the strong constrains on the property of CDM particles from astrophysical and cosmological observations, the particle physics standard model (SM) fails to give a satisfactory candidate. On the other hand, a new theory, supersymmetry, was proposed with the goal of unifying fundamental forces, and introduced extra particles [35, 36]. In this theory, each particle in the SM will get a supersymmetric counterpart and the most stable one (neutralino) is possible to be a candidate of DM, called weakly interacting massive particles (WIMPs) [37, 38]. The coincidence is that the annihilation cross section needed for the relic abundance of DM in the Universe is on the weak scale $\langle \sigma v \rangle \simeq 3 \times 10^{-26} \mathrm{cm}^3/\mathrm{s}$ matching well with that of WIMPs. This makes the WIMP a potential candidate for the CDM in the next several decades. Due to its particle physics origin, many direct detection researches, e.g., Ref. [39], and collider experiments, e.g., Ref. [38], are set up to search for the signals from WIMPs.

1.3 Small Scale Problems

While more simulations begin to focus on galaxy formations on the small scales, a number of discrepancies between predictions from the CDM paradigm and observations emerge. CDM-only simulations show that the DM density profiles can be approximately described by a universal form, i.e., the Navarro-Frenk-White (NFW) profile [40, 41, 42, 43], despite of the size of DM halos ranging from a dwarf galaxy to a galaxy cluster. A specific feature for this profile is the density cusp close to the center $\rho \propto r^{-1}$, hence cuspy-like.

However, many observed rotation curves of dwarf galaxies with low surface brightnesses indicate shallower profiles than those expected from CDM simulations. This implies the DM densities prefer core-like profiles in the central regions of these galaxies. This contradiction is coined as the core-cusp problem [44, 45]. Though these systems are mainly DM dominated, the existence and evolution of baryons may generate impacts on the distributions of DM. For example, supernova explosions are possible to expel much gas from the center to the outer region, and further lower the DM density through decreasing the gravitational potential [46, 47]. As a result, dwarf galaxies are thought as good targets to test the CDM predictions and baryonic feedback models.

After systematically studying a large sample of spiral galaxies, Oman et al. highlighted a more general problem, i.e., the diversity problem, related to the shapes of rotation curves [48]. Oman et al. classified dwarf galaxies based on the magnitude of their last measured velocities. Each group consists of galaxies with similar last measured velocities which indicates that they are hosted by similar-size DM halos. They found that the galaxies within each group exhibit a great diversity in the shape of the rotation curves in the inner regions. Some of them have rotation curves growing slowly and reaching the maximum velocity after extending to several kpcs. Others may reach the flat region of the rotation curves within 1-2 kpc. However, hydrodynamical simulations [48] show the simulated results could match the observed ones with steep rotation curves, but not those rising slowly.

There is also discrepancy between CDM predictions and observations of satellite dwarf galaxies in the Milky Way. The observed satellite galaxies are expected to be hosted by CDM halos with $V_{\mathrm{max}} < 25$ km/s based on the estimates from stellar velocity dispersions

[49, 50], where V_{max} is the maximum rotation velocity solely in a CDM halo. However, the sub-halos of a Milky Way-size CDM halo in simulations contain ones with V_{max} much larger than 25 km/s [49, 50]. According to abundance matching, the most luminous satellites in the Milky Way should be hosted by the most massive CDM sub-halos [51]. The mismatch between the sub-halos from simulations and observations means either the CDM simulations over produced the massive sub-halos or the massive sub-halos are too big to fail the star formation.

1.4 Self-Interacting Dark Matter

SIDM was originally proposed to solve these small scale issues [52]. It departs from the original CDM model mainly in the inner region of galaxies due to the introduction of self-interactions between DM particles. In recent years, the idea of SIDM has received significant attentions in the astrophysics and particle physics communities [53, 54, 55, 56, 57, 58, 59, 60, 61, 62, 63, 64, 65, 66, 67, 68, 69, 70, 71], demonstrates its great potential to relieve the tension on small scales [72, 73] and offers alternative DM detection mechanisms [74, 75, 76, 77, 78].

With a simple addition of self-interactions, characterized by the cross section per unit mass $\mathcal{O}(1-100)$ cm^2/g, between DM particles, the success of CDM on large scales is preserved. On the other hand, DM particles with self-interactions experience sufficient collisions in the center of a galaxy with high mass density and become thermalized during the galaxy life time. This leads to two distinct predictions. Compared to a CDM halo, the DM particles in the inner SIDM halo are thermally connected to the outer region with an almost constant velocity dispersion which is larger than that in a similar size CDM halo. In an equilibrium state, this feature keeps the DM particles from condensating in the central region of the halo and leads to a cored profile for DM dominated systems [79]. The other is that the thermalization constructs a more direct connection between DM and baryons [80]. The deeper the baryon potential is, the higher the DM density could be. Such a feature is exactly what is needed to explain the diversity problem. Additionally, non-equilibrium SIDM halos under certain conditions would experience core collapses or expansions which may offer new mechanisms about black hole and galaxy formations [81, 82, 83, 84].

In this dissertation, we test the SIDM model with spiral and ETGs. We explore the possibility of applying the SIDM model to solve the small scale problems that the CDM paradigm has while studying these galactic systems. In Ch. 2, we study the diversity and uniformity feature in galactic rotation curves by fitting to the SPARC sample [1]. We explore the physical reasons that lead to different abilities of the SIDM model and the CDM model in fitting to the rotation curves, and explain the diversity in detail in Ch. 3. We exam the smallness of DM fractions within effective radii and nearly isothermal total density profiles in ETGs through a comparison between the SIDM model, the adiabatic contracted NFW model and IllustrisTNG simulations in Ch. 4. Conclusions are given in Ch. 5.

Chapter 2

Reconciling the Diversity and Uniformity of Galactic Rotation Curves

The text in Ch. 2 is based on the paper, “Reconciling the Diversity and Uniformity of Galactic Rotation Curves with Self-Interacting Dark Matter”, written with Anna Kwa, Manoj Kaplinghat and Hai-Bo Yu. It was published in Phys.Rev. X9 (2019) no.3, 031020.

2.1 Introduction

Galactic rotation curves of spiral galaxies show a variety of behavior in the inner parts even across systems with similar halo and stellar masses, which lacks a self-consistent explanation in the standard cold dark matter (CDM) model [44, 45, 85, 86, 87, 88, 89, 87, 90, 91, 92, 48, 6]. Along with this diversity, a long-standing observation is that many rotation curves can be understood in terms of Modified Newtonian Dynamics (MOND) phenomenology [93, 94] (see [95] for a review), i.e., there exists a characteristic gravitational acceleration scale, $g_\dagger \approx 10^{-10}$ m/s$^2 \sim cH_0/7$ with H_0 being the present Hubble expansion rate, below which the observed acceleration can be approximated as $\sqrt{g_\dagger g_{\rm bar}}$ with $g_{\rm bar}$ being the baryonic acceleration (a.k.a. Milgrom's law). More recently, McGaugh et al. [96] analyzed the Spitzer Photometry and Accurate Rotation Curves (SPARC) dataset [1] and showed there is a tight relation between the total gravitational acceleration at any radius and the acceleration contributed by the baryons, assuming a constant stellar mass-to-light ratio $\Upsilon_{\star,{\rm disk}} = 0.5 M_\odot/L_\odot$ and $\Upsilon_{\star,{\rm bulge}} = 0.7 M_\odot/L_\odot$ in the 3.6 μm band. The scatter in this radial acceleration relation (RAR) is around 0.1 dex, and the tightness of this relation has been interpreted as a signature of MOND [97].

It has long been argued that the acceleration scale (including the cH_0 dependence) can emerge from hierarchical structure formation predicted in CDM [98, 99]. Recent hydrodynamical simulations of galaxy formation with CDM have clearly shown that a RAR emerges [100, 101, 102]. However, these simulated galaxies do not represent the full range of the diversity in the SPARC dataset and they cannot yet explain the rotation curves of low and high surface brightness galaxies simultaneously.

In this chapter, we show that self-interacting dark matter (SIDM) provides a unified way to understand the diverse rotation curves of spiral galaxies, while reproducing the RAR with a small scatter. We analyze the SPARC dataset based on the SIDM halo model proposed in [80, 72] and demonstrate three key observations leading to this result.

- For cross section per unit mass $\sigma/\mathrm{m} \sim 1\ \mathrm{cm}^2/\mathrm{g}$, dark matter self-interactions thermalize the inner regions at distances less than about 10% of the virial radius of galactic halos, while the outer regions remains unchanged. Thus, SIDM inherits essential features of the ΛCDM hierarchical structure formation model such as the halo concentration-mass relation, which sets the characteristic acceleration scale of halos.

- In the inner halo, thermalization ties dark matter and baryon distributions together [80, 103, 104], and the SIDM halo can naturally accommodate the diverse range of 'cored' and 'cusped' central density profiles, depending on how the baryons are distributed. Combined with the scatter in the concentration-mass relation, this provides the diversity required to explain the rotation curves [72, 73, 105].

- For the same σ/m that addresses the diversity problem, the baryon content of the galaxies and the mass model of their host halos also lead to the RAR with a scatter as small as the one in [96]. In our SIDM fits, the inferred stellar $\Upsilon_{\star,\mathrm{disk}}$ values for individual galaxies have a distribution peaked toward $0.5 M_\odot/L_\odot$, as expected from stellar population synthesis models [106].

The rest of the chapter is organized as follows. In Sec. 2.2, we present the SIDM fits to 135 galaxies from the SPARC sample, which exemplify the full range of the diversity. In Sec. 2.3, we show the radial acceleration relation and the distribution of the stellar mass-to-light ratios from our SIDM fits, compared to the MOND fits. In Sec. 2.4, we discuss the host halo properties and the origin of the acceleration scale. In Sec. 2.5, we show the predicted stellar – halo mass relation and the baryonic Tully-Fisher relation (BTFR). We comment on future directions and conclude in Sec. 2.6. In Sec. 2.7 (Appendix), we provide detailed information about the SIDM model, the fitting procedure and additional results that support the main text, including model fits to simulated halos. SIDM and MOND fits to 135 individual galaxies from the SPARC sample are provided in Appendix A of the dissertation.

2.2 The Diversity of Galactic Rotation Curves

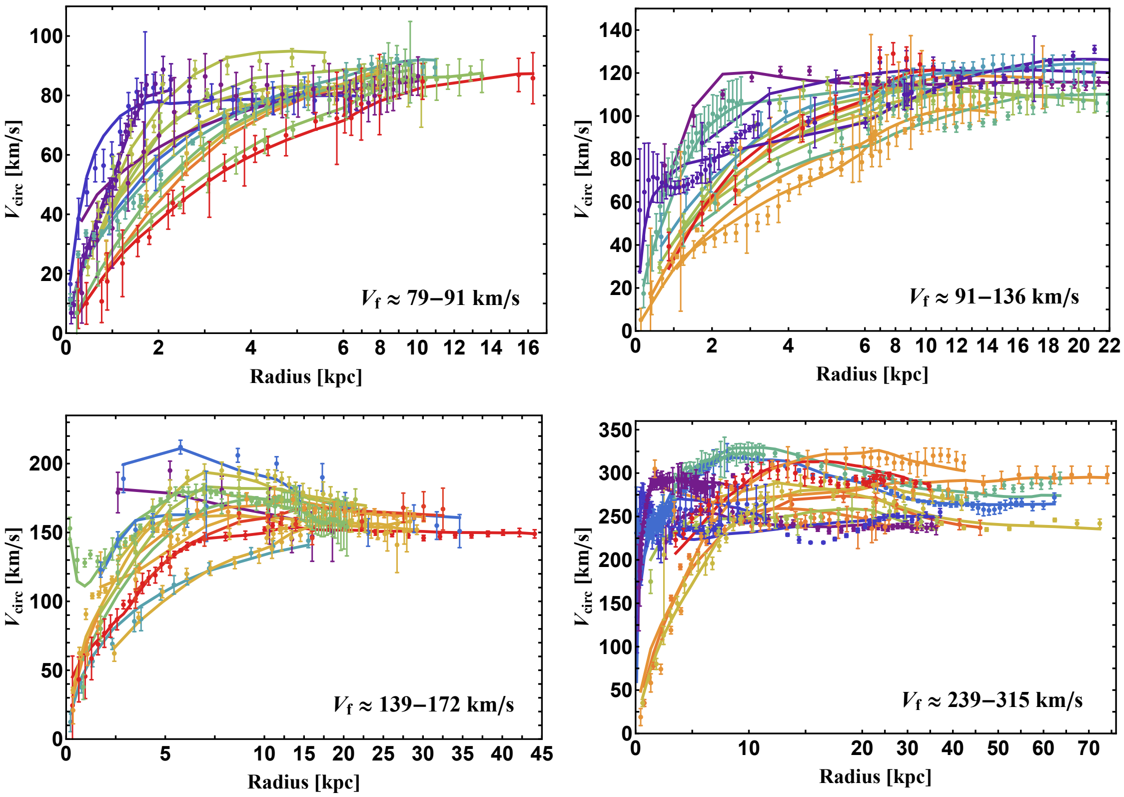

Figure 2.1: SIDM fits (solid) to the diverse rotation curves across a range of spiral galaxy masses, where we take $\sigma/\text{m} = 3\ \text{cm}^2/\text{g}$. The data points with error bars are from the SPARC dataset [1]. Each panel contains 14 galactic rotation curves that are selected to have similar flat rotation velocities at their furthest radial data points, and the corresponding V_f bins are 79–91, 91–126, 139–172 and 239–315 km/s, spanning the mass range of the galaxies considered in this work. The galaxies are colored according to their relative surface brightness in each panel from low (red) to high (violet).

We select 135 out of 175 galaxies in the full SPARC sample based on the criteria that they must have a recorded value for the flat part of the rotation curve, $V_{\rm f}$. In our sample, 87, 42 and 6 galaxies have quality flags 1, 2 and 3, respectively. It spans a wide range of galaxy masses and inner shapes of rotation curves with $V_{\rm f}$ ranging from 20 km/s to 300 km/s. In fitting to the data, we utilize the analytical SIDM halo model [72, 73], where we assume the dark matter distribution in the inner halo follows the isothermal density profile,

$$\rho_{\rm iso}(R,z) = \rho_0 \exp\left(\left[\Phi_{\rm tot}(0,0) - \Phi_{\rm tot}(R,z)\right]/\sigma_{\rm v0}^2\right), \tag{2.1}$$

where ρ_0 is the central dark matter density, $\sigma_{\rm v0}$ is the one-dimensional dark matter velocity dispersion, $\Phi_{\rm tot}(R,z)$ is the total gravitational potential and R, z are cylindrical coordinates aligned with the stellar disk. We match this isothermal profile to a Navarro-Frenk-White (NFW) form [41, 42] at r_1, where a dark matter particle has scattered $\mathcal{O}(1)$ times over the age of the galaxy, assuming continuity in both the density and the enclosed mass at r_1. In this way, the isothermal parameters (ρ_0, $\sigma_{\rm v0}$) directly map on to the NFW parameters (r_s, ρ_s) or ($r_{\rm max}$, $V_{\rm max}$). This model provides an approximate way to calculate the SIDM distribution in a halo if its CDM counterpart is known, and vice versa. It correctly predicts the halo central density and its scalings with the outer halo properties, stellar profiles and cross section, as confirmed in both isolated and cosmological N-body simulations with and without baryons, see, e.g., [72, 104, 105, 107, 108]. See Sec. 2.7.1 (Mothods) and Sec. 2.7.2 (Supplemental Material) for a detailed description of the model and additional comparisons between model predictions and cosmological simulations.

We adopt two independent but complementary approaches to perform the analysis. In the controlled sampling (CS) approach, we demand that the host halos follow the concentration-mass relation within a 2σ range predicted in cosmological simulations [2]. We model the stellar distribution as an axisymmetric thin disk as in [73], which directly enters into the calculation of the density profile of SIDM through the gravitational potential $\Phi(R, z)$. In the CS fits, we start with the outer NFW halo and find the SIDM density profile that matches its mass and density at r_1. In the second approach, we use the Markov Chain Monte Carlo (MCMC) sampling (MS) to explore the full likelihood. To save computational time, we assume spherical symmetry by spreading the mass within the disk at radius R into a sphere of the same radius [80, 104]. The rotation curves generated from two approaches agree well and the differences in the fits are small (see Appendix A). For our main results, we show inferences from both of the approaches.

In Fig. 2.1, we show the SIDM fits to the diverse rotation curves from the controlled sampling with $\sigma/\mathrm{m} = 3\ \mathrm{cm}^2/\mathrm{g}$. In each panel, galaxies are selected to have similar flat rotation velocities at their outermost data points. The rise up to V_f within their central regions displays a wide variety of slopes and the SIDM halo model provides equally good fits to the shallow and steeply rising rotation curves. The fits for the other galaxies in the sample are as good as those in Fig. 2.1 (see Appendix A).

The success of the SIDM halo model stems from a combination of the following effects. First, SIDM thermalization ties the baryon and dark matter distributions together. For low surface brightness galaxies, thermalization leads to a shallow density core and a circular velocity profile that rises mildly with radius [52, 109, 79, 110, 111, 112, 113]. While, for high surface brightness ones, the core shrinks in response to the deeper baryonic potential and the central SIDM density increases accordingly [80, 104, 105, 108]. The galaxies in our sample have a variety of central surface brightnesses, resulting in diverse central dark matter densities. Second, scatter in the cosmological halo concentration-mass relation leads to scatter in the characteristic SIDM core density and radius, which is reflected in the rotation curves [72]. Ref. [73] fitted 30 galaxies and illustrated the importance of these effects in explaining the diverse rotation curves. In this work, we fit a larger sample of galaxies and demonstrate that the observed galaxies are fully consistent with the SIDM predictions.

We have assumed a constant cross section to fit the SPARC sample because it is hard to pin down the cross section for individual galaxies. For low surface brightness galaxies with a large core, a large cross section, such as $\sigma/\mathrm{m} = 3~\mathrm{cm}^2/\mathrm{g}$ is preferred [73]. However, since the central SIDM density varies mildly with the cross section in range of 1–10 cm^2/g [114, 115], a feature that is well-captured in our analytical model [72], an even larger cross section may work as well. For high surface brightness galaxies, to which most of galaxies with high V_f belong, the fits are insensitive to the cross section because of the degeneracy between σ/m and $\Upsilon_\star$ [73]. The effect in the SIDM fits induced by varying σ/m can be compensated by a minor change in the stellar mass-to-light ratio, and many of these systems are actually compatible with an NFW profile. The cross section may have a mild velocity dependence over the sample, as implied by the constraint from galaxy clusters [72, 116, 117], but it is impossible to extract it from the SPARC dataset given the reasons discussed above. In this work, we present the results for fixed $\sigma/\mathrm{m} = 3~\mathrm{cm}^2/\mathrm{g}$ and they remain the same qualitatively for other values larger than $\sim 1~\mathrm{cm}^2/\mathrm{g}$ on galaxy scales.

An important consequence of the large cross section is that the SIDM profile is driven quickly to be isothermal in the inner regions. This implies that the resultant SIDM fits will not depend sensitively on the formation history of individual galaxies [73], but the *final* stellar and gas distributions [80]. This has been explicitly confirmed in recent hydrodynamical SIDM simulations [107] and those with idealized disk growth [104]. Furthermore, in our fits r_1 is close to r_s, which is well outside the stellar disk or budge in the galaxies. It is unlikely that a viable baryonic feedback process could change the halo mass profile significantly at that far distance. Thus, our analytical model takes into account the realistic baryon distribution for individual galaxies and encodes this effect on the SIDM halo profile through the matching procedure.

2.3 The Radial Acceleration Relation in SIDM

In the RAR described in Ref. [96], the gravitational acceleration $g_{\rm tot}$ at radius r is found to be related to the acceleration $g_{\rm bar}$ at the same radius. This relation can be fit to a functional form with a single parameter $g_\dagger$:

$$g_{\rm tot}(r) = g_{\rm bar}(r)\left(1 - e^{-\sqrt{g_{\rm bar}(r)/g_\dagger}}\right)^{-1}. \tag{2.2}$$

Their best-fit value of $g_\dagger = 1.2 \times 10^{-10}$ m/s^2 is the oft-quoted MOND acceleration scale.

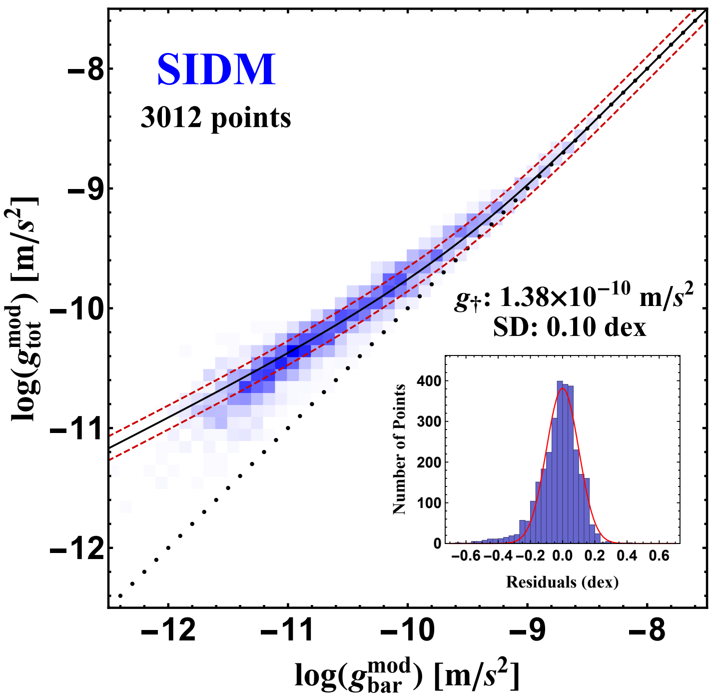

Figure 2.2: The radial acceleration relation from the SIDM fits, where $g_{\rm tot}^{\rm mod}$ and $g_{\rm bar}^{\rm mod}$ are inferred from the $\sigma/{\rm m} = 3$ cm^2/g fits. The black solid line is the best fit to Eq. 2.2; the two red dashed curves correspond to the 1σ deviation from this fit. The black dotted line is the one-to-one reference line. **Insets**: Corresponding histograms of residuals after subtracting the fit function with the best-fitting scale parameter $g_\dagger = 1.38 \times 10^{-10}$ m/s^2, together with the Gaussian fits to the residuals, which have 1σ widths of 0.10 dex.

In Fig. 2.2, we show the inferred total and baryonic acceleration values from the controlled sampling, where $g_{\rm tot}^{\rm mod}$ and $g_{\rm bar}^{\rm mod}$ are *calculated* from the SIDM fits, using the halo parameters and the best-fit $\Upsilon_\star$ values for each galaxy. The intensity of color in Fig. 2.2 reflects the density of points. After fitting the data with the empirical relation given in Eq. 2.2, we find the best-fit value of $g_\dagger$ is 1.38×10^{-10} cm^2/g and the resulting dispersion in the residuals is 0.10 dex. Fig. 2.3 (left) shows $\Upsilon_{\star,{\rm disk}}$ distribution from the SIDM fits (solid). It is peaked toward $\Upsilon_{\star,{\rm disk}} = 0.5 M_\odot/L_\odot$, in good agreement with predictions from stellar population synthesis models [106]. This is remarkable because *no* priors based on the stellar population synthesis models were used. We have also reproduced the analysis in Ref. [96] with $\Upsilon_{\star,\text{disk}}$ and $\Upsilon_{\star,\text{bulge}}$ were fixed to $0.5M_\odot/L_\odot$ and $0.7M_\odot/L_\odot$, respectively. For this fixed $\Upsilon_\star$ case, we obtained $g_\dagger = 1.19 \times 10^{-10}$ m/s^2 and dispersion 0.12 dex, both in agreement with previous work [96].

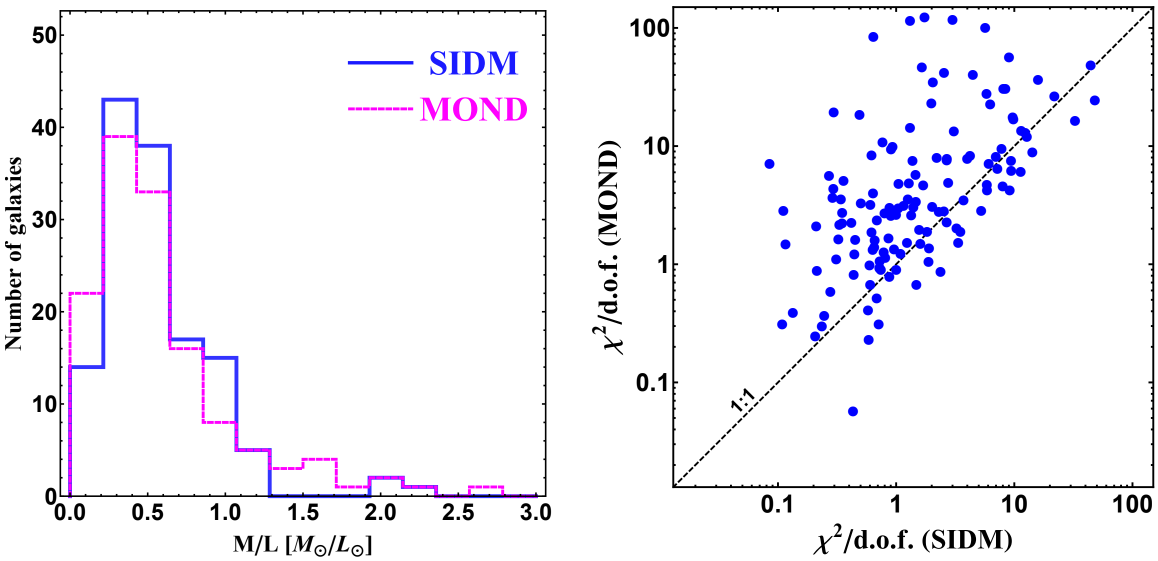

Figure 2.3: *Left*: Inferred $\Upsilon_{\star,\text{disk}}$ distributions for the SIDM and MOND fits. *Right*: distribution of χ^2/d.o.f. values for individual galaxies from the SIDM and MOND fits.

For a more detailed comparison, we also fit the sample of 135 SPARC galaxies using the MOND relation in Eq. 2.2, where we fixed $g_\dagger = 1.2 \times 10^{-10}$ m/s^2, but varied $\Upsilon_{\star,\text{disk}}$ and $\Upsilon_{\star,\text{bulge}}$ in the range of $0.1 < \Upsilon_\star/(M_\odot/L_\odot) < 10$ (same as MCMC SIDM fits) using MCMC sampling (see also [118]). The results look similar if we set $g_\dagger$ to 1.0×10^{-10} or 1.4×10^{-10} m/s^2. The left panel of Fig. 2.3 shows the $\Upsilon_{\star,\text{disk}}$ distribution from the MOND fits (dotted), which closely tracks the one from the SIDM fits. The right panel shows the distribution of minimum χ^2/d.o.f. values for individual galaxies from the SIDM and MOND fits. The SIDM model provides a better fit than MOND for most of the galaxies

($\sim 77\%$), while maintaining a tight RAR. In fact, 72% (45%) of them have χ^2/d.o.f. ≤ 3 (1) in the controlled SIDM fits and those with a large χ^2/d.o.f. value have either tiny errors or wiggles in the observed rotation curves that cannot be reproduced by MOND either. We have also compared our fits with the MOND fits in Li et al. [97]. The major difference is that they marginalized over both the distance and inclination uncertainties, while we did not. The MOND fits in [97] are slightly better than our MOND fits due to the two additional variables (distance and inclination), but still only about 20% of the galaxies are fit with χ^2/d.o.f. ≤ 1. For comparison, we have checked over 60% of the MCMC SIDM fits have χ^2/d.o.f. ≤ 1, which is vastly superior.

We emphasize that the diversity in the inner rotation curves is also reflected in the $g_{\rm tot}$–$g_{\rm bar}$ plane, as explicitly demonstrated in Sec. 2.7.2, where we show the $g_{\rm tot}$ vs $g_{\rm bar}$ plot, but now split the sample into two sets: radii outside and inside $2R_{\rm d}$ with $R_{\rm d}$ being the scale radius of the stellar disk. The scatter is relatively large for radii $< 2R_{\rm d}$, and this is due to the different shapes in the inner rotation curves and not just the result of random errors (see also [119]). On the other hand, there is a clear ordered behavior of $g_{\rm tot}$ vs $g_{\rm bar}$ curves for radii $> 2R_{\rm d}$, which is a reflection of the BTFR: the tight correlation between the flat circular velocity, $V_{\rm f}$, and the total baryonic mass, $M_{\rm bar}$ for spiral galaxies [120]. In this regime, $g_{\rm tot} \approx \sqrt{g_\dagger g_{\rm bar}}$, where $g_{\rm tot} \approx V_{\rm f}^2/r$ and $g_{\rm bar} \approx GM_{\rm bar}/r^2$, hence we have $V_{\rm f}^4/(GM_{\rm bar}) \approx g_\dagger$. This is the success of MOND, i.e., if one assumes $M_{\rm bar} \propto V_{\rm f}^4$, then the normalization of the BTFR also predicts the rotation curve, which in many cases is a good fit to the observed one. Many studies do find $M_{\rm bar} \propto V_{\rm f}^s$ with $3 < s < 4$ [4, 121, 122], as we will also show in Sec. 2.5; $s = 4$ is not forced upon us by the data, but it is not ruled out either. However, the MOND relation (Eq. 2.2) cannot explain the full range of the diversity in the inner rotation curves, while the success of SIDM is deeply rooted to hierarchical structure formation, as we discuss in the next section.

2.4 The Concentration-Mass Relation and Origin of the Characteristic Acceleration Scale

We have demonstrated that SIDM explains *both* the diversity and the tight RAR exhibited in the rotation curves, as dark matter self-interactions thermalize the inner halo in the presence of the baryonic potential. Here, we show the host halos in the SIDM fits are consistent with predictions in the hierarchical structure formation model, see, e.g., [123, 124, 2]. Since the outer halo ($r \gtrsim r_1$) remains unchanged for $\sigma/\mathrm{m} = 3\ \mathrm{cm}^2/\mathrm{g}$, we parameterize an SIDM halo using the concentration and mass or, equivalently, the maximal circular velocity ($V_{\max}$) and the associated radius ($r_{\max}$) of its CDM counterpart. Ideally, one would measure these halo parameters directly from the kinematics data and compare them with simulations. Unfortunately, most rotation curves do not have the radial extent needed to sufficiently constrain them. In this work, we impose the cosmological concentration-mass relation [2] as a prior similar to Ref. [125] and examine the consistency between its consequences and observations.

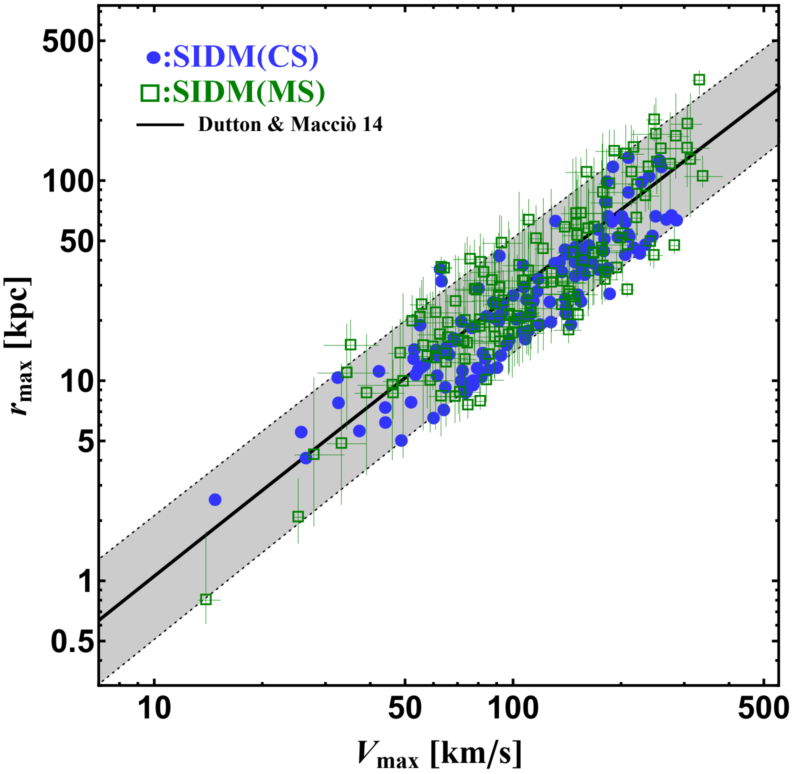

Figure 2.4: $r_{\max}$–$V_{\max}$ distributions of the host halos in the SIDM fits with controlled (circles) and MCMC (squares) samplings. We also show the mean relation (black solid) and 2σ scatter (gray shaded) predicted in cosmological CDM simulations [2].

In Fig. 2.4, we show the $r_{\max}$–$V_{\max}$ distributions from our controlled (circles) and MCMC (squares) samplings. For the former, we intend to seek the best SIDM fits to the rotation curves following the mean relation (solid) from simulations. For the sample we consider, 97% galaxies can be fitted within the 2σ band (gray shaded), calculated from the relation $\log_{10} c_{200} = 0.905 - 0.101 \log_{10}(M_{200}/10^{12}h^{-1}M_{\odot})$ with an intrinsic scatter of 0.11 (1σ) [2]. For the latter, we impose the c_{200}–M_{200} relation as a top-hat prior within the 3σ range in our MCMC sampling, together with an additional constrain on $V_{\max}$, $1/\sqrt{2} < V_{\max}/V_{\rm f} < \sqrt{2}$. The resulting inferences (median and 1σ error) are shown in the figure. The two results agree well with each other. It is remarkable that even with the stringent constraints on $V_{\rm max}$ and $r_{\rm max}$ (through the c_{200}–M_{200} relation), the SIDM halo model is able to fit the diverse rotation curves, as illustrated in Figs. 2.1 and 2.2. Indeed, with the concentration-mass relation, we find the $\Upsilon_{\star,\rm disk}$ distribution is peaked toward $0.5M_\odot/L_\odot$ in the fits, shown in Fig. 2.3 (left).

To see the MOND acceleration scale emerging from the hierarchical structure formation model, we parametrize a CDM halo with its gravitational acceleration at $r = 0$ as $g_{\rm NFW}(0) = GM/r^2|_{r\to 0} \approx 2\pi G\rho_s r_s \approx 2\pi V_{\rm max}^2/(1.26 r_{\rm max})$, where $V_{\rm max} \approx \sqrt{0.58 G\rho_s r_{\rm max}^2}$ and $r_{\rm max} \approx 2.16 r_s$. Taking the mean cosmological $V_{\rm max}$–$r_{\rm max}$ relation, $r_{\rm max} = 27$ kpc$(V_{\rm max}/100~{\rm km/s})^{1.4}$, we have $g_{\rm NFW}(0) \approx 1.0\times10^{-10}~{\rm m/s^2}~(V_{\rm max}/240~{\rm km/s})^{0.6}$, which is close to the MOND acceleration parameter $g_\dagger$. This is the underlying reason why the empirical MOND relation captures the overall stellar kinematics of spiral galaxies well. In the presence of dark matter self-interactions and baryons, the actual central acceleration deviates from $g_{\rm NFW}(0)$, but the general argument still holds. For example, we can characterize a halo with the acceleration at the scale radius r_s, where the impact of dark matter self-interactions and influence of baryons tend to be small, $g_{\rm NFW}(r_s) \approx 0.39 g_{\rm NFW}(0)$, slightly smaller than $g_{\rm NFW}$ at the center. The characteristic halo acceleration has a mild dependence on $V_{\rm max}$, ranging from 20 to 300 km/s in the sample, and it also varies with the scatter in the cosmological relation. This variation is important, as shown in Fig. 2.4. Since MOND does not have such flexibility (see also [126]), its overall fits are worse than the SIDM ones, as illustrated in Fig. 2.3 (right). We emphasize that $g_\dagger = 1.38\times10^{-10}~{\rm m/s^2}$ inferred from our SIDM fits in Sec. 2.3 is an average quantity over the sample after fitting to Eq. 2.2, not a universal value for all the galaxies as in MOND.

The calculation of the acceleration due to dark matter toward the center is more subtle. Inside a constant density core $g_{\mathrm{SIDM}}(r) \propto r$, and we need to specify the radius where the acceleration is being computed. The half-light radius ($r_{1/2}$), which encloses half the luminosity, is typically used to characterize the size of the stellar distribution, so that is a natural radius to compute the acceleration at $r_{1/2}$. On average, the stellar half-light radius is empirically observed to track the virial radius as $r_{1/2} \approx 0.015 r_{\mathrm{vir}}$ [127], and we have $r_{1/2} \approx 1.7 R_{\mathrm{d}}$ for an exponential disk model. Without a significant contribution from baryons to the gravitational potential, SIDM predicts that $g_{\mathrm{SIDM}}(r_{1/2}) = 10^{-11}\ \mathrm{m/s^2} (V_{\max}/100\ \mathrm{km/s})^{0.2}$ for the median halo concentration, and its dependence on the halo mass is extremely mild. When baryons contribute, g_{tot} does not increase linearly with g_{bar} since both the central SIDM density and the core radius depend on the gravitational potential contributed by the baryons. The net result is a strong correlation between g_{tot} and g_{bar}, which is clearly evident in Fig. 2.2. The model predictions have a definite width in the g_{tot} vs g_{bar} plane and we have shown clearly that this scatter is required to fully explain the diversity in the rotation curve data.

2.5 The Correlations between the Total Luminous and Dark Matter Masses

We have seen the SIDM fits to the rotation curves require values for the halo concentration parameter that are completely in line with N-body simulations of structure formation using the cosmological parameters from the Planck experiment [128, 129]. In addition, the stellar mass-to-light ratios are consistent with the results from stellar population models [106].

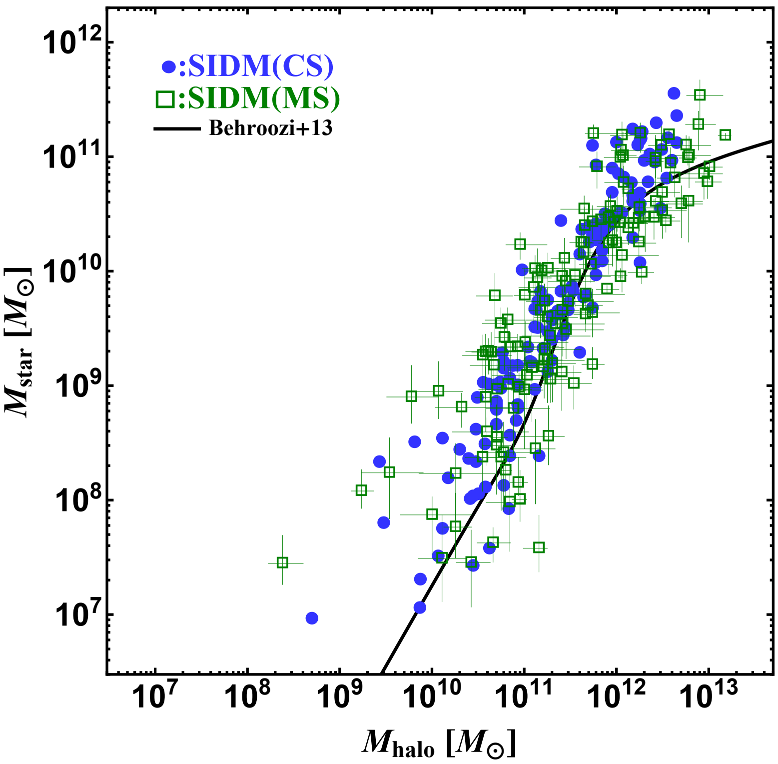

Figure 2.5: Halo virial mass vs galaxy stellar mass from the SIDM fits. The black solid line corresponds to the abundance matching inference from [3].

This leads to a natural question: what is the predicted halo mass for a given stellar mass in the SIDM model? Since we assume the primordial matter power spectrum is unchanged from the CDM one for the scales we are interested in, there should be a relation consistent with the abundance matching results in the literature. In Fig. 2.5, we show the stellar mass vs halo mass relation derived using the mass-to-light ratios from controlled (circles) and MCMC (squares) samplings. The error bars on the MCMC points denote the 1σ widths from the posteriors ($16^{\rm th}$ and $84^{\rm th}$ percentiles). Our results are consistent with the overall trend in the relation from abundance matching (solid) [3] (see [119] for the CDM case). We also note that there is tendency for our data points to lie a bit the left of the abundance matching line. The halo masses inferred from our fits seem to be systematically lower than those inferred in [3]. This could be due to different assumptions on the cosmological parameters in deriving the halo concentration-mass relation, or other differences in the analyses. A systematic investigation of this subject would be a fruitful avenue for future research. In addition, there are a few outliers on the left side of the black line in the low-mass regions, and many of them have low-quality observational data, as we will discuss later.

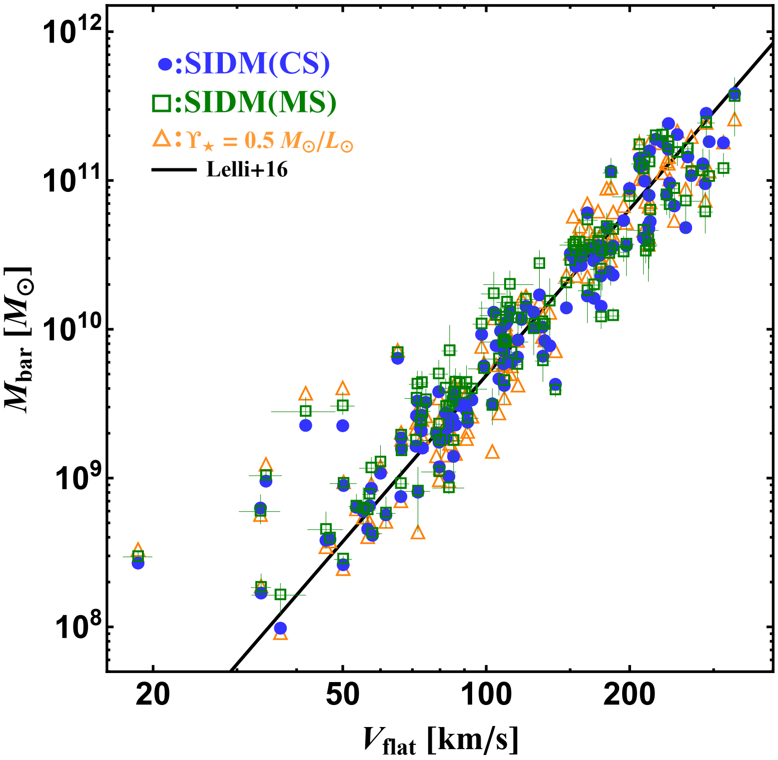

Figure 2.6: total baryonic mass vs flat circular velocity for the 135 galaxies, where $M_{\rm bar}$ is inferred from our SIDM fits (circles and squares). For comparison, we also show the case (triangles) when $\Upsilon_{\star,\rm disk}$ and $\Upsilon_{\star,\rm bulge}$ are fixed to $0.5M_\odot/L_\odot$ [4]. The black solid line is the mean baryonic Tully-Fisher relation from [4], derived from 118 SPARC galaxies with $\Upsilon_{\star,\rm disk} = \Upsilon_{\star,\rm bulge} = 0.5M_\odot/L_\odot$, at which the scatter is minimized.

We have already alluded to the importance of the BTFR in our discussion of the RAR. Lelli et al. [4] selected 118 SPARC galaxies and found that their $V_{\rm f}$–$M_{\rm bar}$ inferences can be fitted with a simple relation: $\log(M_{\rm bar}) = s\log(V_{\rm f}) + \log(A)$, where $s = 3.71 \pm 0.08$ and $\log(A) = 2.27 \pm 0.18$ for $\Upsilon_{\star,\rm disk} = \Upsilon_{\star,\rm bulge} = 0.5M_\odot/L_\odot$. Fig. 2.6 shows the $V_{\rm f}$–$M_{\rm bar}$ inferences with the $\Upsilon_{\star,\rm disk}$ and $\Upsilon_{\star,\rm bulge}$ values from the controlled (circles) and MCMC (squares) fits. The error bars in $M_{\rm bar}$ on the MCMC points denote the 1σ widths in the stellar mass-to-light ratios from the posteriors, and the errors in $V_{\rm f}$ are taken directly from the SPARC dataset [1]. We also show the fit from [4] as the solid line of Fig. 2.6. Note that this fit used 118 galaxies and a few outliers at the low V_{f} end were not included. For comparison, we plot the 135 galaxies in our sample as triangles by fixing $\Upsilon_{\star,\mathrm{disk}} = \Upsilon_{\star,\mathrm{bulge}} = 0.5 M_{\odot}/L_{\odot}$. We see that their distribution in the V_{f}–M_{bar} plane is almost identical to the one from our SIDM fits. This is not surprising, as the $\Upsilon_{\star,\mathrm{disk}}$ values inferred from the SIDM fits are peaked toward 0.5 $M_{\odot}/L_{\odot}$ as shown in Fig. 2.3 (left). Thus, we conclude that the SIDM fits also lead to a tight BTFR relation. For our fits, we find $s \approx 3.46$ (CS), 3.27 (MS) and 3.58 ($0.5 M_{\odot}/L_{\odot}$), excluding six obvious outliers on the left side of the black line. Note five of them, F 561-1, PGC 51017, UGC 04305, UGC 06628 and UGC 09992, have either low-quality rotation curves or small inclination angles, and they may not be well-suited for dynamical analysis. We have also checked that these galaxies are also the outliers in the low-mass regions of the M_{star}–M_{halo} relation, shown in Fig. 2.5.

We note that there is no evidence in the data for $s = 4$ exactly, i.e., $M_{\mathrm{bar}} \propto V_{\mathrm{f}}^4$, which is the motivation for MOND, in either the constant $\Upsilon_{\star}$ fits or in the SIDM fits. We note that V_{f} may not be a good proxy for the asymptotic velocity of every galaxy in the sample and systematic effects could lead to a shallower BTFR slope [130]. Many of the recent CDM simulations with efficient baryonic feedback seem to get something akin to the BTFR with $s \approx 3.6$–3.8 [131, 132, 133, 134], but it is fair to say that this is still not well understood theoretically, in particular, the smallness of the scatter in the BTFR, equivalent to the one seen in the RAR [135]. We expect that there will be interplay between dark matter self-interactions and baryonic feedback in changing the halo potential, and understanding how the BTFR emerges in SIDM is fertile territory for research in galaxy formation.

2.6 Discussion and Conclusions

In this work, we have investigated SIDM as a solution to two puzzles that are present in galactic rotation curves: (1) the diversity of inner rotation curves in galaxies that have similar baryon content and similar flat circular velocities, and (2) the small scatter in the radial acceleration relation between the total gravitational acceleration and the one inferred from the baryonic mass content, i.e., uniformity.

We have fitted our SIDM halo model to the rotation curves of 135 SPARC galaxies, and found that it reproduces the observed diversity in the inner regions. The distribution of resulting 3.6 μm stellar disk mass-to-light ratios for the sample peaks at $\Upsilon_{\star,\mathrm{disk}} \approx 0.5\ M_\odot/L_\odot$, in good agreement with the stellar population models. Our fits lead to a radial acceleration relation described by the characteristic acceleration scale $\sim 10^{-10}\mathrm{m/s^2}$, with tight scatter of 0.10 dex. The host halos are fully consistent with the Planck cosmology. The inferred stellar mass-halo mass relation agrees with the result from the abundance matching method, and the fits also predict a tight BTFR. These results provide compelling arguments in favor of the idea that the inner halos of galaxies are kinematically thermalized due to dark matter self-interactions.

The SIDM model automatically inherits all of the successes of the CDM model on large scales, as the predictions are indistinguishable at distances larger than about 10% of the virial radius of galactic halos. The required cross section is similar to the proton-neutron elastic scattering cross section and this may be a strong hint that the dark matter sector replicates some elements of the standard model. The large cross section keeps the inner halo isothermal and this makes the predictions for the central halo profile at later times insensitive to the star formation history, as confirmed in recent hydrodynamical N-body simulations [107, 136]. This implies that a large variety of feedback models, e.g, [47, 137, 138, 139, 140, 5], can be compatible with the SIDM model we have discussed here. The predictions are quantitatively the same for $\sigma/\mathrm{m} \gtrsim 1\ \mathrm{cm}^2/\mathrm{g}$. This makes our results robust, but it makes hard to precisely determine the cross section from kinematic datasets on galaxy scales [73].

There are a number of promising directions that can further test SIDM and explore galaxy formation and evolution in this framework. Here, we highlight a few of them. SIDM simulations predict a correlation between the half-light radius of the stars and the dark matter core size in dwarf and low surface brightness galaxies [103], which should be further explored and may provide an observational test of SIDM. Similarly, the ultra-diffuse galaxies in the clusters could be a test laboratory [141]. A related issue is the origin of the large spread in the surface brightness of galaxies, which remains poorly understood. Interestingly, hydrodynamical simulations of galaxy clusters show that the stellar density profiles in SIDM are more diverse than in their CDM counterparts [107]. Is this a more general feature in SIDM due to the dynamical interplay between core formation and feedback? How does this interplay impact the emergence of the BTFR? Finally, at the lowest mass end, the dwarf spheroidal galaxies, including the so-called ultra-faint dwarfs, in the Local Group could provide a key test of SIDM (see [142, 143]). Dedicated SIDM simulations with the baryons will be required to explore these exciting topics.

The predictive power of the SIDM model, the clear connection to cosmology, and its rich implications for other astrophysical observations and particle physics phenomenology [144], all taken together make a clear case that it should be treated on the same footing as the CDM model. The economical explanation, with the addition of just one parameter, for the diverse rotation curves across the entire range of observed galaxies argues in favor of the idea that the dark matter particles have a large affinity for the self-interactions.

2.7 Appendix

2.7.1 Methods

We provide a detailed description of the analytical model developed previously [72, 73] and the fitting procedure in this section. We divide the halo into an inner and an outer region [79] with the aim that the outer halo is not significantly changed by the self-scattering process. In the inner region, dark matter self-interactions thermalize the halo in the presence of the baryonic potential, and we model the dark matter distribution using the isothermal density profile, $\rho_{\rm iso} \propto \exp(-\Phi_{\rm tot}(R,z)/\sigma_{\rm v0}^2)$. Poisson's equation relates $\Phi_{\rm tot}$ to the dark matter and baryon profiles as

$$\nabla^2\Phi_{\rm tot}(R,z) = 4\pi G[\rho_{\rm iso}(R,z) + \rho_{\rm b}(R,z)]. \tag{2.3}$$

For the outer halo, where the self-scattering effect becomes negligible, we model the dark matter distribution with an NFW profile $\rho_{\rm NFW}(r) = \rho_s r_s^3/r(r+r_s)^2$. To construct the full SIDM halo profile, we define a radius r_1, where dark matter particles had one interaction on average over the age of the galaxy. We join the spherically-averaged isothermal ($\rho_{\rm iso}$) and spherical NFW ($\rho_{\rm NFW}$) profiles at $r = r_1$ such that the mass and density are continuous at r_1. Thus, the isothermal parameters (ρ_0, $\sigma_{\rm v0}$) directly map on to the NFW parameters (r_s, ρ_s) or ($r_{\rm max}$, $V_{\rm max}$).

The value of r_1 is determined by the following condition,

$$\langle \sigma v_{\rm rel}\rangle\, \rho_{\rm NFW}(r_1) t_{\rm age}/m = N_{\rm sc}, \tag{2.4}$$

where σ is the self-scattering cross section, m is the dark matter particle mass, $v_{\rm rel}$ is the dark matter relative velocity in the halo, $\langle ... \rangle$ denotes averaging over the Maxwellian velocity distribution, $t_{\rm age}$ is the age of the galaxy, and $N_{\rm sc}$ is a factor of order unity, to be determined by calibrating to simulations. In this work, we have set $t_{\rm age} = 10$ Gyr and $N_{\rm sc} = 1$, which reproduce simulation results well; see Sec. 2.7.2. In principle, we should use different ages for each galaxy, say between 10 Gyr and 13 Gyr. However, our model can only constrain the combination of the cross section and the age. More importantly, we have set $\sigma/{\rm m}$ to a large enough value that the SIDM density profile is insensitive to small changes in the cross section. We assume that this cross section is a constant over the SPARC sample, so $\langle \sigma v_{\rm rel} \rangle = \sigma(4/\sqrt{\pi})\sigma_{\rm v0}$. In this work, we present our results for $\sigma/{\rm m} = 3~{\rm cm}^2/{\rm g}$ on galaxy scales, which can be naturally realized in particle physics models of SIDM [53, 54, 55, 56, 57, 58, 59, 60, 61, 62, 63, 64, 65, 66, 67, 68, 69, 70, 71].

We take two independent but complementary approaches. In the first one, we assume a thin-disk profile for the stellar disk in solving Eq. (2.3), $\rho_{\rm b}(R, z) = \Sigma_0 \exp(-R/R_{\rm d})\delta(z)$, where Σ_0 is the central surface density and $R_{\rm d}$ is the scale radius. For each galaxy, we reconstruct the Σ_0 and $R_{\rm d}$ values by fitting the profile to the disk contribution of the rotation curve as in [73]. We neglect the baryonic influence on the SIDM halo from the gas and bulge potentials, but include all the mass components in modeling the total circular velocity. This is a reasonable approximation for the following reasons: (1) the gas is less centrally concentrated and so its impact on the SIDM density profile is smaller, (2) the bulge (when present) mainly affects the innermost region, while the disk contributes in this region as well as at farther radii. Ref. [73] solved Eq. (2.3) with the thin-disk approximation and created numerical templates for the isothermal density profile on the grid of $a \equiv 8\pi G\rho_0 R_{\rm d}^2/(2\sigma_{\rm v0}^2)$ and $b \equiv 8\pi G\Sigma_0 R_{\rm d}/(2\sigma_{\rm v0}^2)$. When the stellar profile is known, the parameters a and b give the central density and dispersion of the isothermal dark matter halo, which completely specify the inner density profile. We interpolate the templates to generate rotation curves for any set of $(\rho_0, \sigma_{v0}, \Sigma_0, R_d)$. The fixed value of the cross section allows us to match this density profile to the outer spherically-symmetric NFW density profile. Since $r_1 \sim r_s \gg R_d$ in our fits, the influence of the baryons on the SIDM halo shape becomes negligible and the SIDM halo recovers spherical symmetry at r_1; see Sec. 2.7.2.

In fitting to the SPARC sample with the templates, we take a controlled sampling approach. For a given galaxy, we start with the mean $r_{\max}$–$V_{\max}$ relation from cosmological ΛCDM simulations [2] and an NFW profile that matches the flat part of the rotation curve. Then, we choose an appropriate $\Upsilon_{\star,\text{disk}}$ ($\Upsilon_{\star,\text{bulge}}$) value to reproduce the inner rotation curve. We calculate a χ^2/d.o.f. value for each fit and iterate this process manually by adjusting the parameters until a good fit is achieved. For most galaxies, the very first step provides decent fits, showcasing the simplicity of the model and its ability to fit the observed data simultaneously. For each galaxy, we demand the ($r_{\max}$, $V_{\max}$) values to be within the $\sim 2\sigma$ band. In this way, we have good control over the halo parameters in the fits. The goal is to see to what degree are the galaxy halos of the SPARC sample consistent with predictions of the hierarchical structure formation scenario, and the extracted $\Upsilon_\star$ values consistent with stellar population synthesis model results [106].

In our second approach, we perform a MCMC sampling of the SIDM model parameter space. Since it is computationally expensive to use the templates, we use a spherical approximation to model the baryon distribution [80, 104]. We create a spherical baryonic mass profile from the stellar and gas masses, such that the baryonic mass within a sphere of radius r is $M_{\rm b}(r) = (V_{\rm disk}^2 + V_{\rm bulge}^2 + V_{\rm gas}^2)r/G$, where $V_{\rm disk}$ is the contribution to the rotation curve from the disk at radius r and similarly for the bulge and gas. Below the smallest radii at which the baryonic contribution is tabulated in the SPARC database, we assume that the density in baryons is constant. Outside the last tabulated radii, we assume that mass is constant. We have tested some galaxies where we change the constant central density to a smoothly matched Hernquist sphere [80] and found no difference.

We solve Eq. (2.3) in the spherical limit by taking $r = \sqrt{R^2 + z^2}$ using the python module `scipy.integrate.odeint`, which uses `LSODA` from the FORTRAN library `odepack`. We compute $\rho_{\rm iso}(r)$ starting at a small radius (10% of the innermost data point) assuming a core, i.e., $d\rho_{\rm iso}/dr = 0$, and integrate the equation to larger radii using the default settings in `scipy.integrate.odeint`. We compared the isothermal halos from this spherical approximation to those from the axisymmetric case (templates) and found agreement within 10–20%. Thus, while we expect some variance in the inferred parameters between the two methods, the overall features should be very similar. This expectation is borne out by our final fits.

We match the isothermal density profile $\rho_{\rm iso}$, parameterized by $(\rho_0, \sigma_{\rm v0})$, to the NFW density profile at r_1, and this determines $(V_{\rm max}, r_{\rm max})$. Thus, the spherical model has four parameters, two for the entire halo and two for the mass-to-light ratios: $(\rho_0, \sigma_{\rm v0}, \Upsilon_{\star,\rm disk}, \Upsilon_{\star,\rm bulge})$. We use the `emcee` implementation of the Affine invariant MCMC ensemble sampler [145] to infer the posteriors of these four model parameters. To streamline the calculation of r_1 at each point in parameter space for matching onto the outer NFW radius, we use the rate of scatterings, $\Gamma_0 = \rho_0(\sigma/\mathrm{m})(4/\sqrt{\pi})\sigma_{\mathrm{v}0}$, within the isothermal core as the MCMC parameter in lieu of the core density ρ_0.

The prior distributions used for the halo parameters and the mass-to-light ratios in the MCMC scan are as follows:

- Γ_0: Uniform prior on $\log_{10}\Gamma_0$ in the range of $2 < \Gamma_0 \times 10$ Gyr $< 10^5$.
- σ_0: Uniform prior on $\log_{10}\sigma_0$ in the range of $2 < \sigma_0/(\mathrm{km/s}) < 500$.
- $\Upsilon_\star$: Uniform prior on both $\Upsilon_{\star,\mathrm{disk}}$ and $\Upsilon_{\star,\mathrm{bulge}}$ in the range of $0.1 < \Upsilon_\star/(M_\odot/L_\odot) < 10$. The parameter $\Upsilon_{\star,\mathrm{bulge}}$ is only included for galaxies whose surface brightness profiles have a stellar bulge decomposition provided in the SPARC dataset. All galaxies have $\Upsilon_{\star,\mathrm{disk}}$ as a parameter describing their stellar disk.

We have also added a term to the χ^2 that imposes the c_{200}–M_{200} relation. This term has a mean value for $\log_{10} c_{200}$ given by the relation $0.905 - 0.101\log_{10}(M_{200}/10^{12}h^{-1}M_\odot)$ [2], with an error of 0.33 dex.

Additionally, we also impose two regularization priors.

- We add 5% of V_f in quadrature for calculating the likelihood function. This allows the code to disregard the points deep within the central regions and those with tiny errors, so that they do not skew the fits. We have checked that it doesn't change the inference of cores/cusps. We *do not* include this regularization error when quoting χ^2 values.
- We impose a uniform regulation prior on V_max: $1/\sqrt{2} < V_\mathrm{max}/V_\mathrm{f} < \sqrt{2}$. For most of the galaxies ($\sim$ 80%), our MCMC program can find physical fits without this prior.

However, the MCMC sampler tends to pick up fits not consistent with hierarchical structure formation predictions in some cases; typically the dark matter density is unreasonably low in the central regions. This is due to the lack of an extended rotation curve to fully constrain the halo parameters. The additional regularization prior fixes this issue. We have also checked that the results are similar if we consider a more generous range $1/2 < V_{\rm max}/V_{\rm f} < 2$ (see Sec. 2.7.2).

2.7.2 Supplemental Material

We provide additional information and results to supplement the results in the main text.

- In Table 2.1, we list the galaxies that are shown in Fig. 1 of the main text.
- Fig. 2.7 shows the total acceleration vs the baryonic acceleration for the inner and outer regions.
- Fig. 2.8 shows $r_{\rm max}$–$V_{\rm max}$, $M_{\rm star}$–$M_{\rm halo}$, and $M_{\rm bar}$–$V_{\rm flat}$ relations, similar to Fig. 3 of the main text, but we impose the top-hat prior on the concentration-mass relation with a wider $V_{\rm max}$ regulation, $1/2 < V_{\rm max}/V_{\rm f} < 2$. In addition, we show the results with a Gaussian prior on the concentration-mass relation and $1/\sqrt{2} < V_{\rm max}/V_{\rm f} < \sqrt{2}$.
- Fig. 2.9 shows the SIDM density profiles predicted in the analytical model, compared to cosmological N-body simulations from Elbert et al. MNRAS 453 (2015) no. 1, 29-37, and Creasey et al., MNRAS 468 (2017) no. 2, 2283-2295.

- Fig. 2.10 shows the SIDM density profiles predicted in the analytical model, compared to cosmological N-body simulations from Rocha et al. MNRAS 430 (2013) no. 1, 81-104.

- Fig. 2.11 shows the SIDM fit to NGC 6503 with the numerical templates and the corresponding dark matter density contours.

- Fig. 2.12 and 2.13 shows the MCMC SIDM fits to four galaxies and the corresponding posterior distributions.

- Fig. 2.14 shows the MCMC SIDM fits to two galaxies with and without the regularization prior $1/\sqrt{2} < V_{\rm max}/V_{\rm f} < \sqrt{2}$.

Name	V_f [km/s]	Name	V_f [km/s]	Name	V_f [km/s]	Name	V_f [km/s]
UGC06923	79.6	UGC04278	91.4	F571-8	139.7	NGC7331	239.0
UGC05721	79.7	NGC0247	104.9	NGC4138	147.3	NGC3992	241.0
UGC06446	82.2	NGC0024	106.3	NGC3198	150.1	NGC6674	241.3
UGC08286	82.4	UGC06930	107.2	UGC09037	152.3	IC4202	242.6
NGC2915	83.5	UGC06917	108.7	NGC2683	154.0	UGC06787	248.1
UGC06667	83.8	NGC1003	109.8	NGC6015	154.1	NGC6195	251.7
UGC06399	85.0	NGC4183	110.6	NGC4051	157.0	NGC5005	262.2
NGC2976	85.4	F568-V1	112.3	NGC4100	158.2	UGC02953	264.9
NGC0055	85.6	UGC05986	113.0	NGC6946	158.9	UGC11455	269.4
F583-1	85.8	NGC6503	116.3	NGC3949	163.0	NGC2841	284.8
UGC02259	86.2	NGC3769	118.6	NGC1090	164.4	UGC11914	288.1
NGC0100	88.1	NGC4559	121.2	NGC3726	168.0	UGC02885	289.5
NGC5585	90.3	NGC4010	125.8	NGC3877	168.4	NGC5985	293.6
UGC04325	90.9	UGC03580	126.2	NGC4088	171.7	ESO563-G021	314.6

Table 2.1: Galaxies shown in Fig. 2.1 of the main text.

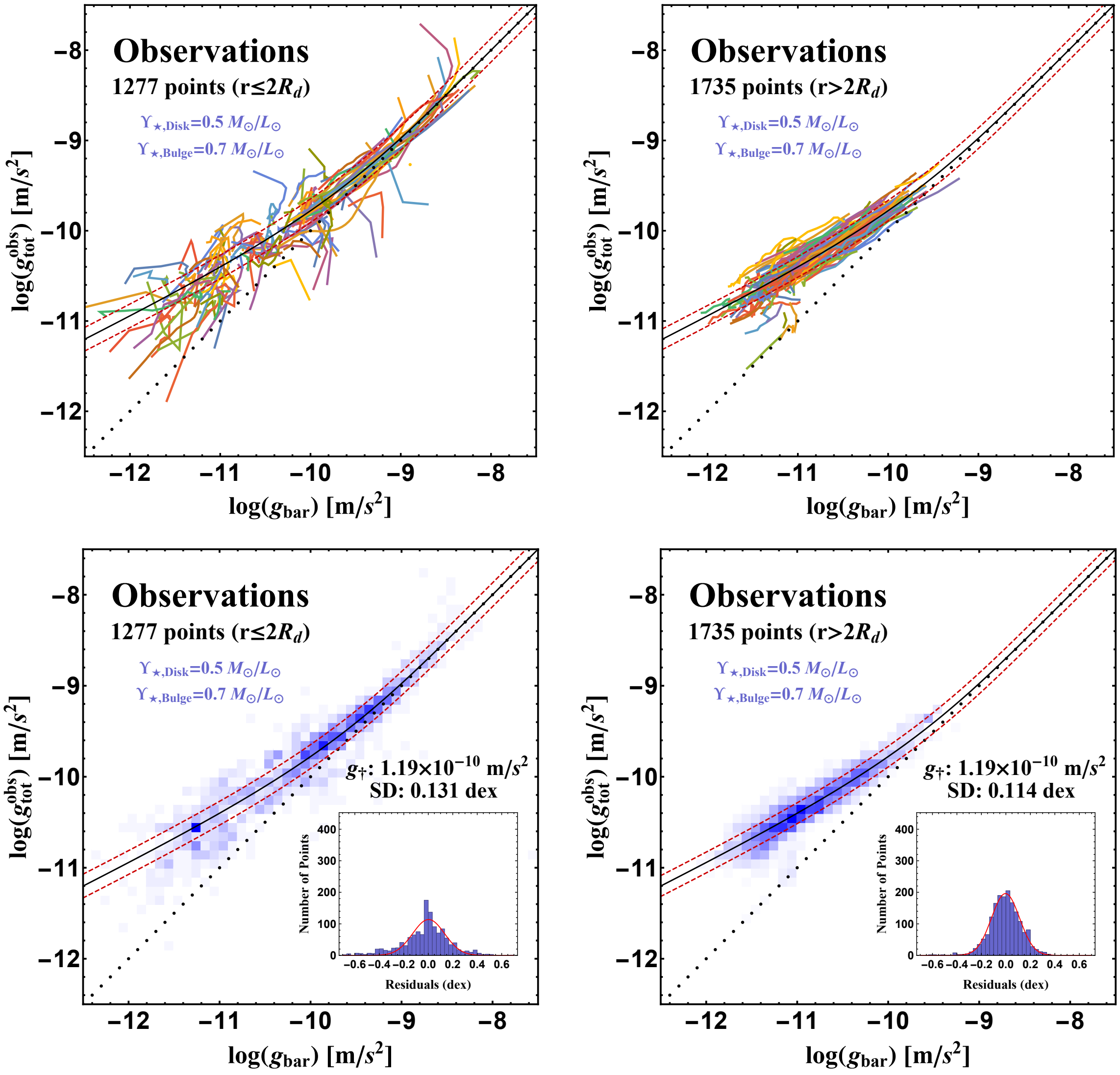

Figure 2.7: *Upper*: the total acceleration vs the baryonic acceleration (colored) for the inner ($r \leq 2R_\mathrm{d}$, left) and outer ($r > 2R_\mathrm{d}$, right) regions, where R_d is the scale radius of the stellar disk. *Lower:* The g_tot–g_bar relation with a different color scheme, where the intensity is proportional to the density of points. The scatter in the g_tot–g_bar relation of the inner regions is visibly larger (black solid).

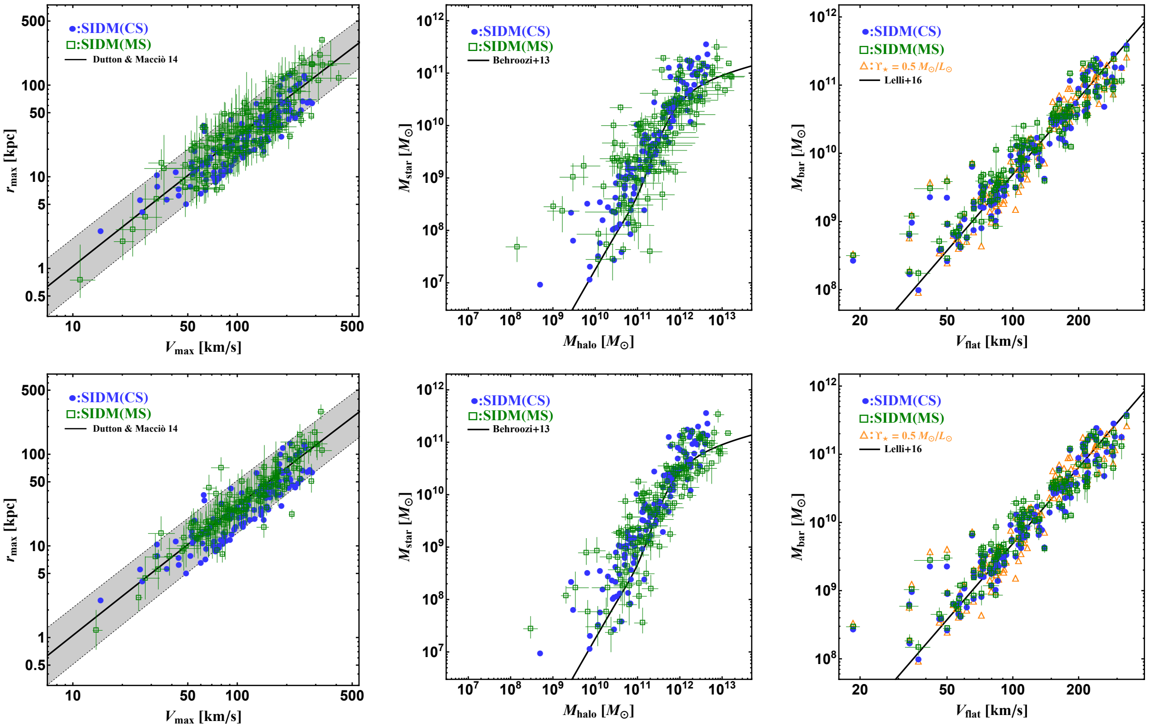

Figure 2.8: *Upper*: Similar to Fig. 2.4 2.5 and 2.6 of the main text, but we impose the top-hat prior on the concentration-mass relation with a wider $V_{\rm max}$ regulation, $1/2 < V_{\rm max}/V_{\rm f} < 2$. *Lower*: Similar to Fig. 2.4 2.5 and 2.6 of the main text, but with a Gaussian prior on the concentration-mass relation (with width 0.11 dex) and $1/\sqrt{2} < V_{\rm max}/V_{\rm f} < \sqrt{2}$.

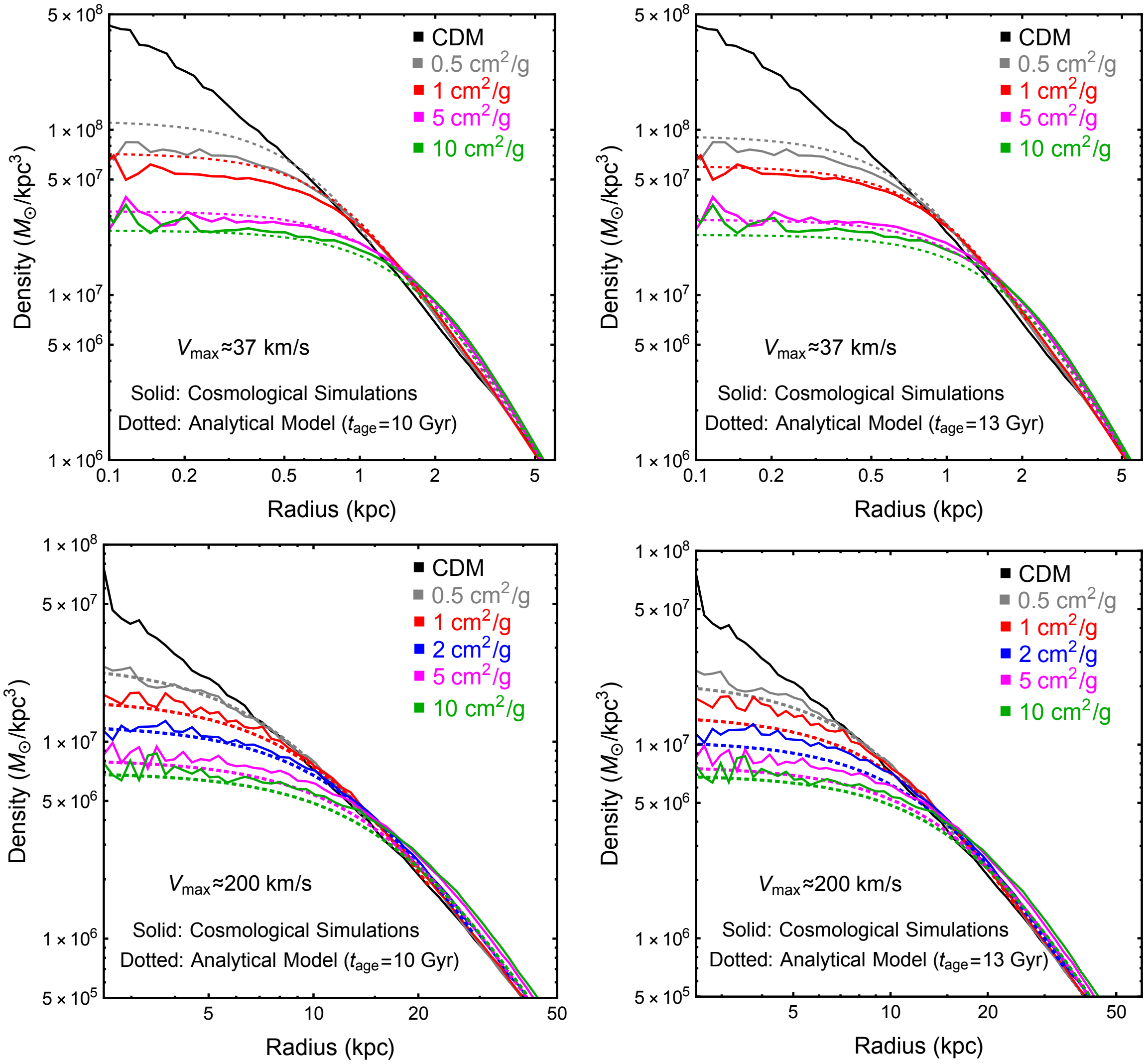

Figure 2.9: *Upper:* Density profiles predicted in the analytical model (dotted), compared with simulations (solid) from Elbert et al., MNRAS 453 (2015) no. 1, 29-37, based on the SIDM code developed Rocha et al. MNRAS 430 (2013) no. 1, 81-104. *Lower:* A similar comparison with simulations from Creasey et al., MNRAS 468 (2017) no. 2, 2283-2295, which used the code developed in Vogelsberger et al., MNRAS 423 (2012) no. 4, 3740-3752. Despite the fact that we impose the exact matching condition at r_1, i.e., $\rho_{\rm iso} = \rho_{\rm NFW}$ and $M_{\rm iso} = M_{\rm NFW}$, and the agreement is better than $\sim$ 5–20% for $\sigma/{\rm m} \geq 1$ cm^2/g and the results change very mildly from $t_{\rm age} = 10$ Gyr to 13 Gyr. Sokolenko et al., JCAP 1812 (2018) no.12, 038, also showed the core sizes predicted in this analytical model are consistent with their simulations, see the core size comparison in Fig. 22 (left panel); the other comparisons in that paper are for different analytic models. The agreement can be further improved through tweaks to this model by including small halo mass or cross section dependence in the r_1 definition or allowing freedom in the matching at the level of $\sim$ 5%. In the paper, we take $\sigma/{\rm m} = 3$ cm^2/g, $t_{\rm age} = 10$ Gyr and the exact matching condition.

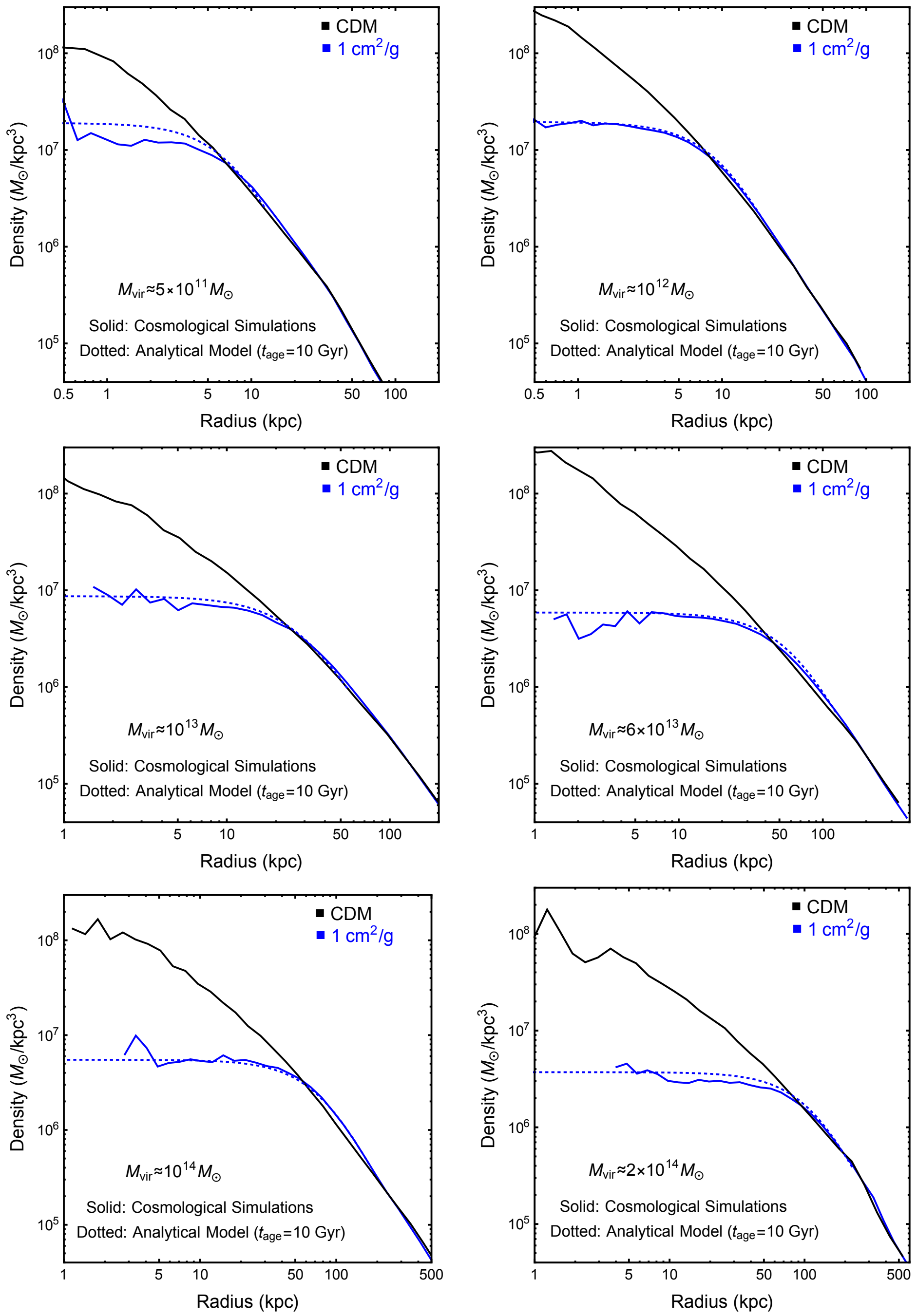

Figure 2.10: Density profiles predicted in the analytical model (dotted), compared with simulations (solid) from Rocha et al. MNRAS 430 (2013) no. 1, 81-104. Our model reproduces the simulation results over a wide range of halo masses.

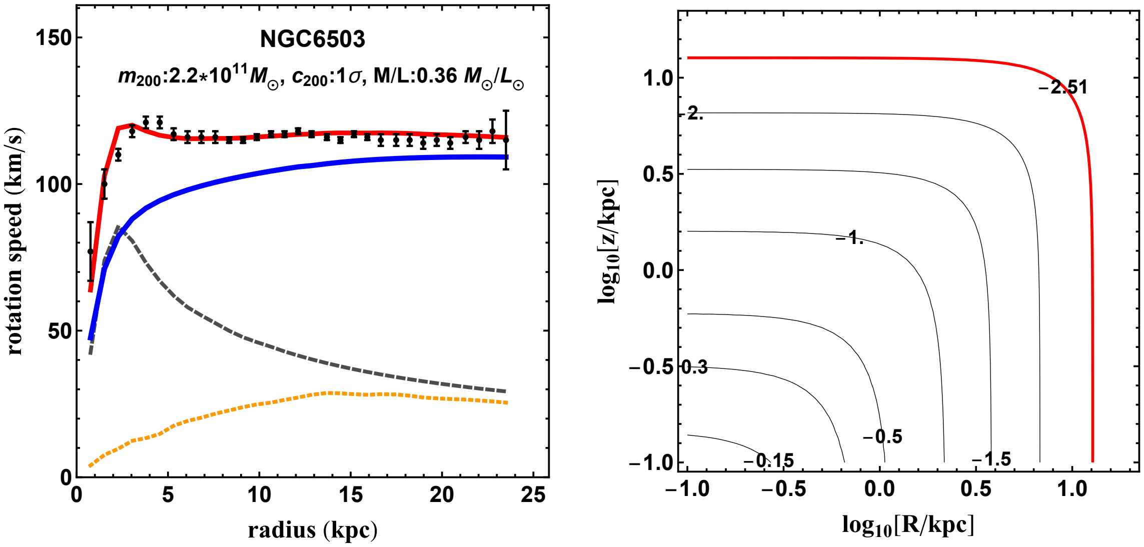

Figure 2.11: *Left*: SIDM fit to NGC 6503 with the numerical templates. *Right:* Contours for the normalized dark matter density, $\log_{10}[\rho(r,z)/\rho_0]$. For this galaxy, the scale radius of the NFW profile is $r_s = 10$ kpc, $r_1 = 12.7$ kpc and the scale radius of the disk $r_d = 1$ kpc. At r_1, the SIDM halo profile is spherically symmetric (red) and it matches to the outer NFW profile naturally.

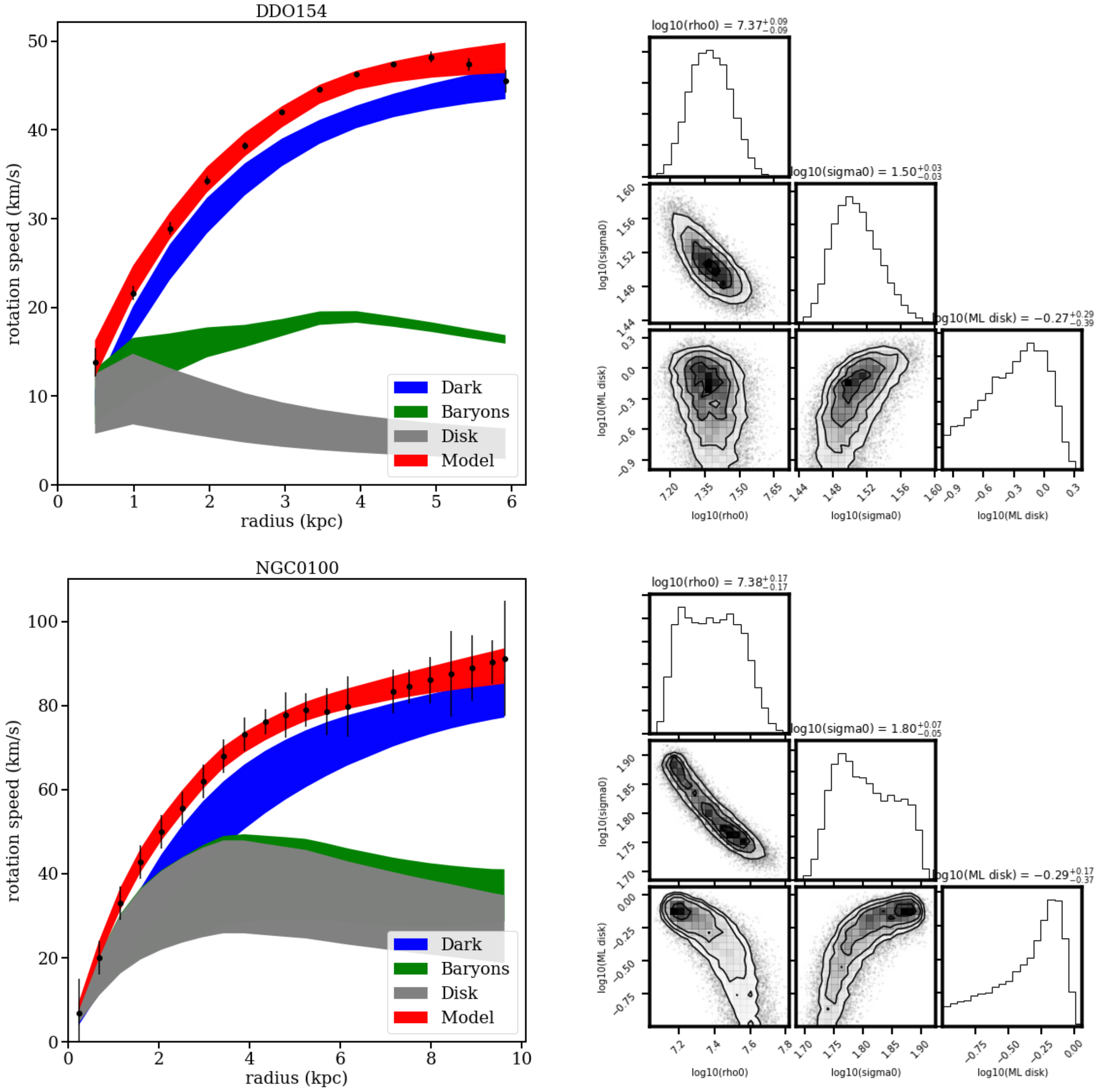

Figure 2.12: *Left*: Example MCMC SIDM fits to two galaxies. *Right:* the corresponding posterior distributions in 2D with contours enclosing probabilities $p = 1 - \exp(-x^2/2)$ for $x = 0.5,\ 1,\ 1.5$ and 2.

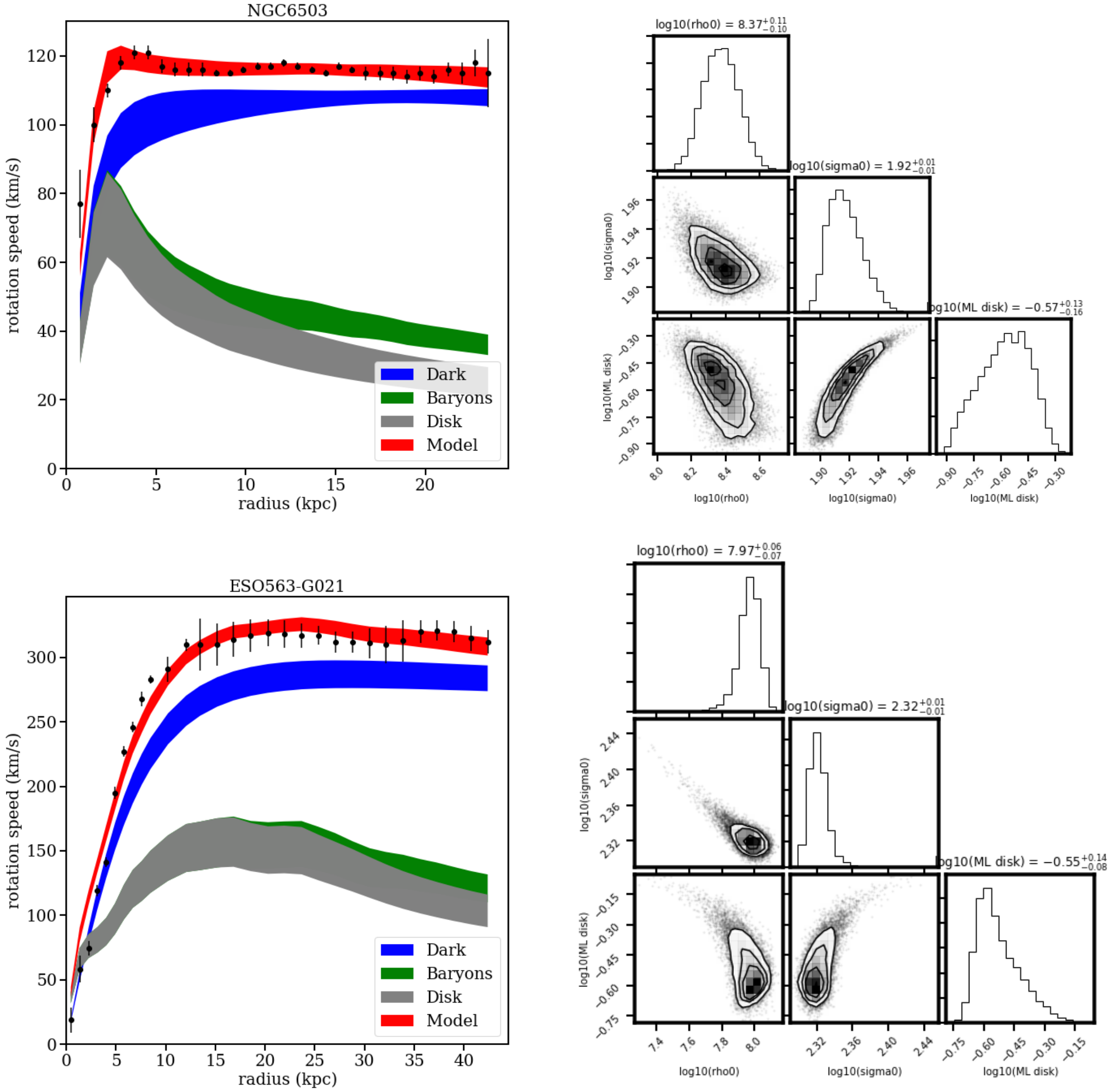

Figure 2.13: *Left*: Example MCMC SIDM fits to two galaxies. *Right:* the corresponding posterior distributions in 2D with contours enclosing probabilities $p = 1 - \exp(-x^2/2)$ for $x = 0.5,\ 1,\ 1.5$ and 2.

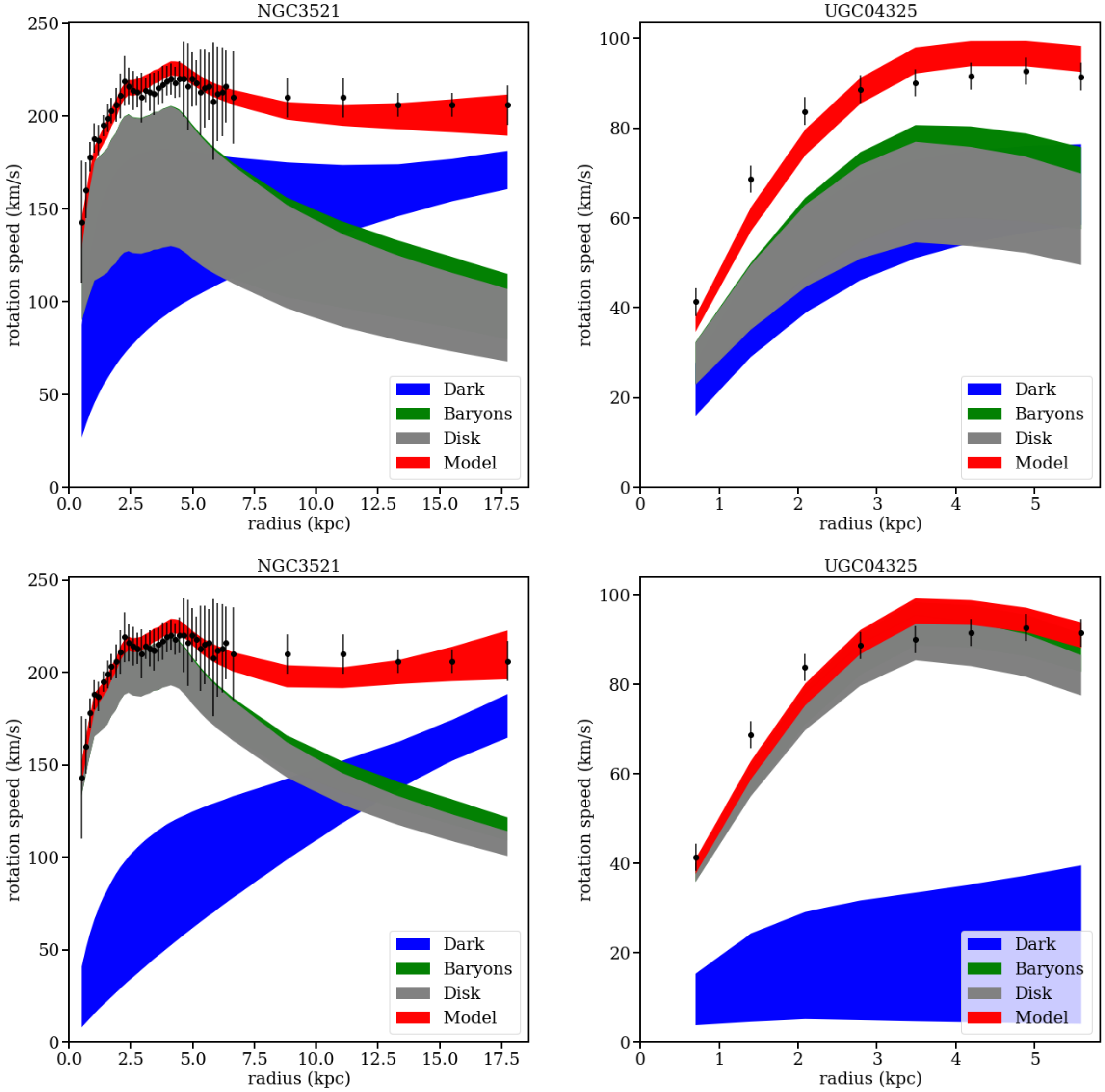

Figure 2.14: MCMC SIDM fits with (top) and without (bottom) the regularization prior $1/\sqrt{2} < V_{\rm max}/V_{\rm f} < \sqrt{2}$ for NGC 3521 and UGC 0435. For the two galaxies, the regularization prior is important to achieve fits consistent with expected from the hierarchical structure formation model. These examples demonstrate that the MCMC scans without the regularization prior can get stuck in regions of parameter space that have very low density of dark matter, which is not consistent with expectations based on the standard cosmological model.

2.7.3 Diversity and Uniformity: Two Sides of One Coin

In the main text, we have discussed how the $g_{\rm tot}$ and $g_{\rm bar}$ are related in the outer region of galaxies with the Tully-Fisher relation, how the dark matter halos from the hierarchical structure formation roughly determine the fundamental acceleration scale, and why the SIDM model performs better than MOND on fitting to the rotation curves. In this subsection, we build a link between the SIDM formalism and the whole functional form of MOND. The idea is from the following observation. The MOND formula actually offers a way to calculate the $g_{\rm tot}$ from $g_{\rm bar}$. On the other side, $g_{\rm tot}$ is linked to $\Phi_{\rm tot}$, the total gravitational potential, through $g_{\rm tot} = -\nabla\Phi_{\rm tot}$ in Newtonian gravity. More importantly, $\Phi_{\rm tot}$ plays an important role in the SIDM model, that is, it determines the dark matter density distribution in the thermalized region in a large sense through $\rho_{\rm iso}(\vec{x}) = \rho_0 \cdot \exp(-\Phi_{\rm tot}(\vec{x})/\sigma_0^2)$. These links make us imagine that in the Newtonian gravity, the MOND formula is actually describing a tight correlation between baryons and dark matter, which is realized through the thermalization of dark matter particles with self-interactions.

Fig. 2.15 shows the first supporting evidence to the above argument. In Fig. 2.15, the $g_{\rm tot}$ and $g_{\rm bar}$ from 3012 total data points in SIDM model are divided into two groups based on whether it is within r_1 (left) or out of r_1 (right). It shows 87.6% of the total data points are in the thermalized region within r_1. These data points occupy the most part and weight of the RAR and play an important role to determine the $g_\dagger$ in the fitting formula, i.e., the black fitting curves and statistical deviation as shown in Fig. 2.15 (left). On the contrary, the data points out of r_1 are less dominant and are mainly located at the low left corner of the fitting curve as shown in Fig. 2.15 (right). They may effect the location of the fitting curve and standard deviations sightly, but are not in a determining role.

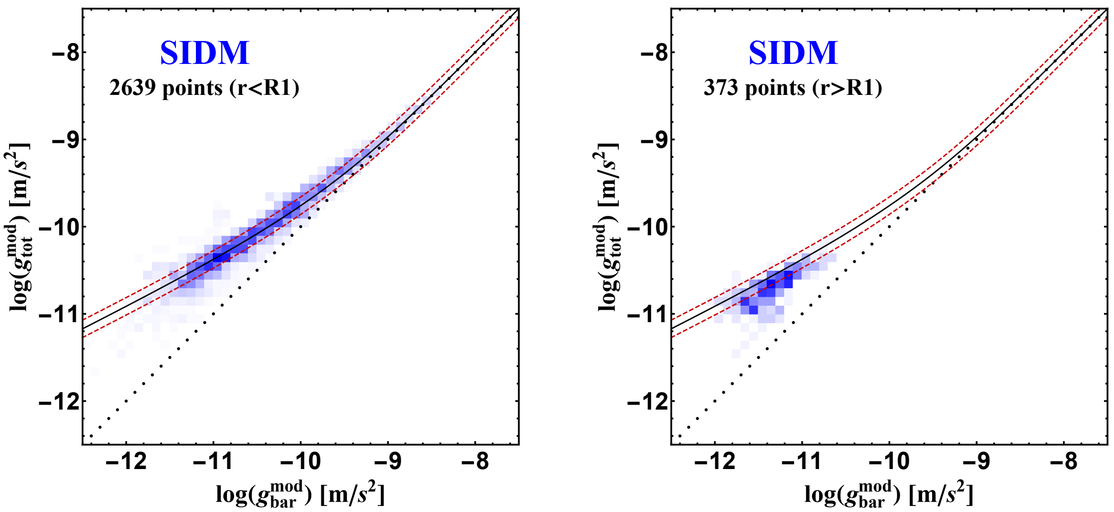

Figure 2.15: *Left*: Similar to the radial acceleration relation shown in Fig. 2.2 but only with the data points within r_1 in each galaxy. *Right*: $g_{\rm tot}^{\rm mod}$ and $g_{\rm bar}^{\rm mod}$ for data points outside of r_1. In both plots, the color intensity is proportional to the local number density of data points. The black solid line, two red dashed curves and the black dotted line in each plot are the same as those in Fig. 2.2.

Then we derive a more clear link between a thermalized SIDM halo and the MOND formula (RAR). The dark matter density in the isothermal region, $\rho_{\rm iso}(\vec{x}) = \rho_0 \cdot \exp(-\Phi_{\rm tot}(\vec{x})/\sigma_0^2)$, and the relation $g_{\rm tot} = -\nabla\Phi_{\rm tot}$ together imply:

$$g_{\rm tot} = -\frac{\sigma_0^2}{r_{\rm d}}\frac{1}{r_{\rm n}}\frac{{\rm dln}(\rho_{\rm iso})}{{\rm dln}(r)},\ r_{\rm n} = r/r_{\rm d} \tag{2.5}$$

We can write it in a more concise way:

$$g_{\rm tot} = g_0 \cdot f(r_{\rm n}) \tag{2.6}$$

with

$$g_0 = \frac{\sigma_0^2}{r_{\rm d}},\ f(r_{\rm n}) = |\frac{{\rm logSlope}(r_{\rm n})}{r_{\rm n}}|,\ {\rm logSlope}(r_{\rm n}) = \frac{{\rm dln}(\rho_{\rm iso})}{{\rm dln}(r)}. \tag{2.7}$$

On the MOND side, the formula from RAR is

$$g_{\rm obs} = \frac{g_{\rm bar}}{1 - \exp(-\sqrt{g_{\rm bar}/g_{\dagger}})} \tag{2.8}$$

After simplification, it becomes following:

$$g_{\rm obs} = g_{\dagger} \cdot f(x) \tag{2.9}$$

with

$$x = g_{\rm bar}/g_{\dagger},\ f(x) = \frac{x}{1 - \exp(-\sqrt{x})} \tag{2.10}$$

The similarity is obvious from the comparison between Eq. 2.6 and Eq. 2.9. $g_0 = \sigma_0^2/r_{\rm d}$ and $f_{\rm SIDM}$ in the SIDM model correspond to $g_{\dagger}$ and $f_{\rm MOND}$ in the MOND theory. However, the meanings of them are different. In the MOND theory, $g_{\dagger}$ is a fundamental acceleration scale which is fixed. $f_{\rm MOND}$ is a determined function that is used to calculate the total acceleration from the baryon contribution. They are the same for all the galaxies. If there is any difference, that would be the different input and output from various galaxies. In the SIDM model, g_0 is an acceleration scale related to the dark matter velocity dispersion and galaxy scale, which would be unique to each galaxy. $f_{\rm SIDM}$ contains the logarithmic slope and radial information of dark matter density profile, which also varies among different galaxies.

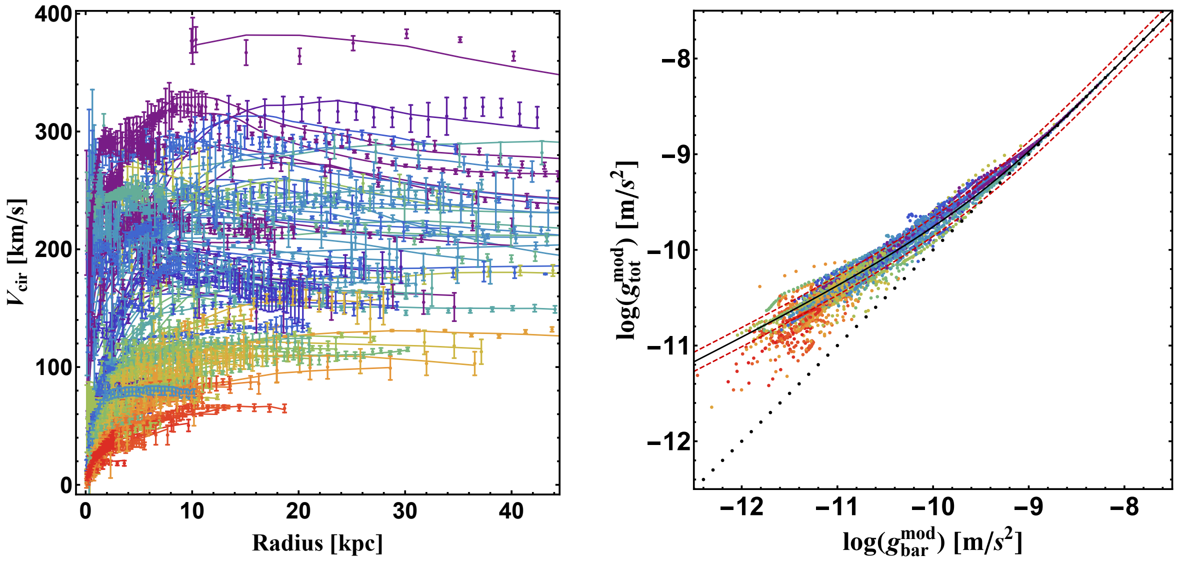

Figure 2.16: *Left*: The 135 selected SPARC rotation curves and SIDM $\sigma/\mathrm{m} = 3\ \mathrm{cm}^2/\mathrm{g}$ fits. Each of them is color coded based on its $M_{\rm bar}/r_{\rm d}^2$ value. From small to large $M_{\rm bar}/r_{\rm d}^2$ value, the galaxies are shown from red to violet. *Right*: Similar to the radial acceleration relation shown in Fig. 2.2, the data points for each galaxy are shown directly and color coded based on its $M_{\rm bar}/r_{\rm d}^2$ value as *Left*.

In Fig. 2.16, we distinguish different galaxies in RAR plot by color coding each galaxy based on its value of $M_{\rm bar}/r_{\rm d}^2$, which can be converted to a featured acceleration for the baryon component in each galaxy directly by multiplying G, the gravitational constant, and which is also proportional to the surface brightness of that galaxy. $M_{\rm bar}/r_{\rm d}^2$ will usually be small (red) for extended dwarfs and be large (purple) for compact galaxy with high luminosities. This point is illustrated in Fig. 2.16 (left), where colors of galaxies with small to large flat velocities changes from red to purple gradually. In Fig. 2.16 (right), from upper right to lower left, the color changes from purple to red which indicates the RAR are a combined result from compact massive galaxies on the upper right to dark matter dominated dwarf galaxies on the low left.

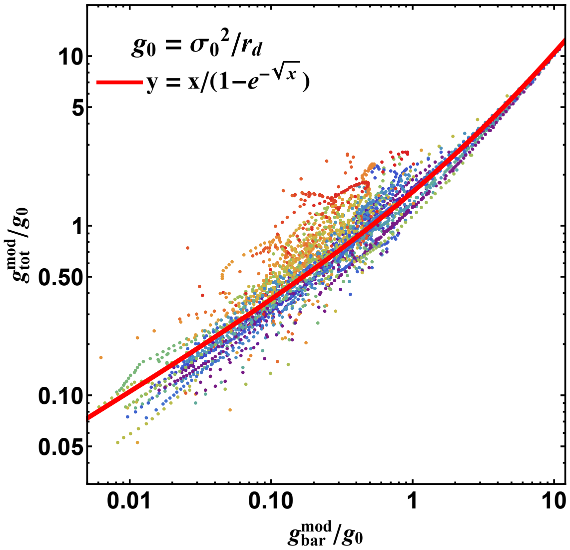

Figure 2.17: The relation between normalized total and baryon accelerations. The $g_{\rm tot}^{\rm mod}$ and $g_{\rm bar}^{\rm mod}$ for each galaxy inferred from the $\sigma/{\rm m} = 3$ cm^2/g fits are normalized by its characteristic acceleration scale $g_0 = \sigma_0^2/r_{\rm d}$. The galaxies are color coded as in Fig. 2.16.

In the MOND formalism with $g_{\rm obs} = g_\dagger \cdot f(x)$ and $x = g_{\rm bar}/g_\dagger$, we can change it to $y = f(x)$ with $y = g_{\rm obs}/g_\dagger$ and $x = g_{\rm bar}/g_\dagger$, so that all the accelerations are normalized. This inspires us to do the same transformation to the SIDM formula Eq. 2.6, that is, to normalize $g_{\rm obs}$ and $g_{\rm bar}$ by $g_0 = \sigma_0^2/r_{\rm d}$. The normalized results are shown in Fig. 2.17. Since g_0s are usually unique to each galaxy, we don't expect the total and baryon acceleration after normalization still hold a tight relation. To our surprise, the $g_{\rm tot}/g_0$s and $g_{\rm bar}/g_0$s are still correlated to each other and the correlations are well described by $f_{\rm MOND}$. This indicates from SIDM's point of view, $f_{\rm MOND}$ actually is an approximate description of how the baryon ($g_{\rm bar}/g_0$) will effect the shape of dark matter profiles ($g_{\rm tot}/g_0 = |\frac{\rm logSlope(r_n)}{r_{\rm n}}|$). We can show that $\langle g_0 = \frac{\sigma_0^2}{r_{\rm d}} \rangle = 1.33 \times 10^{-10}$ m/s^2 in the sample, where $\langle ... \rangle$ means normal average here. If we treat this averaged acceleration $\langle g_0 \rangle = 1.33 \times 10^{-10}$ m/s^2 as $g_\dagger$ and use $f_{\rm MOND}$ to approximate $f_{\rm SIDM}$, then we make our MOND from the SIDM model. We should also notice deviations between the SIDM results and f_{MOND} are obvious for some dwarf galaxies (yellow to red) with relatively low stellar surface densities. It's these differences that cause the inability of MOND to fit the rotation curves of those galaxies as illustrated by the MOND fitting results in Appendix A.

Chapter 3

A Challenge from Diverse Baryon Distributions

3.1 Introduction

The cold dark matter (CDM) paradigm has been exceedingly successful in explaining the matter distribution of the Universe on large scales [34] and many important aspects of galaxy formation [146, 147]. However, challenges emerge on galactic scales. The CDM paradigm predicts a universal cuspy dark matter (DM) density profile, i.e., Navarro-Frenk-White (NFW) profile, when baryons are not taken into account [40, 41, 42, 43]. On the contrary, the observation of rotation curves in dwarf galaxies where baryons are thought to be unimportant expects DM density profiles with large cores near the center [44, 45]. This is the famous "core vs cusp" problem. Recently, this "core vs cusp" issue is generalized to the diversity problem by Oman et al. after they examined a sample of dwarf galaxies [48].

The diverse behaviors in galactic rotation curves revealed in Ref. [48] show that not only galaxies of different sizes can have rotation curves with dissimilar shapes, but even with similar flat circular velocities, the rotation curves could show various growth rates in the inner regions. Some may rise gently and extend to several kpcs, while others may just grow rapidly and reach the flat region within 1-2 kpc. This diversity feature is captured by the scatter of circular velocities at 2 kpc when the maximum circular velocity is roughly fixed. By comparing observed rotation curves with those from cosmological hydrodynamical simulations (e.g., EAGLE and LOCAL GROUPS), Oman et al. illustrated that the rotation curves with similar maximum circular velocities from the simulations show significantly less variations and that the ratio between the highest and lowest velocity at 2 kpc is ~ 4 in observations but it is only ~ 2 in the simulations. Their results also indicate the observed dwarf galaxies could enclose much less mass in the central regions than what expected from CDM halos. This implies these simulations lack a mechanism to remove the inner baryons and DM mass outwards.

Modeling realistic galaxy formation processes in CDM simulations is a possible solution to explain the diversity in the rotation curves. The baryons can contract the inner DM halo through adiabatic contraction [148, 149, 150]. However, strong supernovae explosions can generate shallow DM cores by causing the outflow of gas from the halo central region and further perturbing the underlying gravitational potential [46, 47, 151, 132]. Di Cintio et al. showed the net result of these two opposite effects from baryons on the DM halo can be captured by a mass-dependent halo density profile in which the expansion of DM halo due to the baryon feedback effect is parameterized by the ratio between the stellar mass and halo mass [151]. This profile is used in Ref. [152, 125] to explore the diversity feature of rotation curves analytically. They concluded that the diversity in rotation curves is possible to be reproduced in the CDM paradigm. To test this, the rotation curves from SPARC dataset and those from NIHAO simulations are compared [5]. I. Santos-Santos et al. showed both the average trend and the scatter (not for each individual galaxy) in rotation curve shapes of NIHAO galaxies are in reasonable agreement with those from SPARC galaxies with DM core expansions. Though the simulation results get the overall features of observed galaxies, there are still about 11 outliers couldn't get explained and the majority of them are starbursts or emission-line galaxies [153], with steep rotation curves and small effective radii. In contrast to Oman et al.'s result, the rotation curves from NIHAO simulations need more baryons or DM in the central regions in order to explain the outliers.

On the other hand, Ren et al. have shown that SIDM can explain the diversity of spiral galaxies in the SPARC sample [154]. The inner region of a DM halo is thermalized because of sufficient collisions over the age of galaxy. As a result, the final DM distribution is related to the baryon potential thermally. The deeper the baryon potential is, the steeper the DM density profile becomes. We implemented two independent ways in the previous work [154]. With suitable constrains (like a regulator for Markov Chain Monte Carlo sampling), we recovered the cosmological relation [2] and abundance matching result [3]. Stellar mass-to-light ratios (M/L) have a peak around 0.5 $M_{\odot}/L_{\odot}$, the value suggested by stellar population synthesis models [155, 106] and color-magnitude diagrams of resolved stellar populations [156]. The previous work is based on the analytical modeling, and it would be interesting to test the results in simulations with realistic feedback environment. Though a related simulation work [105] reproduced the diversity by mainly considering the gravitational effect from baryonic disks in isolated runs, whether baryonic feedback effects would limit the formation of diverse baryon disks in SIDM halos and change the final result need further investigations.

In this work, we compare the SIDM fitting results with those from CDM simulations in detail. Our focus is on figuring out the key differences in the properties of DM and baryon profiles in both cases. By exploring the baryonic influence on the inner shapes of DM density profiles in both SIDM framework and CDM simulations, we highlight existing challenges. The structure of this paper is organized as follows. In Sec. 3.2, we briefly review the galaxy sample and methods used in [154] (Ch. 2) and discuss the effect of different self-interaction cross sections on the SIDM fits including ones with the collissionless NFW profiles. In Sec. 3.3, we compare the rotation curves and detailed components of the outlier galaxies. In Sec. 3.4, we study the shapes of inner DM halos in terms of the logarithmic slopes of their density profiles. The correlations between the logarithmic slope and other model parameters in SIDM are checked in Sec. 3.5. In Sec. 3.6, we conclude with potential challenges and point out possible future directions.

3.2 The SIDM fits

In this section, we briefly review the galaxy sample selected from the SPARC dataset, SIDM halo modeling and methods used to fit to rotation curves based on our previous work [154] (Ch. 2). The SPARC dataset contains 175 disk galaxies in the nearby

Universe with both high quality rotation curves and near-infrared ($3.6\mu m$) surface photometry. These galaxies cover very wide ranges in luminosity, surface brightness and rotation curve shapes. These features make it an ideal testing ground for the studies of diversity in rotation curves. For this work, we select 135 galaxies from the full SPARC sample by requiring each galaxy to have a measured velocity for the flat region of its rotation curve. When fitting to these galaxies, we model the baryon contribution by scaling the disk and bulge circular velocity data using the mass-to-light ratios of disk ($\Upsilon_{\star,\mathrm{disk}}$) and bulge ($\Upsilon_{\star,\mathrm{bulge}}$), i.e., $\mathrm{V}_{\mathrm{bar}} = (\mathrm{V}^2_{\mathrm{gas}} + \Upsilon_{\star,\mathrm{disk}} * \mathrm{V}^2_{\mathrm{disk}} + \Upsilon_{\star,\mathrm{bulge}} * \mathrm{V}^2_{\mathrm{bulge}})^{1/2}$. For the SIDM contribution, the inner halo is assumed to be thermalized due to strong self-interactions [72, 70] and it follows the isothermal density profile $\rho_{\mathrm{iso}}(\vec{r}) = \rho_0 \times \exp[-\Phi_{\mathrm{tot}}(\vec{r})/\sigma^2_{\mathrm{v0}}]$, where ρ_0 is the central DM density, $\Phi_{\mathrm{tot}} = \Phi_{\mathrm{Bar}} + \Phi_{\mathrm{DM}}$ is the total gravitational potential from DM and baryons (we set $\Phi_{\mathrm{tot}}(\vec{0}) = 0$) and σ_{v0} is the one dimensional DM velocity dispersion. This profile is matched to the density and enclosed mass of an NFW halo [41, 42] continually at r_1, where the average scattering times for one DM particle over the age of a galaxy is $\mathcal{O}(1)$.

The baryon and DM distributions are couple to each other through the Poisson equation $\nabla^2\Phi_{\mathrm{tot}} = 4\pi G(\rho_{\mathrm{iso}} + \rho_{\mathrm{b}})$ in the isothermal region within r_1. In order to solve this equation and perform the fitting process, we adopted two independent methods. In the controlled sampling (CS), we use an axisymmetric exponential thin disk to model the stellar distribution [73] and constrain the DM halo concentration within the 2σ range of the concentration-mass relation predicted in cosmological simulations [2]. We start with an NFW halo, solve the SIDM profile, and iterate manually until the rotation curve gets a wonderful fit. This method captures the thin and axisymmetric baryon distribution, however it is relatively slow to perform. In Markov Chain Monte Carlo (MCMC) sampling (MS), we adopt a uniform prior for $\Upsilon_{\star,\rm disk}$ and $\Upsilon_{\star,\rm bulge}$, and another uniform prior to encode the concentration-mass relation. The difference from CS is that we assume spherical symmetry for baryons by spreading the mass within the disk at one radius into a sphere of the same radius [80, 104]. This method is so fast to implement that makes us able to explore a large parameter space and probability distributions. See Sec. 2.7.1 in Ch. 2 for more details.

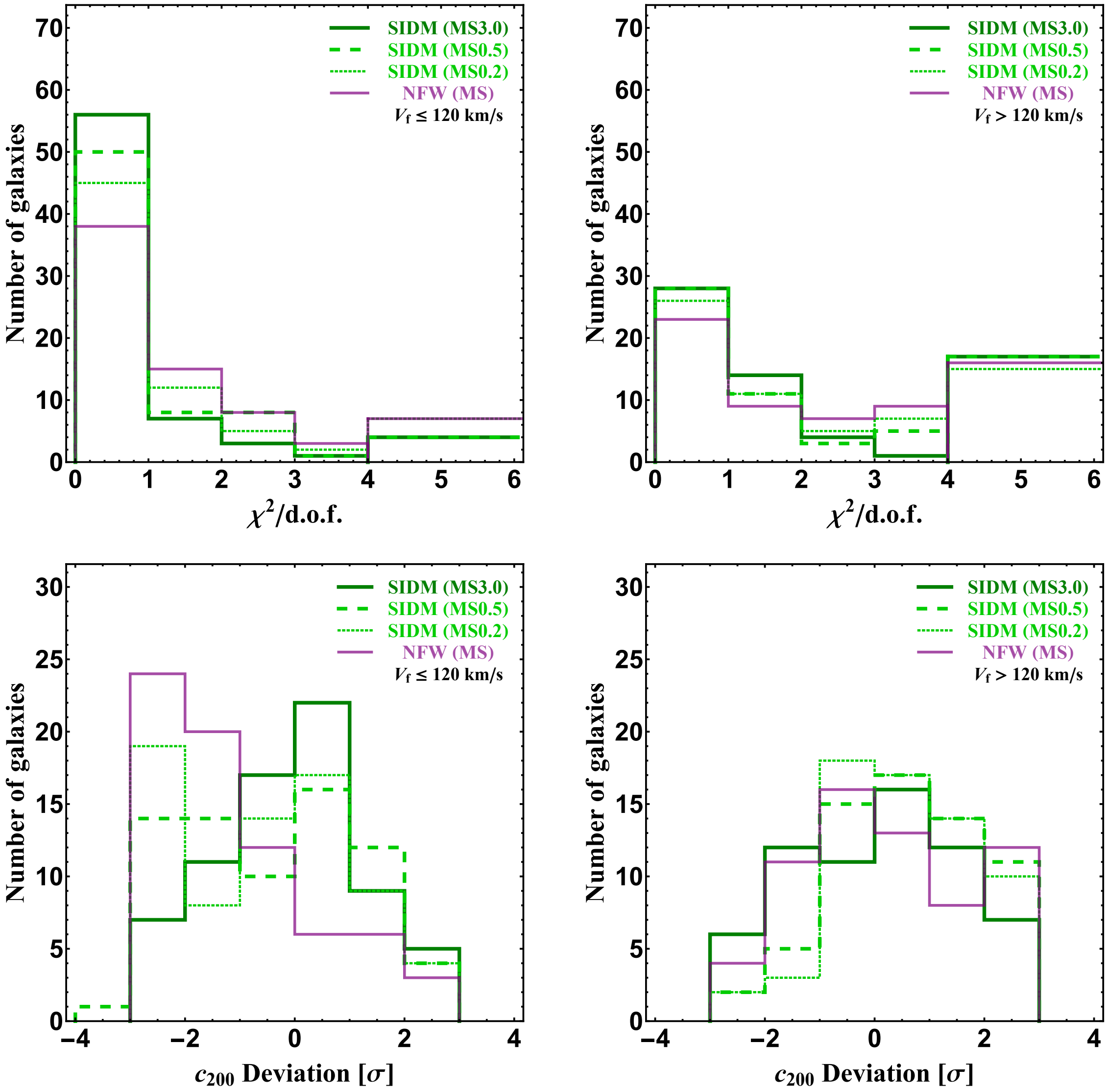

Figure 3.1: *Upper:* The χ^2/d.o.f. distributions. For massive galaxies with $V_\mathrm{f} > 120$ km/s, three SIDM results and NFW fits have similar χ^2/d.o.f. distributions. A larger σ/m value leads to slight improvements on the fitting quality. While for those with $V_\mathrm{f} \leq 120$ km/s, the increase of the σ/m value results in more significant improvements on the χ^2/d.o.f. distributions. *Lower:* Distributions of c_{200} deviations with respect to the mean values in a unit of the standard deviation from the cosmological simulations [2]. For massive galaxies with $V_\mathrm{f} > 120$ km/s, all the fitting results have c_{200} deviation distributions with broad peaks around the medium value. While for those with $V_\mathrm{f} \leq 120$ km/s, the peaks of c_{200} deviation distributions shift from a region around ~ -2 to the medium value region ~ 0 by increasing the σ/m value.

The self-interaction cross section per unit mass (σ/m) is an important quantity measuring the significance of dark matter self-interactions. Though it maybe hard to determine the magnitude precisely with rotation curve data due to uncertainties, we study the effect of different cross sections (3.0, 0.5, 0.2 and 0 cm^2/g) on the fitting results of the selected sample. Especially, the none self-interaction case indeed corresponds to fitting with the NFW profiles. Fig. 3.1 upper panels show the fitting quality in terms of χ^2/d.o.f. distributions. The whole sample is divided into small (left) and large (right) mass groups in terms of whether the galaxy's $\mathrm{V_f}$ is smaller or larger than 120 km/s. For small galaxies (upper left), from the NFW case to the SIDM result with $\sigma/m = 3.0\ \mathrm{cm}^2/\mathrm{g}$, the larger the cross section is, the better the fitting results are. For large galaxies (upper right), the fitting quality are close to each other, however the SIDM result with a large cross section still performs slightly better. The lower panels show the distribution of deviations from the mean cosmological halo concentration-mass relation [2]. For small galaxies (lower left), results with the NFW profiles prefer less concentrated halos. When the σ/m value increases, the concentration of halos increase and more galaxies shift to the region around the medium concentration. For large galaxies (lower right), the changes of the deviation distributions corresponding to different σ/m values are not as large as those in small galaxies (lower left). A qualitative explanation for the shift in concentration distributions among small galaxies could be that many dwarf galaxies in the small galaxy group need a cored profile to get a good fit. The NFW profile can only lower the concentration to decrease the inner DM contribution, however the SIDM profile could also lower the DM component through strong self-interactions. The core size of an SIDM halo usually will increase with the self-interaction strength. Fig. 3.2 (left) restates the differences in halo concentrations of the NFW and SIDM ($\sigma/m = 3.0$ cm^2/g) results with a tophat prior on the concentration-mass relation using the $\mathrm{r_{max}} - \mathrm{V_{max}}$ plot, where $r_{\max}$ is the radius of the maximum rotation velocity $V_{\max}$ based solely on the NFW profile. The markers of large galaxies from two fitting results roughly overlap with each other. However, among small galaxies, the NFW halos (purple diamonds) locate systematically above the mean $\mathrm{r_{max}} - \mathrm{V_{max}}$ relation (solid black line) and are less concentrated comparing to the SIDM halos (green squares). Similar results but with a gaussian prior on the concentration-mass relation are shown in Fig. 3.2 (right). Thus, the conclusion, i.e., the NFW halos are less concentrated than the SIDM halos in fitting the small galaxies, is independent of the priors we use.

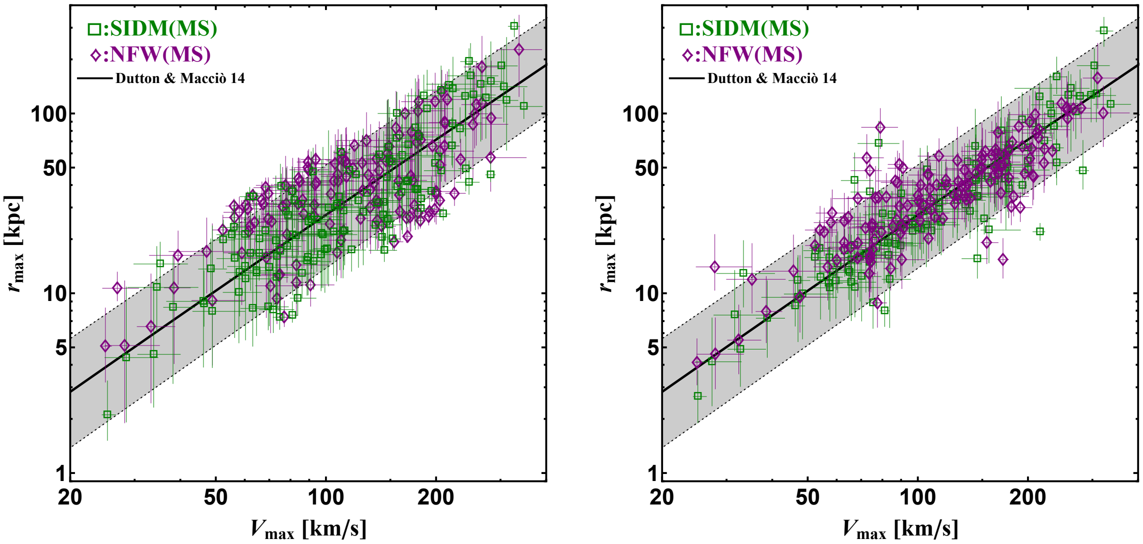

Figure 3.2: Medium $r_{\max}$–$V_{\max}$ distributions with 1σ errors inferred from the SIDM ($\sigma/m = 3$ cm^2/g, squares) and NFW (diamonds) fits, using the tophat (left) and Gaussian (right) priors on the concentration-mass relation. The hosting halos in the NFW fits are systematically less concentrated than their SIDM counterparts for galaxies with $V_{\rm f} \leq 120$ km/s. The results are independent of the priors we choose.

The fits in Ch. 2 are the results with $\sigma/m = 3.0\ \mathrm{cm}^2/\mathrm{g}$. Our fits demonstrate the diversity in the SPRAC rotation curves can be successfully reproduced in the SIDM framework. No matter the galaxy is a dwarf with low surface brightnesses or a big one with large bulge contributions, the SIDM model is able to provide excellent fits to their rotation curves. Furthermore, other galaxy properties from the fits are also consistent with the observations, theoretical considerations and simulation results. For example, our results recovered a correlation between the total and baryon accelerations with small scatters, i.e., the radial acceleration relation [96], and generated a tight baryonic Tully-Fisher relation [4]. The stellar mass-to-light ratios get a distribution as expected from the stellar population models [106]. The DM halos are in good agreement with the Planck cosmology, and the stellar mass-halo mass relation matches well with the abundance matching method [3]. In the following sections, we compare the results with $\sigma/m = 3.0\ \mathrm{cm}^2/\mathrm{g}$ to those from CDM simulations.

3.3 Outliers

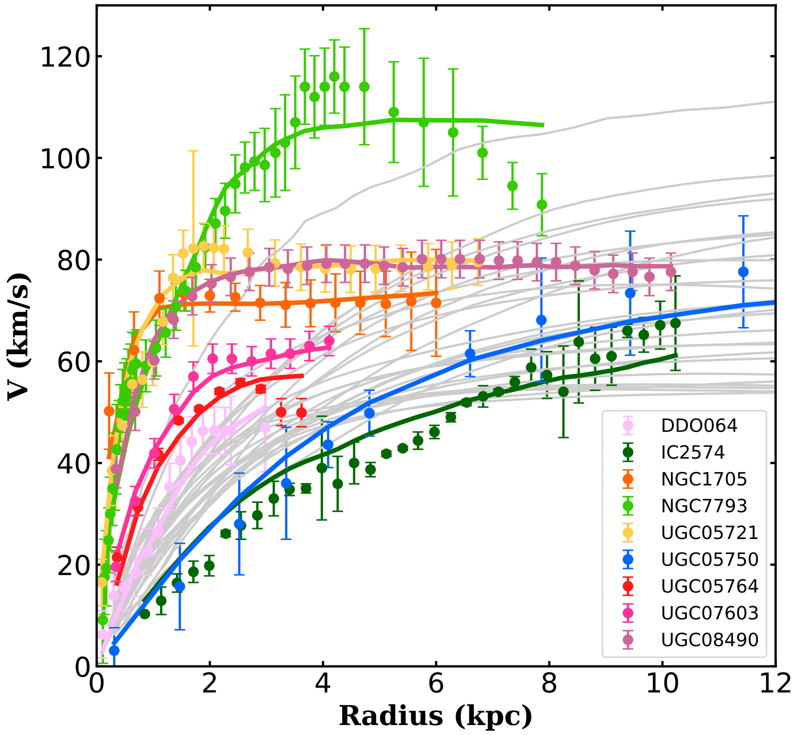

Figure 3.3: Comparisons of rotation curves for outlier galaxies. The observational data from the SPARC dataset [1] are shown as colored dots with error bars. The colored solid curves are fits from the SIDM (CS) results. Simulated rotation curves from NIHAO [5] are shown in light gray curves with the outmost measured velocities ranging from 47 to 90 km/s.

Although NIHAO CDM simulations with strong baryonic feedback can reproduce the general trend and scatter of the diversity feature in the rotation curves of the SPARC sample, there are still several galaxies whose rotation curves are either too steep or too flat [5] to be explained. In this section, we select nine SPARC galaxies whose velocity at 2 kpc is more than $\pm 3\sigma$ away from the corresponding mean value at that radius of similar-size galaxies in the NIHAO simulations [5]. We then compare the data of these outlier galaxies, their SIDM fits and NIHAO rotation curves. In Fig. 3.3, nine rotation curves for the outlier galaxies from observations are shown as colored dots with error bars. Light gray lines denote predicted rotation curves from NIHAO simulations, and the colored solid curves denote fits using the SIDM model. These nine galaxies have similar flat velocities in the range of 50-80 km/s, however their inner parts of rotation curves demonstrated diverse shapes. For example, the rotation velocity around 2 kpc spreads from the lowest one (dark green, IC2574) $\sim$ 20 km/s to the highest one (light green, NGC7793) $\sim$ 80 km/s. This is almost a factor of 4 and illustrates the diversity feature in the rotation curves.

The rotation curves of IC2574 (dark green) and UGC5750 (blue) rise most slowly. Their shallow rotation curves imply that not only the baryon distributions are extended, but their DM components should contain a large core as well. Though the simulated ones (light gray) are slightly higher than both rotation curves in the inner region (e.g. r $\lesssim$ 5 kpc), I. Santos-Santos et al. argued that a remarkable agreement with observational data could be achieved by using the true circular velocity that takes into account the precise mass distribution of the galaxy [5]. In contrast to the slowly rising behavior in IC2574 and UGC5750, other outliers have more steep rotation curves. Only two galaxies, DDO064 (pink) and UGC05764 (red), are within the range of the simulation results. Other galaxies (NGC7793 (light green), UGC05721(yellow), UGC08490 (purple), NGC1705 (orange) and UGC07603 (magenta)) are so steep that those simulated rotation curves even can't match the observed ones from the most inner points. In term of the velocity contributions, this means either the baryons or the DM components are very concentrated in these observed galaxies, but this is not the case for the NIHAO simulations. On the contrary, the SIDM model (the colored solid curves) does a better job in fitting to the outliers. The predicted rotation curves from the SIDM fits can not only extend out and go as shallow as that of IC2574 (dark green) but also grow rapidly like that of NGC1705 (orange). Apparently, the predicted rotation curves from the SIDM framework demonstrate more diversity than those from NIHAO simulations. More quantitatively, the ratio of the maximum to minimum circular velocity at 2 kpc is almost 4 in the SIDM model while 2 in the simulations.

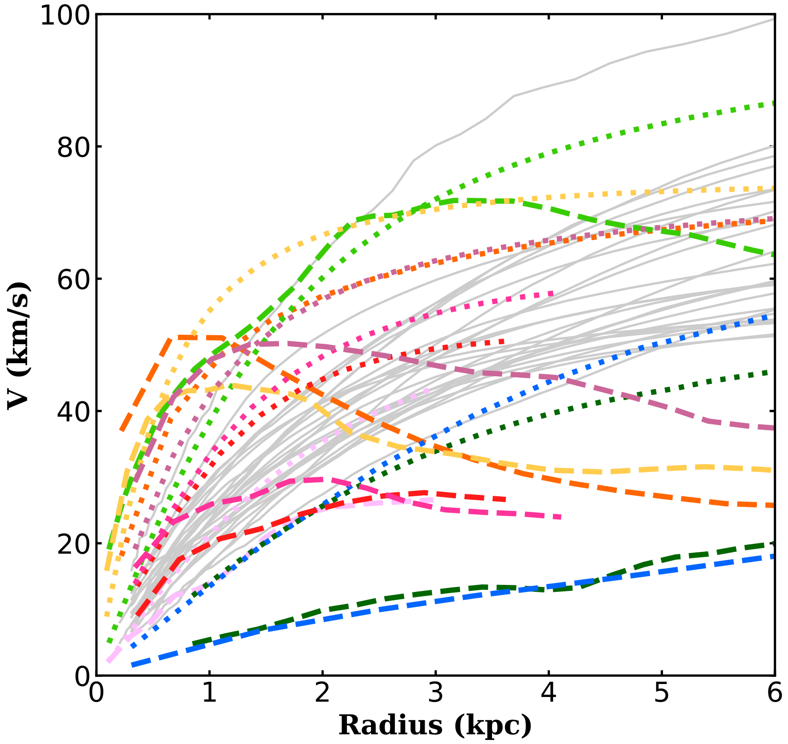

Figure 3.4: Comparisons between the decomposed SIDM (CS) fits in Fig. 3.3 to the simulated rotation curves. The thick dashed curves stand for baryon velocity contributions. The dotted curves are velocity contributions from SIDM. The colors follow those of observed rotation curves in Fig. 3.3. The gray curves are the total rotation curves from the NIHAO simulations.

The differences in the SIDM and simulated fits can be traced back to baryon and DM distributions. We extract the baryon and DM velocity contributions for each outlier galaxy from the SIDM fits, and compare them to the total NIHAO rotation curve since the detailed DM and baryon components from the simulations are not available to the public yet. In Fig. 3.4, the baryon contributions from SIDM fits are shown as dashed lines and the DM contributions are shown as dotted lines. The baryon velocity contributions from IC2574 (dark green) and UGC05750 (blue) are extended as expected. The DM velocity curves also spread out just like the baryon ones, and they are relatively shallow compared to other galaxies. DM dominates in both galaxies and whether there is a link between the baryon expansion and the DM core expansion in these systems is an interesting question to explore. Meanwhile, the galaxies with steep rotation curves have baryon components that are comparable to the total simulated rotation curves from NIHAO, such as DDO064 (pink), UGC07603 (magenta) and UGC05764 (red). The corresponding DM contributions that make up the good fits already touch the upper bound of the simulation results. NGC7793 (light green), UGC05721 (yellow), UGC08490 (purple) and NGC1705 (orange) all have very steep baryon and DM contributions. Their baryon contributions could even reach 2 times of the total simulated ones in the region around 0.5-1 kpc, such as NGC1705 (orange). These concentrated baryon distributions also contract the thermalized DM profiles through their deep baryon potentials. Thus, the SIDM model also explain the rotation curves with steep rising.

For the outliers with steep rising rotation curves, we can assume if the baryon contributions are lower than those in the SIDM fits, then in order to get a good fit, the DM contribution should be higher, but what makes the contraction of DM will be unclear theoretically. From this point of view, large baryon contributions are required for reasonable fits to these starburst galaxies. This again indicates that the baryon distributions in the

NIHAO simulations are quite different from the observed ones. For many dwarf galaxies, the observed ones are more concentrated, while the ones from NIHAO are relatively extended. NIHAO simulations span a wide range of masses and merger histories, but it seems they still miss galaxy analogs with high baryon concentrations. Since the NIHAO simulations can reproduce the flat ones somehow, this implies that either the baryonic feedback effect is too strong to form concentrated baryon distributions, or some other feedback processes are missing in the simulations.

3.4 Inner Dark Matter Density Profiles

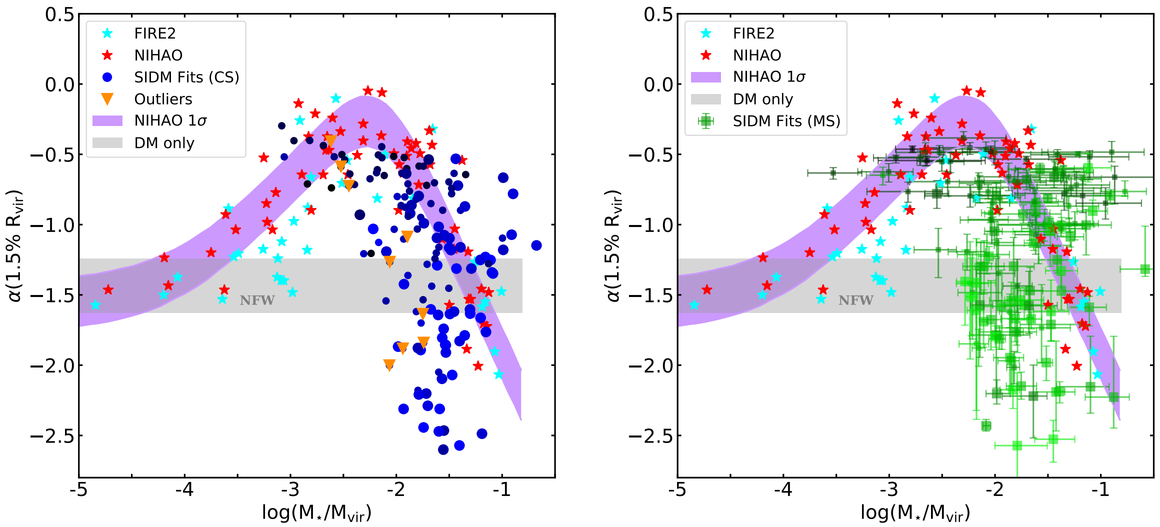

Figure 3.5: The logarithmic slope (α) of the inner DM density profile at $r = 1.5\% R_{\rm vir}$ as a function of $\log(\mathrm{M}_\star/\mathrm{M}_{\rm vir})$. Large α values (e.g., $\alpha \gtrsim -0.8$) correspond to cored profiles , and small α values (e.g., $\alpha \lesssim -0.8$) indicate cuspy ones. The slope values from the DM-only simulations, i.e., results that correspond to the Navarro-Frenk-White (NFW) profiles, are shown in the gray band with concentration scatters [6]. Results from the NIHAO simulations are shown in red stars and the purple band is a fit with 1σ scatter [6]. The blue stars are results from FIRE-2 simulations [7, 8]. SIDM CS results are shown in the left panel with blue dots, and those from MS are in the right panel shown as green squares with error bars. Small markers denote galaxies with $V_{\rm f} \le 120$km/s, while large ones with $V_{\rm f} > 120$km/s. The brightness of the marker color is positively correlated with the average surface stellar mass density of galaxies.

While using the velocity rotation curve is one way to capture the diversity visually and to see the relative contribution of baryons and DM, the logarithmic slope of a DM halo in the inner region (e.g., at $\sim 1.5\%$ of the halo virial radius $\mathrm{R}_{\rm vir}$) is another signature to show some additional information. The slope indicates the shape of the inner density profile and it captures the influence of baryons on DM halos. If the DM halo contains a big core in the center, the slope would be close to 0, while if it contains a cusp, the slope would be a negative values (e.g., -1.5). Different DM models can have different DM density profiles.

For example, the DM-only simulations show the inner slope for a CDM halo is intrinsically ~ -1.5 while the slope of an SIDM-only halo is ~ -0.5. In the presence of baryons, the final DM profile can be modified from its original form. Thus, by looking at the degree of the modification, we can infer information about the relative weight of baryons, baryon-DM interplay and so on.

Fig. 3.5 shows the DM density logarithmic slope (α) at $1.5\%\mathrm{R_{vir}}$ from different models and methods as a function of the ratio of stellar to halo masses, i.e., $\log(\mathrm{M_\star}/\mathrm{M_{vir}})$. The gray band ($-1.63 \lesssim \alpha \lesssim -1.24$) is from CDM-only simulations (NFW profiles) with concentration scatters [6]. The red stars and the purple band are from NIHAO simulations [157] while the light blue stars are from FIRE-2 [7, 8]. Though they belong to two completely different sets of simulations, their results are consistent with each other in term of the logarithmic slope trend. When $\log(\mathrm{M_\star}/\mathrm{M_{vir}})$ is below -3 corresponding to classical and ultra-faint dwarfs, the slope is close to that from the results with NFW profiles due to the small baryon component and negligible feedback effects. When $\log(\mathrm{M_\star}/\mathrm{M_{vir}})$ is between -3 and -2, baryons are able to generate influential feedback effects to create DM cores. However in larger galaxies, the profile becomes cuspy again because the contraction effects from large baryon mass begins to play a dominant role and gradually beats the core expansion due to the baryonic feedback effect. We include two SIDM results in Fig. 3.5. In the left panel, the blue dots are from the CS, while in the right panel, the green squares with 1σ errors are from the MS. There are two properties attached to both SIDM data, the marker size and the brightness of color. The galaxies with flat velocities ($\mathrm{V_f}$) less than 120 km/s are plotted in small markers (71 galaxies), and larger markers (64 galaxies) for those with

$V_{\rm f}$ greater than 120 km/s. The lightness and darkness of color indicates the average surface stellar mass density ($\propto M_\star/R_{\rm d}^2$) of the galaxy. The larger the average surface stellar mass density is, the brighter the marker color is.

Both SIDM results show consistent distribution patterns in Fig. 3.5. In the region where most of SIDM points are located, i.e., $-2.5 \leq \log(\rm M_\star/M_{vir}) \leq -1.0$, the slopes spread from ~ -0.5 to -2.8, while results from the NIHAO and FIRE-2 simulations mainly located within a range between -0.5 to -1.5. This huge difference indicates the significant variation in the form of DM density profiles. The simulated one are more alike to each other and show less variations. In contrast, the wide spread in the SIDM results indicates the SIDM density profiles vary from large cores to sharp cusps. There are 75 (CS, left) and 80 (MS, right) galaxies whose slopes are larger than -1.2, or above the upper bound of the results from NFW profiles (the gray band). These galaxies are shown in darker color, meaning low average surface stellar mass densities, especially for those with logarithmic slopes ~ -0.5. Among them, 51 (CS) and 60 (MS) are small galaxies (small markers) with $V_{\rm f} < 120$ km/s. On the other side, there are 60 (CS) and 55 (MS) galaxies have slope values smaller than -1.2. Their markers look more bright indicating their high average surface stellar mass densities. Among them, 40 (CS) and 44 (MS) are large galaxies with $V_{\rm f} > 120$ km/s. A slight difference between two SIDM results is the marker locations in the regions above and below $\alpha \approx -1, 2$. In the upper region, the MS results are slightly shifted rightward comparing to the CS results. The MS markers crowd at where $-1.5 \leq \log(\rm M_\star/M_{vir}) \leq -2$, while CS markers locate around $-2 \leq \log(\rm M_\star/M_{vir}) \leq -1.5$. In the lower region, the situation is reversed. The CS markers have a collection center around $\log(\rm M_\star/M_{vir}) \sim -1.6$

while $\log(\mathrm{M}_\star/\mathrm{M}_{\mathrm{vir}}) \sim -2$ for MS markers. These location differences on the horizontal direction can be traced back to the detailed components of baryons and DM. We address this point in the next section.

From Fig. 3.5, we see the agreement between the SIDM and simulation results are acceptable in the upper region ($\alpha \gtrsim -1.2$), at least the marker groups from the both SIDM results match with the NIHAO purple band. This is a region where galaxies tending to have density cores. In the CDM simulations, the core is formed through active baryonic feedback effects (indicated by $\log(\mathrm{M}_\star/\mathrm{M}_{\mathrm{vir}})$) and weak baryon contractions (indicated by the low surface mass density). The core in the SIDM model is a result from the strong self-interactions and weak baryon effects due to a shallow baryon potential. The dramatic deviation happens in the lower region ($\alpha \lesssim -1.2$). The slope values from the SIDM fits get a spread from -1.2 to -2.8 without changing $\log(\mathrm{M}_\star/\mathrm{M}_{\mathrm{vir}})$ that much. These sharp density profiles are mainly driven by the deep baryon (and DM) potential indicated by the large average surface stellar mass density. In order to get similar slope values in the simulations, one needs to get $\log(\mathrm{M}_\star/\mathrm{M}_{\mathrm{vir}})$ close to -1 as shown in Fig. 3.5 so that the baryon contraction effect is enhanced and overcomes the feedback core expansion. This comparison points to a potential problem in the current CDM simulations. To generate steep DM density profiles, the method could be not only the contraction effect from huge baryon mass (i.e., large $\log(\mathrm{M}_\star/\mathrm{M}_{\mathrm{vir}})$), but the contraction effect from baryons' condensation even if it is a dwarf galaxy. We use 4 outlier galaxies (NGC7793, NGC1705, UGC08490, UGC05721), which are the ones with most steep inner rotation curves and below the NFW gray band (see Fig. 3.5 left), to illustrate this point. If their rotation curves get fitted but the baryon components are smaller than those from the SIDM fits, the DM profile should be more concentrated (though it may be impossible theoretically). If the baryon components are comparable or even larger in the simulations, the contraction effect should dominate in the inner region for baryons and DM, and the DM gets a steeper density profile. In other words, the DM density profiles are not cored as expected from the NIHAO purple band in these galaxies.

It seems current CDM simulations do not reproduce dwarf galaxies with high baryon concentrations. The discrepancy between the observed and simulated rotation curves shown in Fig. 3.3 are an indication of the lack of diversity in both baryon and dark matter distributions. In the SIDM case, the baryon contributions are not generated through simulations but taken from observations directly, and they are scaled with $\Upsilon_{\star,\rm disk}$ and $\Upsilon_{\star,\rm bulge}$ so that their condensations are preserved in the fitting processes. The SIDM inner halos are thermalized and respond to the baryonic potential thermally. Thus, in the SIDM fits, the diverse slope spread in fact is a reflection of the diverse baryon components.

3.5 Slope Correlations

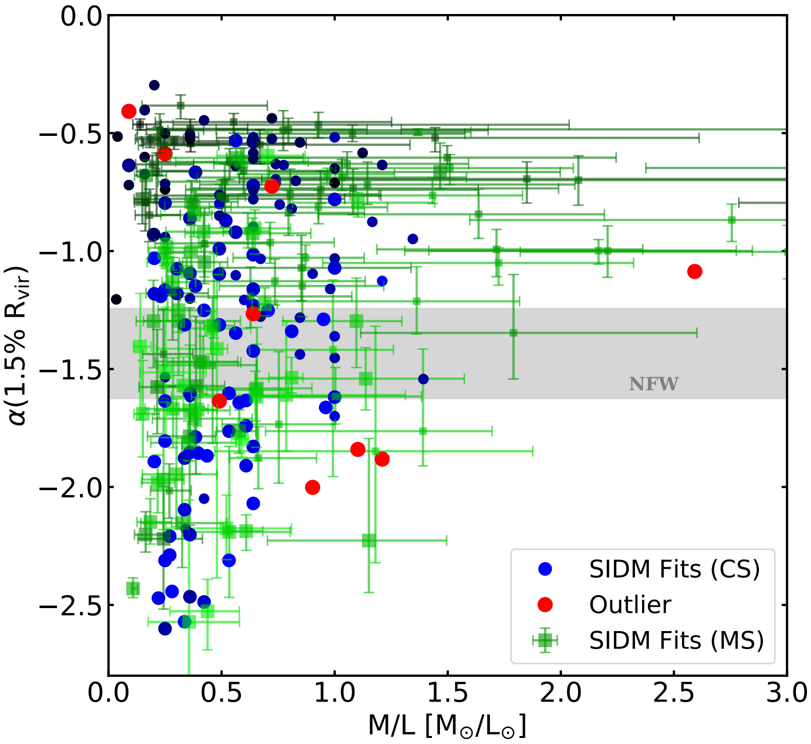

Figure 3.6: Correlations between the logarithmic slopes (αs) of inner DM density profiles and disk mass-to-light ratios.

In the last section, we have studied the correlation between the logarithmic slope in the inner region of DM halos and the ratio of stellar to halo masses, here we further examine the correlation between the logarithmic slope and other parameters in the SIDM model. In Fig. 3.6, the logarithmic slopes are plotted against stellar mass-to-light ratio ($\Upsilon_{\star,\rm disk}$). We can see the M/Ls from both SIDM results are mainly distributed from 0.2 to 1 and most of fits have M/L values around 0.5. There are minor differences between two SIDM results. In the upper region ($\alpha \gtrsim -1.2$), M/Ls from MS show wider scatters and prefer larger values. This makes the galaxies in the upper region obtain larger stellar masses compared to those in CS. In the lower region ($\alpha \lesssim -1.2$), though MS M/Ls still contain wider scatter, CS results are slightly larger in values and so are the stellar masses. These are the main reasons that lead to the minor differences in the distributions of SIDM fits shown in Fig. 3.5. Given that our sample is large and covers a very broad range in galaxy properties, we conclude that the logarithmic slope is not determined by or strongly correlated to the stellar mass-to-light ratio.

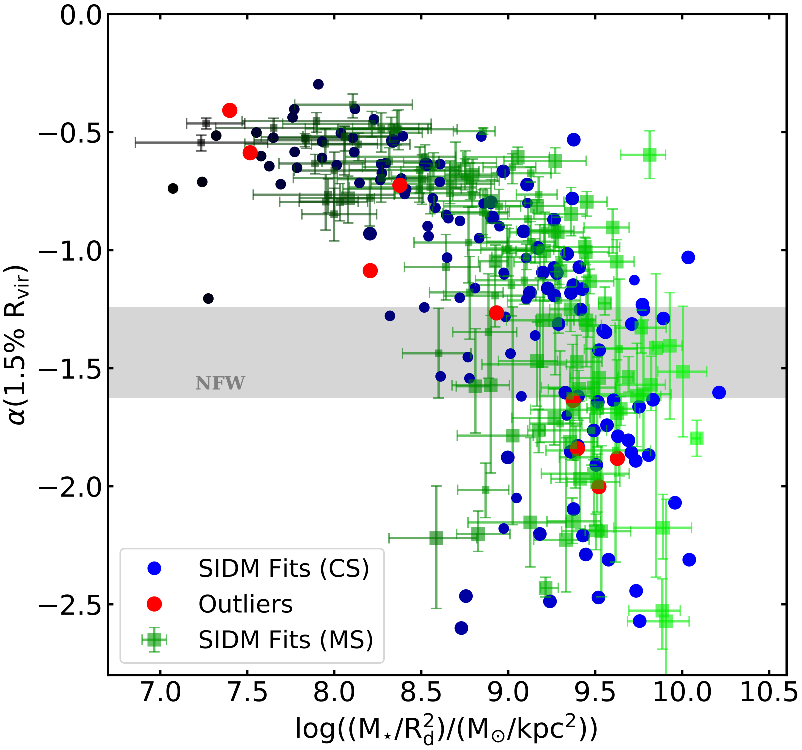

Figure 3.7: Correlations between the inner DM density slopes (αs) and the $M_\star/R_\mathrm{d}^2$ values. $M_\star/R_\mathrm{d}^2$ measures how much baryons one galaxy has and how concentrated they distribute at the same time, and it is proportional to the average surface density and baryon potential directly. The single blue point with $\log(\mathrm{M}_\star/\mathrm{R}_\mathrm{d}^2) \simeq 7.3$ is PGC51017, which is an ultra-faint galaxy with a tiny stellar mass and a large gas contribution.

In Fig. 3.7, we plot the logarithmic slope against $\log(\mathrm{M}_\star/\mathrm{R}_\mathrm{d}^2)$. The stellar mass $\mathrm{M}_\star$ is inferred from the observed total luminosity and the M/L from the SIDM fits. R_d is taken from observations directly. $\mathrm{M}_\star/\mathrm{R}_\mathrm{d}^2$ is a quantity that is directly proportional to the average surface stellar mass density. It measures not only how much stellar mass the galaxy has, but also how concentrated the stars are distributed. It includes the additional gravitational information when compared to the average surface brightness. We can see there is a clear correlation. When $\log(\mathrm{M}_\star/\mathrm{R}_\mathrm{d}^2)$ is small (~ 7.5), which indicates a tiny dwarf galaxy ($M_\star$ is small) or an extended stellar distribution (R_d is large), the logarithmic slope is round -0.5 with small scatters, and the halos prefer cores. For these galaxies, the baryons have little influence on the halo and dark matter self-interactions produce a density core. When $\log(\mathrm{M}_\star/\mathrm{R}_\mathrm{d}^2)$ increases and so as the baryonic influence, the value of the slope gets larger, which means the core of the density profile shrinks and the profile becomes more and more cuspy. At the same time, we see the scatter is also getting larger. Since the surface stellar mass density is related to $\mathrm{M}_\star$ or M_halo, the logarithmic slope has a correlation with them as well, as indicated in Fig. 3.8. However, we found the correlations are not as tight as the one with the average surface stellar mass density ($\propto \log(\mathrm{M}_\star/\mathrm{R}_\mathrm{d}^2)$). Small galaxies with $V_\mathrm{f} \leq 120$ km/s have stellar masses roughly ranging from $\sim 10^7$ to $10^{9.5} M_\odot$ and halo masses ranging from $\sim 10^9$ to $10^{11.5} M_\odot$. Most of them have low surface stellar mass densities and prefer cored profiles with α between -0.5 to -1.0. Larger galaxies with $V_\mathrm{f} \geq 120$ km/s have stellar masses mainly from $10^{9.5}$ to $10^{11.5} M_\odot$ and halo masses ranging from $\sim 10^{11.5}$ to $10^{13} M_\odot$. Although the spread in the slopes is relatively large, both plots show a pattern, that is, the larger the stellar mass or halo mass is, the smaller the slope value is. This pattern can be traced back to the abundance matching relation and a positive correlation between the surface stellar mass density, the stellar mass and the halo mass.

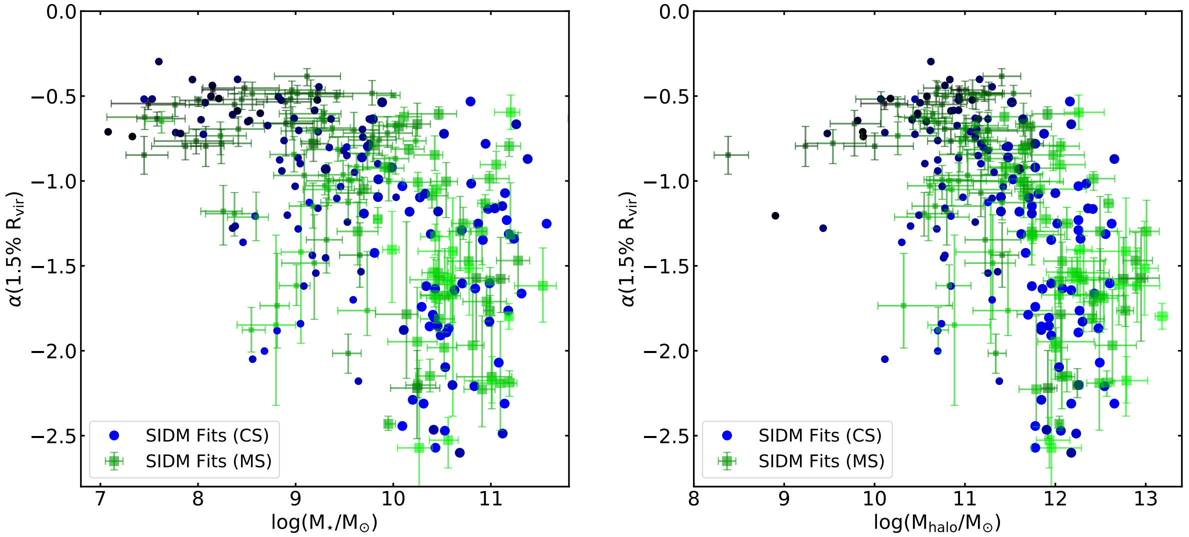

Figure 3.8: The correlations between the logarithmic slope (α) of DM density profiles, the stellar mass (left) and the halo mass (right) from two SIDM models.

The tight correlation between the logarithmic slope and the average surface stellar mass density is consistent with expectations from the SIDM model. As we can see from the isothermal expression for the DM density distribution $\rho_{\rm iso}(\vec{r}) = \rho_0 \times \exp[-(\Phi_{\rm DM}(\vec{r}) + \Phi_{\rm Bar}(\vec{r}))/\sigma_{\rm v0}^2]$ where the $\Phi_{\rm Bar}$ term is directly proportional to the average surface stellar mass density, the diverse baryon density profiles from the observations lead to different $\Phi_{\rm Bar}$ and $\Phi_{\rm DM}$ weights in each individual system. For a dwarf with a small and extended baryon component (small $\log(\rm M_\star/R_d^2)$), $\Phi_{\rm DM}$ is dominant and a cored profile follows. Since this is intrinsic to the SIDM model, a small scatter is expected. In a galaxy with a relative large and condensed baryon component (large $\log(\rm M_\star/R_d^2)$), $\Phi_{\rm Bar}$ is more important resulting in a cuspy profile. However, $\log(\rm M_\star/R_d^2)$ is such a simple quantity that can't stand for the baryon potential completely. Other galactic properties like the radial dependence of the baryon potential will also effect the shape of the DM halo. This is the reason for the large scatter in Fig. 3.7 when $\log(\mathrm{M}_\star/\mathrm{R}_\mathrm{d}^2)$ is large. All of these lead to the diverse behaviors in the total rotation curves. They also indicates the broad spread of the logarithmic slope distribution is necessary for explaining the diversity with the SIDM model as well as for other DM models or simulations since the observed baryon distribution is almost fixed up to the M/L factor.

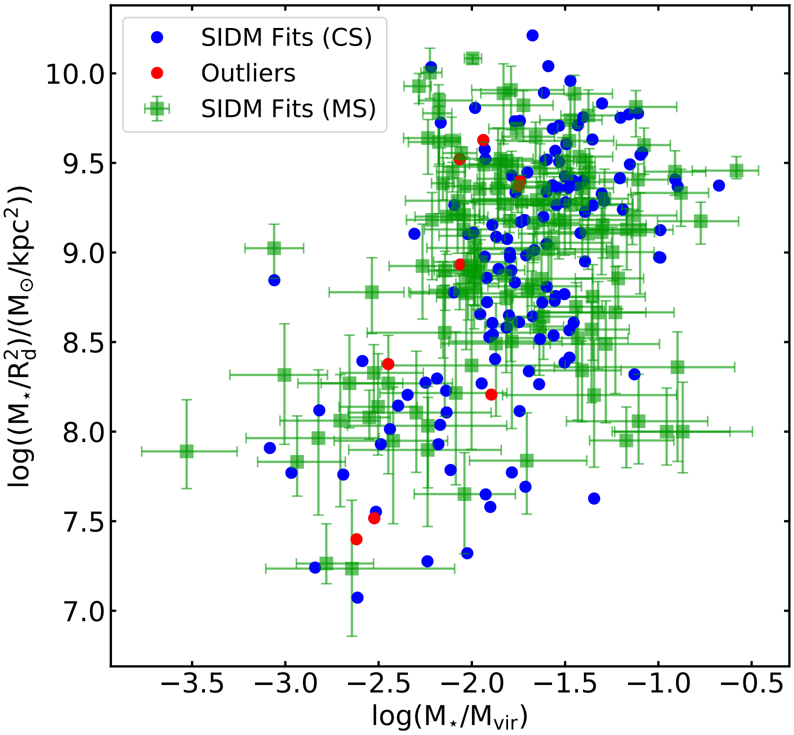

Figure 3.9: The correlation between $\mathrm{M}_\star/\mathrm{R}_\mathrm{d}^2$ and $\log(\mathrm{M}_\star/\mathrm{M}_\mathrm{vir})$ inferred from the SIDM CS fits (blue) and the SIDM MS fits (green). Nine outliers are shown in red based on the SIDM CS fits.

We have shown in Fig. 3.5 that how the logarithmic slopes (αs) of DM density profiles follow the ratios of the stellar to halo masses ($\log(\mathrm{M}_\star/\mathrm{M}_\mathrm{vir})$) for the SIDM and simulation results. We also illustrates a clear correlation between the logarithmic slope (α) and $\mathrm{M}_\star/\mathrm{R}_\mathrm{d}^2$ calculated from each galaxy. The ratio of stellar to halo masses ($\log(\mathrm{M}_\star/\mathrm{M}_\mathrm{vir})$)

is important to parameterize the feedback effect in the simulations. The $\log(\mathrm{M}_\star/\mathrm{R}_\mathrm{d}^2)$ values are inferred from the SIDM fits and they are closely related to the observations. We take one more step further to show how $\mathrm{M}_\star/\mathrm{R}_\mathrm{d}^2$ changes with $\mathrm{M}_\star/\mathrm{M}_\mathrm{vir}$, as shown in Fig. 3.9. When $\log(\mathrm{M}_\star/\mathrm{M}_\mathrm{vir})$ is small around -2.5, the $\log(\mathrm{M}_\star/\mathrm{R}_\mathrm{d}^2)$ values scatter around 8.0, and the deviations are close to one order of magnitude. However, when $\log(\mathrm{M}_\star/\mathrm{M}_\mathrm{vir})$ increases to about -2, there is a steep increase for the scatter of $\log(\mathrm{M}_\star/\mathrm{R}_\mathrm{d}^2)$, and the values could be from 7.5 to 10.0 beyond two orders of magnitude. The nine outliers are in this transition region. It remains to be seen whether CDM simulations with strong baryonic feedback can reproduce such a scatter for $\log(\mathrm{M}_\star/\mathrm{M}_\mathrm{vir}) \approx -2$.

3.6 Discussion and Conclusions

In this work, we used results from the SIDM fits to the SPARC rotation curves as references and pointed out that the challenges of the current CDM simulations in fully explaining the diverse rotation curves of spiral galaxies, especially those with high baryon concentrations. We have compared SIDM fitting results with different self-interaction cross sections including the collisionless case (i.e., using the NFW profiles). The SIDM model with a large cross section (e.g., $\sigma/m = 3.0\ \mathrm{cm}^2/\mathrm{g}$) demonstrates better performance on the fitting quality as well as better consistence with constraints from observations (e.g., the M/L distribution) and simulations (e.g., the cosmological relation).

We have shown the SIDM model can fit both slow and steep rising rotation curves, including those outliers for the NIHAO simulations. For some galaxies, the baryon contributions to the total rotation velocities inferred from the SIDM fits are higher than the total predicted velocities in NIHAO analogs. Through the comparison of the DM inner density profile characterized by the logarithmic slope around the central region, we showed the slope values from the SIDM model have a much wider spread covering both cored and cuspy profiles than those inferred from the simulations which prefer cores in the domain of dwarf galaxies. This spread of slope values is closely correlated to the average surface stellar mass density in the SIDM model. We argued that the existence of rich average surface stellar mass density, i.e., the diverse baryon profiles, around dwarf galaxy scales could lead to diverse DM profiles and therefore the diverse feature of the rotation curves.

The advantage for the simulations with baryonic feedback effects is that the results are generated under more realistic situations. However current simulations do not reproduce the most slow and steep rising rotation curves at the same time. Our results emphasize that rather than focusing on the diversity in the total rotation curves as originally proposed, the detailed baryon and DM components and their interplay offer more valuable information. For example, the diverse rotation curves in the dwarf galaxies actually imply rich baryon profiles, while the important baryon profiles are generated through the galaxy formation process in the simulations. The lack of variations among them makes the simulations couldn't address the diversity problem throughly. More importantly, these profiles are observable and could be directly compared to those from the simulations. Modifying current baryonic feedback models in the simulations is necessary to accommodate with the observations. On the other hand, the SIDM results are from an analytical model with the isothermal assumption for the inner region of a DM halo. The baryon contributions are from observations and scaled by two factors $\Upsilon_{\star,\mathrm{disk}}$ and $\Upsilon_{\star,\mathrm{bulge}}$. We expect that the SIDM fits are robust to the baryon feedback, because the final SIDM distributions are determined by the final baryon distributions, but not detailed formation histories due to the SIDM thermalization.

There are a number of promising directions to explore and test different DM models and galaxy formation models. For example, generating the extended and contracted baryon profiles simultaneously is the key for the CDM simulations to fully explain the diversity. This requires various strengths of baryonic feedback effects rather than a monotonic model in similar galactic systems. Such variations could be due to different formation histories. In SIDM simulations, we expect SIDM halos and baryons will behave differently from those in CDM simulations. Unlike collisionless CDM particles, the disturbed SIDM particles due to feedback effects can relax quickly due to strong self-interactions. Whether this effect will help maintain more baryons in the halo inner region and generate desired diverse baryon profiles needs tests from future researches. Especially, when the baryon mass is small and the gravitational potential is shallow, e.g., $\log(\mathrm{M}_\star/\mathrm{M}_{\mathrm{vir}}) \leq -2.5$, the SIDM halo tends to have a core, i.e., the logarithmic slope is between -0.5 and 0, while the CDM simulations predict a cusp, i.e., the slope will be close to the NFW case. The former one is mainly caused by strong self-interactions, and the later one is an intrinsic prediction from the CDM simulations due to little feedback and contraction effects. This difference can be used to test different DM models through observations of ultra-faint dwarf galaxies.

Chapter 4

Dark Matter and Baryon Conspiracy in Early-Type Galaxies

4.1 Introduction

Early-type galaxies (ETGs) are composed of ellipticals and lenticulars which are much rounder, more smooth and featureless in term of their observed visual appearance when compared to spiral galaxies. The characteristic stellar disks and rich cold gas in spiral galaxies facilitate the measurement of stellar dynamics and further study of the hosting dark matter (DM) halos. ETGs, however, don't have enough HI gas for dynamical measurements, have weak star formation activity and contain mainly old stars. Most of current observed results for ETGs are from dynamical studies using stellar kinematics, planetary nebulae etc. [158, 159, 160, 161] and strong gravitational lensing [162, 163, 10, 164].

With various dynamical tracers, we are able to get insights of the stellar components and total dynamical mass distributions in ETGs. One of the most famous results is the fundamental plane [165]. It describes a tight correlation between the structure (effective radius), the dynamics (line-of-sight velocity dispersion) and the luminosity (average surface brightness) of these galaxies. Recently ETGs are found to have nearly isothermal total density profiles extending to several effective radii, i.e., $\rho_{\rm tot} \propto r^{-\gamma}$ where the logarithmic slope (log-slope) γ approximates to 2 with small scatters [166, 12, 167, 168]. Interestingly, when it comes to the DM and stellar components separately, neither of them is expected to have density profiles like the isothermal type and to offer any clues for the small scatters. This indicates the isothermal density profiles in ETGs are probably a result of the interplay and "conspiracy" between DM and stellar components during the galaxy formation process.

The inner DM mass fractions and inner log-slopes of DM density profiles in ETGs are two important but not well understood properties. The DM-only simulations predict a universal DM density profile, i.e., the NFW profile, which has an inner log-slope value commonly around -1. However, the existence of baryons is able to make the DM distribution more condensed through adiabatic contraction [148, 149], and also lower the slope value by repelling the DM from the central region through supernova feedback at the same time [151, 132, 125]. The information contained in the amount of DM and the slope of density profile are closely related to these two competing effects, which offers the possibility to test the validity of DM models, baryon feedback mechanisms and galaxy formation theories. There are numerous studies showing the smallness of DM fractions in the central regions of ETGs. Cappellari et al. inferred a 3D median DM fraction $\rm f_{DM}(r = R_e)$ around 13% within the effective radius R_e from the $ALTAS_{3D}$ 260 early-type galaxies [159]. Sonnenfeld et al. used 78 strong leasing and stellar velocity dispersion data from SL2S and SLACS lenses [10] and found that the average inner slope of the DM halos is consistent with that of an NFW profile and the mean projected DM fraction within R_e is $f_{DMe} = 33\%$. However no consistent results are shown in CDM simulations. Xu et al. indicate with Illustris simulations that the centrally concentrated baryon component is able to make the inner DM slope notably steeper than the NFW prediction, and that the central DM fraction is relatively higher than those inferred from observations and stellar dynamical studies [169]. Similar results appear again in the recent work from IllustrisTNG simulations [11, 170]. Lovell et al. in [11] showed that the simulated ETGs get larger DM fractions than those from Cappellari et al.'s work [159] and Barnade et al.'s results [171] using the Chabrier IMF, but they are more comparable to Barnade et al.'s outcomes [171] when the Salpeter IMF is applied. It seems the contracting effect on DM halos from concentrated baryons doesn't appear in the observations with stellar dynamical studies. These inconsistent results from observations and simulations are actually indicating potential challenges to the stellar formation theory, feedback models or even DM properties adopted in the studies.

A successful DM theory should be able to explain observations in different galactic systems. In this work, we apply the SIDM model to understand DM distributions in ETGs. DM self-interactions thermalize the inner halos in the presence of the baryons over the age of galaxies. This will lead to a thermal connection between DM and baryon distributions [80]. If the final baryon distribution is observed and the halo parameters are chosen, the DM distribution could be determined for a halo in equilibrium. We introduce the data and modeling methods for baryon density profiles, SIDM halos and adiabatically-contracted NFW profiles in Sec. 4.2. In Sec. 4.3, we analyze one example in detail and compare the DM fractions from our modelings and IllustrisTNG simulations. In Sec. 4.4, we discuss the mechanism behind the isothermal total density profiles and compare results from SIDM and adiabatic contracted NFW modelings. We conclude in Sec. 4.5.

4.2 Modeling Baryon and Dark Matter Distributions

In this section, we briefly review the data and the methods we use for modeling baryon, SIDM and adiabatically-contracted NFW density distributions. We take the data of 29 early-type galaxies from the work of Sonnenfel et al. [10]. These data contain the properties of ETGs, including the redshifts, effective radii, stellar mass for reproducing baryon density profiles, and DM mass and fractions within a certain radius for comparison purposes.

The surface-brightness profiles of ETGs can be effectively described by the Sersic model [172, 173] as following,

$$\Sigma(R) = \Sigma_0 \times \exp\left(-b_n \left(\frac{R}{R_e}\right)^{\frac{1}{n}}\right),\ b_n = 2n - 1/3 + 0.009876/n. \tag{4.1}$$

In this work, we fix Sersic index $n = 4$ and take the effective radius ($\mathrm{R_e}$) and stellar mass ($\mathrm{M_\star}$) directly from [10]. Different stellar profiles, such as Hernquist and Jaffe profiles, and variations in the effective radius have been tested in [10] which shows consistent results. To get the 3 dimensional (3D) baryon distribution, we assume spherical symmetry and apply the inverse Abel transformation to deproject the Sersic model as following,

$$\rho_{\rm b}(r) = -\frac{1}{\pi}\int_r^\infty \frac{dR}{\sqrt{R^2-r^2}}\frac{d\Sigma}{dR}. \tag{4.2}$$

We consider the DM halo under the influence of the baryon component and assume the ratio of stellar-to-halo masses to be 1.5% [174]. With DM self-interactions, scatterings between DM particles are more prevalent in the relative inner region where the DM density is high. It is useful to divide the halo into two regions, separated by a characteristic radius r_1 where the average scattering rate per particle times the age of galaxy ($t_{\rm age}$) is close to unity, i.e.,

$$\text{rate} \times \text{time} \approx \frac{\langle \sigma v\rangle}{m}\rho(r_1)t_{\rm age} \approx 1. \tag{4.3}$$

In Eq. 4.3, σ is the scattering cross section, m is the DM particle mass, v is the relative velocity between DM particles, $\langle ...\rangle$ denotes ensemble average over the isothermal velocity distritution and $t_{\rm age} = 10$ Gyr is set for ETGs.

For the outer halo ($r \geq r_1$), where scatterings have occurred less than once per particle on average, we expect the DM density to be close to an NFW profile. For the halo within r_1 ($r \leq r_1$), DM particles are thermalized. Under the complete hydrostatic equilibrium assumption, the gravitational attraction gets balanced by the repelling pressure gradient due to the random motions of DM particles, i.e., $\nabla p = -\rho_{\rm iso}\nabla\Phi_{\rm tot}$, with $p = \rho_{\rm iso} \times \sigma_0^2$, where p and $\rho_{\rm iso}$ are the DM dynamical pressure and mass density, σ_0 is the one-dimensional velocity dispersion, and $\Phi_{\rm tot}$ is the total gravitational potential of DM and baryons, which satisfies Poisson's equation $\nabla^2\Phi_{\rm tot} = 4\pi G(\rho_{\rm iso} + \rho_{\rm b})$, where G is the gravitational constant and $\rho_{\rm b}$ is the baryon mass density. We solve the SIDM density profile $\rho_{\rm iso}$ by requiring the continuity of density and mass to the outer NFW profile. The full SIDM profile are described as following:

$$\rho(r) = \begin{cases} \rho_{\rm iso}(r), & r < r_1 \\ \\ \rho_{\rm NFW}(r), & r > r_1. \end{cases} \tag{4.4}$$

Similar to the SIDM halo, we treat the NFW profile as a base line to model the CDM halo modified by the baryons. Since ETGs are at a stage with little gas and rare star formation, we assume the baryon effects on the DM halos are mainly in the form of adiabatic contraction. We apply the improved analytical adiabatic contraction model [149] to calculate the contracted CDM density profile. Compared to the original adiabatic contraction model proposed by Blumenthal et al. [148], the improved version is able to avoid over-predicting the DM density within 5% of the virial radius and account for the orbital eccentricities of DM particles. During the contraction process,

$$M(\bar{r})r = \text{constant} \tag{4.5}$$

is conserved, where r is radius, M is the total mass within $\bar{r}$ and $\bar{r} = Ar^w$ with $A = 0.85 \pm 0.05$ and $w = 0.8 \pm 0.02$ [149]. By assuming an NFW profile for the DM and baryon distribution at the very begin and choosing a reasonable baryon to total mass fraction within the virial radius, i.e., $M_{\rm B}/(M_{\rm B} + M_{\rm DM})$, the final DM mass profile can be calculated from the following equation

$$(M_{\rm DM}(\bar{r}_{\rm f}) + M_{\rm B}(\bar{r}_{\rm f})) \cdot r_{\rm f} = (M'_{\rm DM}(\bar{r}_{\rm i}) + M'_{\rm B}(\bar{r}_{\rm i})) \cdot r_{\rm i} \tag{4.6}$$

with $M_{\rm DM}(\bar{r}_{\rm f}) = M'_{\rm DM}(\bar{r}_{\rm i})$, and hence the final contracted density profile. In Eq. 4.6, $M_{\rm DM}$ is the final DM mass distribution, $M_{\rm B}$ is the final baryon mass distribution from the Sersic modeling, M'_{DM} and M'_{B} are the initial mass profiles for DM and baryons based on their assumed initial NFW density profiles.

4.3 Dark Matter Fractions

The interplay between DM and baryons during the galaxy formation process is complex. After severe mergers between galaxies, the DM and baryon components begin to settle down and finally become the ETGs we observe today. Since ETGs are usually poor of gas and have old star populations, the influence of baryons on the DM distribution can be considered always from their gravitational effect. With different DM properties, however, DM particles will go through different histories. In the CDM case, the collisionless DM particles are theoretically proposed to experience the adiabatic contraction due to the sink of baryon as described in the previous section. If there exist self-interactions between DM particles, collisions among them would happen in the central regions with high DM densities. A direct consequence is the thermalization of the inner halo. Typically, the pressure from the random motions of DM particles could keep the DM distribution from condensation to some degree. This leads to the expectation that the SIDM halo would be less contracted due to the baryon effect than the CDM halo through the adiabatic contraction.

Fig. 4.1 illustrates different responses of an SIDM halo and a CDM halo to the same baryon distribution taken from the SL2S data. The yellow curve is the NFW profile describing a CDM halo with $\mathrm{M_{halo}} = 2.2 \times 10^{13}\mathrm{M}_{\odot}$ and a medium concentration, which is what one can usually expect from the CDM-only simulations. The stellar density distribution is shown as the green curve. It corresponds to the stellar profile of an ETG with

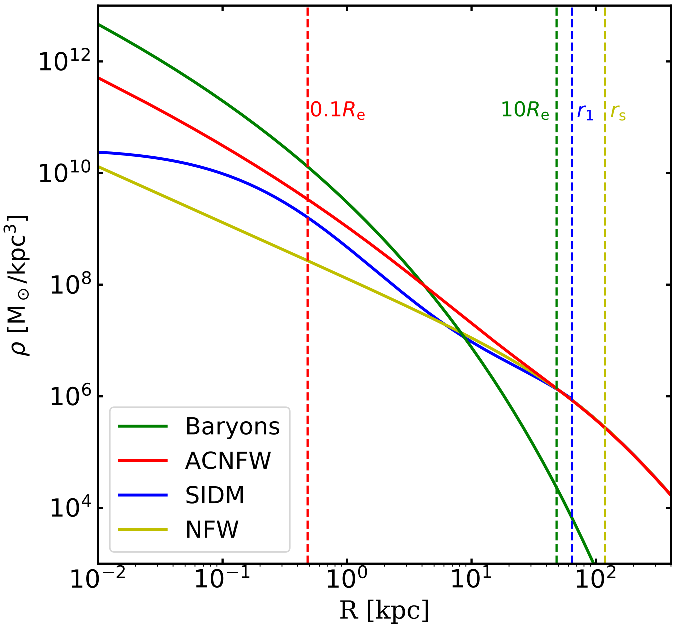

Figure 4.1: Different density profiles in an ETG with stellar mass $M_\star = 3.3 \times 10^{11} M_\odot$, halo mass $M_{\rm halo} = 2.2 \times 10^{13} M_\odot$, halo concentration = medium, effective radius $R_e = 4.82$ kpc and Sersic index $n = 4$. The green, red, blue and yellow solid lines denote the stellar component, adiabatically-contracted NFW profiles, SIDM profile and NFW profile. The red, green, blue, and yellow dashed lines denote $0.1R_e$, $10R_e$, r_1 and r_s.

stellar mass $M_\star = 3.3 \times 10^{11} M_\odot$, effective radius $R_e = 4.82$ kpc and Sersic index $n = 4$. The blue and red curves denote the DM density profiles for the SIDM and CDM halo respectively, after taking into account the effects from the baryons. The red, green, blue, and yellow dashed curves indicate some important radiuses for reference, i.e. 0.1 R_e, 10 R_e, r_1 and r_s. The adiabatically-contracted NFW (ACNFW) density is increased by a factor of 80 in the inner region $r < 0.1$ kpc and is gradually approaching the original NFW profile towards the outer regions. The SIDM density is enhanced by a factor of 10 near 0.1 kpc compared to the NFW profile. It is relatively flat in the central region (r < 0.1 kpc) due to the thermalization, and then quickly drops and approaches the NFW profile. The SIDM density becomes smaller than that of the NFW profile after around 10 kpc and match onto the NFW profile at r_1. This shape is intrinsic to the SIDM model under the constrains of the matching condition for its density and mass. By contrast, the ACNFW profile can have higher density than the NFW profile all the way towards r_1 and beyond.

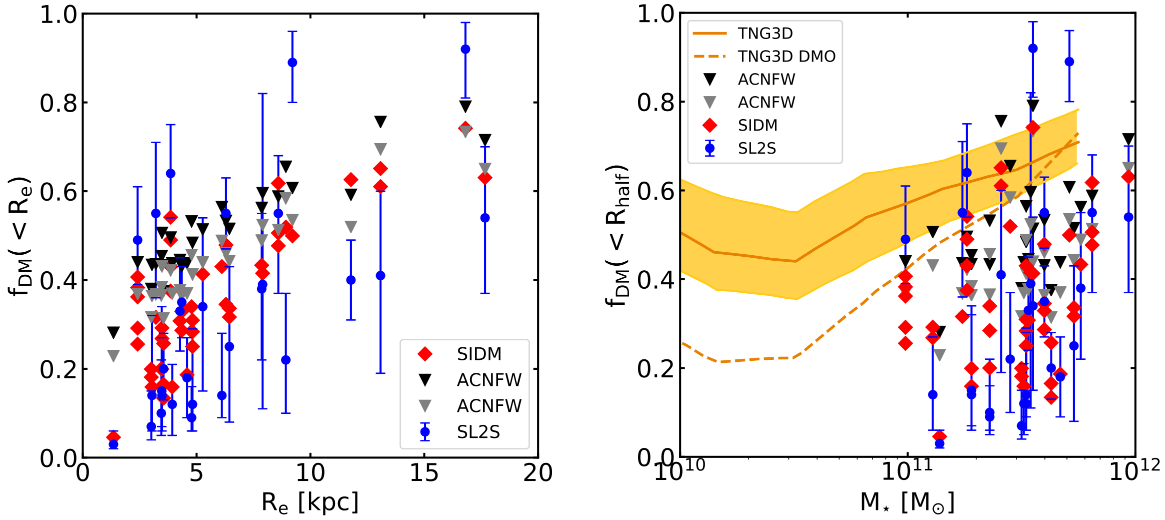

Figure 4.2: *Left*: DM fractions within 2D effective radii. SL2S data are shown in blue dots with error bars. SIDM data are represented by red diamonds. Black and gray triangles correspond to data from adiabatically-contracted NFW profiles with medium and -2σ concentrations. *Right*: Comparison between DM fractions in half-mass radii from IllustrisTNG simulations and those shown in the left panel. 3D half-mass radius is used in the simulation result. Data in the left panel is based on 2D half-mass radius, i.e., the effective radius. The solid orange curve indicates the median DM fraction of simulated ETGs and the yellow band denotes 1σ deviation. The dashed orange curve denotes the corresponding DM fraction in simulation runs only with DM.

We have shown that the SIDM and CDM halos respond to the presence of the baryons differently. The ACNFW profile has a higher DM density than that of SIDM within r_1. In Fig. 4.2, we show the detailed DM fractions in such systems and compare them with results from CDM simulations. Fig. 4.2 (left) shows the projected DM mass fractions within the effective radius (2D half-mass radius). The blue dots with error bars denote the results inferred from the measurements of strong lensing and stellar velocity dispersions [10]. They exhibit a general trend that when the effective radius increases so does the DM fraction within it. The red diamonds denote the SIDM predictions. For each galaxy, we vary the halo concentration within $\pm 2\sigma$ range [2] for the SIDM model. The black and gray triangles denote the results for the ACNFW profiles with medium and -2σ halo concentrations. Both models match the general trend of data distribution, i.e., the DM fraction increases with the effective radius. There could be several factors determining the DM fraction, such as the total mass of baryons and DM and their distribution condensations. Fig. 4.2 (left) shows the effect from the condensation of the baryon distributions qualitatively. The smaller the effective radius is, the more compact the baryon distribution is. This means with a small effective radius value, much more baryon mass is in the inner region so that the DM fraction gets smaller. For extended baryon distribution like $\mathrm{R_{eff}} > 7.5\mathrm{kpc}$, both ACNFW and SIDM results have close DM fractions and match well with the medium values from SL2S data. However, for the relatively compact ones, the ACNFW model predicts higher DM fractions than the SIDM model. Even for low halo concentrations (-2σ), the values from the ACNFW model barely reach as low as 30%. On the other hand, by varying the halo concentration, we show that the SIDM predictions are consistent with the overall trend of the observations.

In Fig. 4.2 (right), we compare the SL2S, ACNFW and SIDM results with IllustrisTNG simulations. We note that the DM fractions in the simulations are inferred within the 3D half-mass radii. If the 3D DM fraction is transferred to 2D projected one, it will increase by $5 - 15\%$ accordingly based on the ACNFW and SIDM analysis. The solid orange curve denotes the median DM fraction of the simulated ETGs in the full physics environment and the yellow band denotes $\pm 1\sigma$ range. The dashed orange curve indicates the corresponding DM fraction if the halos are taken from DM-only simulations. Under the baryons' influence, the DM fraction is obviously higher than that in the DM-only runs, which indicates the halo is contracted due to the existence of the baryons. However, these values from the IllustrisTNG simulations are significantly larger than 80% of the SL2S results. They are even larger than the analytical results from the adiabatic contraction with median halo concentrations. This indicates when the stellar mass is given for one ETG, either the DM gets more contracted in the IllustrisTNG simulations than those in the analytical cases, or the baryon component is relatively extended comparing to those got from the SL2S analysis.

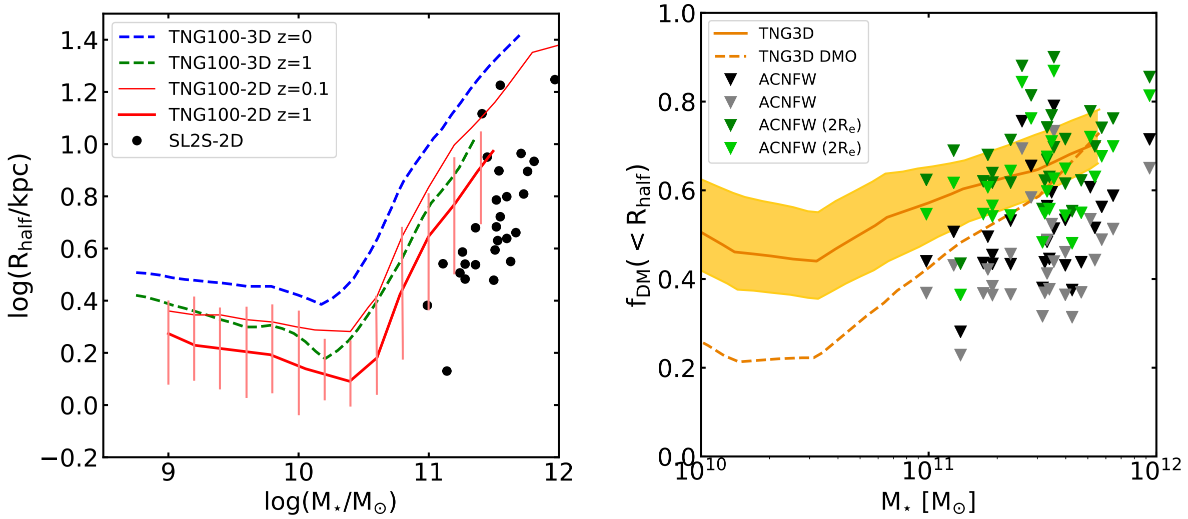

Figure 4.3: *Left*: Comparison between half-mass radii from the IllustrisTNG simulations and SL2S data. The blue and green dashed curves [9] correspond to 3D half-mass radii in TNG100 with $z = 0$ and $z = 1$. The thin and thick red solid curves [9] denotes 2D half-mass radii in TNG100 with $z = 0.1$ and $z = 1$. 2D effective radii from the SL2S data [10] are shown as black dots. *Right*: Comparison of DM fractions in the half-mass radii from the IllustrisTNG simulations and adiabatically-contracted NFW profiles. The difference is that the simulation results use the 3D half-mass radii and ones from adiabatically-contracted NFW profiles adopt the 2D half-mass radii, i.e., the effective radii. The solid orange curve [11] indicates the median DM fraction in the simulations and the yellow band [11] denotes the $\pm 1\sigma$ deviations. The dashed orange curve denotes the corresponding DM fractions from DM-only simulations [11]. The black and gray triangles represent results calculated with original effective radii, while dark and light green triangles denote results with doubled effective radii.

To explore the reasons for the discrepancy between the DM fractions from the simulations and observations, we examine the half-mass radii of the baryon profiles from the IllustrisTNG simulations with those from the SL2S samples in Fig. 4.3 (left). The 3D half-mass radii (the blue and green dashed curves) are larger than those 2D ones (red curves) in general. This is because when the 2D definition is changed to the 3D one, the baryon mass within a 2D half-mass radius leaks to the outside so that it's necessary to enclose more mass by increase the radius. By comparing the curves from the simulations and the dots from the SL2S samples, we find the effective radii from the SL2S samples are systematically smaller than those from the Illustris simulations, indicating that the baryon profiles in the SL2S samples are more compact for given stellar mass values. To test whether this will cause high DM fractions in the simulations, we apply the adiabatic contraction algorithm to the same halos but adjust the stellar effective radii to be two times of the initial values. We show the results in Fig. 4.3 (right). The dark and light green colors correspond to the medium and -2σ halo concentrations. Compared to the black and gray triangles calculated from the original baryon profiles, the dark and light green ones are systematically shifted upward and are more consistent with the yellow band from the IllustrisTNG simulations. Despite the expected difference between the 2D and 3D projected DM fractions, about $5-10\%$, the agreement is still much better compared to the results with the initial baryon profiles.

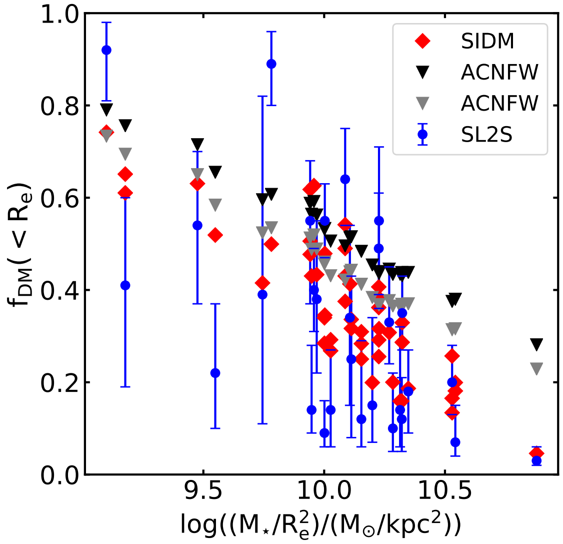

Figure 4.4: Correlation between DM fractions within effective radii and stellar condensations measured by $M_\star/R_{\rm eff}^2$. The results from the SL2S samples are shown as blue dots with error bars. Red diamonds represent the SIDM results. Black and gray triangles correspond to results from the adiabatically-contracted NFW profiles with medium and -2σ halo concentrations.

Thus, it seems that the illustrisTNG simulations do not produce galaxy analogs with high baryon concentrations, similar to the NIHAO and FIRE-2 simulations for spiral galaxies. Another supporting evidence is shown in Fig. 4.4, where we see there is a strong anti-correlation between the DM fraction and the stellar surface density, $M_\star/R_e^2$, measuring the compactness of the baryon distribution. However, the galaxies with small DM fractions indicating high baryon concentrations are missing in the simulations as shown in Fig. 4.2 (right).

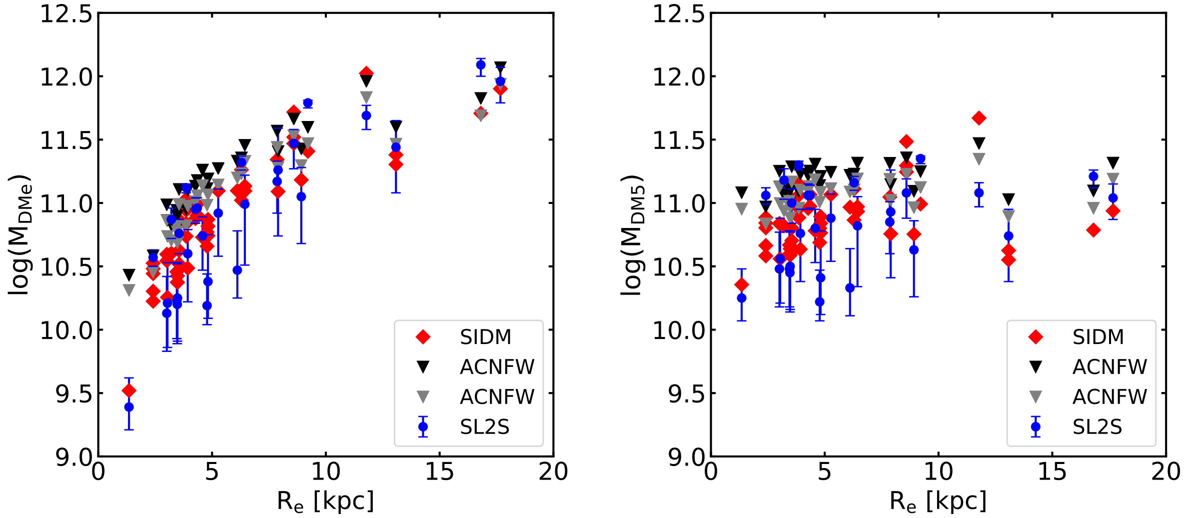

Figure 4.5: *Left*: DM mass within effective radii (R_e). *Right*: DM mass within 5 kpc. In both plots, blue dots with error bars denote the results from the SL2S sample. Red diamonds represent the SIDM results. Black and gray triangles correspond to data from adiabatically-contracted NFW profiles with medium and -2σ concentrations.

For completeness, we compare the projected DM masses within R_es and 5 kpc with those from the SIDM and ACNFW models. Fig. 4.5 (left) shows an obvious positive correlation between R_es and the projected DM mass. As the R_e increases, the enclosed region gets larger and contains more DM. Fig. 4.6 (right) illustrates that the project DM mass within 5 kpc. We see the variation for different galaxies is small and there is no obvious correlation between the R_es and the DM masses. From the both panels, we see that the DM fractions predicted in the ACNFW model are all towards the upper end of the SL2S results, even if the halo concentration is 2σ below the cosmological mean. On the other hand, the SIDM predictions match with the SL2S results reasonably well.

4.4 Isothermal Density Profiles

In the last section, we discussed the fraction of DM in the total enclosed mass and the discrepancy between the results from the observations and cosmological simulations. In this section, we focus on the universal isothermal total density profiles of ETGs. The isothermal density profile describes the distribution of ideal gas under the influence of gravity and has a uniform log-slope value of -2. Since the total density profile of an ETG consists of contributions from DM and baryons, the total density slope should implicitly depend on those of DM and baryon profiles. We use the normalized density forms as introduced in Ref. [12] and define the local log-slope of DM, stellar, and total density profiles to be α, β, and γ,

$$\mathrm{d}(\log_{10}(\frac{\rho_{\mathrm{DM}}}{\rho_{\mathrm{eDM}}})) = \alpha \times \mathrm{d}(\log_{10}(\frac{r}{R_{\mathrm{e}}})), \tag{4.7}$$

$$\mathrm{d}(\log_{10}(\frac{\rho_{\mathrm{star}}}{\rho_{\mathrm{estar}}})) = \beta \times \mathrm{d}(\log_{10}(\frac{r}{R_{\mathrm{e}}})), \tag{4.8}$$

$$\mathrm{d}(\log_{10}(\frac{\rho_{\mathrm{tot}}}{\rho_{\mathrm{etot}}})) = \gamma \times \mathrm{d}(\log_{10}(\frac{r}{R_{\mathrm{e}}})), \tag{4.9}$$

where ρ_e is the corresponding density value at R_e (effective radius). The relationship between three density profiles is,

$$\frac{\rho_{\mathrm{tot}}}{\rho_{\mathrm{etot}}} = \frac{\rho_{\mathrm{DM}} + \rho_{\mathrm{star}}}{\rho_{\mathrm{eDM}} + \rho_{\mathrm{estar}}}. \tag{4.10}$$

From Eq. 4.10, taking derivative of Eq. 4.9 leads to a simple result,

$$\gamma = \frac{\alpha \times 1 + \beta \times f(r)}{1 + f(r)}, \tag{4.11}$$

where $f(r) = \rho_{\mathrm{star}}/\rho_{\mathrm{DM}}$, the ratio of the local stellar-to-DM densities at radius r. This formula states that the log-slope of the total density profile is the density-weighted average of the DM and stellar density ones.

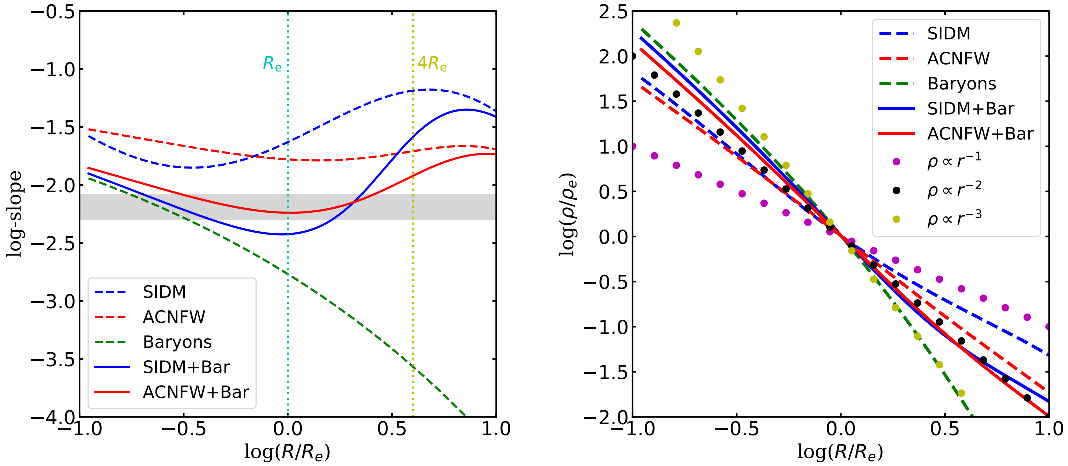

Figure 4.6: *Left*: The log-slope profiles for different components of the ETG example in Fig. 4.1. The blue, red and green dashed curves denote the SIDM, ACNFW and stellar models respectively. The log-slope for total density profiles are shown as blue solid (SIDM+baryons) and red solid (ACNFW+baryons). The gray band is the result from Cappellari et al. [12] within 1σ scatter. *Right*: The normalized density profiles for different colored components in the left panel. The purple, black and yellow dotted lines are for reference and denote the following density profiles $\rho \propto r^{-1}$, $\rho \propto r^{-2}$ and $\rho \propto r^{-3}$ respectively.

In Fig. 4.1, we have shown the density profiles of different components for a typical ETG. The stellar density dominates in the region ($r \lesssim 10$ kpc). From $0.1\mathrm{R_e}$ to $1\mathrm{R_e}$, the ratio of stellar-to-DM densities varies roughly from 20 to 10. According to Eq. 4.11, we expect the total density log-slope will be mainly controlled by the stellar component in this region for both the SIDM and ACNFW models. In the region where $r \gtrsim 10$ kpc, the SIDM and ACNFW profiles gradually merge onto the NFW profile. The stellar profile drops much faster than that of DM, and the stellar-to-DM density ratio is less than 0.01 beyond r_1 or 100 kpc. This ratio is so small that the DM component determines the log-slope of the total density.

The left panel of Fig. 4.6 shows the log-slope curves (from $0.1\mathrm{R_e}$ to $10\mathrm{R_e}$) of the different density profiles in Fig. 4.1. The ACNFW profile (red dashed) has a log-slope close to -1.5 over the whole range. Similarly, the log-slope of the SIDM profile (blue dashed) is around -1.5 but with obvious wiggles. Both of them show a tendency to have smaller log-slopes beyond $10\mathrm{R_e}$. In contrast to the almost constant slope values of both DM profiles, the log-slope of the stellar profile (dashed green) drops along the radius. The stellar density profile becomes more and more steep from ~ -2.0 at $0.1 R_\mathrm{e}$ to smaller than -4.0 round $10\ R_\mathrm{e}$. The log-slope of the total density profile stays in the middle between the curves of DM and stellar components. Within $\mathrm{R_e}$, it is close to the stellar curve since the stellar component dominates in this region. At a larger radius, the log-slope curve of the total density profile gradually deviates from the stellar curve and approaches the DM ones due to the much quicker drop of the stellar density.

In the right panel of Fig. 4.6, we show the normalized density profiles. Their behaviors closely follow the results shown in the left panel. Within R_e, the SIDM profile (blue dashed) is slightly steeper than the ACNFW one (red dashed). Both of them are below the $\rho \propto r^{-2}$ reference line. Outside of R_e, the SIDM profile becomes less steeper than the ACNFW one and deviates from the $\rho \propto r^{-2}$ line due to the imposed matching conditions. The stellar curve (green dashed) starts between the $\rho \propto r^{-2}$ and $\rho \propto r^{-3}$ lines, gradually matches onto and even becomes steeper than the $\rho \propto r^{-3}$ line. None of them shows the feature of an isothermal profile for a long range. However, for both SIDM and ACNFW models, the total normalized density profile shows a surprisingly consistent isothermal feature and follows the $\rho \propto r^{-2}$ line closely all the way from $0.1\ R_\mathrm{e}$ to $10\ R_\mathrm{e}$. We have discussed that this is due to a combined result of the log-slope values and the relative density magnitudes. In the inner region (e.g., within R_e), the stellar density dominates and has a log-slope around -2. For DM profiles, their reasonable log-slope values should be in the range from -3 to 0. As long as the stellar component dominates in this region, the total log-slope value should be close to -2. In the outer region (e.g., outside of R_{e}), since the stellar density drops much faster, the DM component begins to be dominant. The DM profile finally matches onto or approaches the NFW profile in the outer region. This limits the log-slope value of the DM profile in this range to be around -2, the log-slope value of the NFW profile at r_{s}. (For DM halos of ETGs, we usually have $r_s \gtrsim 10R_e$.) As a consequence, the total log-slope value is maintained around -2 for a large range. We can also find in Fig. 4.6 (left) that around $10R_e$ the total log-slope values are approximately -1.5 following the log-slope values of the DM profile. These values will approach -2 because of the constrains from the NFW profile, so that we can expect the isothermal density profiles continues to radii beyond $r_s \sim \mathcal{O}(100)$ kpc. This is the mechanism behind the DM-baryon conspiracy.

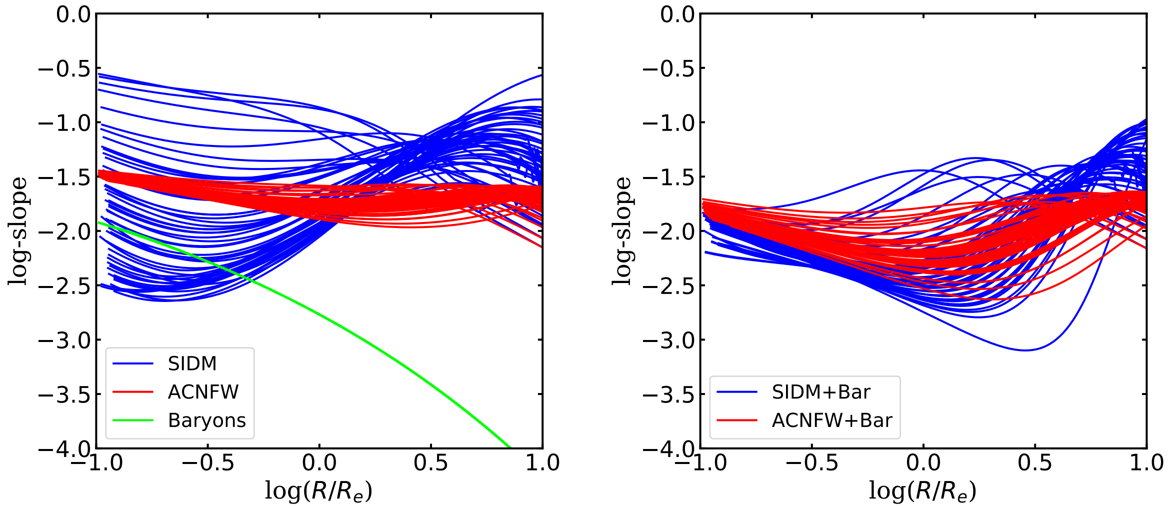

Figure 4.7: *Left*: The log-slope profiles for DM and stellar components respectively. The blue solid curves represent for 49 SIDM density profiles. The red solid curves denotes 58 ACNFW profiles with medium or -2σ halo concentrations. The green solid curves stands for all the stellar components which overlap with each other due to the normalization, Sersic model and index. *Right*: The log-slope profiles for the total density. 49 curves from the SIDM case are in blue and 58 ones from the ACNFW case are in red.

After discussing the slope and density profiles of one typical ETG example in detail, we focus on the whole sample and pay attention to the responses of DM halos to different baryon profiles in this section. Fig. 4.7 (left) shows the log-slope curves along the normalized radius. It contains 58 log-slope curves from the ACNFW profiles (red). Each of them correspond to an individual SL2S sample with a medium or -2σ halo concentration. The stellar log-slope curves (green) overlap with each other due to the normalization and the common Sersic model and index. Though the original stellar density profiles are different from each other, the ACNFW log-slope curves show a remarkable similarity in the plot. All of them are crowded around the log-slope value ~ -1.5. On the contrary, 49 SIDM log-slope profiles exhibit a great diversity. This demonstrates that the SIDM halos are more responsive to the variation of baryon density profiles. The log-slope curves for two kinds of total density profiles as shown in Fig. 4.7 (right). These curves have values centered around −2. The scatter in the SIDM model has decreased, but it is still larger than that in the ACNFW model even if its scatter has increased after combining the ACNFW profiles and baryons.

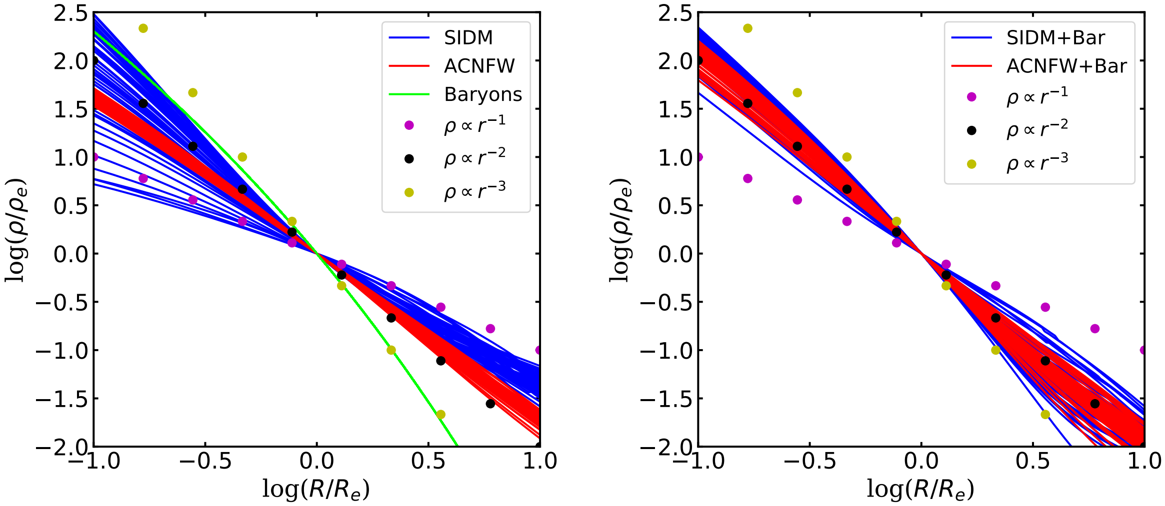

Figure 4.8: *Left*: Density profiles for different components. The blue solid curves represent for 49 SIDM density profiles. The red solid curves indicates 58 ACNFW profiles with medium or -2σ concentrations. The green solid curves denote all the stellar components which overlap with each other due to the normalization, Sersic model and index. *Right*: Total density profiles for the SIDM and ACNFW models. 49 curves from the SIDM model are in blue and 58 ones from the ACNFW model are in red.

The normalized density profiles for different components are shown in Fig. 4.8 (left). The SIDM profiles (blue) are much more diverse than the ACNFW ones (red). The ACNFW profiles stay close to each other and are slightly shallower than the $\rho \propto r^{-2}$ reference line. The normalized total density profiles are shown in Fig. 4.8 (right). The total density profiles in the SIDM model have a slightly larger scatter than those in the ACNFW model. For reference, we fit $\rho \propto r^{-\gamma}$ to the total density profiles in both models. We find $\langle\gamma\rangle = 2.00$ with $\sigma = 0.24$ for the SIDM model and $\langle\gamma\rangle = 2.07$ with $\sigma = 0.16$ fo the ACNFW model. Though the ACNFW model achieves a better result than the SIDM model in terms of the smallness of the scatter, both results are consistent with each other and with the results from Cappellari et al. [12]. Lastly, we comment that we did not directly impose the constraints on the density profiles from strong lensing and stellar kinematics.

4.5 Discussion and Conclusions

Our results suggest that the SIDM model can simultaneously explain the observed DM fractions within effective radii and the nearly isothermal total density profiles in ETGs. Not only the inferred DM fractions from the SIDM halos match the general growing trend of DM fractions while increasing the effective radius, but the values of DM mass within certain radius, e.g., $\mathrm{R_e}$ or 5 kpc, match well with the data. We found that the total log-slope actually is the density-weighted average of the DM and baryon log-slopes and the subdominant role of DM in the central regions of ETGs is necessary to explain the isothermal density profiles. The dominant baryon has log-slope values slightly smaller than -2 in the inner region and builds up the trend of the total density profile from this region. The DM density becomes dominant when the baryon density drops rapidly towards large radii, and its profile matches onto the NFW profile whose log-slope value decreases slowly to -2 at r_s, a large radius compared to R_e ($r_s \gtrsim 10\ R_e$).

We compared the DM fractions from the SIDM model, the ACNFW model, the IllustrisTNG simulations and the SL2S data together and showed the SIDM model can explain the data better. The values from the ACNFW profiles are systematically higher than those inferred from the SL2S data, especially for the compact ETGs. Thus, the adiabatically-contracted halo profile is incompatible with the observations. Additionally, we also found that the observed and the ACNFW values are also systematically lower than those from the IllustrisTNG simulations. This tension is probably caused by the more extended baryon profiles in the simulations compared to those from the SL2S data. We also studied the total density profiles from the SIDM and ACNFW models. We found that in the ACNFW model, the normalized DM density profiles show less variations and the total density profiles are possible to have a smaller scatter compared to the SIDM model. However, considering the performance in reproducing both the smallness of DM fractions and nearly isothermal total density profiles, we conclude the SIDM model works better.

We could further improve our analysis. Our SIDM model is completely analytical and based on the equilibrium assumption. The matching condition for the DM density and mass at r_1 is not perfectly satisfied. The uncertainties are about 5% for the most of cases. It would be of great interest to implement the SIDM model in cosmological simulations and further test our predictions. In addition, we did not directly include the lensing and kinematic data in our analysis. And there is a degeneracy effect between the galaxy age and the cross section. More work is needed to further test the SIDM model with ETGs.

Chapter 5

Conclusions

Our findings indicate that the novel DM model, SIDM, has the strong potential to solve the challenges the traditional CDM paradigm has while studying spiral galaxies and ETGs. By fitting to the rotation curve data from the SPARC sample, we reproduce the observed diversity and uniformity in the spiral galaxy sample. In addition, the required concentrations of the DM halos are fully consistent with the concentration-mass relation predicted by the Planck cosmological model. The inferred stellar M/Ls (3.6 μm) scatter around $0.5 M_{\odot}/L_{\odot}$, as expected from population synthesis models, leading to a tight radial acceleration relation and a baryonic Tully-Fisher relation. The inferred stellar-halo mass relation is consistent with the expectations from the abundance matching. Similarly, we adopt the SL2S data to model the SIDM halos and baryon density profiles in ETGs. We demonstrate the DM fractions from the SIDM model agree better with the data from lensing and kinematic studies than those predicted in the CDM model. The total density profiles show isothermal behaviors and are consistent with observations. We also show the

DM-baryon conspiracy is closely associated with the log-slope and the weights of DM and baryons in different regions.

The comparison between the SIDM fitting results and those from simulations, such as NIHAO simulations, illustrated the importance of diverse baryon profiles in reproducing the rotation curves. Especially, the lack of condensed baryon distributions is an important reason for the inability to cover the steep outliers in NIHAO simulations. Similar results appear in the study of ETGs, when we compare the effective radii derived from lensing and stellar kinematics with those in IllustrisTNG simulations. The simulated ETGs are less condensed with larger effective radii and this could be partial reasons for the high DM fractions in these systems. Such a coincidence makes us to suspect that some important factors are missing to generate condensed baryon profiles in simulations. In the analytical SIDM model, the baryon contributions are taken from observations and scaled by the stellar M/Ls. In the future, it would be of great interests to test whether hydrodynamical SIDM simulations could reproduce observed baryon distributions. In addition, we could further improve our analysis for ETGs by including both stellar kinematics and strong lensing data together.

We conclude that the diversity and uniformity in spiral galaxies, and the DM fractions and nearly isothermal total density profiles in ETGs that are not well understood in the CDM paradigm can be reasonably reproduced and explained with the SIDM model. These results suggest the thermalization of the inner halos in different galaxies is highly possible. Though improved baryon physics in the CDM paradigm, such as baryonic feedback mechanisms, is conventionally expected to offer solutions, it would be constructive to increase the weight of SIDM in galaxy formation research among simulations and analytical studies.

Bibliography

[1] F. Lelli, S. S. McGaugh, and J. M. Schombert, "Sparc: mass models for 175 disk galaxies with spitzer photometry and accurate rotation curves," *The Astronomical Journal*, vol. 152, no. 6, p. 157, 2016.

[2] A. A. Dutton and A. V. Macciò, "Cold dark matter haloes in the planck era: evolution of structural parameters for einasto and nfw profiles," *Monthly Notices of the Royal Astronomical Society*, vol. 441, no. 4, pp. 3359–3374, 2014.

[3] P. S. Behroozi, R. H. Wechsler, and C. Conroy, "The average star formation histories of galaxies in dark matter halos from z= 0-8," *The Astrophysical Journal*, vol. 770, no. 1, p. 57, 2013.

[4] F. Lelli, S. S. McGaugh, and J. M. Schombert, "The small scatter of the baryonic tully–fisher relation," *The Astrophysical Journal Letters*, vol. 816, no. 1, p. L14, 2016.

[5] I. M. Santos-Santos, A. Di Cintio, C. B. Brook, A. Macciò, A. Dutton, and R. Domínguez-Tenreiro, "Nihao–xiv. reproducing the observed diversity of dwarf galaxy rotation curve shapes in λcdm," *Monthly Notices of the Royal Astronomical Society*, vol. 473, no. 4, pp. 4392–4403, 2017.

[6] J. S. Bullock and M. Boylan-Kolchin, "Small-scale challenges to the λ cdm paradigm," *Annual Review of Astronomy and Astrophysics*, vol. 55, pp. 343–387, 2017.

[7] A. Fitts, M. Boylan-Kolchin, O. D. Elbert, J. S. Bullock, P. F. Hopkins, J. Oñorbe, A. Wetzel, C. Wheeler, C.-A. Faucher-Giguère, D. Kereš, *et al.*, "Fire in the field: simulating the threshold of galaxy formation," *Monthly Notices of the Royal Astronomical Society*, vol. 471, no. 3, pp. 3547–3562, 2017.

[8] P. F. Hopkins, A. Wetzel, D. Kereš, C.-A. Faucher-Giguère, E. Quataert, M. Boylan-Kolchin, N. Murray, C. C. Hayward, S. Garrison-Kimmel, C. Hummels, *et al.*, "Fire-2 simulations: physics versus numerics in galaxy formation," *Monthly Notices of the Royal Astronomical Society*, vol. 480, no. 1, pp. 800–863, 2018.

[9] S. Genel, D. Nelson, A. Pillepich, V. Springel, R. Pakmor, R. Weinberger, L. Hernquist, J. Naiman, M. Vogelsberger, F. Marinacci, *et al.*, "The size evolution of star-

forming and quenched galaxies in the illustristng simulation," *Monthly Notices of the Royal Astronomical Society*, vol. 474, no. 3, pp. 3976–3996, 2017.

[10] A. Sonnenfeld, T. Treu, P. J. Marshall, S. H. Suyu, R. Gavazzi, M. W. Auger, and C. Nipoti, "The sl2s galaxy-scale lens sample. v. dark matter halos and stellar imf of massive early-type galaxies out to redshift 0.8," *The Astrophysical Journal*, vol. 800, no. 2, p. 94, 2015.

[11] M. R. Lovell, A. Pillepich, S. Genel, D. Nelson, V. Springel, R. Pakmor, F. Marinacci, R. Weinberger, P. Torrey, M. Vogelsberger, *et al.*, "The fraction of dark matter within galaxies from the illustristng simulations," *Monthly Notices of the Royal Astronomical Society*, vol. 481, no. 2, pp. 1950–1975, 2018.

[12] M. Cappellari, A. J. Romanowsky, J. P. Brodie, D. A. Forbes, J. Strader, C. Foster, S. S. Kartha, N. Pastorello, V. Pota, L. R. Spitler, *et al.*, "Small scatter and nearly isothermal mass profiles to four half-light radii from two-dimensional stellar dynamics of early-type galaxies," *The Astrophysical Journal Letters*, vol. 804, no. 1, p. L21, 2015.

[13] F. Zwicky, "Die rotverschiebung von extragalaktischen nebeln," *Helvetica Physica Acta*, vol. 6, pp. 110–127, 1933.

[14] F. Zwicky, "On the masses of nebulae and of clusters of nebulae," *The Astrophysical Journal*, vol. 86, p. 217, 1937.

[15] K. C. Freeman, "On the disks of spiral and s0 galaxies," *The Astrophysical Journal*, vol. 160, p. 811, 1970.

[16] H. W. Babcock, "The rotation of the andromeda nebula," *Lick Observatory Bulletin*, vol. 19, pp. 41–51, 1939.

[17] J. P. Ostriker and P. J. Peebles, "A numerical study of the stability of flattened galaxies: or, can cold galaxies survive?," *The Astrophysical Journal*, vol. 186, pp. 467–480, 1973.

[18] F. Hohl, "Numerical experiments with a disk of stars," *The Astrophysical Journal*, vol. 168, p. 343, 1971.

[19] J. Binney and S. Tremaine, *Galactic dynamics*, vol. 20. Princeton university press, 2011.

[20] D. Rogstad and G. Shostak, "Gross properties of five scd galaxies as determined from 21-centimeter observations," *The Astrophysical Journal*, vol. 176, p. 315, 1972.

[21] G. Shostak and D. Rogstad, "Aperture synthesis study of neutral hydrogen in ngc 2403 and ngc 4236. i. observations.," *Astronomy and Astrophysics*, vol. 24, pp. 405–410, 1973.

[22] M. S. Roberts and R. N. Whitehurst, "The rotation curve and geometry of m31 at large galactocentric distances.," *The Astrophysical Journal*, vol. 201, pp. 327–346, 1975.

[23] M. Roberts, "The rotation curves of galaxies," in *Symposium-International Astronomical Union*, vol. 69, pp. 331–340, Cambridge University Press, 1975.

[24] V. C. Rubin, W. K. Ford Jr, and N. Thonnard, "Extended rotation curves of high-luminosity spiral galaxies. iv-systematic dynamical properties, sa through sc," *The Astrophysical Journal*, vol. 225, pp. L107–L111, 1978.

[25] A. Bosma, *The distribution and kinematics of neutral hydrogen in spiral galaxies of various morphological types.* PhD thesis, Rijksuniversiteit te Groningen., 1978.

[26] P. Peebles, "The black-body radiation content of the universe and the formation of galaxies.," *The Astrophysical Journal*, vol. 142, p. 1317, 1965.

[27] P. J. Peebles and J. Yu, "Primeval adiabatic perturbation in an expanding universe," *The Astrophysical Journal*, vol. 162, p. 815, 1970.

[28] E. L. Wright, "Theoretical overview of cosmic microwave background anisotropy," *arXiv preprint astro-ph/0305591*, 2003.

[29] E. Kolb, *The early universe.* CRC Press, 2018.

[30] G. R. Blumenthal, S. Faber, J. R. Primack, and M. J. Rees, "Formation of galaxies and large-scale structure with cold dark matter," *Nature*, vol. 311, no. 5986, p. 517, 1984.

[31] P. Peebles, "Large-scale background temperature and mass fluctuations due to scale-invariant primeval perturbations," 1982.

[32] J. R. Bond, A. S. Szalay, and M. S. Turner, "Formation of galaxies in a gravitino-dominated universe," *Physical Review Letters*, vol. 48, no. 23, p. 1636, 1982.

[33] G. R. Blumenthal, H. Pagels, and J. R. Primack, "Galaxy formation by dissipationless particles heavier than neutrinos," *Nature*, vol. 299, no. 5878, p. 37, 1982.

[34] M. Tegmark, M. R. Blanton, M. A. Strauss, F. Hoyle, D. Schlegel, R. Scoccimarro, M. S. Vogeley, D. H. Weinberg, I. Zehavi, A. Berlind, *et al.*, "The three-dimensional power spectrum of galaxies from the sloan digital sky survey," *The Astrophysical Journal*, vol. 606, no. 2, p. 702, 2004.

[35] H. Miyazawa, "Baryon number changing currents," *Progress of Theoretical Physics*, vol. 36, no. 6, pp. 1266–1276, 1966.

[36] H. Miyazawa, "Spinor currents and symmetries of baryons and mesons," *Physical Review*, vol. 170, no. 5, p. 1586, 1968.

[37] G. Jungman, M. Kamionkowski, and K. Griest, "Supersymmetric dark matter," *Physics Reports*, vol. 267, no. 5-6, pp. 195–373, 1996.

[38] J. L. Feng, "Dark matter candidates from particle physics and methods of detection," *Annual Review of Astronomy and Astrophysics*, vol. 48, pp. 495–545, 2010.

[39] E. Aprile, M. Alfonsi, K. Arisaka, F. Arneodo, C. Balan, L. Baudis, B. Bauermeister, A. Behrens, P. Beltrame, K. Bokeloh, *et al.*, "Observation and applications of single-electron charge signals in the xenon100 experiment," *Journal of Physics G: Nuclear and Particle Physics*, vol. 41, no. 3, p. 035201, 2014.

[40] J. Dubinski and R. Carlberg, "The structure of cold dark matter halos," *The Astrophysical Journal*, vol. 378, pp. 496–503, 1991.

[41] J. F. Navarro, "Jf navarro, cs frenk, and sdm white, astrophys. j. 462, 563 (1996).," *Astrophys. J.*, vol. 462, p. 563, 1996.

[42] J. F. Navarro, C. S. Frenk, and S. D. White, "A universal density profile from hierarchical clustering," *The Astrophysical Journal*, vol. 490, no. 2, p. 493, 1997.

[43] B. Moore, T. Quinn, F. Governato, J. Stadel, and G. Lake, "Cold collapse and the core catastrophe," *Monthly Notices of the Royal Astronomical Society*, vol. 310, no. 4, pp. 1147–1152, 1999.

[44] R. A. Flores and J. R. Primack, "Observational and theoretical constraints on singular dark matter halos," *arXiv preprint astro-ph/9402004*, 1994.

[45] B. Moore, "Evidence against dissipation-less dark matter from observations of galaxy haloes," *Nature*, vol. 370, no. 6491, p. 629, 1994.

[46] F. Governato, C. Brook, L. Mayer, A. Brooks, G. Rhee, J. Wadsley, P. Jonsson, B. Willman, G. Stinson, T. Quinn, *et al.*, "Bulgeless dwarf galaxies and dark matter cores from supernova-driven outflows," *Nature*, vol. 463, no. 7278, p. 203, 2010.

[47] F. Governato, A. Zolotov, A. Pontzen, C. Christensen, S. Oh, A. Brooks, T. Quinn, S. Shen, and J. Wadsley, "Cuspy no more: how outflows affect the central dark matter and baryon distribution in λ cold dark matter galaxies," *Monthly Notices of the Royal Astronomical Society*, vol. 422, no. 2, pp. 1231–1240, 2012.

[48] K. A. Oman, J. F. Navarro, A. Fattahi, C. S. Frenk, T. Sawala, S. D. White, R. Bower, R. A. Crain, M. Furlong, M. Schaller, *et al.*, "The unexpected diversity of dwarf galaxy rotation curves," *Monthly Notices of the Royal Astronomical Society*, vol. 452, no. 4, pp. 3650–3665, 2015.

[49] M. Boylan-Kolchin, J. S. Bullock, and M. Kaplinghat, "Too big to fail? the puzzling darkness of massive milky way subhaloes," *Monthly Notices of the Royal Astronomical Society: Letters*, vol. 415, no. 1, pp. L40–L44, 2011.

[50] M. Boylan-Kolchin, J. S. Bullock, and M. Kaplinghat, "The milky ways bright satellites as an apparent failure of λcdm," *Monthly Notices of the Royal Astronomical Society*, vol. 422, no. 2, pp. 1203–1218, 2012.

[51] Q. Guo and S. White, "Numerical resolution limits on subhalo abundance matching," *Monthly Notices of the Royal Astronomical Society*, vol. 437, no. 4, pp. 3228–3235, 2013.

[52] D. N. Spergel and P. J. Steinhardt, "Observational evidence for self-interacting cold dark matter," *Physical Review Letters*, vol. 84, no. 17, p. 3760, 2000.

[53] J. L. Feng, M. Kaplinghat, H. Tu, and H.-B. Yu, "Hidden charged dark matter," *Journal of Cosmology and Astroparticle Physics*, vol. 2009, no. 07, p. 004, 2009.

[54] J. L. Feng, M. Kaplinghat, and H.-B. Yu, "Halo-shape and relic-density exclusions of sommerfeld-enhanced dark matter explanations of cosmic ray excesses," *Physical Review Letters*, vol. 104, no. 15, p. 151301, 2010.

[55] M. R. Buckley and P. J. Fox, "Dark matter self-interactions and light force carriers," *Physical Review D*, vol. 81, no. 8, p. 083522, 2010.

[56] A. Loeb and N. Weiner, "Cores in dwarf galaxies from dark matter with a yukawa potential," *Physical Review Letters*, vol. 106, no. 17, p. 171302, 2011.

[57] M. T. Frandsen and S. Sarkar, "Asymmetric dark matter and the sun," *Physical review letters*, vol. 105, no. 1, p. 011301, 2010.

[58] M. T. Frandsen, S. Sarkar, and K. Schmidt-Hoberg, "Light asymmetric dark matter from new strong dynamics," *Physical Review D*, vol. 84, no. 5, p. 051703, 2011.

[59] L. G. van den Aarssen, T. Bringmann, and C. Pfrommer, "Is dark matter with long-range interactions a solution to all small-scale problems of λ cold dark matter cosmology?," *Physical Review Letters*, vol. 109, no. 23, p. 231301, 2012.

[60] J. M. Cline, Z. Liu, G. D. Moore, and W. Xue, "Composite strongly interacting dark matter," *Physical Review D*, vol. 90, no. 1, p. 015023, 2014.

[61] F. Kahlhoefer, K. Schmidt-Hoberg, M. T. Frandsen, and S. Sarkar, "Colliding clusters and dark matter self-interactions," *Monthly Notices of the Royal Astronomical Society*, vol. 437, no. 3, pp. 2865–2881, 2013.

[62] S. Tulin, H.-B. Yu, and K. M. Zurek, "Beyond collisionless dark matter: particle physics dynamics for dark matter halo structure," *Physical Review D*, vol. 87, no. 11, p. 115007, 2013.

[63] K. Schutz and T. R. Slatyer, "Self-scattering for dark matter with an excited state," *Journal of Cosmology and Astroparticle Physics*, vol. 2015, no. 01, p. 021, 2015.

[64] K. K. Boddy, J. L. Feng, M. Kaplinghat, and T. M. Tait, "Self-interacting dark matter from a non-abelian hidden sector," *Physical Review D*, vol. 89, no. 11, p. 115017, 2014.

[65] Y. Hochberg, E. Kuflik, T. Volansky, and J. G. Wacker, “Mechanism for thermal relic dark matter of strongly interacting massive particles,” *Physical review letters*, vol. 113, no. 17, p. 171301, 2014.

[66] Y. Hochberg, E. Kuflik, H. Murayama, T. Volansky, and J. G. Wacker, “Model for thermal relic dark matter of strongly interacting massive particles,” *Physical review letters*, vol. 115, no. 2, p. 021301, 2015.

[67] F.-Y. Cyr-Racine, K. Sigurdson, J. Zavala, T. Bringmann, M. Vogelsberger, and C. Pfrommer, “Ethosan effective theory of structure formation: From dark particle physics to the matter distribution of the universe,” *Physical Review D*, vol. 93, no. 12, p. 123527, 2016.

[68] M. Blennow, S. Clementz, and J. Herrero-Garcia, “Self-interacting inelastic dark matter: A viable solution to the small scale structure problems,” *Journal of Cosmology and Astroparticle Physics*, vol. 2017, no. 03, p. 048, 2017.

[69] K. K. Boddy, M. Kaplinghat, A. Kwa, and A. H. Peter, “Hidden sector hydrogen as dark matter: small-scale structure formation predictions and the importance of hyperfine interactions,” *Physical Review D*, vol. 94, no. 12, p. 123017, 2016.

[70] A. Kamada, H. J. Kim, and H. Kim, “Self-heating of strongly interacting massive particles,” *Physical Review D*, vol. 98, no. 2, p. 023509, 2018.

[71] E. Braaten, D. Kang, and R. Laha, “Production of dark-matter bound states in the early universe by three-body recombination,” *Journal of High Energy Physics*, vol. 2018, no. 11, p. 84, 2018.

[72] M. Kaplinghat, S. Tulin, and H.-B. Yu, “Dark matter halos as particle colliders: unified solution to small-scale structure puzzles from dwarfs to clusters,” *Physical Review Letters*, vol. 116, no. 4, p. 041302, 2016.

[73] A. Kamada, M. Kaplinghat, A. B. Pace, and H.-B. Yu, “Self-interacting dark matter can explain diverse galactic rotation curves,” *Physical review letters*, vol. 119, no. 11, p. 111102, 2017.

[74] J. Liu, X. Chen, and X. Ji, “Current status of direct dark matter detection experiments,” *Nature Physics*, vol. 13, no. 3, p. 212, 2017.

[75] M. Kaplinghat, S. Tulin, and H.-B. Yu, “Direct detection portals for self-interacting dark matter,” *Physical Review D*, vol. 89, no. 3, p. 035009, 2014.

[76] E. Del Nobile, M. Kaplinghat, and H.-B. Yu, “Direct detection signatures of self-interacting dark matter with a light mediator,” *Journal of Cosmology and Astroparticle Physics*, vol. 2015, no. 10, p. 055, 2015.

[77] H. An, B. Echenard, M. Pospelov, and Y. Zhang, “Probing the dark sector with dark matter bound states,” *Physical review letters*, vol. 116, no. 15, p. 151801, 2016.

[78] Y. Tsai, L.-T. Wang, and Y. Zhao, “Dark matter annihilation decay at the lhc,” *Physical Review D*, vol. 93, no. 3, p. 035024, 2016.

[79] M. Rocha, A. H. Peter, J. S. Bullock, M. Kaplinghat, S. Garrison-Kimmel, J. Onorbe, and L. A. Moustakas, “Cosmological simulations with self-interacting dark matter–i. constant-density cores and substructure,” *Monthly Notices of the Royal Astronomical Society*, vol. 430, no. 1, pp. 81–104, 2013.

[80] M. Kaplinghat, R. E. Keeley, T. Linden, and H.-B. Yu, “Tying dark matter to baryons with self-interactions,” *Physical review letters*, vol. 113, no. 2, p. 021302, 2014.

[81] R. Essig, S. D. McDermott, H.-B. Yu, and Y.-M. Zhong, “Constraining dissipative dark matter self-interactions,” *arXiv preprint arXiv:1809.01144*, 2018.

[82] H. Nishikawa, K. K. Boddy, and M. Kaplinghat, “Accelerated core collapse in tidally stripped self-interacting dark matter halos,” *arXiv preprint arXiv:1901.00499*, 2019.

[83] O. Sameie, H.-B. Yu, L. V. Sales, M. Vogelsberger, and J. Zavala, “Self-interacting dark matter subhalos in the milky way’s tides,” *arXiv preprint arXiv:1904.07872*, 2019.

[84] F. Kahlhoefer, M. Kaplinghat, T. R. Slatyer, and C.-L. Wu, “Diversity in density profiles of self-interacting dark matter satellite halos,” *arXiv preprint arXiv:1904.10539*, 2019.

[85] A. Burkert, “The structure of dark matter halos in dwarf galaxies,” *The Astrophysical Journal Letters*, vol. 447, no. 1, p. L25, 1995.

[86] M. Persic, P. Salucci, and F. Stel, “The universal rotation curve of spiral galaxiesi. the dark matter connection,” *Monthly Notices of the Royal Astronomical Society*, vol. 281, no. 1, pp. 27–47, 1996.

[87] W. De Blok, F. Walter, E. Brinks, C. Trachternach, S. Oh, and R. Kennicutt Jr, “High-resolution rotation curves and galaxy mass models from things,” *The Astronomical Journal*, vol. 136, no. 6, p. 2648, 2008.

[88] G. Gentile, P. Salucci, U. Klein, D. Vergani, and P. Kalberla, “The cored distribution of dark matter in spiral galaxies,” *Monthly Notices of the Royal Astronomical Society*, vol. 351, no. 3, pp. 903–922, 2004.

[89] R. K. De Naray, S. S. McGaugh, and W. De Blok, “Mass models for low surface brightness galaxies with high-resolution optical velocity fields,” *The Astrophysical Journal*, vol. 676, no. 2, p. 920, 2008.

[90] S.-H. Oh, W. De Blok, E. Brinks, F. Walter, and R. C. Kennicutt Jr, “Dark and luminous matter in things dwarf galaxies,” *The Astronomical Journal*, vol. 141, no. 6, p. 193, 2011.

[91] S.-H. Oh, D. A. Hunter, E. Brinks, B. G. Elmegreen, A. Schruba, F. Walter, M. P. Rupen, L. M. Young, C. E. Simpson, M. C. Johnson, *et al.*, "High-resolution mass models of dwarf galaxies from little things," *The Astronomical Journal*, vol. 149, no. 6, p. 180, 2015.

[92] R. K. de Naray, G. D. Martinez, J. S. Bullock, and M. Kaplinghat, "The case against warm or self-interacting dark matter as explanations for cores in low surface brightness galaxies," *The Astrophysical Journal Letters*, vol. 710, no. 2, p. L161, 2010.

[93] M. Milgrom, "A modification of the newtonian dynamics as a possible alternative to the hidden mass hypothesis," *The Astrophysical Journal*, vol. 270, pp. 365–370, 1983.

[94] M. Milgrom, "A modification of the newtonian dynamics-implications for galaxies," *The Astrophysical Journal*, vol. 270, pp. 371–389, 1983.

[95] B. Famaey and S. S. McGaugh, "Modified newtonian dynamics (mond): observational phenomenology and relativistic extensions," *Living reviews in relativity*, vol. 15, no. 1, p. 10, 2012.

[96] S. S. McGaugh, F. Lelli, and J. M. Schombert, "Radial acceleration relation in rotationally supported galaxies," *Physical Review Letters*, vol. 117, no. 20, p. 201101, 2016.

[97] P. Li, F. Lelli, S. McGaugh, and J. Schombert, "Fitting the radial acceleration relation to individual sparc galaxies," *Astronomy & Astrophysics*, vol. 615, p. A3, 2018.

[98] F. C. van den Bosch and J. J. Dalcanton, "Semianalytical models for the formation of disk galaxies. ii. dark matter versus modified newtonian dynamics," *The Astrophysical Journal*, vol. 534, no. 1, p. 146, 2000.

[99] M. Kaplinghat and M. Turner, "How cold dark matter theory explains milgroms law," *The Astrophysical Journal Letters*, vol. 569, no. 1, p. L19, 2002.

[100] B. Keller and J. Wadsley, "λcdm is consistent with sparc radial acceleration relation," *The Astrophysical Journal Letters*, vol. 835, no. 1, p. L17, 2017.

[101] A. D. Ludlow, A. Benítez-Llambay, M. Schaller, T. Theuns, C. S. Frenk, R. Bower, J. Schaye, R. A. Crain, J. F. Navarro, A. Fattahi, *et al.*, "Mass-discrepancy acceleration relation: a natural outcome of galaxy formation in cold dark matter halos," *Physical review letters*, vol. 118, no. 16, p. 161103, 2017.

[102] J. F. Navarro, A. Benítez-Llambay, A. Fattahi, C. S. Frenk, A. D. Ludlow, K. A. Oman, M. Schaller, and T. Theuns, "The origin of the mass discrepancy–acceleration relation in λcdm," *Monthly Notices of the Royal Astronomical Society*, vol. 471, no. 2, pp. 1841–1848, 2017.

[103] M. Vogelsberger, J. Zavala, C. Simpson, and A. Jenkins, "Dwarf galaxies in cdm and sidm with baryons: observational probes of the nature of dark matter," *Monthly Notices of the Royal Astronomical Society*, vol. 444, no. 4, pp. 3684–3698, 2014.

[104] O. D. Elbert, J. S. Bullock, M. Kaplinghat, S. Garrison-Kimmel, A. S. Graus, and M. Rocha, "A testable conspiracy: simulating baryonic effects on self-interacting dark matter halos," *The Astrophysical Journal*, vol. 853, no. 2, p. 109, 2018.

[105] P. Creasey, O. Sameie, L. V. Sales, H.-B. Yu, M. Vogelsberger, and J. Zavala, "Spreading out and staying sharp–creating diverse rotation curves via baryonic and self-interaction effects," *Monthly Notices of the Royal Astronomical Society*, vol. 468, no. 2, pp. 2283–2295, 2017.

[106] J. M. Schombert and S. McGaugh, "Stellar populations and the star formation histories of lsb galaxies: Iv spitzer surface photometry of lsb galaxies," *Publications of the Astronomical Society of Australia*, vol. 31, 2014.

[107] A. Robertson, R. Massey, V. Eke, S. Tulin, H.-B. Yu, Y. Bahé, D. J. Barnes, R. G. Bower, R. A. Crain, C. Dalla Vecchia, *et al.*, "The diverse density profiles of galaxy clusters with self-interacting dark matter plus baryons," *Monthly Notices of the Royal Astronomical Society: Letters*, vol. 476, no. 1, pp. L20–L24, 2018.

[108] O. Sameie, P. Creasey, H.-B. Yu, L. V. Sales, M. Vogelsberger, and J. Zavala, "The impact of baryonic discs on the shapes and profiles of self-interacting dark matter haloes," *Monthly Notices of the Royal Astronomical Society*, vol. 479, no. 1, pp. 359–367, 2018.

[109] R. Davé, D. N. Spergel, P. J. Steinhardt, and B. D. Wandelt, "Halo properties in cosmological simulations of self-interacting cold dark matter," *The Astrophysical Journal*, vol. 547, no. 2, p. 574, 2001.

[110] A. H. Peter, M. Rocha, J. S. Bullock, and M. Kaplinghat, "Cosmological simulations with self-interacting dark matter–ii. halo shapes versus observations," *Monthly Notices of the Royal Astronomical Society*, vol. 430, no. 1, pp. 105–120, 2013.

[111] M. Vogelsberger, J. Zavala, and A. Loeb, "Subhaloes in self-interacting galactic dark matter haloes," *Monthly Notices of the Royal Astronomical Society*, vol. 423, no. 4, pp. 3740–3752, 2012.

[112] J. Zavala, M. Vogelsberger, and M. G. Walker, "Constraining self-interacting dark matter with the milky ways dwarf spheroidals," *Monthly Notices of the Royal Astronomical Society: Letters*, vol. 431, no. 1, pp. L20–L24, 2013.

[113] M. Vogelsberger, J. Zavala, F.-Y. Cyr-Racine, C. Pfrommer, T. Bringmann, and K. Sigurdson, "Ethos–an effective theory of structure formation: dark matter physics as a possible explanation of the small-scale cdm problems," *Monthly Notices of the Royal Astronomical Society*, vol. 460, no. 2, pp. 1399–1416, 2016.

[114] O. D. Elbert, J. S. Bullock, S. Garrison-Kimmel, M. Rocha, J. Oñorbe, and A. H. Peter, "Core formation in dwarf haloes with self-interacting dark matter: no fine-tuning necessary," *Monthly Notices of the Royal Astronomical Society*, vol. 453, no. 1, pp. 29–37, 2015.

[115] A. Sokolenko, K. Bondarenko, T. Brinckmann, J. Zavala, M. Vogelsberger, T. Bringmann, and A. Boyarsky, "Towards an improved model of self-interacting dark matter haloes," *Journal of Cosmology and Astroparticle Physics*, vol. 2018, no. 12, p. 038, 2018.

[116] C. Firmani, E. D'Onghia, V. Avila-Reese, G. Chincarini, and X. Hernández, "Evidence of self-interacting cold dark matter from galactic to galaxy cluster scales," *Monthly Notices of the Royal Astronomical Society*, vol. 315, no. 3, pp. L29–L32, 2000.

[117] N. Yoshida, V. Springel, S. D. White, and G. Tormen, "Weakly self-interacting dark matter and the structure of dark halos," *The Astrophysical Journal Letters*, vol. 544, no. 2, p. L87, 2000.

[118] M. T. Frandsen and J. Petersen, "Investigating dark matter and mond models with galactic rotation curve data," *arXiv preprint arXiv:1805.10706*, 2018.

[119] H. Desmond, "A statistical investigation of the mass discrepancy–acceleration relation," *Monthly Notices of the Royal Astronomical Society*, vol. 464, no. 4, pp. 4160–4175, 2016.

[120] S. S. McGaugh, J. M. Schombert, G. D. Bothun, and W. J. G. de Blok, "The baryonic tully-fisher relation," *The Astrophysical Journal*, vol. 533, pp. L99–L102, apr 2000.

[121] J. D. Bradford, M. C. Geha, and F. C. van den Bosch, "A slippery slope: Systematic uncertainties in the line width baryonic tully–fisher relation," *The Astrophysical Journal*, vol. 832, no. 1, p. 11, 2016.

[122] A. A. Ponomareva, M. A. Verheijen, E. Papastergis, A. Bosma, and R. F. Peletier, "From light to baryonic mass: the effect of the stellar mass-to-light ratio on the baryonic tully–fisher relation," *Monthly Notices of the Royal Astronomical Society*, vol. 474, no. 4, pp. 4366–4384, 2017.

[123] F. Prada, A. A. Klypin, A. J. Cuesta, J. E. Betancort-Rijo, and J. Primack, "Halo concentrations in the standard λ cold dark matter cosmology," *Monthly Notices of the Royal Astronomical Society*, vol. 423, no. 4, pp. 3018–3030, 2012.

[124] A. D. Ludlow, J. F. Navarro, R. E. Angulo, M. Boylan-Kolchin, V. Springel, C. Frenk, and S. D. White, "The mass–concentration–redshift relation of cold dark matter haloes," *Monthly Notices of the Royal Astronomical Society*, vol. 441, no. 1, pp. 378–388, 2014.

[125] H. Katz, F. Lelli, S. S. McGaugh, A. Di Cintio, C. B. Brook, and J. M. Schombert, "Testing feedback-modified dark matter haloes with galaxy rotation curves: estimation of halo parameters and consistency with λcdm scaling relations," *Monthly Notices of the Royal Astronomical Society*, vol. 466, no. 2, pp. 1648–1668, 2016.

[126] D. C. Rodrigues, V. Marra, A. del Popolo, and Z. Davari, "Absence of a fundamental acceleration scale in galaxies," *Nature Astronomy*, vol. 2, no. 8, p. 668, 2018.

[127] A. V. Kravtsov, "The size-virial radius relation of galaxies," *The Astrophysical Journal Letters*, vol. 764, no. 2, p. L31, 2013.

[128] P. A. Ade, N. Aghanim, C. Armitage-Caplan, M. Arnaud, M. Ashdown, F. Atrio-Barandela, J. Aumont, C. Baccigalupi, A. J. Banday, R. Barreiro, *et al.*, "Planck 2013 results. xvi. cosmological parameters," *Astronomy & Astrophysics*, vol. 571, p. A16, 2014.

[129] P. A. Ade, N. Aghanim, M. Arnaud, M. Ashdown, J. Aumont, C. Baccigalupi, A. Banday, R. Barreiro, J. Bartlett, N. Bartolo, *et al.*, "Planck 2015 results-xiii. cosmological parameters," *Astronomy & Astrophysics*, vol. 594, p. A13, 2016.

[130] P. Li, F. Lelli, S. S. McGaugh, N. Starkman, and J. M. Schombert, "A constant characteristic volume density of dark matter haloes from sparc rotation curve fits," *Monthly Notices of the Royal Astronomical Society*, vol. 482, no. 4, pp. 5106–5124, 2018.

[131] A. A. Dutton, "The baryonic tully–fisher relation and galactic outflows," *Monthly Notices of the Royal Astronomical Society*, vol. 424, no. 4, pp. 3123–3128, 2012.

[132] T. Chan, D. Kereš, J. Onorbe, P. Hopkins, A. Muratov, C.-A. Faucher-Giguere, and E. Quataert, "The impact of baryonic physics on the structure of dark matter haloes: the view from the fire cosmological simulations," *Monthly Notices of the Royal Astronomical Society*, vol. 454, no. 3, pp. 2981–3001, 2015.

[133] L. V. Sales, J. F. Navarro, K. Oman, A. Fattahi, I. Ferrero, M. Abadi, R. Bower, R. A. Crain, C. S. Frenk, T. Sawala, *et al.*, "The low-mass end of the baryonic tully–fisher relation," *Monthly Notices of the Royal Astronomical Society*, vol. 464, no. 2, pp. 2419–2428, 2016.

[134] A. A. Dutton, A. Obreja, L. Wang, T. A. Gutcke, T. Buck, S. M. Udrescu, J. Frings, G. S. Stinson, X. Kang, and A. V. Macciò, "Nihao xii: galactic uniformity in a λcdm universe," *Monthly Notices of the Royal Astronomical Society*, vol. 467, no. 4, pp. 4937–4950, 2017.

[135] C. Wheeler, P. F. Hopkins, and O. Doré, "The radial acceleration relation is a natural consequence of the baryonic tully-fisher relation," *arXiv preprint arXiv:1803.01849*, 2018.

[136] V. H. Robles, J. S. Bullock, O. D. Elbert, A. Fitts, A. González-Samaniego, M. Boylan-Kolchin, P. F. Hopkins, C.-A. Faucher-Giguère, D. Kereš, and C. C. Hayward, "Sidm on fire: Hydrodynamical self-interacting dark matter simulations of low-mass dwarf galaxies," *Monthly Notices of the Royal Astronomical Society*, vol. 472, no. 3, pp. 2945–2954, 2017.

[137] P. F. Hopkins, D. Kereš, J. Oñorbe, C.-A. Faucher-Giguère, E. Quataert, N. Murray, and J. S. Bullock, "Galaxies on fire (feedback in realistic environments): stellar feedback explains cosmologically inefficient star formation," *Monthly Notices of the Royal Astronomical Society*, vol. 445, no. 1, pp. 581–603, 2014.

[138] J. Oñorbe, M. Boylan-Kolchin, J. S. Bullock, P. F. Hopkins, D. Kereš, C.-A. Faucher-Giguère, E. Quataert, and N. Murray, "Forged in fire: cusps, cores and baryons in low-mass dwarf galaxies," *Monthly Notices of the Royal Astronomical Society*, vol. 454, no. 2, pp. 2092–2106, 2015.

[139] L. Wang, A. A. Dutton, G. S. Stinson, A. V. Macciò, C. Penzo, X. Kang, B. W. Keller, and J. Wadsley, "Nihao project–i. reproducing the inefficiency of galaxy formation across cosmic time with a large sample of cosmological hydrodynamical simulations," *Monthly Notices of the Royal Astronomical Society*, vol. 454, no. 1, pp. 83–94, 2015.

[140] J. Read, G. Iorio, O. Agertz, and F. Fraternali, "The stellar mass–halo mass relation of isolated field dwarfs: a critical test of λcdm at the edge of galaxy formation," *Monthly Notices of the Royal Astronomical Society*, vol. 467, no. 2, pp. 2019–2038, 2017.

[141] T. Carleton, R. Errani, M. Cooper, M. Kaplinghat, J. Peñarrubia, and Y. Guo, "The formation of ultra-diffuse galaxies in cored dark matter haloes through tidal stripping and heating," *Monthly Notices of the Royal Astronomical Society*, vol. 485, no. 1, pp. 382–395, 2019.

[142] M. Valli and H.-B. Yu, "Dark matter self-interactions from the internal dynamics of dwarf spheroidals," *Nature Astronomy*, vol. 2, no. 11, p. 907, 2018.

[143] J. Read, M. Walker, and P. Steger, "The case for a cold dark matter cusp in draco," *Monthly Notices of the Royal Astronomical Society*, vol. 481, no. 1, pp. 860–877, 2018.

[144] S. Tulin and H.-B. Yu, "Dark matter self-interactions and small scale structure," *Physics Reports*, vol. 730, pp. 1–57, 2018.

[145] D. Foreman-Mackey, D. W. Hogg, D. Lang, and J. Goodman, "emcee: the mcmc hammer," *Publications of the Astronomical Society of the Pacific*, vol. 125, no. 925, p. 306, 2013.

[146] V. Springel, C. S. Frenk, and S. D. White, "The large-scale structure of the universe," *Nature*, vol. 440, no. 7088, p. 1137, 2006.

[147] S. Trujillo-Gomez, A. Klypin, J. Primack, and A. J. Romanowsky, "Galaxies in λcdm with halo abundance matching: Luminosity-velocity relation, baryonic mass-velocity relation, velocity function, and clustering," *The Astrophysical Journal*, vol. 742, no. 1, p. 16, 2011.

[148] G. R. Blumenthal, S. Faber, R. Flores, and J. R. Primack, "Contraction of dark matter galactic halos due to baryonic infall," *The Astrophysical Journal*, vol. 301, pp. 27–34, 1986.

[149] O. Y. Gnedin, A. V. Kravtsov, A. A. Klypin, and D. Nagai, "Response of dark matter halos to condensation of baryons: cosmological simulations and improved adiabatic contraction model," *The Astrophysical Journal*, vol. 616, no. 1, p. 16, 2004.

[150] M. G. Abadi, J. F. Navarro, M. Fardal, A. Babul, and M. Steinmetz, "Galaxy-induced transformation of dark matter haloes," *Monthly Notices of the Royal Astronomical Society*, vol. 407, no. 1, pp. 435–446, 2010.

[151] A. D. Cintio, C. B. Brook, A. A. Dutton, A. V. Macciò, G. S. Stinson, and A. Knebe, "A mass-dependent density profile for dark matter haloes including the influence of galaxy formation," *Monthly Notices of the Royal Astronomical Society*, vol. 441, no. 4, pp. 2986–2995, 2014.

[152] C. B. Brook, "The variation of rotation curve shapes as a signature of the effects of baryons on dark matter density profiles," *Monthly Notices of the Royal Astronomical Society*, vol. 454, no. 2, pp. 1719–1724, 2015.

[153] J. Read, G. Iorio, O. Agertz, and F. Fraternali, "Understanding the shape and diversity of dwarf galaxy rotation curves in λcdm," *Monthly Notices of the Royal Astronomical Society*, vol. 462, no. 4, pp. 3628–3645, 2016.

[154] T. Ren, A. Kwa, M. Kaplinghat, and H.-B. Yu, "Reconciling the diversity and uniformity of galactic rotation curves with self-interacting dark matter," *Physical Review X*, vol. 9, no. 3, p. 031020, 2019.

[155] S. S. McGaugh and J. M. Schombert, "Color-mass-to-light-ratio relations for disk galaxies," *The Astronomical Journal*, vol. 148, no. 5, p. 77, 2014.

[156] M. Eskew, D. Zaritsky, and S. Meidt, "Converting from 3.6 and 4.5 μm fluxes to stellar mass," *The Astronomical Journal*, vol. 143, no. 6, p. 139, 2012.

[157] E. Tollet, A. V. Macciò, A. A. Dutton, G. S. Stinson, L. Wang, C. Penzo, T. A. Gutcke, T. Buck, X. Kang, C. Brook, *et al.*, "Nihao–iv: core creation and destruction in dark matter density profiles across cosmic time," *Monthly Notices of the Royal Astronomical Society*, vol. 456, no. 4, pp. 3542–3552, 2016.

[158] N. Napolitano, A. J. Romanowsky, M. Capaccioli, N. G. Douglas, M. Arnaboldi, L. Coccato, O. Gerhard, K. Kuijken, M. Merrifield, S. P. Bamford, *et al.*, "The pn. s elliptical galaxy survey: a standard λcdm halo around ngc 4374?," *Monthly Notices of the Royal Astronomical Society*, vol. 411, no. 3, pp. 2035–2053, 2011.

[159] M. Cappellari, N. Scott, K. Alatalo, L. Blitz, M. Bois, F. Bournaud, M. Bureau, A. F. Crocker, R. L. Davies, T. A. Davis, *et al.*, "The atlas3d project–xv. benchmark for early-type galaxies scaling relations from 260 dynamical models: mass-to-light ratio, dark matter, fundamental plane and mass plane," *Monthly Notices of the Royal Astronomical Society*, vol. 432, no. 3, pp. 1709–1741, 2013.

[160] A. Agnello, N. Evans, A. J. Romanowsky, and J. Brodie, "Dynamical models of elliptical galaxies–ii. m87 and its globular clusters," *Monthly Notices of the Royal Astronomical Society*, vol. 442, no. 4, pp. 3299–3314, 2014.

[161] A. Wasserman, A. J. Romanowsky, J. Brodie, P. van Dokkum, C. Conroy, A. Villaume, D. A. Forbes, J. Strader, A. Alabi, and S. Bellstedt, "The sluggs survey: The inner dark matter density slope of the massive elliptical galaxy ngc 1407," *The Astrophysical Journal*, vol. 863, no. 2, p. 130, 2018.

[162] A. Sonnenfeld, T. Treu, R. Gavazzi, P. J. Marshall, M. W. Auger, S. H. Suyu, L. V. Koopmans, and A. S. Bolton, "Evidence for dark matter contraction and a salpeter initial mass function in a massive early-type galaxy," *The Astrophysical Journal*, vol. 752, no. 2, p. 163, 2012.

[163] A. B. Newman, T. Treu, R. S. Ellis, and D. J. Sand, "The density profiles of massive, relaxed galaxy clusters. ii. separating luminous and dark matter in cluster cores," *The Astrophysical Journal*, vol. 765, no. 1, p. 25, 2013.

[164] D. Leier, I. Ferreras, P. Saha, S. Charlot, G. Bruzual, and F. La Barbera, "Strong gravitational lensing and the stellar imf of early-type galaxies," *Monthly Notices of the Royal Astronomical Society*, vol. 459, no. 4, pp. 3677–3692, 2016.

[165] S. Djorgovski and M. Davis, "Fundamental properties of elliptical galaxies," *The Astrophysical Journal*, vol. 313, pp. 59–68, 1987.

[166] P. J. Humphrey and D. A. Buote, "The slope of the mass profile and the tilt of the fundamental plane in early-type galaxies," *Monthly Notices of the Royal Astronomical Society*, vol. 403, no. 4, pp. 2143–2151, 2010.

[167] N. Lyskova, E. Churazov, and T. Naab, "Mass density slope of elliptical galaxies from strong lensing and resolved stellar kinematics," *Monthly Notices of the Royal Astronomical Society*, vol. 475, no. 2, pp. 2403–2414, 2018.

[168] S. Bellstedt, D. A. Forbes, A. J. Romanowsky, R.-S. Remus, A. R. Stevens, J. P. Brodie, A. Poci, R. McDermid, A. Alabi, L. Chevalier, *et al.*, "The sluggs survey: a comparison of total-mass profiles of early-type galaxies from observations and cosmological simulations, to 4 effective radii," *Monthly Notices of the Royal Astronomical Society*, vol. 476, no. 4, pp. 4543–4564, 2018.

[169] D. Xu, V. Springel, D. Sluse, P. Schneider, A. Sonnenfeld, D. Nelson, M. Vogelsberger, and L. Hernquist, "The inner structure of early-type galaxies in the illustris simulation," *Monthly Notices of the Royal Astronomical Society*, vol. 469, no. 2, pp. 1824–1848, 2017.

[170] Y. Wang, M. Vogelsberger, D. Xu, S. Mao, V. Springel, H. Li, D. Barnes, L. Hernquist, A. Pillepich, F. Marinacci, *et al.*, "Early-type galaxy density profiles from illustristng: I. galaxy correlations and the impact of baryons," *arXiv preprint arXiv:1811.06545*, 2018.

[171] M. Barnabè, O. Czoske, L. V. Koopmans, T. Treu, and A. S. Bolton, "Two-dimensional kinematics of slacs lenses–iii. mass structure and dynamics of early-type lens galaxies beyond z 0.1," *Monthly Notices of the Royal Astronomical Society*, vol. 415, no. 3, pp. 2215–2232, 2011.

[172] J. Sérsic, “Influence of the atmospheric and instrumental dispersion on the brightness distribution in a galaxy,” *Boletin de la Asociacion Argentina de Astronomia La Plata Argentina*, vol. 6, p. 41, 1963.

[173] N. Caon, M. Capaccioli, and M. D’onofrio, “On the shape of the light profiles of early-type galaxies,” *Monthly Notices of the Royal Astronomical Society*, vol. 265, no. 4, pp. 1013–1021, 1993.

[174] K.-H. Chae, M. Bernardi, and A. V. Kravtsov, “Modelling mass distribution in elliptical galaxies: mass profiles and their correlation with velocity dispersion profiles,” *Monthly Notices of the Royal Astronomical Society*, vol. 437, no. 4, pp. 3670–3687, 2013.

[175] M. Schwarzschild, “Mass distribution and mass-luminosity ratio in galaxies,” *The Astronomical Journal*, vol. 59, p. 273, 1954.

[176] P. J. E. Peebles, *The large-scale structure of the universe.* Princeton university press, 1980.

[177] Y. Tsai, T. Xu, and H.-B. Yu, “Displaced lepton jet signatures from self-interacting dark matter bound states,” *arXiv preprint arXiv:1811.05999*, 2018.

[178] V. C. Rubin, W. K. Ford Jr, and N. Thonnard, “Rotational properties of 21 sc galaxies with a large range of luminosities and radii, from ngc 4605/r= 4kpc/to ugc 2885/r= 122 kpc,” *The Astrophysical Journal*, vol. 238, pp. 471–487, 1980.

[179] T. Ren, A. Kwa, M. Kaplinghat, and H.-B. Yu, “Reconciling the diversity and uniformity of galactic rotation curves with self-interacting dark matter,” *arXiv preprint arXiv:1808.05695*, 2018.

[180] S. McGaugh, “Baryonic tully-fisher relations,” *arXiv preprint astro-ph/0009338*, 2000.

[181] A.-M. Weijmans, D. Krajnović, G. Van De Ven, T. A. Oosterloo, R. Morganti, and P. De Zeeuw, “The shape of the dark matter halo in the early-type galaxy ngc 2974,” *Monthly Notices of the Royal Astronomical Society*, vol. 383, no. 4, pp. 1343–1358, 2008.

[182] A. J. Romanowsky, N. G. Douglas, M. Arnaboldi, K. Kuijken, M. R. Merrifield, N. R. Napolitano, M. Capaccioli, and K. C. Freeman, “A dearth of dark matter in ordinary elliptical galaxies,” *Science*, vol. 301, no. 5640, pp. 1696–1698, 2003.

[183] A. Dekel, F. Stoehr, G. Mamon, T. Cox, G. Novak, and J. Primack, “Lost and found dark matter in elliptical galaxies,” *Nature*, vol. 437, no. 7059, p. 707, 2005.

[184] V. Pota, A. J. Romanowsky, J. P. Brodie, J. Peñarrubia, D. A. Forbes, N. R. Napolitano, C. Foster, M. G. Walker, J. Strader, and J. C. Roediger, “The sluggs survey: multipopulation dynamical modelling of the elliptical galaxy ngc 1407 from stars and globular clusters,” *Monthly Notices of the Royal Astronomical Society*, vol. 450, no. 3, pp. 3345–3358, 2015.

[185] L. Ferrarese and D. Merritt, "A fundamental relation between supermassive black holes and their host galaxies," *The Astrophysical Journal Letters*, vol. 539, no. 1, p. L9, 2000.

[186] W. G. Mathews and F. Brighenti, "Hot gas in and around elliptical galaxies," *Annual Review of Astronomy and Astrophysics*, vol. 41, no. 1, pp. 191–239, 2003.

[187] C. R. Keeton, "Cold dark matter and strong gravitational lensing: Concord or conflict?," *The Astrophysical Journal*, vol. 561, no. 1, p. 46, 2001.

[188] A. Bosma, "21-cm line studies of spiral galaxies. i-observations of the galaxies ngc 5033, 3198, 5055, 2841, and 7331," *The Astronomical Journal*, vol. 86, pp. 1791–1824, 1981.

[189] R. H. Sanders and S. S. McGaugh, "Modified newtonian dynamics as an alternative to dark matter," *Annual Review of Astronomy and Astrophysics*, vol. 40, no. 1, pp. 263–317, 2002.

[190] R. B. Tully and J. R. Fisher, "A new method of determining distances to galaxies," *Astronomy and Astrophysics*, vol. 54, pp. 661–673, 1977.

[191] S. Faber and R. E. Jackson, "Velocity dispersions and mass-to-light ratios for elliptical galaxies," *The Astrophysical Journal*, vol. 204, pp. 668–683, 1976.

[192] D. Clowe, A. Gonzalez, and M. Markevitch, "Weak-lensing mass reconstruction of the interacting cluster 1e 0657–558: Direct evidence for the existence of dark matter," *The Astrophysical Journal*, vol. 604, no. 2, p. 596, 2004.

[193] M. Markevitch, A. Gonzalez, D. Clowe, A. Vikhlinin, W. Forman, C. Jones, S. Murray, and W. Tucker, "Direct constraints on the dark matter self-interaction cross section from the merging galaxy cluster 1e 0657–56," *The Astrophysical Journal*, vol. 606, no. 2, p. 819, 2004.

[194] J. Bekenstein and M. Milgrom, "Does the missing mass problem signal the breakdown of newtonian gravity?," *The Astrophysical Journal*, vol. 286, pp. 7–14, 1984.

[195] J. D. Bekenstein, "Relativistic gravitation theory for the modified newtonian dynamics paradigm," *Physical Review D*, vol. 70, no. 8, p. 083509, 2004.

[196] A. A. Penzias and R. W. Wilson, "A measurement of excess antenna temperature at 4080 mc/s.," *The Astrophysical Journal*, vol. 142, pp. 419–421, 1965.

[197] R. A. Alpher, H. Bethe, and G. Gamow, "The origin of chemical elements," *Physical Review*, vol. 73, no. 7, p. 803, 1948.

[198] R. Allen and F. Shu, "The extrapolated central surface brightness of galaxies," *The Astrophysical Journal*, vol. 227, pp. 67–72, 1979.

Appendix A

SIDM and MOND Fitting Results

A.1 Fits

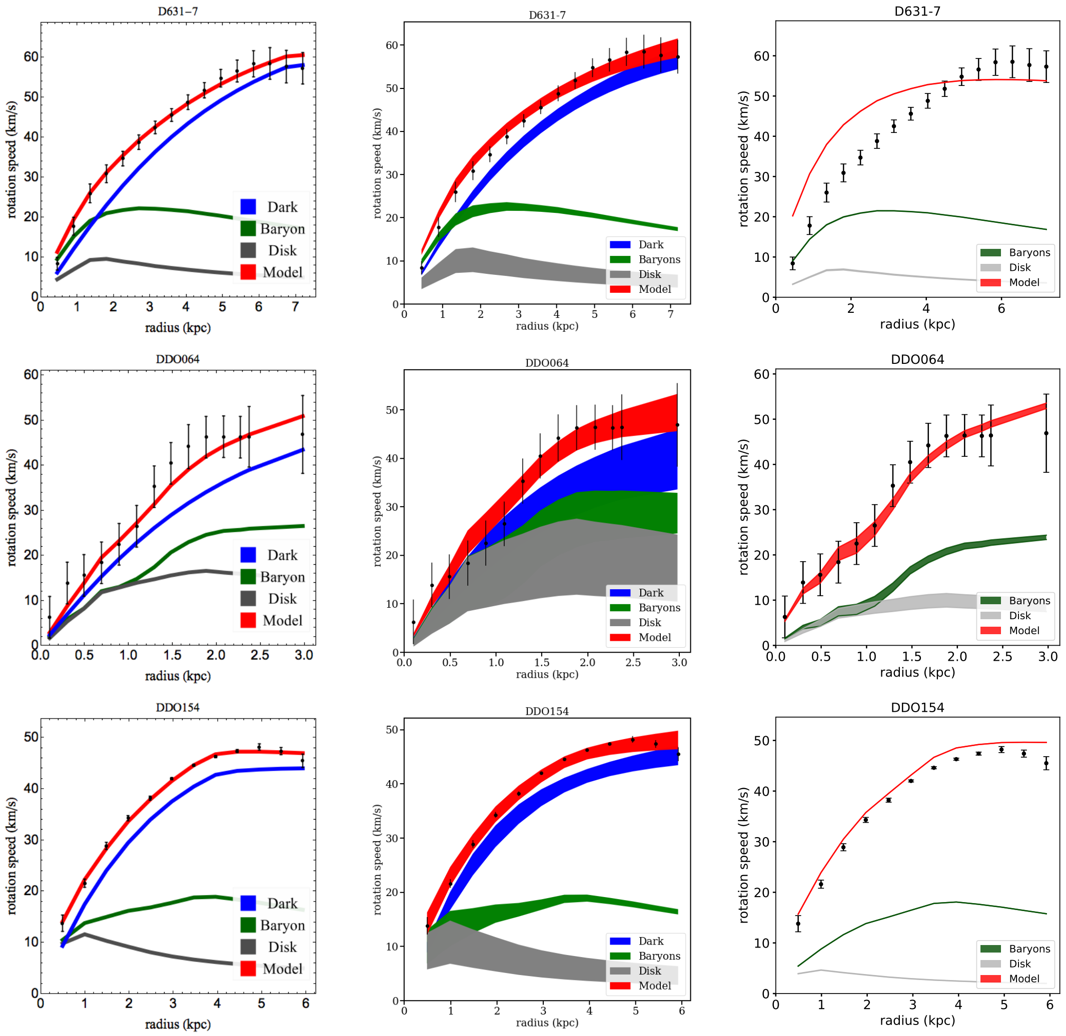

Figure A.1: Detailed SIDM fits to the 135 SPARC galaxies with the controlled (left) and MCMC (tophat prior, middle) sampling methods, with $\sigma/m = 3$ cm^2/g. The model parameters and χ^2/d.o.f. values are collected in Table A.1. The MOND fits (right) are also shown for comparison. The observational data are taken from Lelli et al. Astron. J. **152**, 157 (2016), 1606.09251.

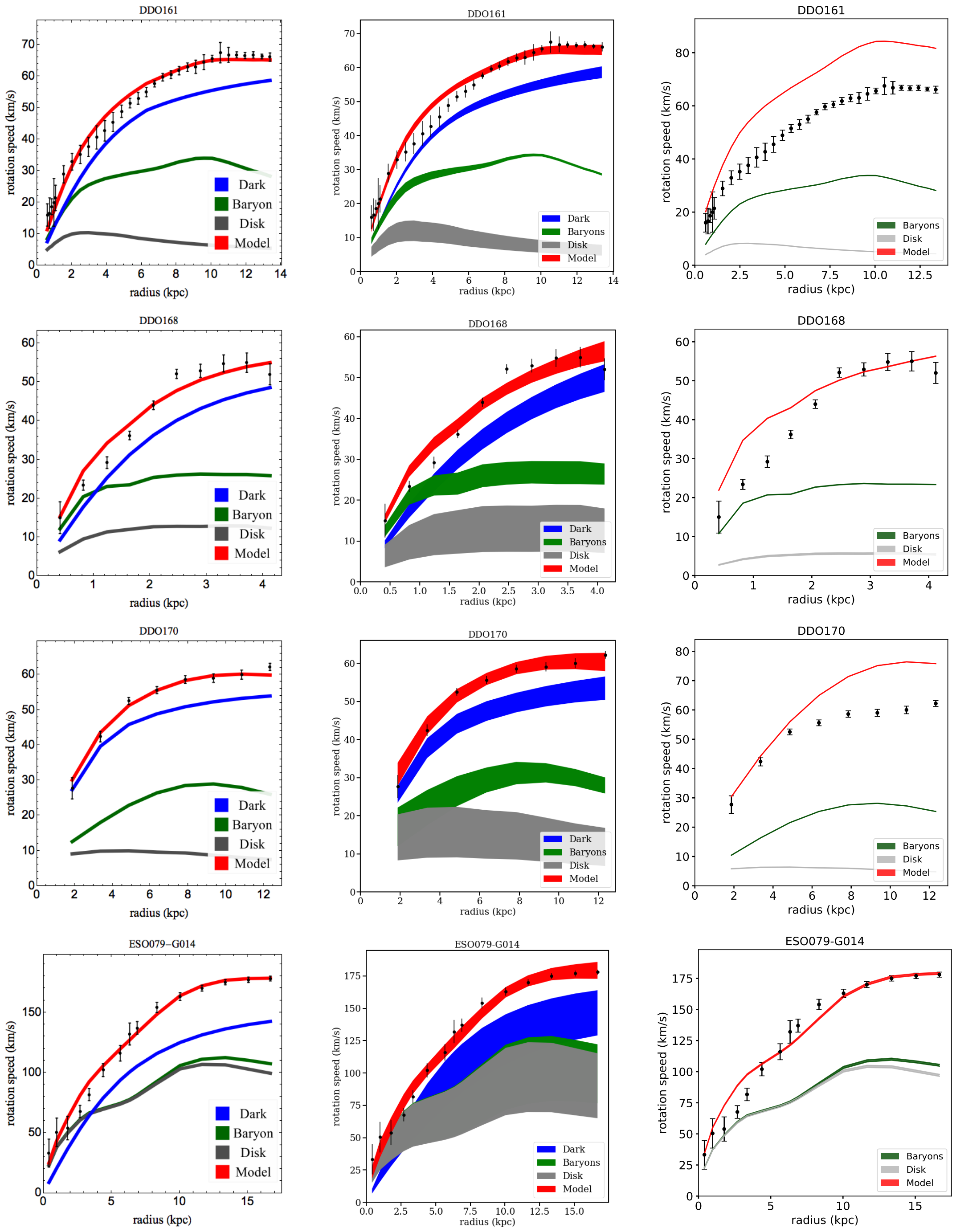

Figure A.1: Continued.

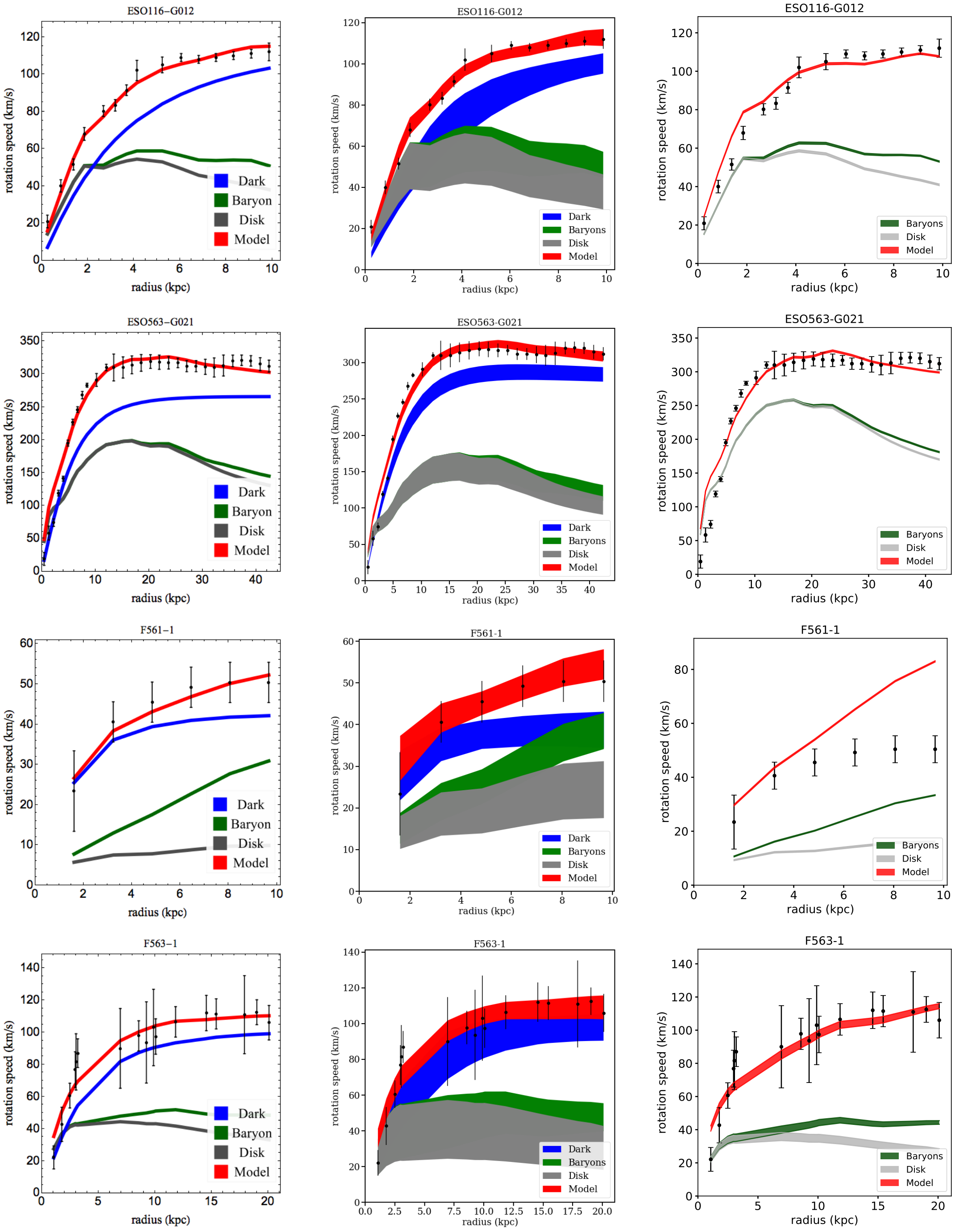

Figure A.1: Continued.

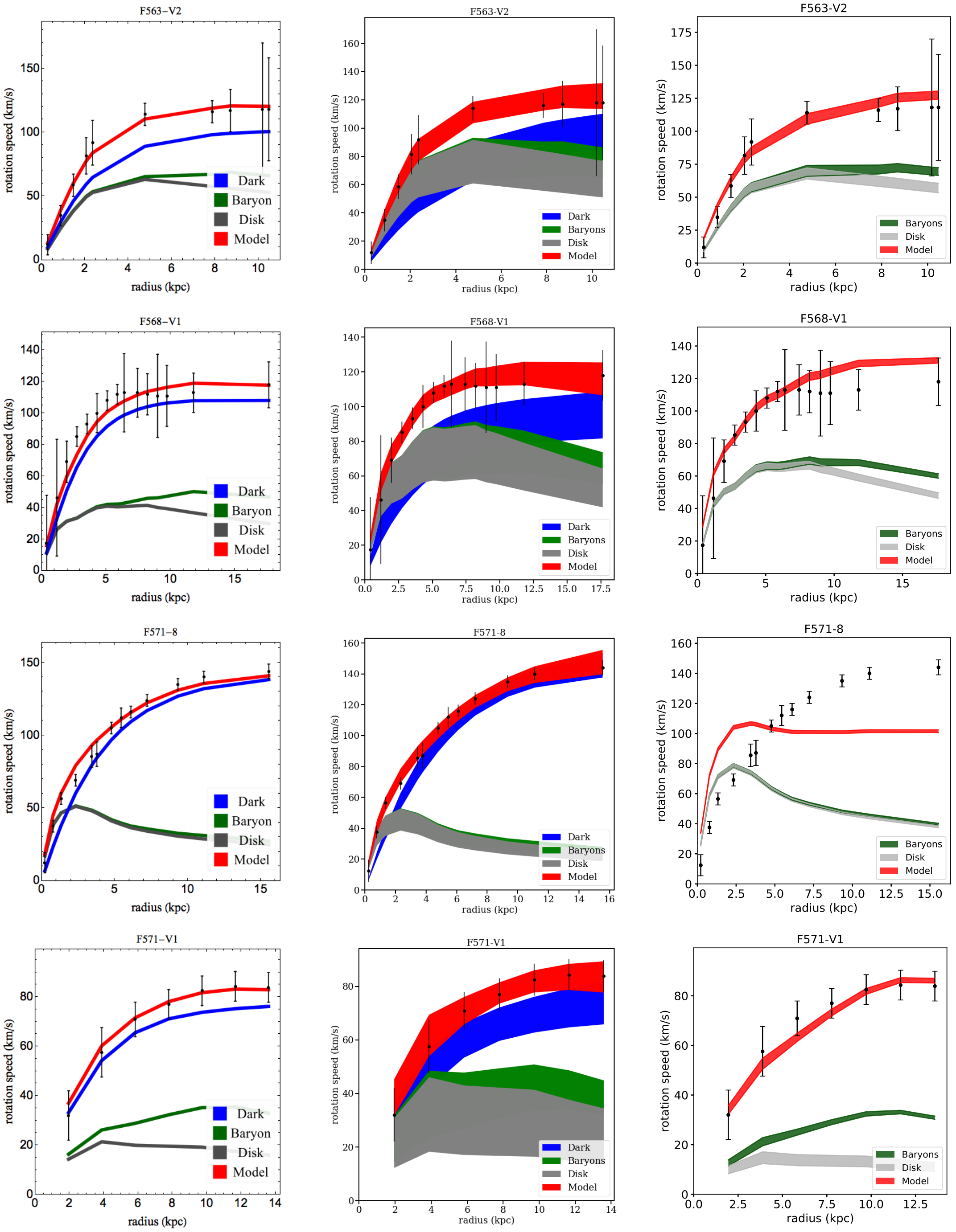

Figure A.1: Continued.

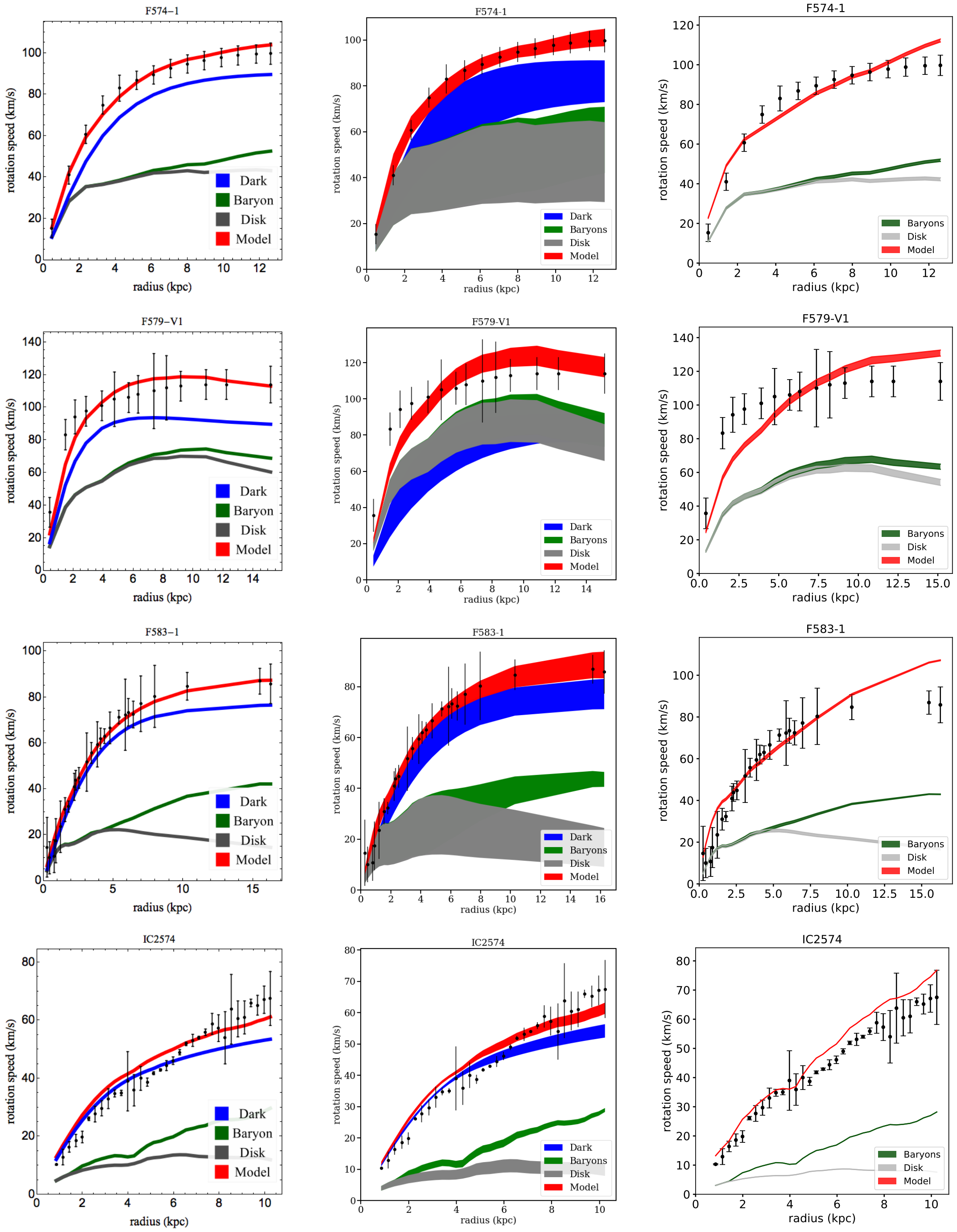

Figure A.1: Continued.

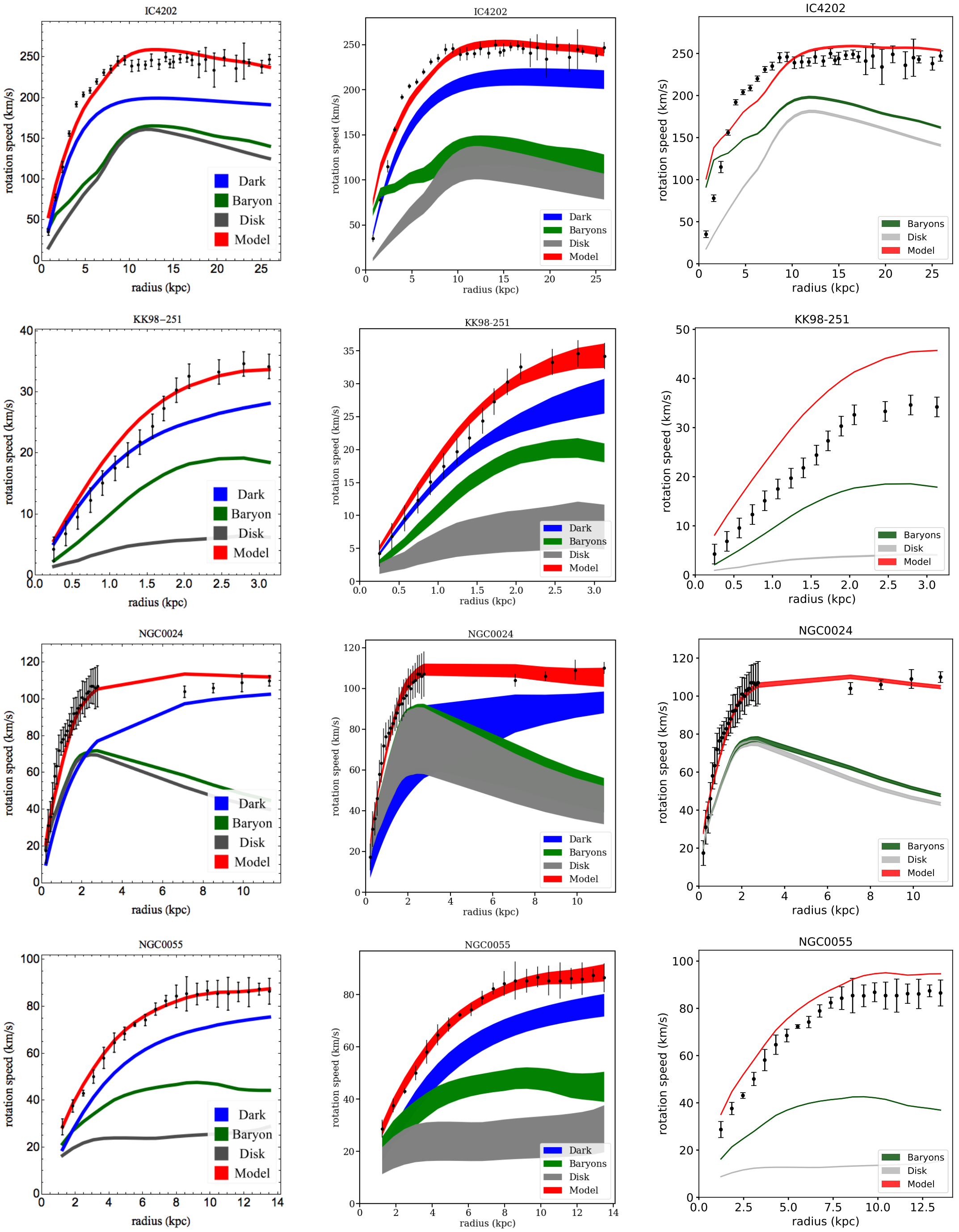

Figure A.1: Continued.

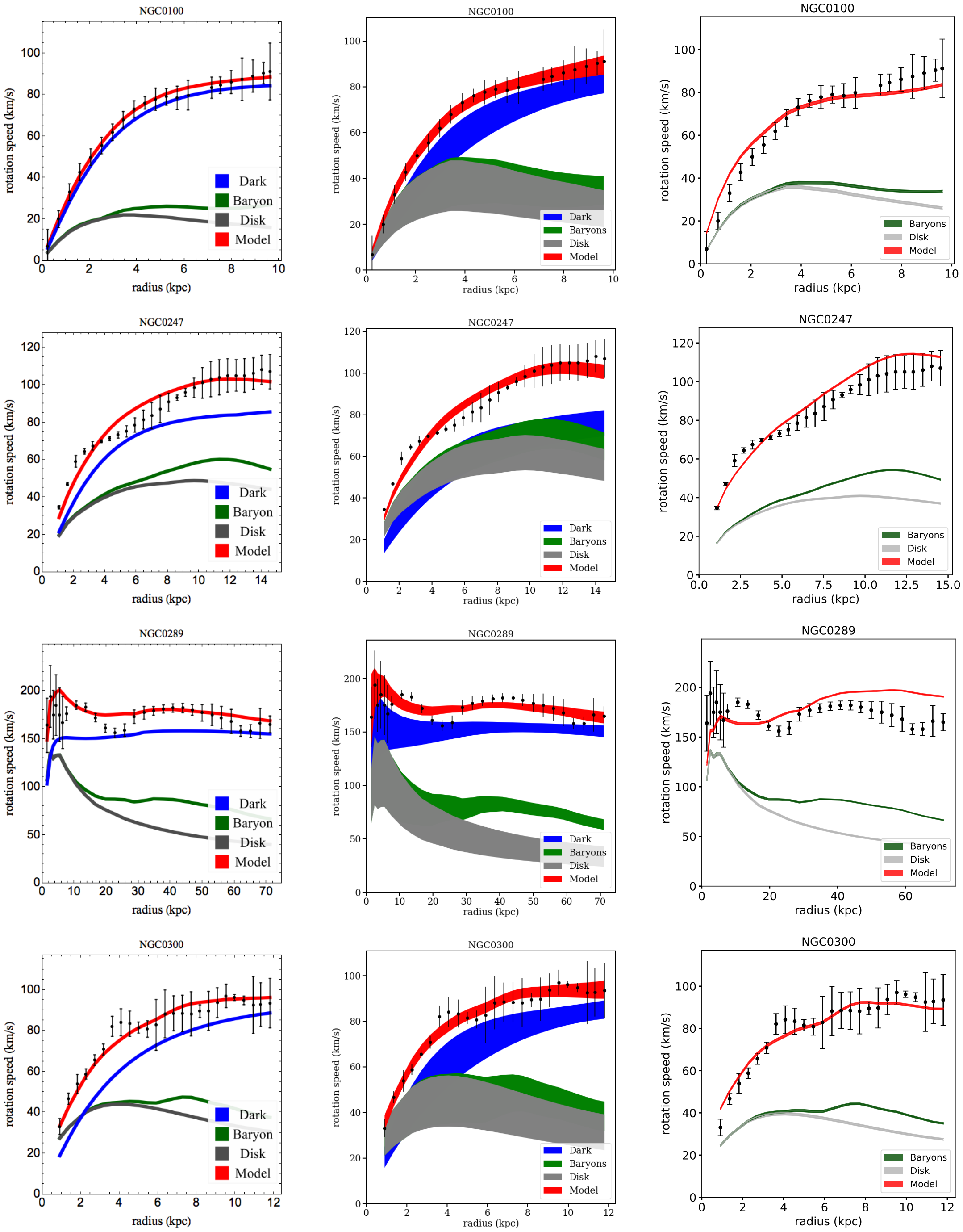

Figure A.1: Continued.

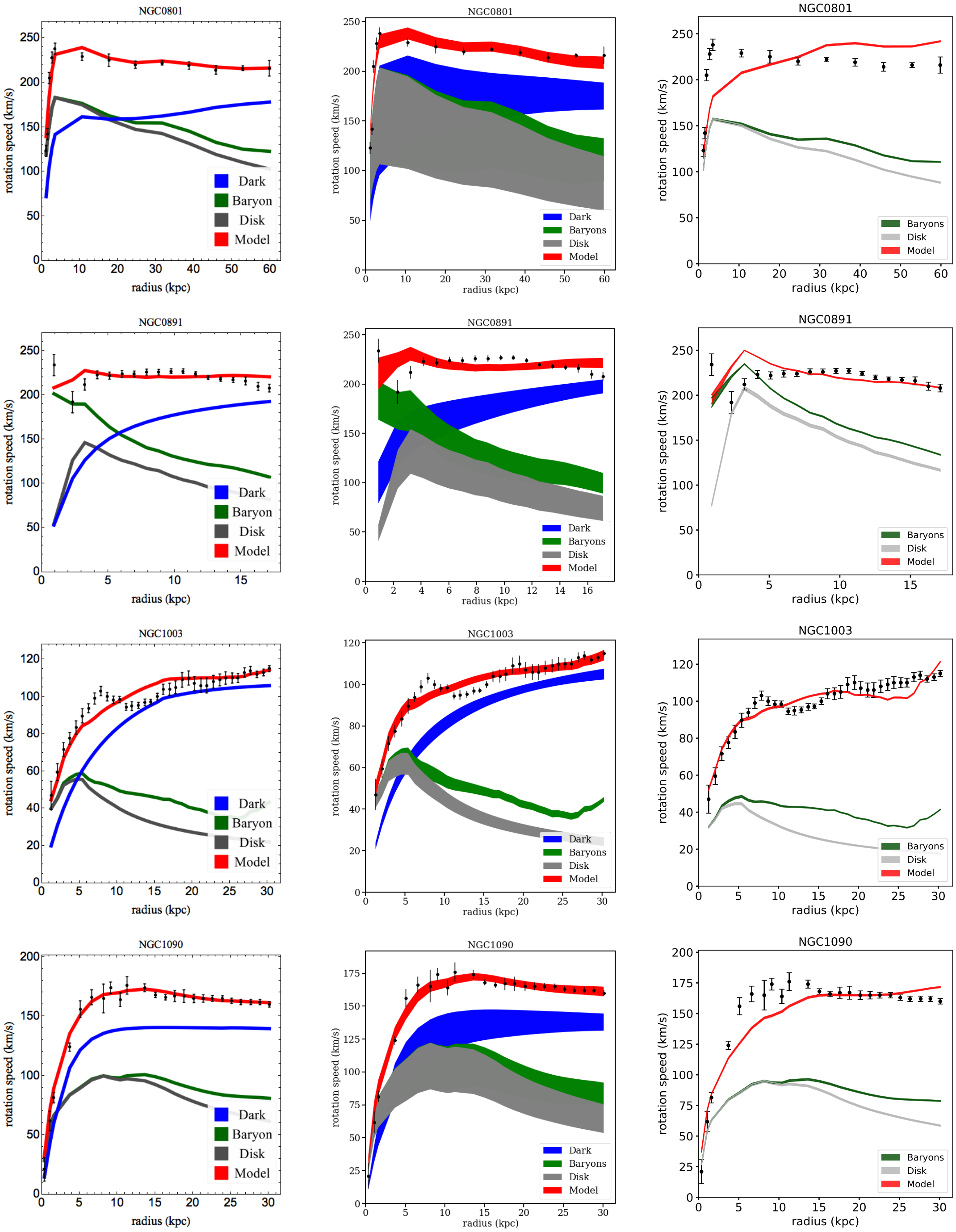

Figure A.1: Continued.

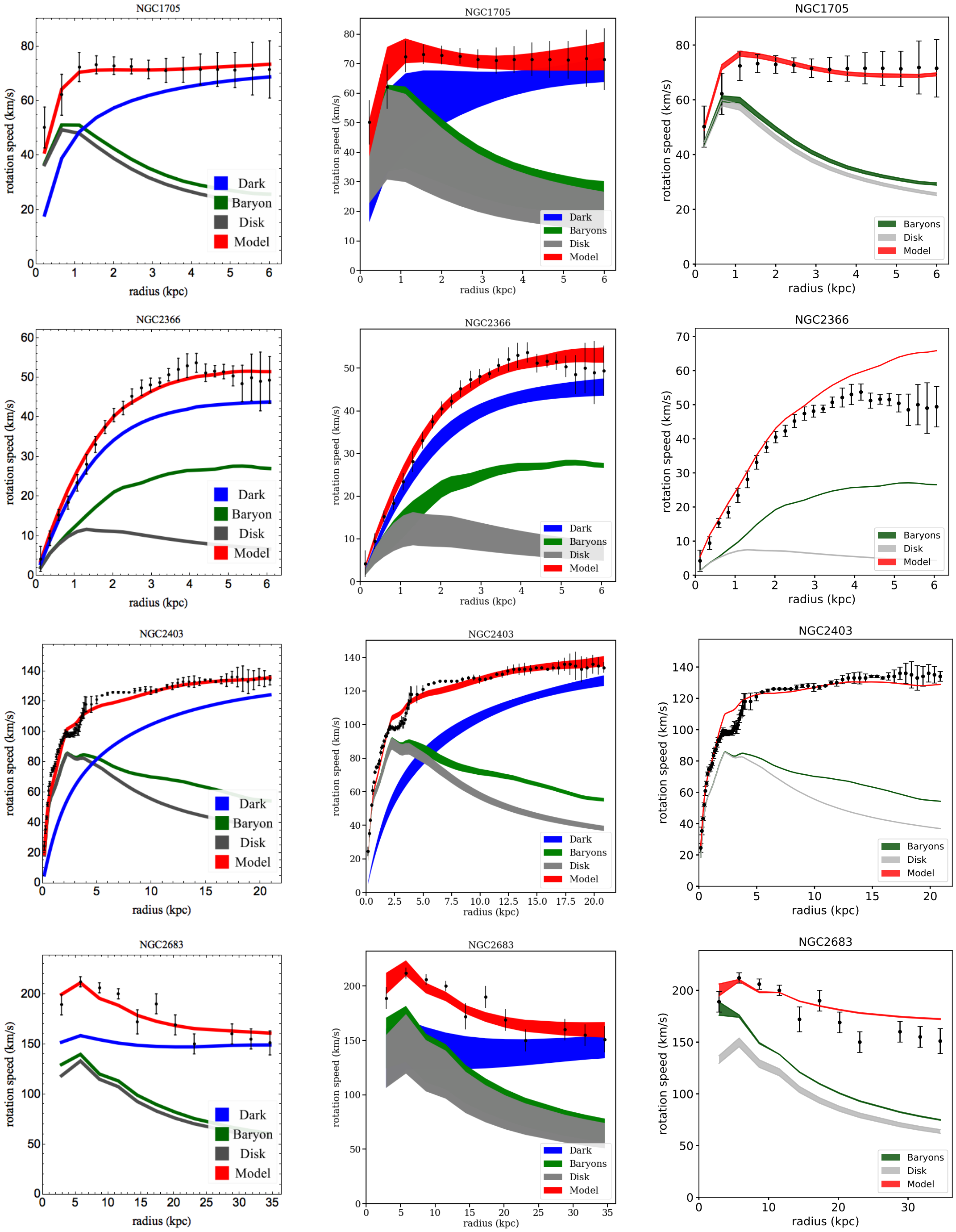

Figure A.1: Continued.

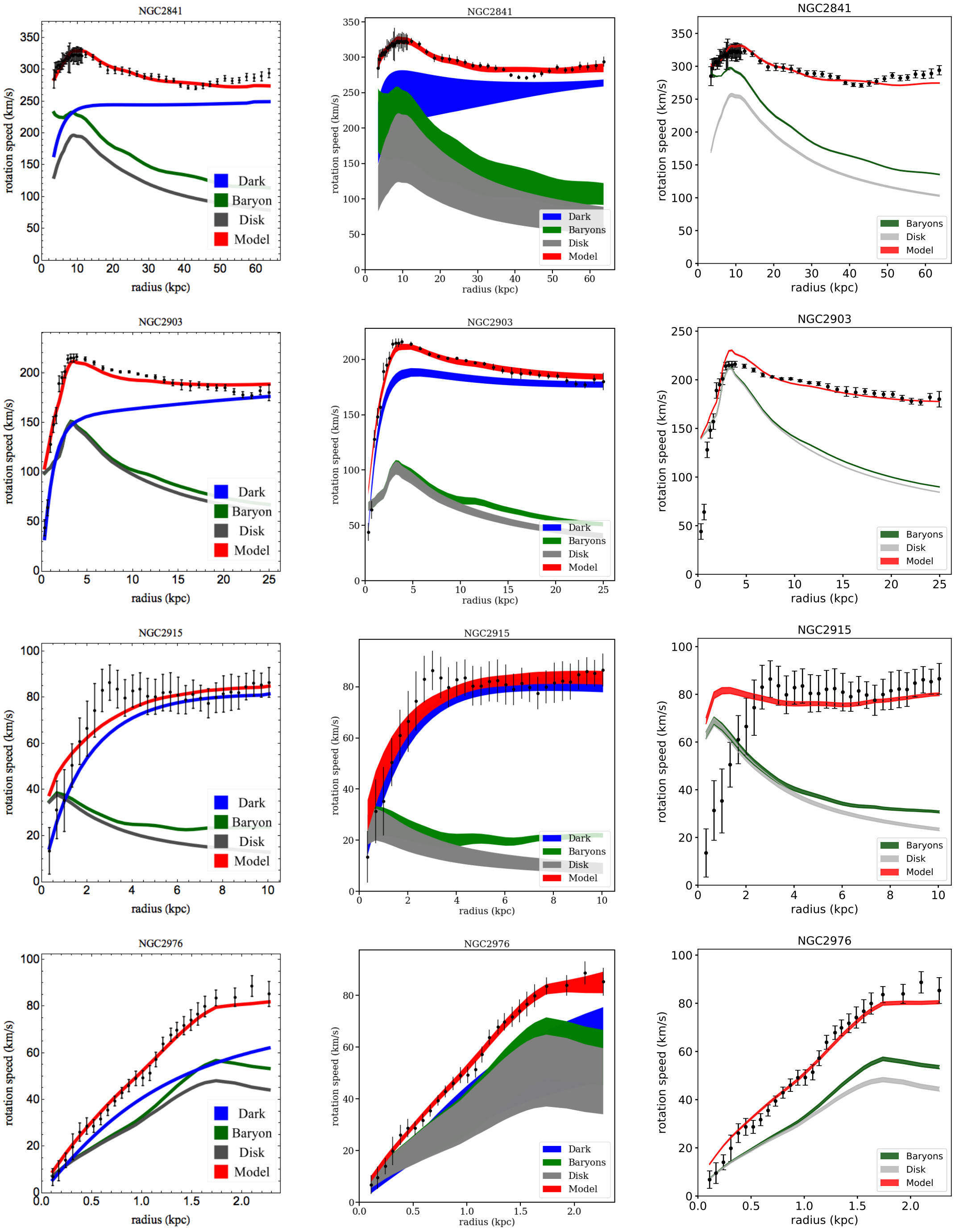

Figure A.1: Continued.

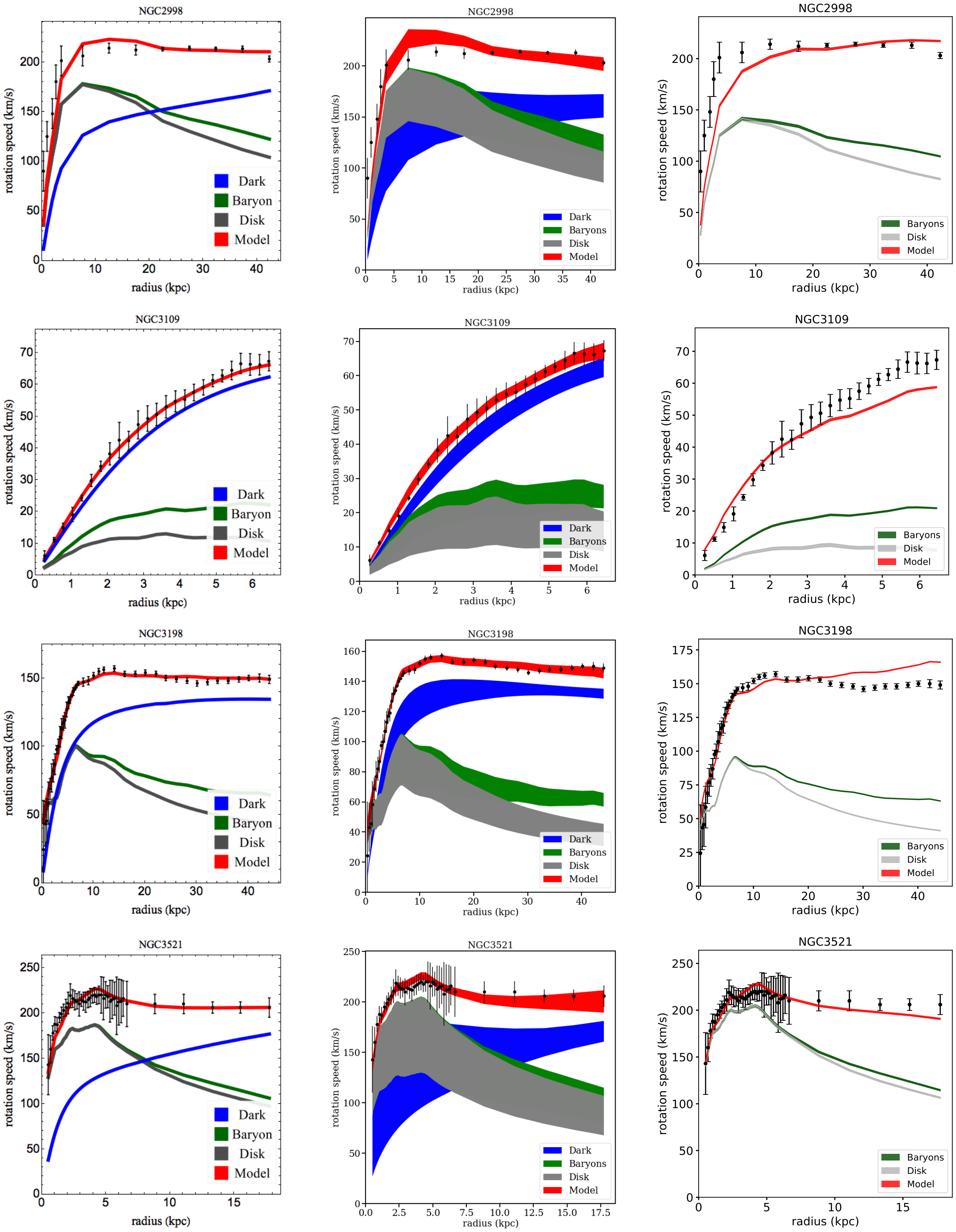

Figure A.1: Continued.

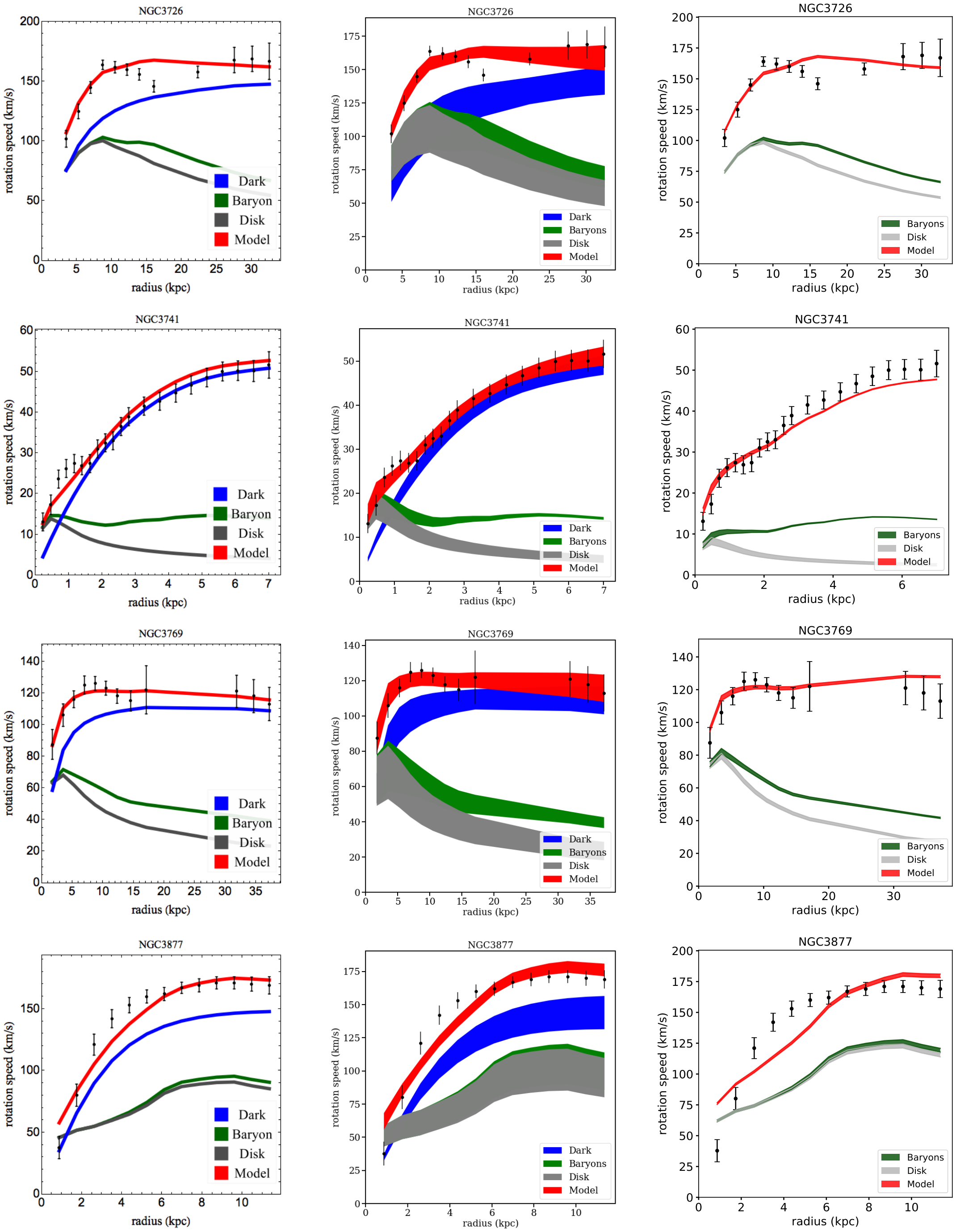

Figure A.1: Continued.

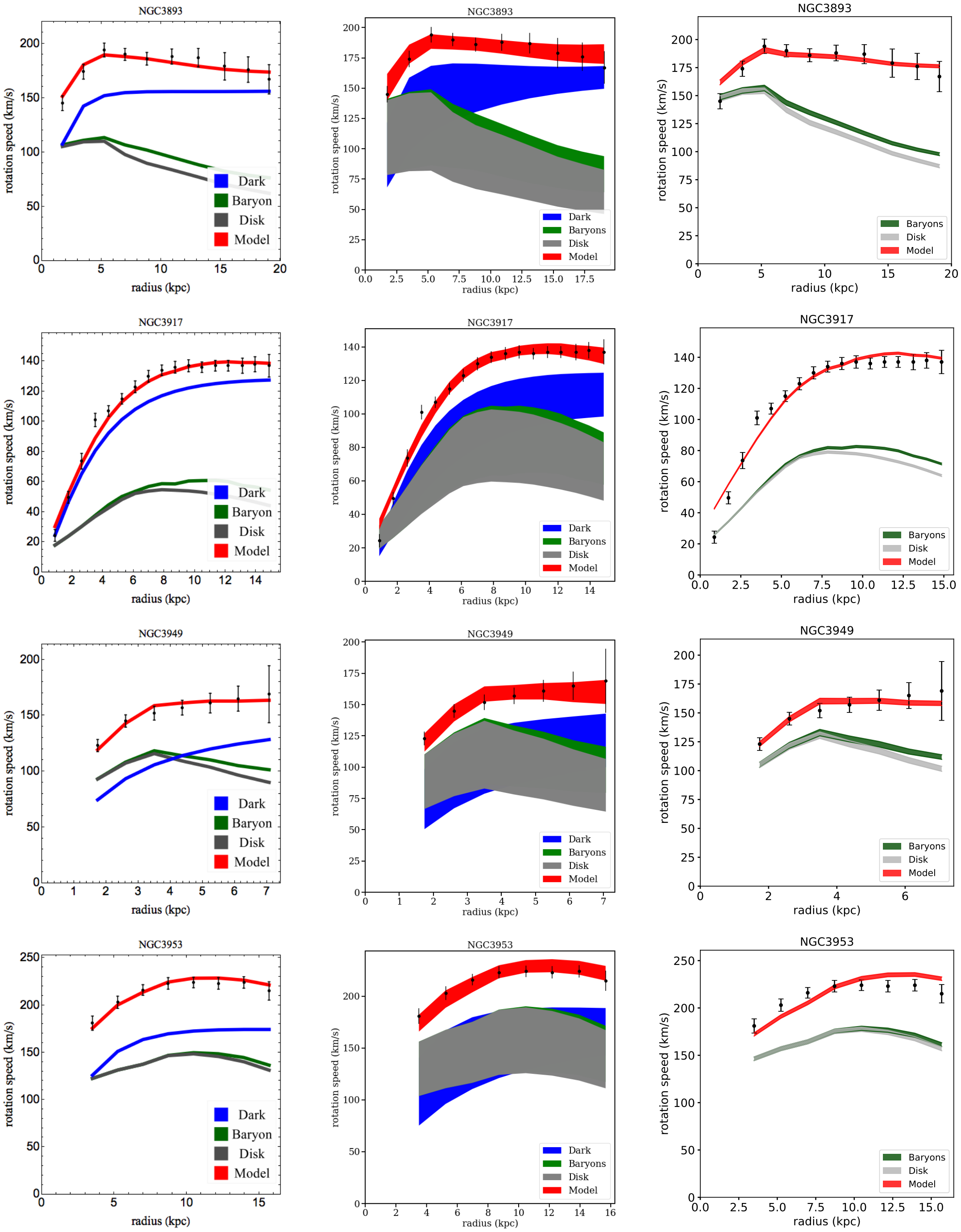

Figure A.1: Continued.

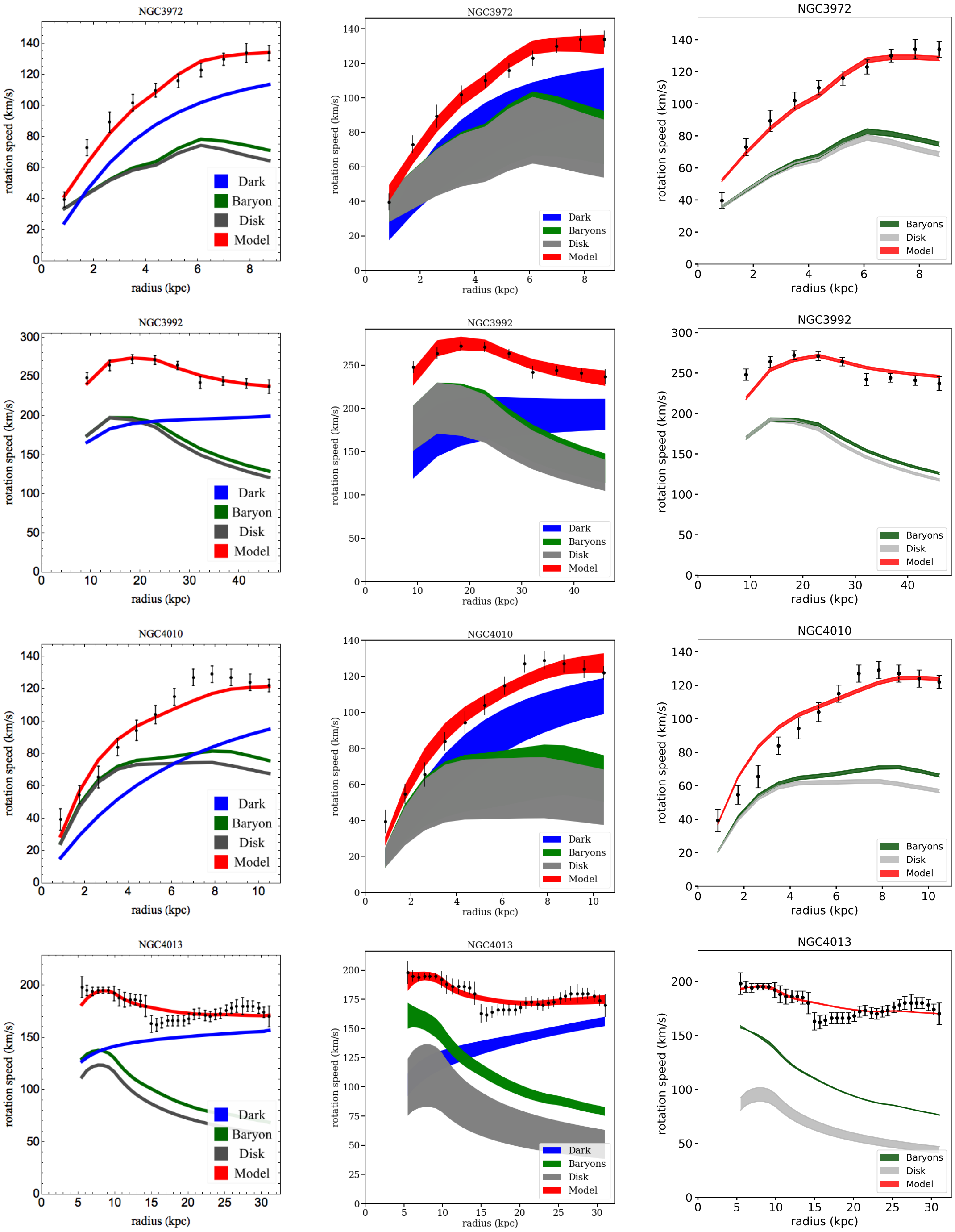

Figure A.1: Continued.

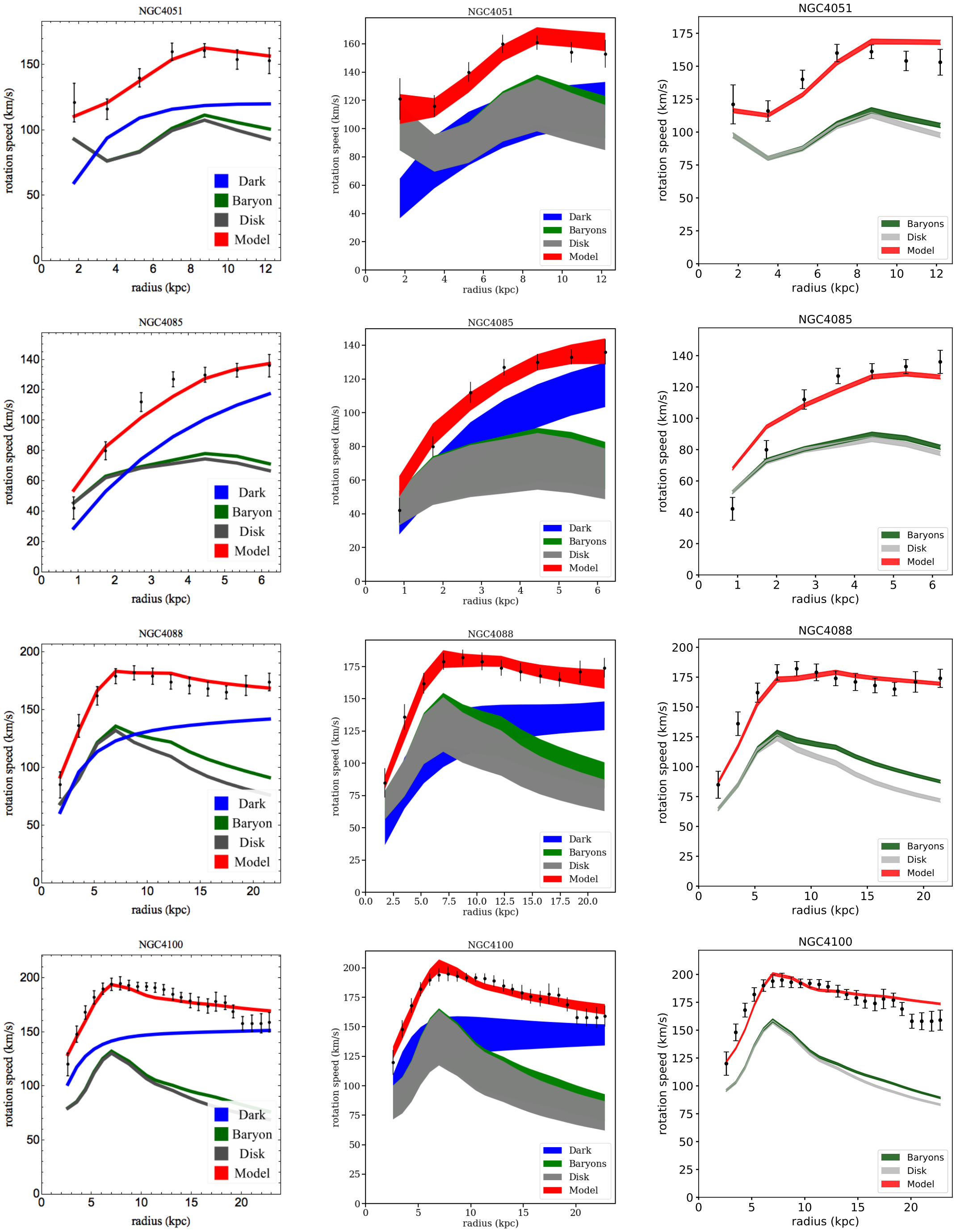

Figure A.1: Continued.

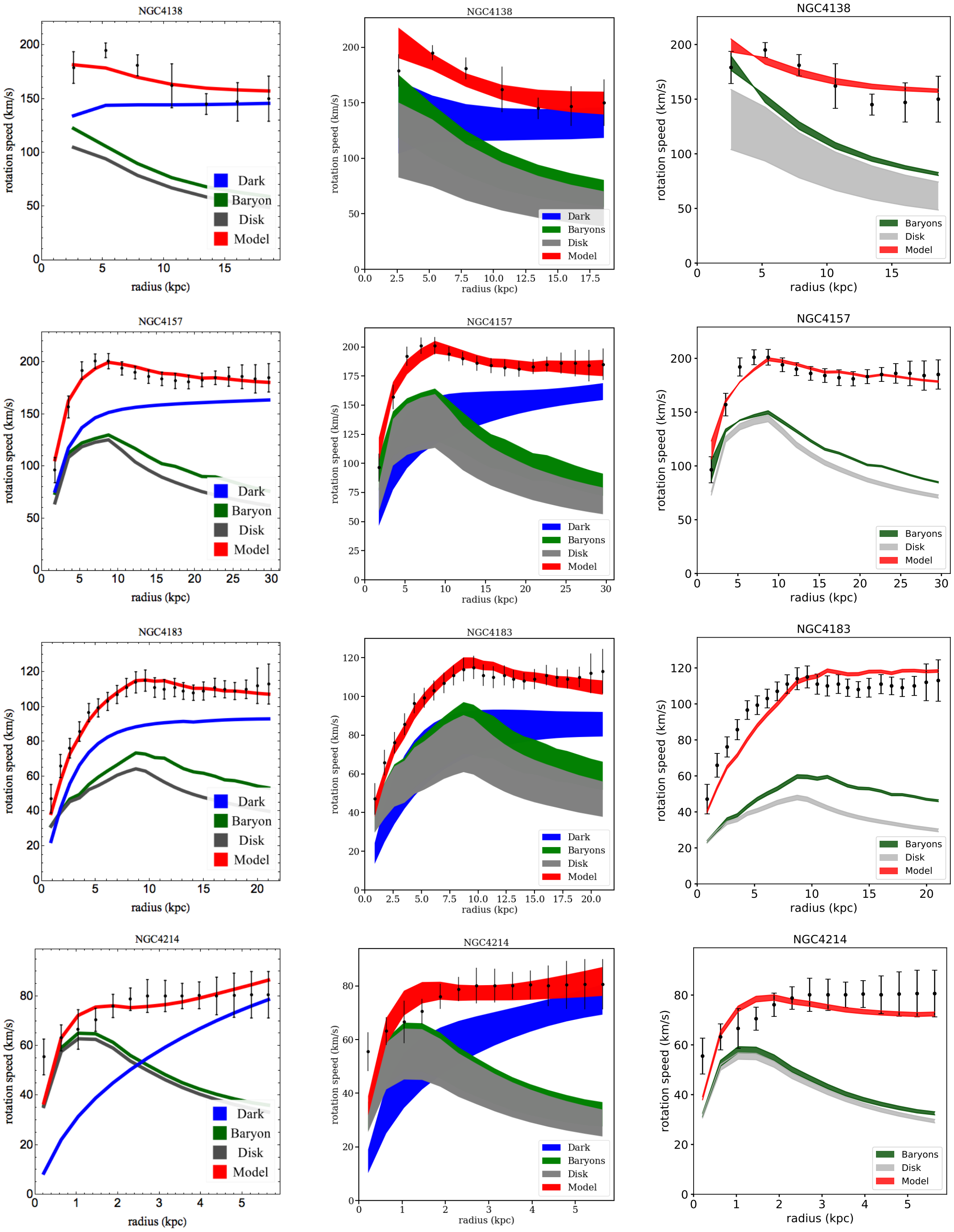

Figure A.1: Continued.

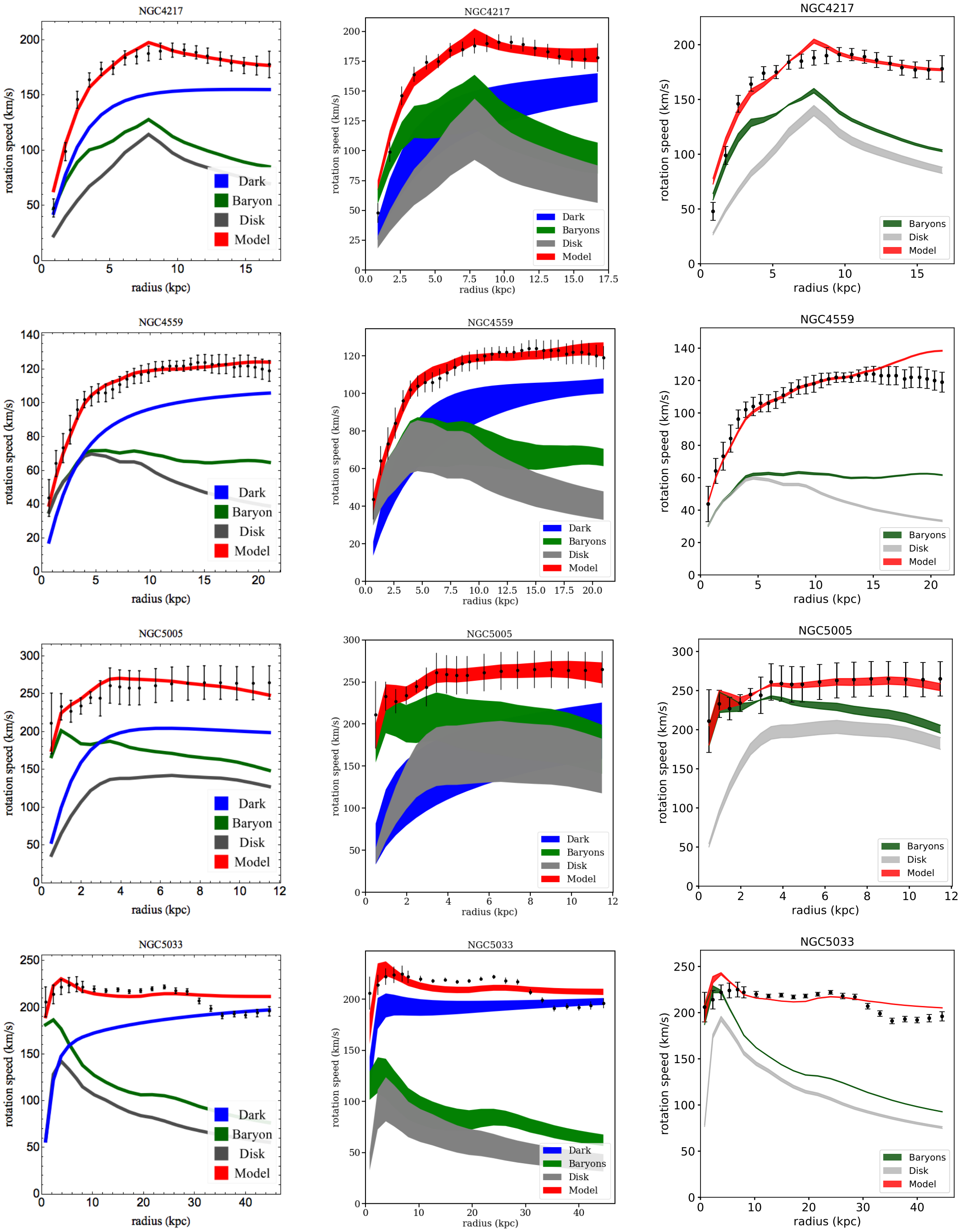

Figure A.1: Continued.

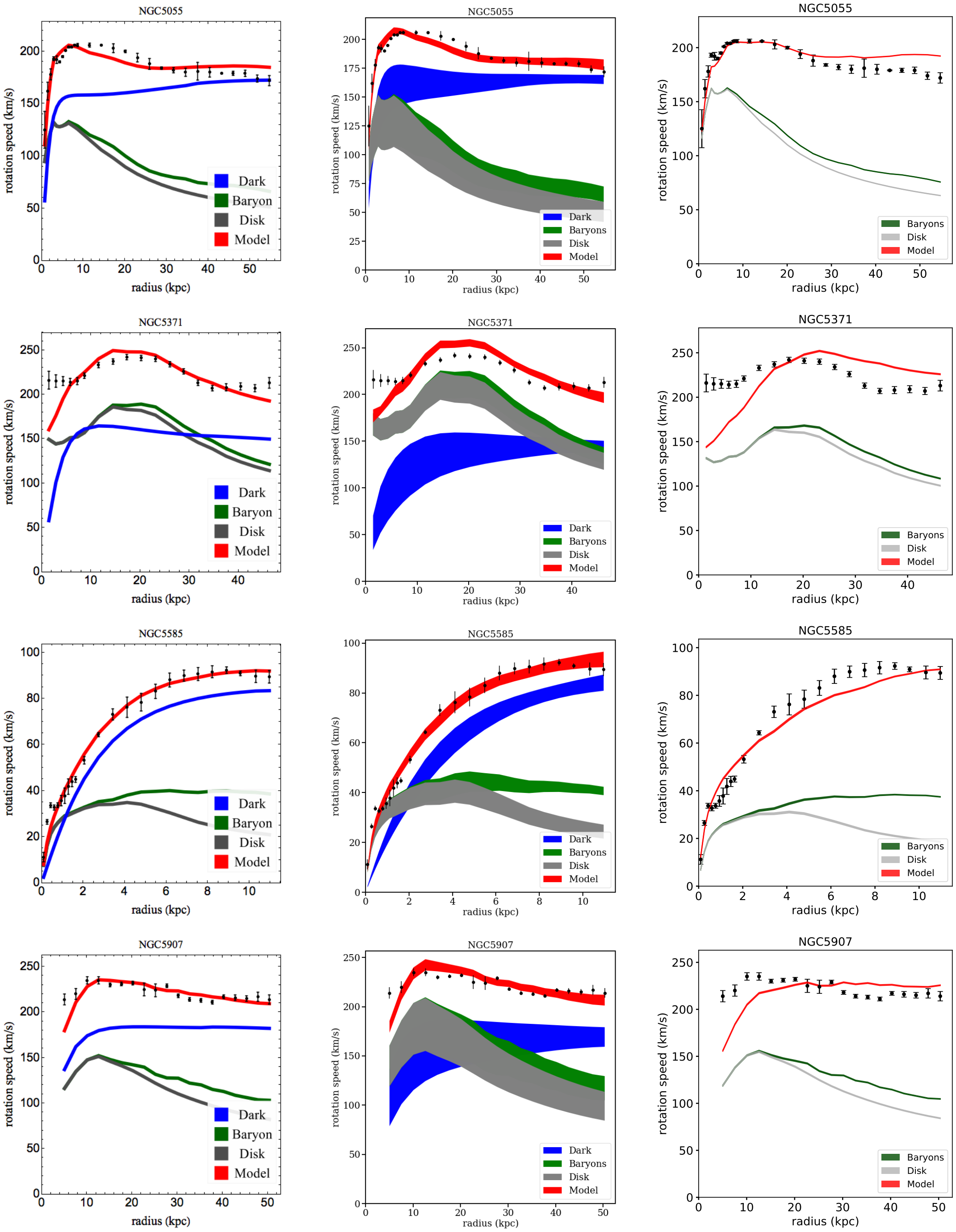

Figure A.1: Continued.

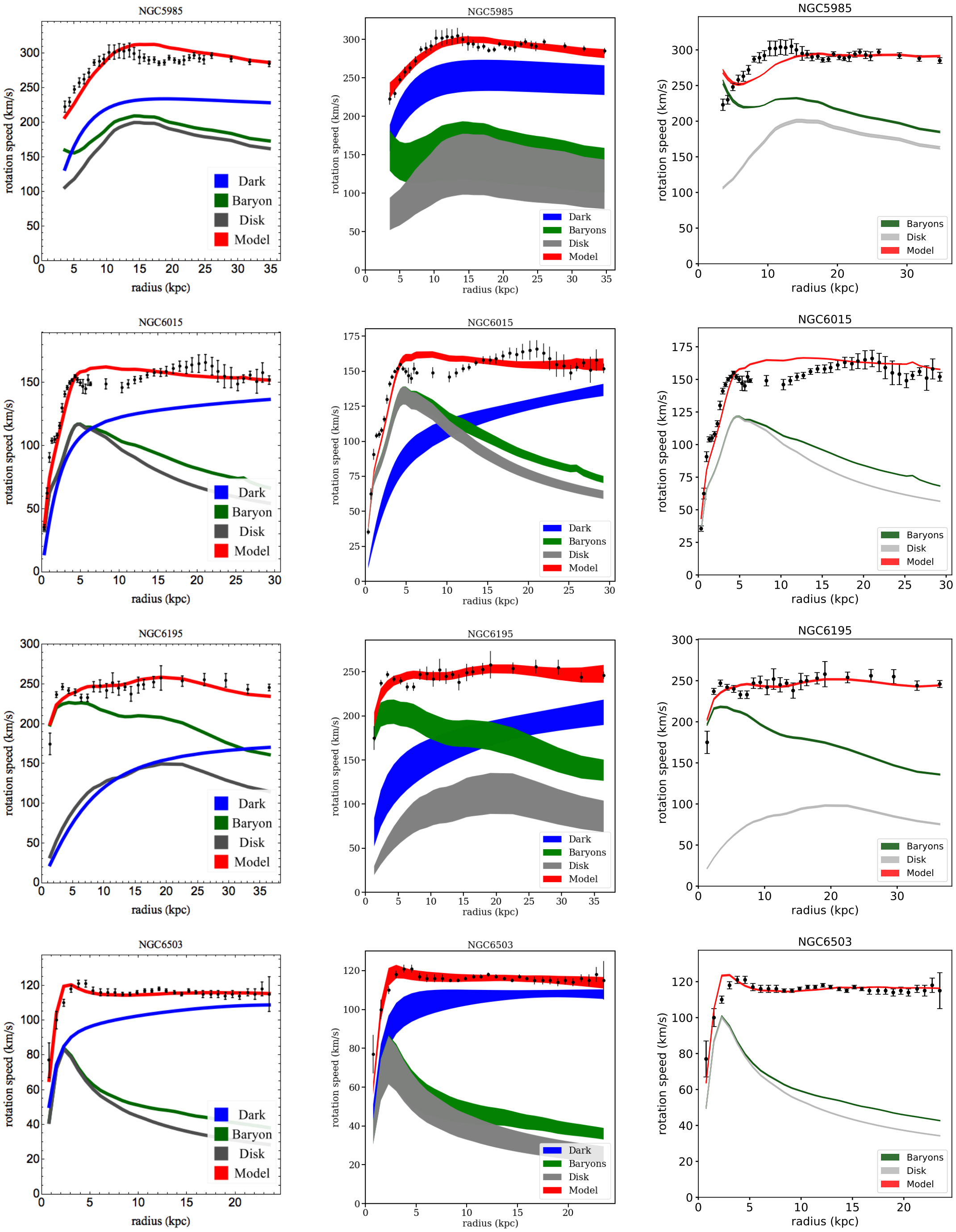

Figure A.1: Continued.

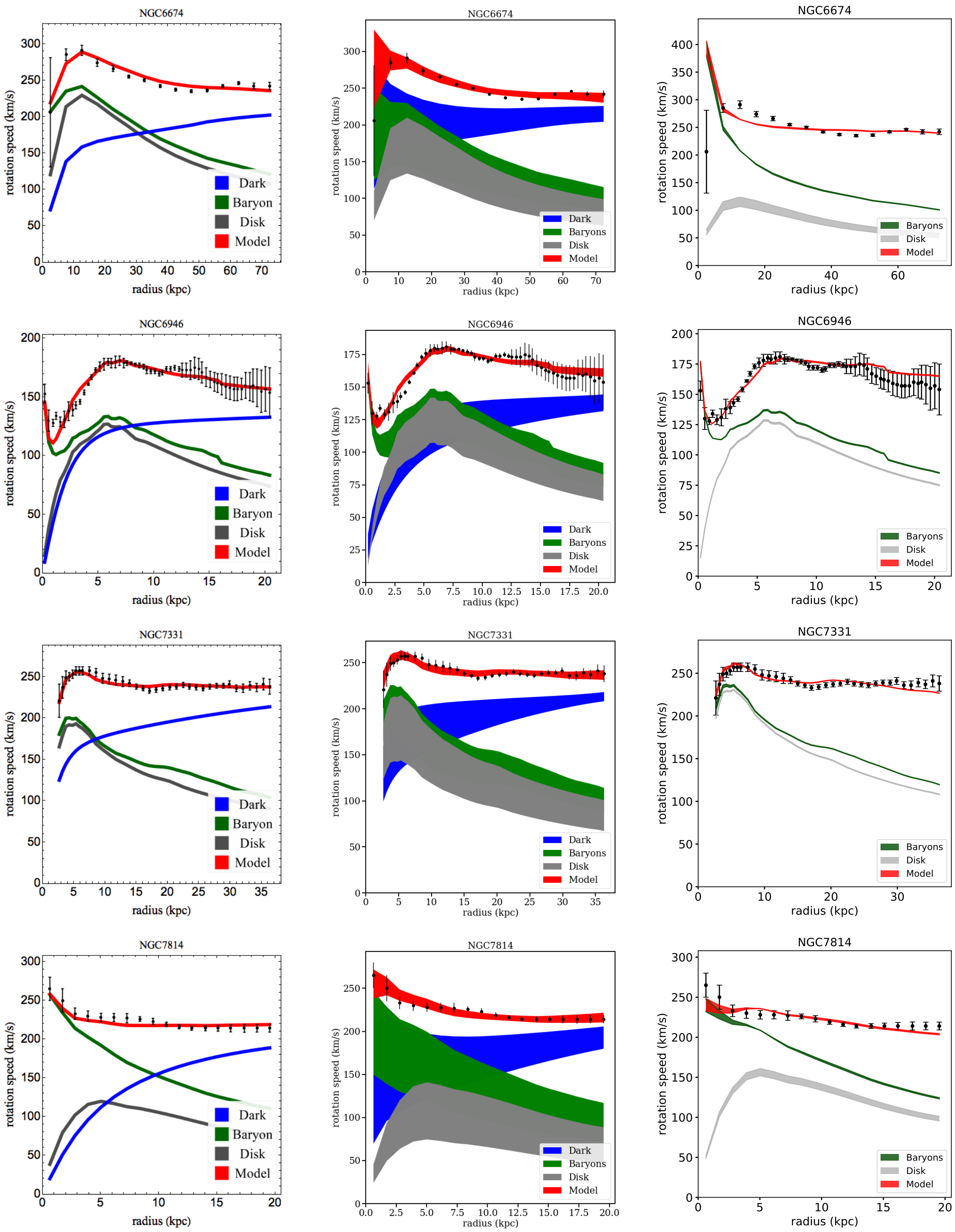

Figure A.1: Continued.

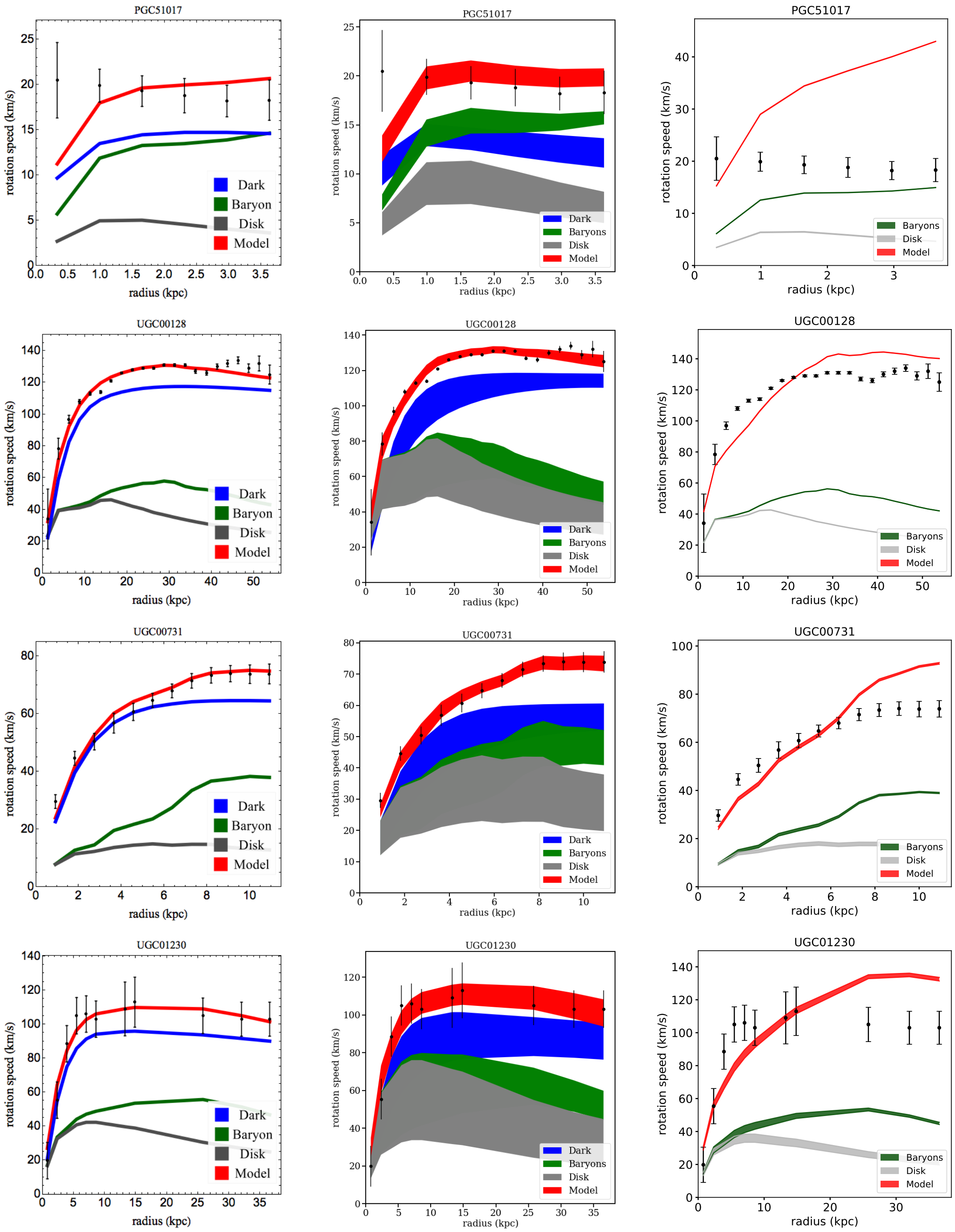

Figure A.1: Continued.

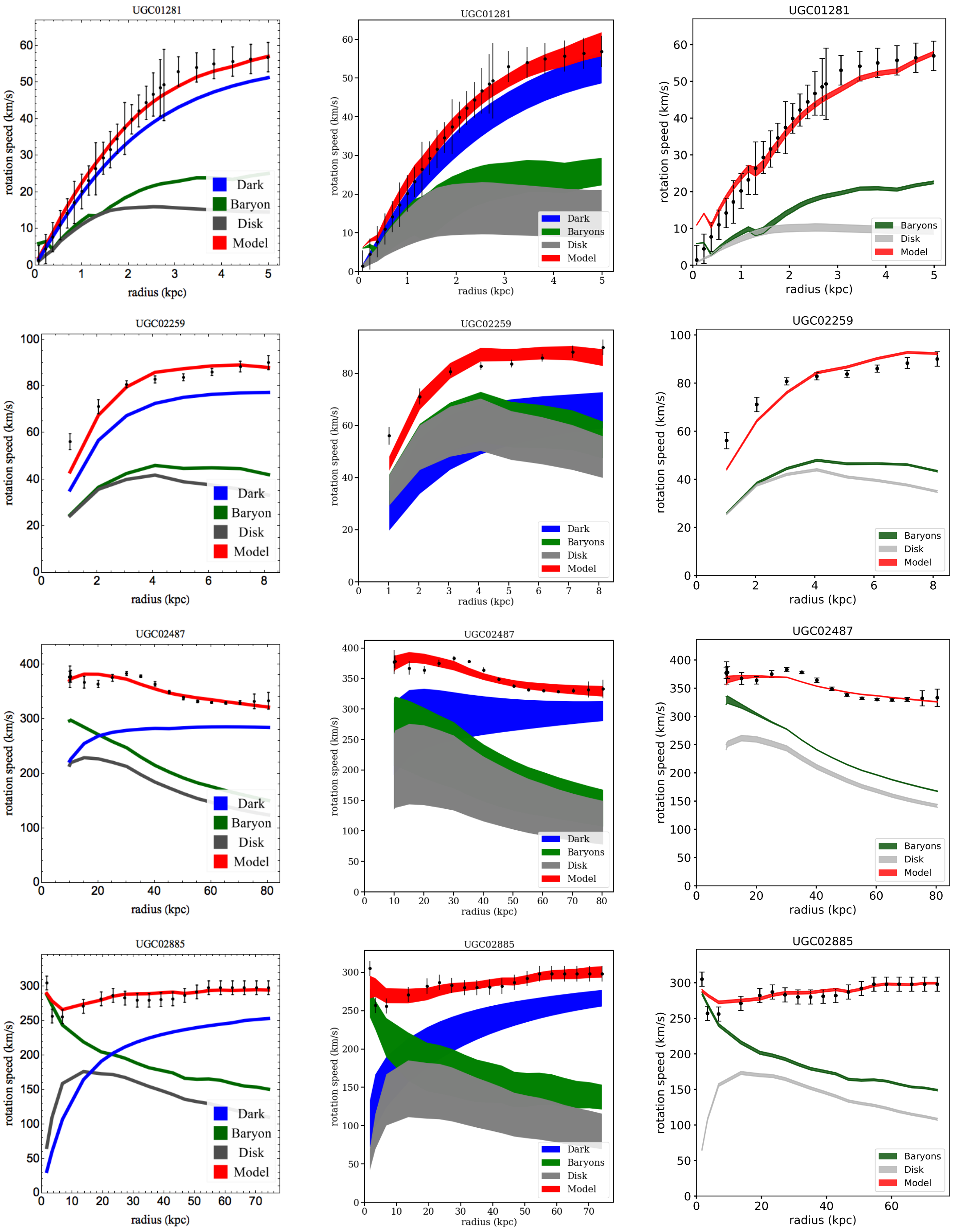

Figure A.1: Continued.

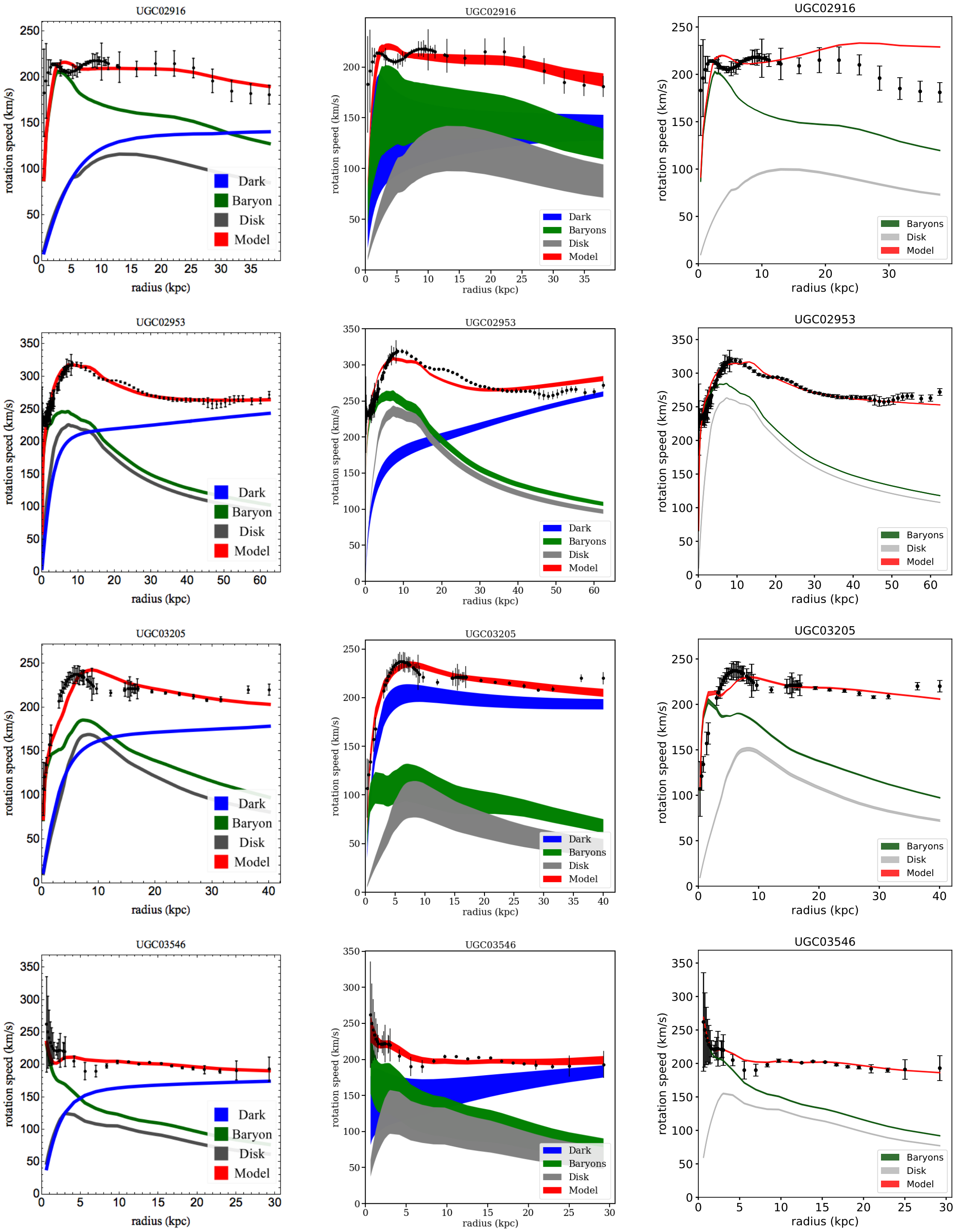

Figure A.1: Continued.

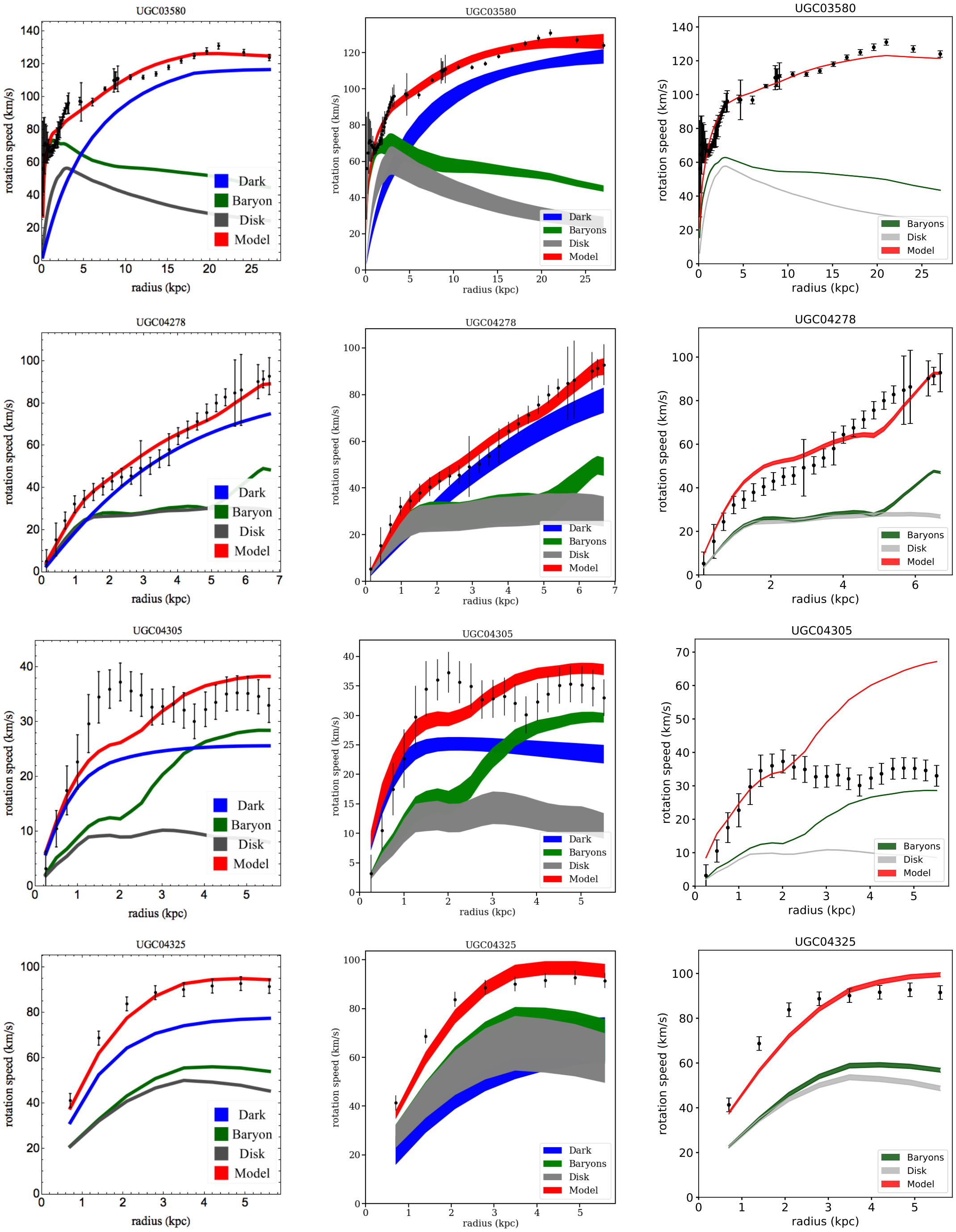

Figure A.1: Continued.

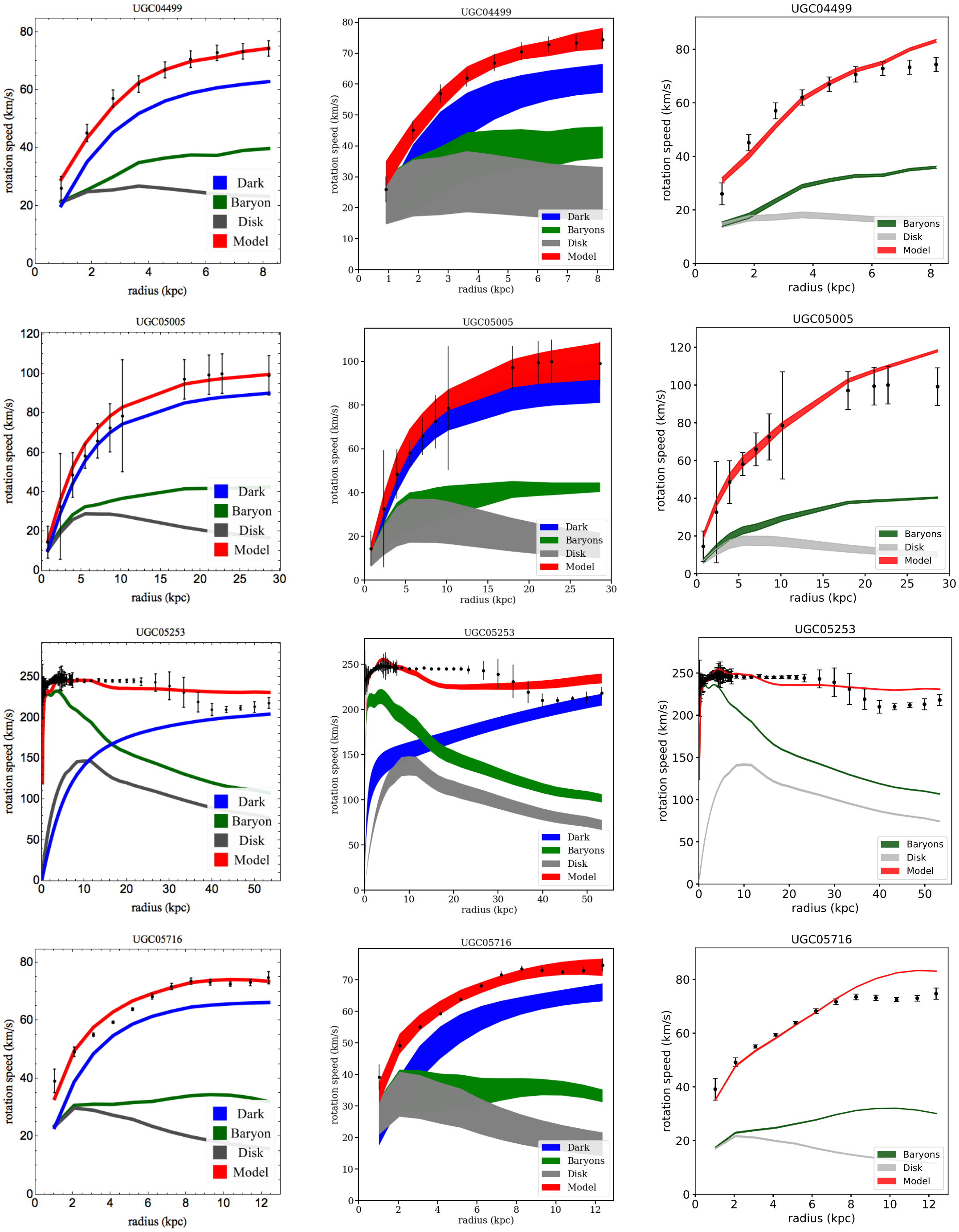

Figure A.1: Continued.

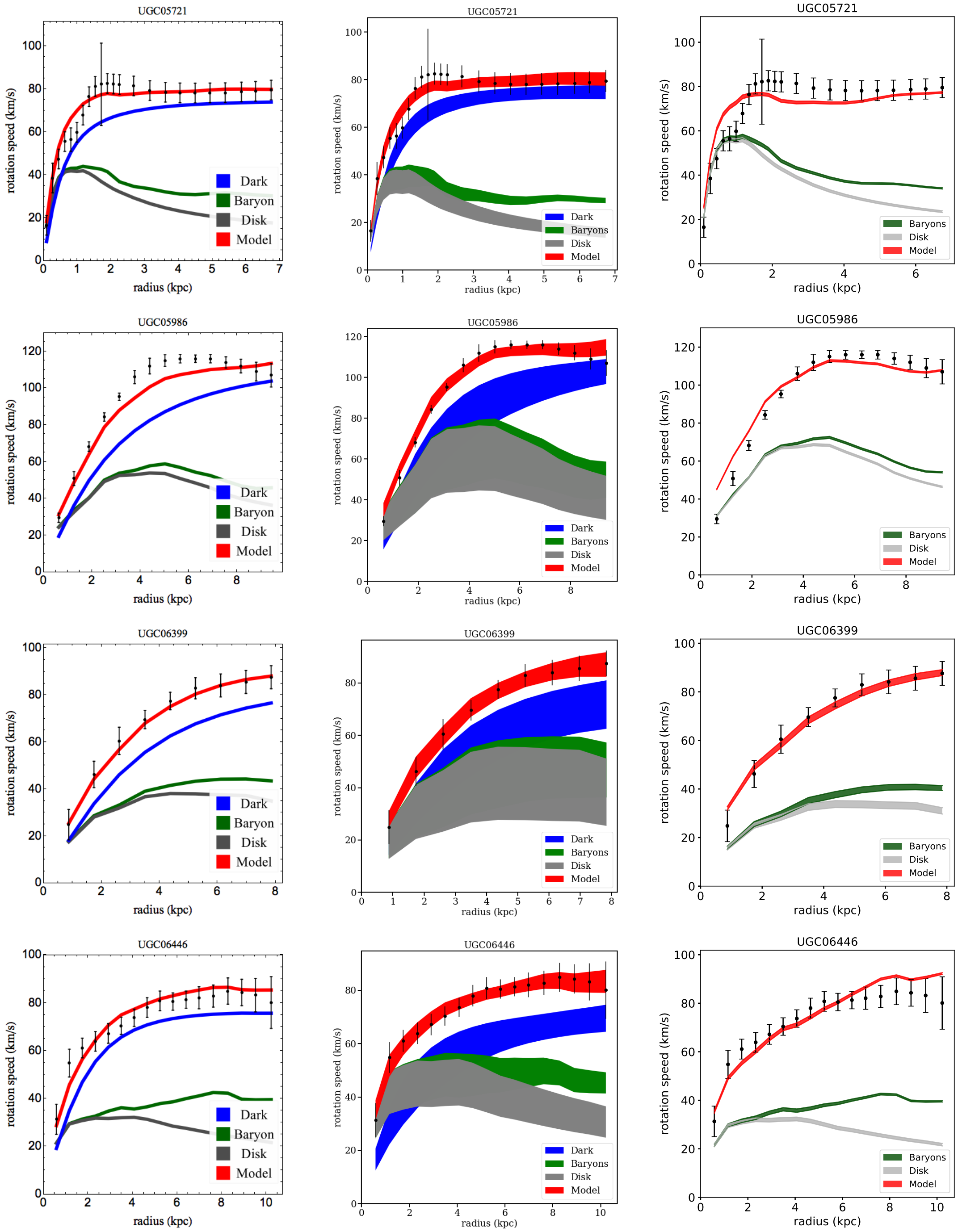

Figure A.1: Continued.

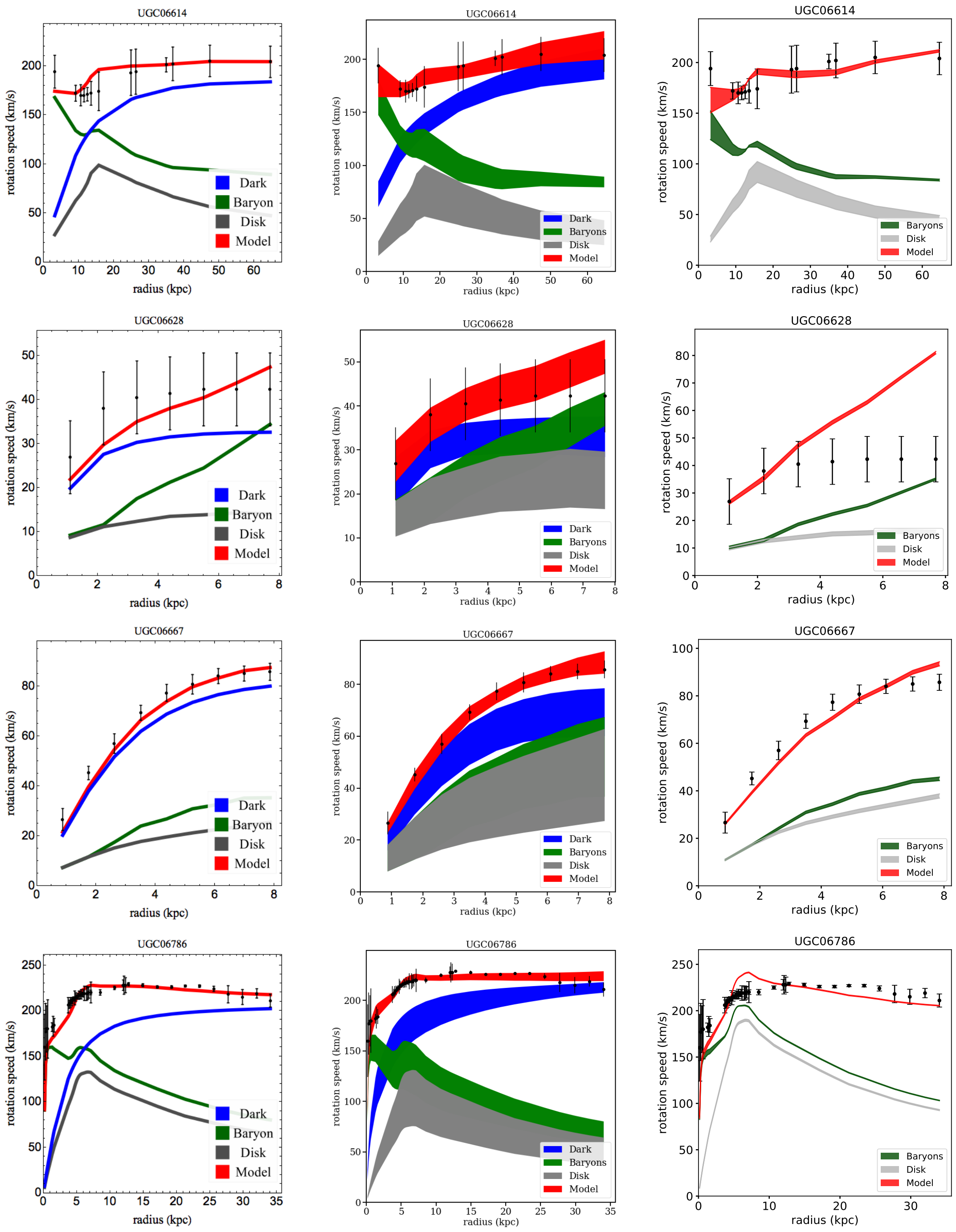

Figure A.1: Continued.

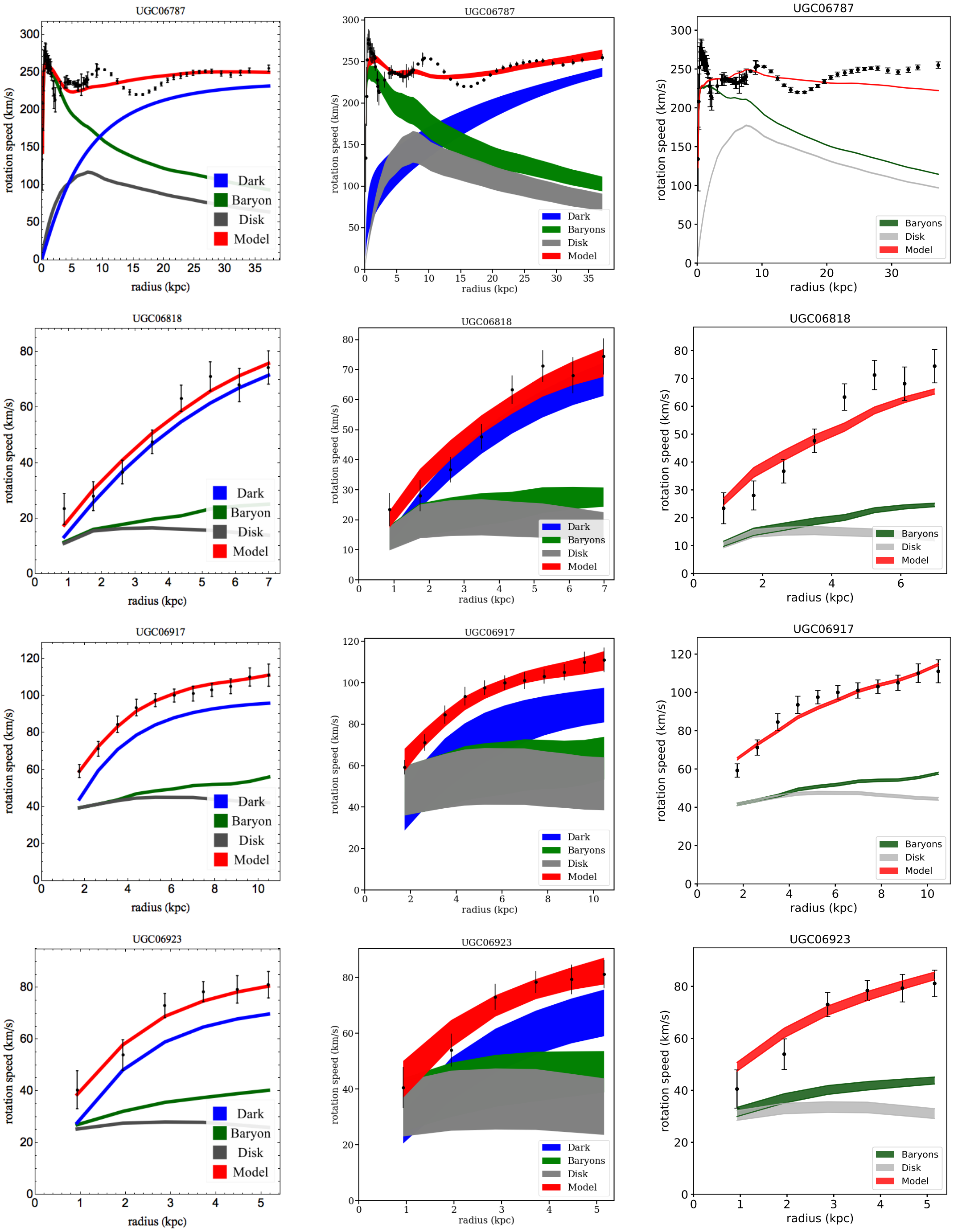

Figure A.1: Continued.

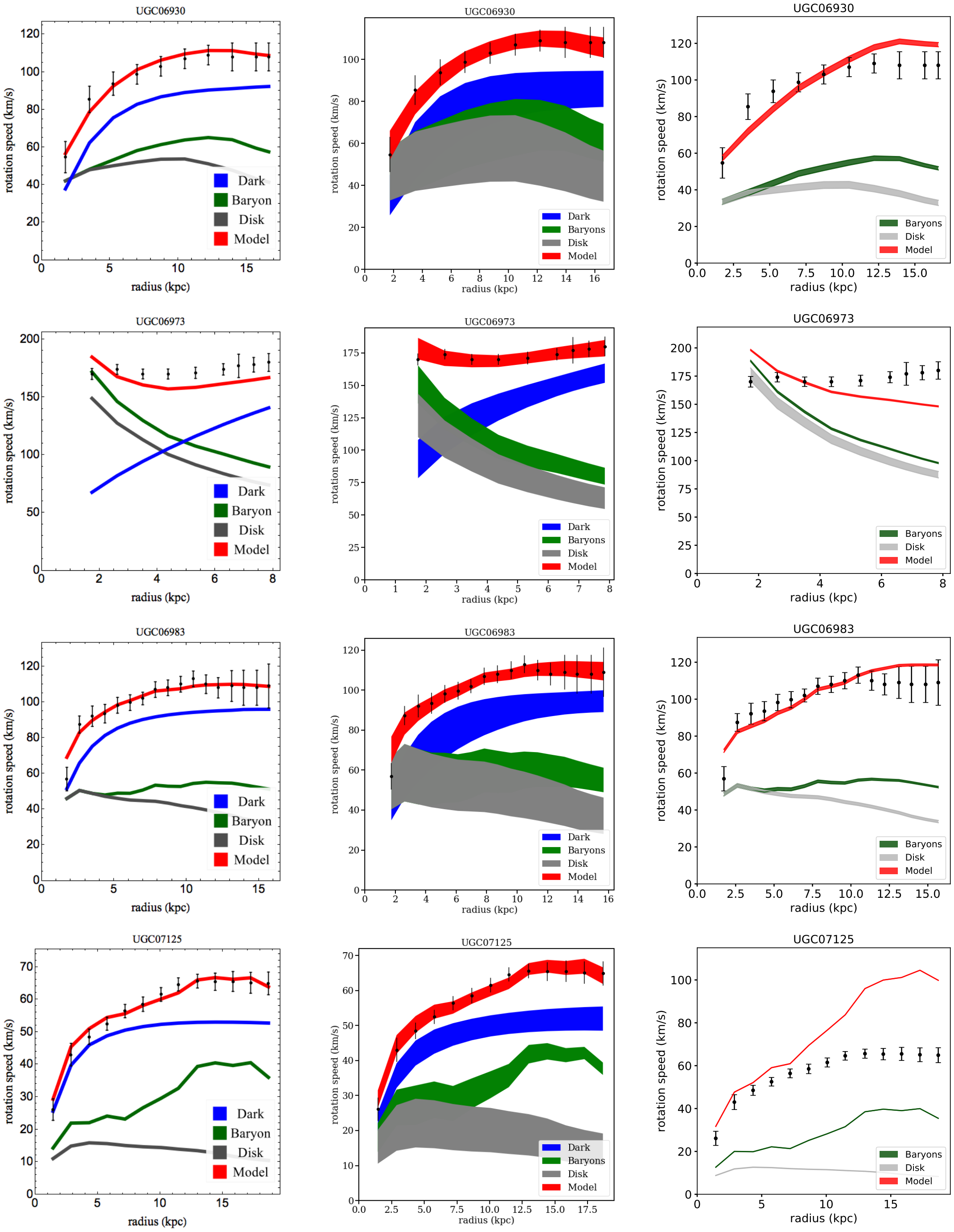

Figure A.1: Continued.

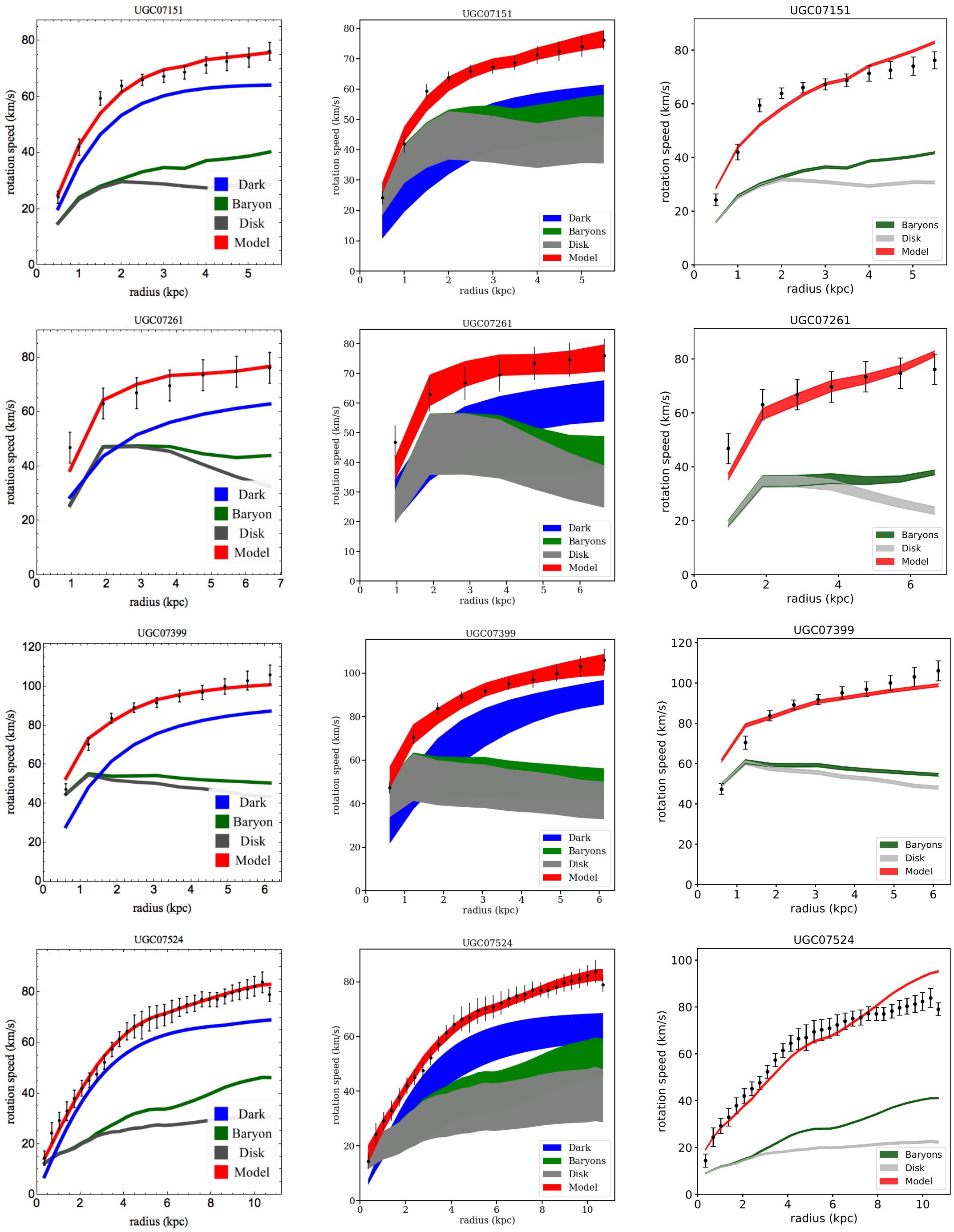

Figure A.1: Continued.

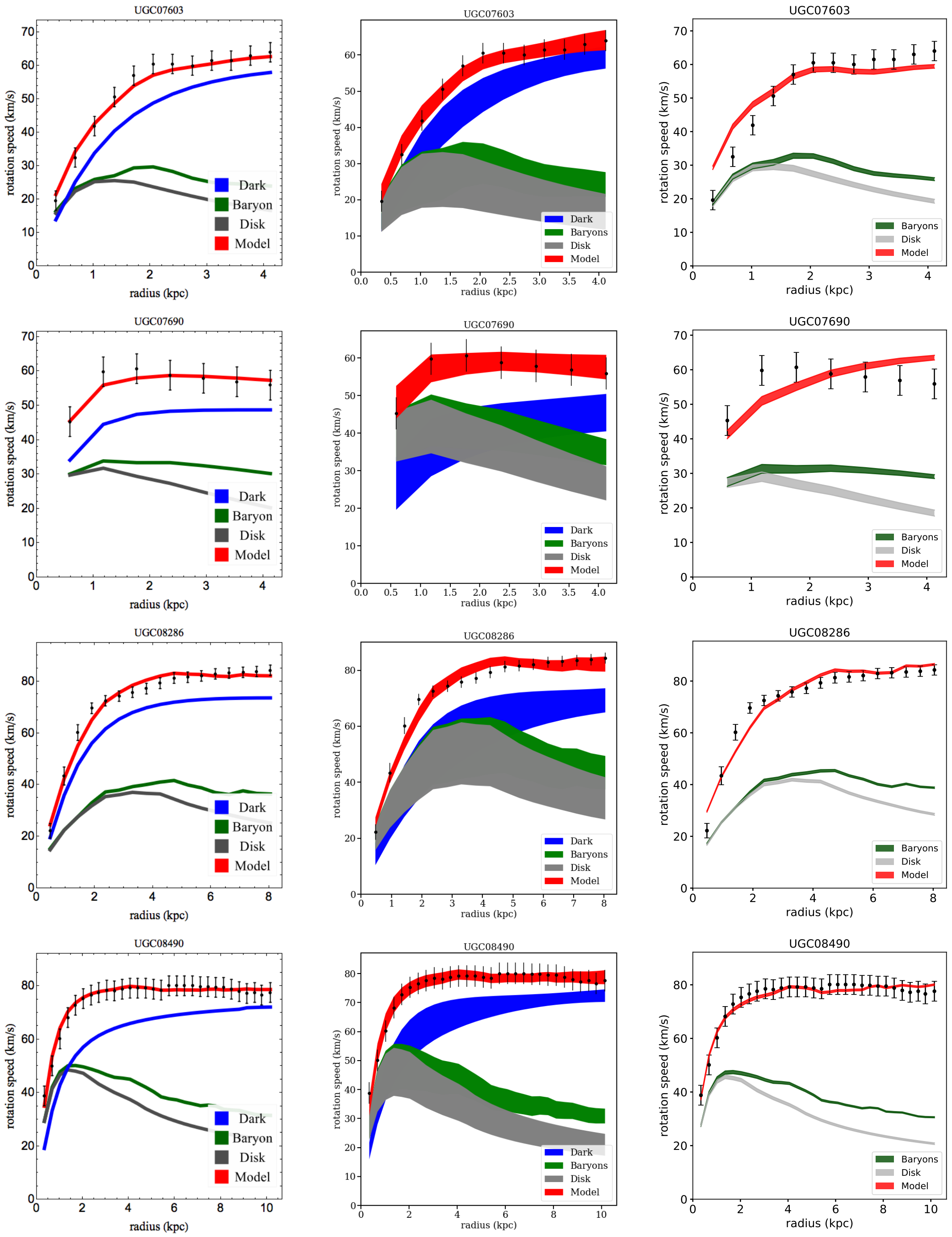

Figure A.1: Continued.

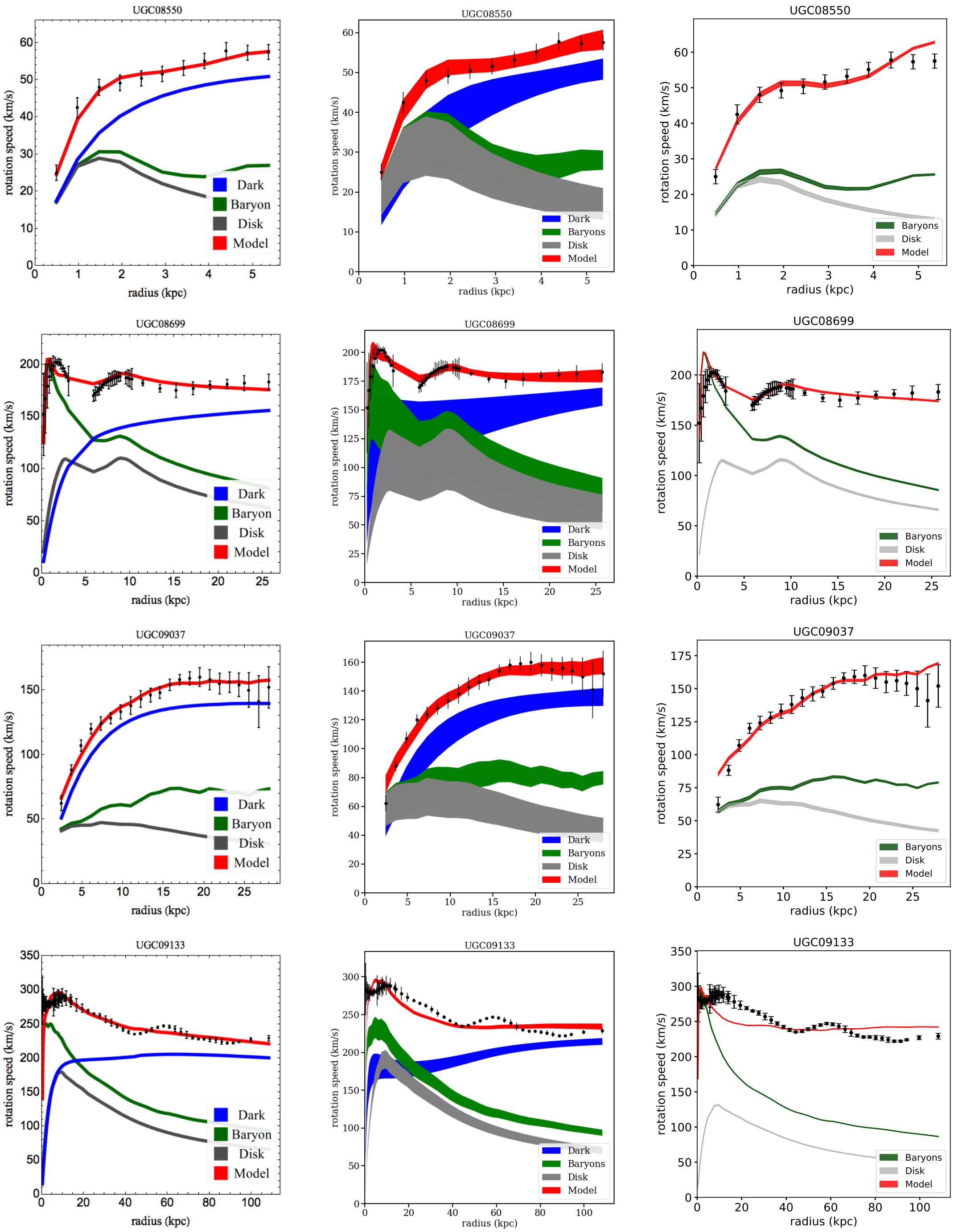

Figure A.1: Continued.

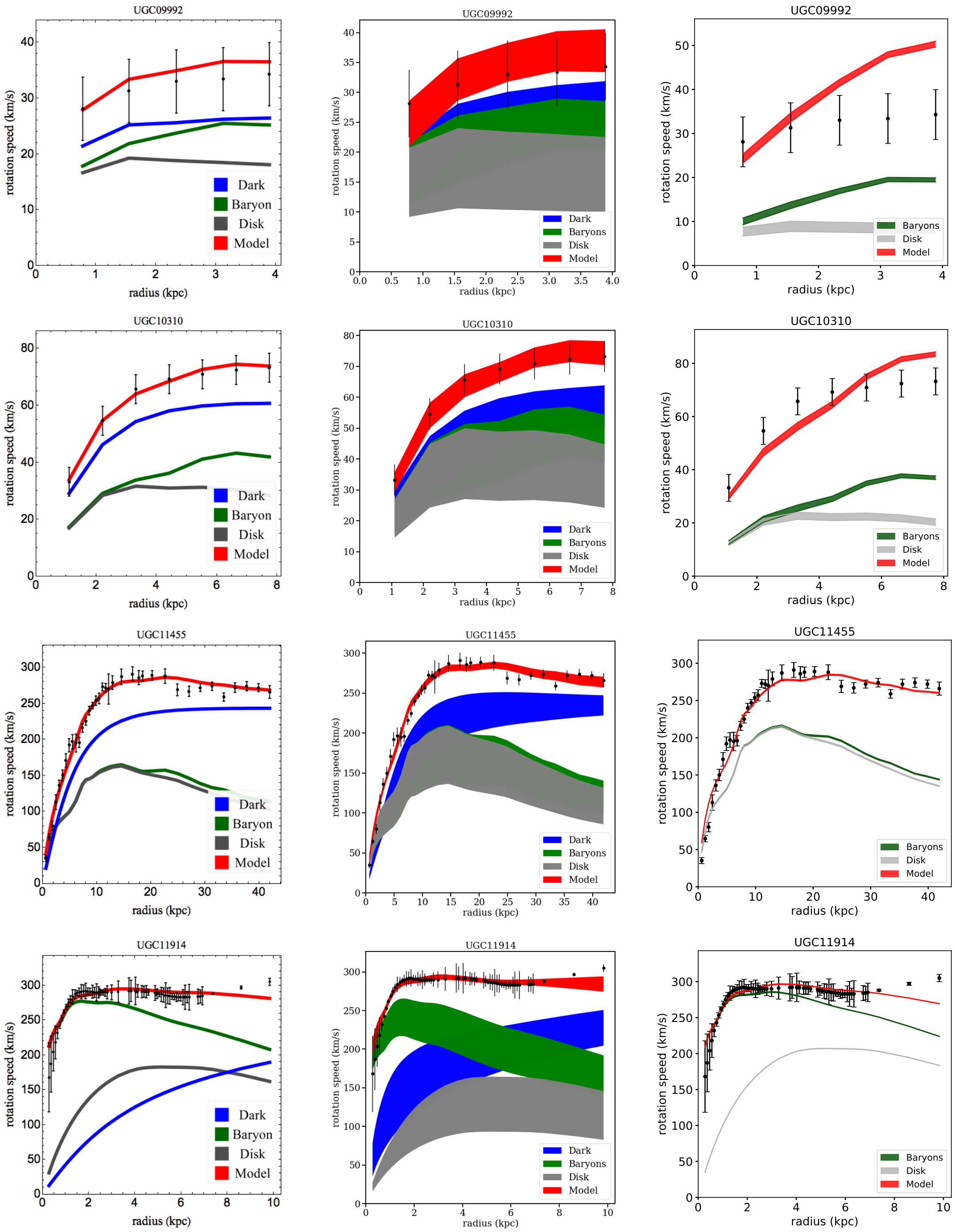

Figure A.1: Continued.

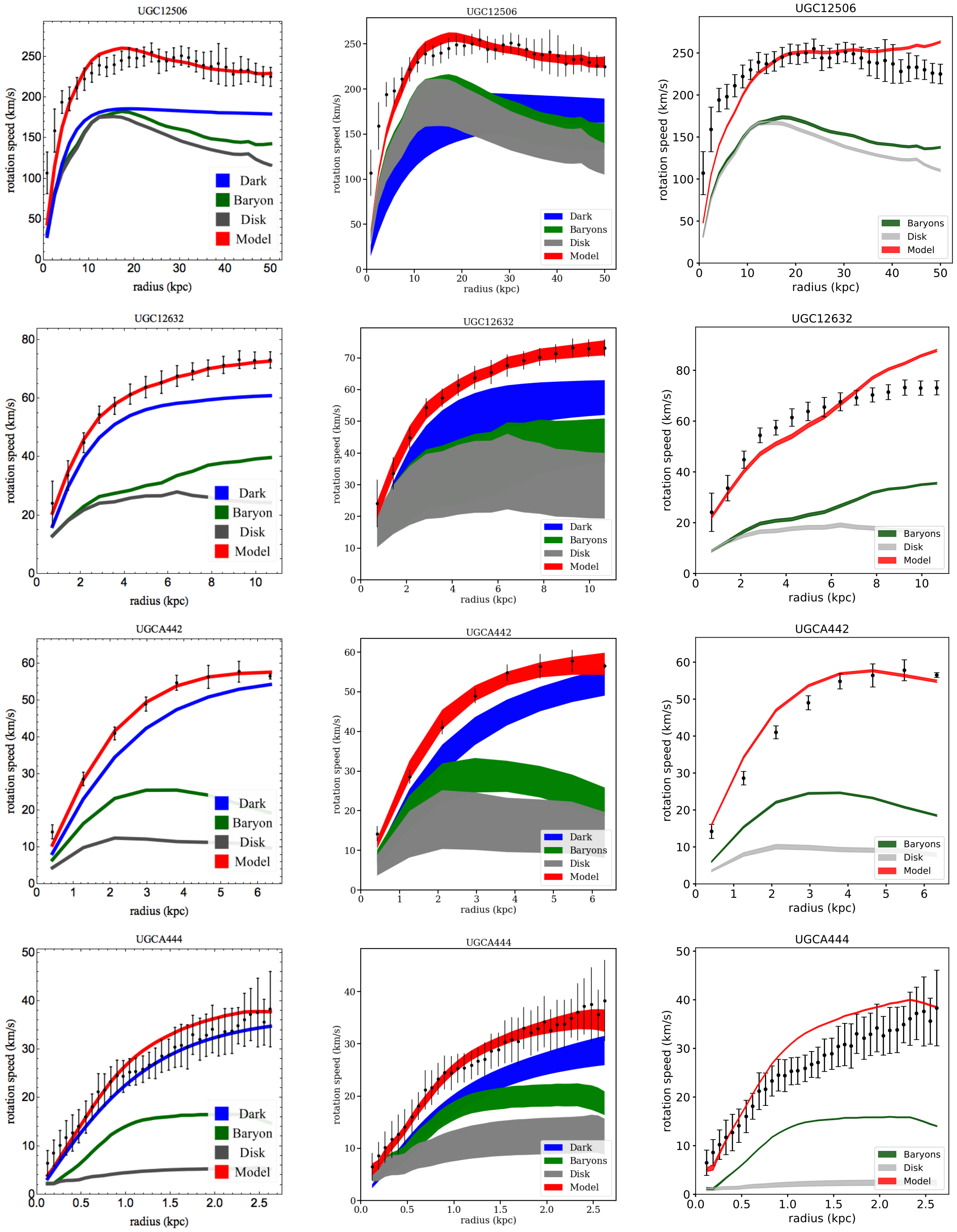

Figure A.1: Continued.

A.2 Parameters

Name (1)	$V_{\max}$ [km/s] (2)	$r_{\max}$ [kpc] (3)	$\rho_0 \times 10^7$ $[M_\odot/\mathrm{kpc}^3]$ (4)	σ_0 [km/s] (5)	$-\alpha$ (6)	$\Upsilon_{\star,\mathrm{disk}}$ $[M_\odot/L_\odot]$ (7)	$\Upsilon_{\star,\mathrm{bulge}}$ $[M_\odot/L_\odot]$ (8)	χ^2/d.o.f. (9)
D631-7	60.96	14.56	1.10	38.15	0.30	0.20	0.00	0.49
	82.92	47.16	1.16	47.56	0.57	0.10	0.00	0.47
	$75.88^{+4.56}_{-7.87}$	$40.36^{+7.01}_{-9.02}$	$1.36^{+0.22}_{-0.13}$	$44.49^{+2.17}_{-3.07}$	$0.63^{+0.04}_{-0.04}$	$0.19^{+0.18}_{-0.07}$	$0.00^{+0.00}_{-0.00}$	
DDO064	54.42	11.61	3.47	35.00	0.73	0.72	0.00	0.59
	45.76	4.37	5.45	31.69	0.64	0.11	0.00	0.31
	$46.06^{+13.59}_{-9.17}$	$9.48^{+9.26}_{-5.47}$	$3.60^{+1.88}_{-1.17}$	$34.96^{+6.01}_{-5.24}$	$0.73^{+0.11}_{-0.08}$	$1.08^{+0.91}_{-0.71}$	$0.00^{+0.00}_{-0.00}$	
DDO154	44.09	6.33	2.47	28.13	0.52	0.64	0.00	2.05
	48.71	12.94	2.29	32.11	0.58	0.36	0.00	1.14
	$48.46^{+5.28}_{-3.53}$	$13.69^{+6.63}_{-3.93}$	$2.34^{+0.54}_{-0.43}$	$31.99^{+2.28}_{-1.81}$	$0.62^{+0.07}_{-0.06}$	$0.54^{+0.50}_{-0.32}$	$0.00^{+0.00}_{-0.00}$	
DDO161	63.21	32.15	0.94	35.19	0.40	0.16	0.00	1.31
	72.26	52.61	0.93	43.53	0.57	0.23	0.00	0.70
	$64.29^{+3.23}_{-3.17}$	$36.35^{+4.01}_{-5.69}$	$1.11^{+0.10}_{-0.07}$	$41.75^{+1.38}_{-1.33}$	$0.53^{+0.04}_{-0.02}$	$0.18^{+0.15}_{-0.07}$	$0.00^{+0.00}_{-0.00}$	
DDO168	53.51	10.96	3.16	34.03	0.64	0.56	0.00	6.25
	70.01	17.90	2.82	46.15	0.68	0.11	0.00	4.44
	$65.78^{+7.21}_{-9.38}$	$19.45^{+7.33}_{-5.90}$	$2.77^{+0.77}_{-0.46}$	$43.98^{+3.58}_{-4.48}$	$0.76^{+0.08}_{-0.07}$	$0.50^{+0.70}_{-0.31}$	$0.00^{+0.00}_{-0.00}$	
DDO170	55.05	19.38	1.66	32.44	0.50	0.25	0.00	1.74
	56.55	19.98	1.34	35.88	0.40	0.11	0.00	1.15
	$55.60^{+5.10}_{-4.00}$	$23.93^{+7.82}_{-7.90}$	$1.23^{+0.37}_{-0.18}$	$36.63^{+2.19}_{-1.96}$	$0.45^{+0.05}_{-0.04}$	$0.55^{+0.70}_{-0.35}$	$0.00^{+0.00}_{-0.00}$	
ESO079-G014	153.58	44.87	3.58	115.72	0.72	0.64	0.00	1.47
	165.46	22.68	3.67	113.59	0.60	0.22	0.00	0.70
	$162.49^{+22.66}_{-19.97}$	$35.15^{+55.56}_{-12.41}$	$2.68^{+0.95}_{-1.14}$	$120.49^{+16.36}_{-8.39}$	$0.60^{+0.03}_{-0.04}$	$0.57^{+0.30}_{-0.29}$	$0.00^{+0.00}_{-0.00}$	
ESO116-G012	113.95	25.61	5.58	77.55	1.03	0.67	0.00	1.28
	104.95	19.08	5.56	76.18	0.97	0.56	0.00	0.90
	$110.29^{+25.78}_{-9.27}$	$27.11^{+28.07}_{-13.74}$	$4.63^{+2.17}_{-1.75}$	$79.80^{+13.09}_{-6.99}$	$0.96^{+0.09}_{-0.09}$	$0.71^{+0.28}_{-0.32}$	$0.00^{+0.00}_{-0.00}$	
ESO563-G021	267.60	65.44	11.13	205.71	1.31	0.49	0.00	9.84
	292.22	40.31	10.98	208.25	1.18	0.19	0.00	6.47
	$281.45^{+8.75}_{-9.10}$	$47.24^{+12.28}_{-4.14}$	$9.32^{+1.30}_{-1.34}$	$209.22^{+5.14}_{-4.28}$	$1.13^{+0.05}_{-0.05}$	$0.28^{+0.10}_{-0.05}$	$0.00^{+0.00}_{-0.00}$	
F561-1	42.29	11.40	2.03	24.97	0.51	0.04	0.00	0.30
	40.98	9.20	2.36	26.82	0.51	0.10	0.00	0.23
	$39.05^{+5.31}_{-2.87}$	$8.65^{+8.44}_{-5.27}$	$2.33^{+3.34}_{-0.92}$	$27.22^{+2.67}_{-2.24}$	$0.52^{+0.16}_{-0.04}$	$0.22^{+0.18}_{-0.09}$	$0.00^{+0.00}_{-0.00}$	

Table A.1: Model parameters and χ^2/d.o.f. values for the SIDM fits shown in Fig. A.1, with controlled sampling (first row associated with each galaxy) and MCMC sampling with the tophat prior (best-fit value, second row; medium with 1σ errors, third row). The α value is the logarithmic slope of the dark matter density profile at $r = 1.5\% r_{\mathrm{vir}}$. Galaxies are listed alphabetically, corresponding to the order in Fig. A.1.

F563-1	100.10	27.27	3.21	68.87	0.75	2.25	0.00	0.73
	104.81	10.30	4.57	67.19	0.63	0.11	0.00	0.55
	$100.94^{+9.62}_{-8.30}$	$19.38^{+31.98}_{-7.60}$	$2.93^{+1.53}_{-1.35}$	$71.28^{+8.27}_{-5.12}$	$0.70^{+0.11}_{-0.10}$	$2.08^{+1.67}_{-1.40}$	$0.00^{+0.00}_{-0.00}$	
F563-V2	102.17	20.74	9.70	75.08	1.22	1.96	0.00	0.13
	94.30	22.72	4.38	82.37	1.01	3.05	0.00	0.11
	$106.32^{+34.97}_{-17.90}$	$31.48^{+40.48}_{-19.15}$	$3.71^{+3.03}_{-1.48}$	$87.69^{+13.82}_{-10.20}$	$1.00^{+0.11}_{-0.11}$	$3.00^{+1.13}_{-1.18}$	$0.00^{+0.00}_{-0.00}$	
F568-V1	108.27	16.51	5.58	73.29	0.82	0.81	0.00	0.71
	102.58	9.94	7.74	73.83	0.93	1.22	0.00	0.06
	$97.71^{+19.49}_{-13.16}$	$21.45^{+35.39}_{-10.42}$	$4.21^{+2.80}_{-2.01}$	$82.47^{+11.12}_{-8.55}$	$0.87^{+0.09}_{-0.07}$	$2.76^{+1.01}_{-1.16}$	$0.00^{+0.00}_{-0.00}$	
F571-8	140.18	22.20	6.41	91.65	0.93	0.20	0.00	1.65
	145.52	21.49	5.08	94.57	0.79	0.13	0.00	0.29
	$148.95^{+11.65}_{-9.57}$	$24.02^{+5.56}_{-3.97}$	$4.80^{+1.22}_{-0.92}$	$97.01^{+7.18}_{-5.85}$	$0.78^{+0.10}_{-0.09}$	$0.15^{+0.06}_{-0.04}$	$0.00^{+0.00}_{-0.00}$	
F571-V1	77.02	18.90	2.15	49.39	0.50	0.36	0.00	0.11
	79.36	19.21	1.63	52.39	0.38	0.11	0.00	0.02
	$78.03^{+15.09}_{-9.60}$	$28.65^{+21.93}_{-14.77}$	$1.34^{+1.04}_{-0.37}$	$55.86^{+7.15}_{-5.38}$	$0.49^{+0.09}_{-0.08}$	$0.77^{+0.91}_{-0.51}$	$0.00^{+0.00}_{-0.00}$	
F574-1	91.22	20.25	3.86	63.50	0.70	0.74	0.00	0.42
	91.51	9.72	4.85	60.55	0.71	0.26	0.00	0.05
	$85.45^{+7.35}_{-9.60}$	$13.47^{+16.47}_{-3.83}$	$3.59^{+1.48}_{-1.67}$	$63.01^{+6.93}_{-3.26}$	$0.74^{+0.06}_{-0.08}$	$0.94^{+0.70}_{-0.60}$	$0.00^{+0.00}_{-0.00}$	
F579-V1	90.25	11.89	13.18	70.42	1.10	0.90	0.00	0.90
	76.31	6.37	6.02	71.35	0.79	1.51	0.00	1.02
	$84.25^{+9.92}_{-4.32}$	$10.06^{+27.07}_{-2.20}$	$4.94^{+0.87}_{-3.24}$	$77.86^{+12.91}_{-5.20}$	$0.76^{+0.03}_{-0.08}$	$1.43^{+0.40}_{-0.37}$	$0.00^{+0.00}_{-0.00}$	
F583-1	76.74	18.80	2.26	49.39	0.52	0.72	0.00	0.21
	79.06	13.67	2.20	51.11	0.42	0.10	0.00	0.11
	$78.17^{+7.31}_{-6.17}$	$18.43^{+13.89}_{-5.02}$	$1.87^{+0.53}_{-0.50}$	$53.16^{+5.52}_{-4.29}$	$0.46^{+0.06}_{-0.05}$	$0.93^{+1.11}_{-0.64}$	$0.00^{+0.00}_{-0.00}$	
IC2574	62.59	36.95	1.28	31.51	0.59	0.25	0.00	21.85
	73.23	58.24	0.83	34.83	0.52	0.11	0.00	7.78
	$63.04^{+4.58}_{-3.80}$	$36.79^{+4.74}_{-4.21}$	$1.01^{+0.08}_{-0.08}$	$33.87^{+2.25}_{-1.86}$	$0.46^{+0.02}_{-0.02}$	$0.14^{+0.09}_{-0.03}$	$0.00^{+0.00}_{-0.00}$	
IC4202	185.86	27.82	18.76	151.11	1.35	0.56	0.07	8.42
	211.98	22.01	17.70	157.58	1.33	0.26	0.14	7.08
	$208.11^{+9.55}_{-10.18}$	$28.42^{+2.46}_{-2.11}$	$14.88^{+2.53}_{-2.15}$	$160.27^{+2.59}_{-2.38}$	$1.25^{+0.09}_{-0.10}$	$0.31^{+0.10}_{-0.09}$	$0.22^{+0.03}_{-0.03}$	

Table A.1: Continued

KK98-251	32.46	10.60	2.59	17.89	0.74	0.25	0.00	1.99
	45.88	26.23	1.27	26.95	0.63	0.11	0.00	0.28
	$35.25^{+6.89}_{-5.55}$	$15.01^{+5.11}_{-4.44}$	$1.52^{+0.26}_{-0.12}$	$23.59^{+3.14}_{-2.94}$	$0.54^{+0.04}_{-0.03}$	$0.36^{+0.51}_{-0.21}$	$0.00^{+0.00}_{-0.00}$	
NGC0024	106.13	21.22	19.65	77.38	1.70	1.00	0.00	1.48
	154.15	120.65	4.60	97.34	1.25	1.79	0.00	0.37
	$103.94^{+33.22}_{-10.28}$	$37.62^{+50.07}_{-25.81}$	$12.74^{+14.16}_{-6.45}$	$81.65^{+10.90}_{-7.53}$	$1.76^{+0.15}_{-0.35}$	$1.39^{+0.31}_{-0.70}$	$0.00^{+0.00}_{-0.00}$	
NGC0055	80.13	29.60	1.71	51.06	0.52	0.36	0.00	0.77
	83.06	29.55	1.33	59.49	0.44	0.20	0.00	0.18
	$82.76^{+9.60}_{-6.76}$	$34.71^{+17.03}_{-11.32}$	$1.24^{+0.34}_{-0.23}$	$60.50^{+4.39}_{-3.68}$	$0.48^{+0.05}_{-0.04}$	$0.36^{+0.25}_{-0.19}$	$0.00^{+0.00}_{-0.00}$	
NGC0100	85.39	11.59	4.11	54.88	0.67	0.16	0.00	0.12
	85.57	17.34	3.07	59.07	0.67	0.34	0.00	0.07
	$91.25^{+21.20}_{-9.19}$	$26.56^{+28.11}_{-13.08}$	$2.41^{+1.18}_{-0.78}$	$63.12^{+10.20}_{-6.70}$	$0.71^{+0.08}_{-0.07}$	$0.51^{+0.24}_{-0.29}$	$0.00^{+0.00}_{-0.00}$	
NGC0247	88.11	25.20	3.07	61.33	0.64	0.77	0.00	9.15
	73.11	47.03	0.86	71.59	0.50	1.76	0.00	3.69
	$81.09^{+10.34}_{-5.38}$	$38.98^{+15.29}_{-21.86}$	$1.07^{+0.96}_{-0.18}$	$70.99^{+5.65}_{-7.84}$	$0.50^{+0.01}_{-0.01}$	$1.37^{+0.23}_{-0.44}$	$0.00^{+0.00}_{-0.00}$	
NGC0289	158.44	43.87	69.18	126.18	2.47	0.36	0.00	2.21
	152.87	44.78	39.97	129.36	2.18	0.36	0.00	1.75
	$156.52^{+4.42}_{-5.20}$	$39.79^{+19.07}_{-11.25}$	$49.87^{+483.68}_{-22.93}$	$127.90^{+4.44}_{-3.69}$	$2.22^{+0.30}_{-0.22}$	$0.24^{+0.17}_{-0.11}$	$0.00^{+0.00}_{-0.00}$	
NGC0300	93.39	24.75	3.31	63.73	0.80	0.76	0.00	0.65
	99.26	39.03	2.37	70.89	0.83	1.01	0.00	0.42
	$91.74^{+23.19}_{-7.08}$	$29.08^{+38.18}_{-16.95}$	$2.81^{+1.73}_{-1.02}$	$67.14^{+9.75}_{-6.95}$	$0.81^{+0.07}_{-0.07}$	$0.93^{+0.31}_{-0.48}$	$0.00^{+0.00}_{-0.00}$	
NGC0801	182.79	101.00	46.42	176.42	2.49	0.42	0.00	4.46
	202.83	27.23	78.13	156.62	2.37	0.10	0.00	4.38
	$181.04^{+17.13}_{-16.30}$	$34.55^{+66.24}_{-6.68}$	$42.94^{+28.59}_{-31.26}$	$161.94^{+14.85}_{-5.82}$	$2.15^{+0.19}_{-0.36}$	$0.33^{+0.20}_{-0.18}$	$0.00^{+0.00}_{-0.00}$	
NGC0891	209.68	54.97	32.61	149.04	1.89	0.20	0.58	4.22
	213.12	59.83	149.33	158.32	2.02	0.11	0.29	4.65
	$233.80^{+21.54}_{-12.71}$	$83.64^{+26.10}_{-13.62}$	$110.29^{+57.63}_{-48.71}$	$168.13^{+10.59}_{-6.13}$	$1.69^{+0.18}_{-0.23}$	$0.15^{+0.07}_{-0.04}$	$0.48^{+0.11}_{-0.10}$	
NGC1003	106.61	38.65	2.15	72.70	0.80	0.49	0.00	5.86
	118.71	92.26	1.73	81.31	1.01	0.76	0.00	2.16
	$110.58^{+6.36}_{-5.87}$	$63.27^{+17.36}_{-17.58}$	$1.94^{+0.32}_{-0.25}$	$78.41^{+2.25}_{-2.66}$	$0.92^{+0.07}_{-0.08}$	$0.62^{+0.10}_{-0.11}$	$0.00^{+0.00}_{-0.00}$	

Table A.1: Continued

NGC1090	140.44	23.86	13.59	109.15	1.31	0.34	0.00	1.38
	147.65	16.51	10.55	109.37	1.11	0.22	0.00	0.78
	$141.51^{+6.36}_{-7.52}$	$21.28^{+19.24}_{-3.84}$	$8.87^{+2.21}_{-3.09}$	$113.25^{+7.15}_{-3.00}$	$1.09^{+0.07}_{-0.06}$	$0.35^{+0.16}_{-0.09}$	$0.00^{+0.00}_{-0.00}$	
NGC1705	71.66	10.21	69.18	50.87	1.88	1.21	0.00	0.24
	73.83	15.79	75.78	54.08	1.83	1.22	0.00	0.14
	$72.85^{+17.45}_{-7.17}$	$15.68^{+13.90}_{-7.82}$	$75.52^{+98.38}_{-38.99}$	$53.58^{+7.74}_{-3.92}$	$1.85^{+0.47}_{-0.53}$	$1.18^{+0.70}_{-0.71}$	$0.00^{+0.00}_{-0.00}$	
NGC2366	44.05	7.52	3.86	28.05	0.71	0.25	0.00	0.91
	45.73	6.93	3.09	32.56	0.50	0.10	0.00	0.34
	$46.30^{+3.48}_{-2.47}$	$8.65^{+4.07}_{-2.18}$	$2.79^{+0.61}_{-0.51}$	$33.57^{+2.46}_{-1.80}$	$0.55^{+0.07}_{-0.05}$	$0.25^{+0.24}_{-0.11}$	$0.00^{+0.00}_{-0.00}$	
NGC2403	130.63	39.52	9.55	91.16	1.42	0.64	0.00	32.70
	126.53	40.62	9.27	96.24	1.34	0.65	0.00	12.07
	$139.26^{+10.38}_{-7.84}$	$58.27^{+15.74}_{-12.33}$	$6.33^{+1.30}_{-1.17}$	$101.17^{+4.14}_{-3.37}$	$1.23^{+0.05}_{-0.07}$	$0.69^{+0.06}_{-0.06}$	$0.00^{+0.00}_{-0.00}$	
NGC2683	149.14	34.11	94.04	124.68	2.57	0.34	0.34	2.54
	147.83	52.47	22.77	134.89	2.49	0.47	0.13	1.65
	$150.71^{+12.58}_{-13.00}$	$53.03^{+47.64}_{-20.26}$	$24.40^{+23.05}_{-10.19}$	$135.24^{+6.20}_{-5.02}$	$2.53^{+0.16}_{-0.13}$	$0.44^{+0.14}_{-0.17}$	$0.45^{+0.57}_{-0.27}$	
NGC2841	249.68	67.87	32.11	193.13	2.07	0.64	0.64	1.83
	280.92	160.58	24.98	221.07	2.16	0.69	0.67	1.13
	$273.98^{+29.19}_{-9.23}$	$120.57^{+97.93}_{-48.81}$	$32.64^{+22.73}_{-15.27}$	$216.19^{+12.30}_{-8.15}$	$2.18^{+0.13}_{-0.14}$	$0.52^{+0.29}_{-0.27}$	$0.60^{+0.19}_{-0.24}$	
NGC2903	188.71	63.79	98.48	138.77	2.31	0.25	0.00	12.38
	177.88	36.63	134.66	135.82	2.46	0.10	0.00	2.66
	$177.72^{+2.59}_{-2.63}$	$37.36^{+3.12}_{-1.79}$	$122.39^{+17.83}_{-14.79}$	$135.70^{+1.64}_{-1.68}$	$2.43^{+0.04}_{-0.05}$	$0.11^{+0.02}_{-0.01}$	$0.00^{+0.00}_{-0.00}$	
NGC2915	81.64	10.68	15.61	53.80	1.21	0.60	0.00	0.88
	81.16	6.69	13.19	53.13	1.17	0.15	0.00	0.36
	$81.00^{+2.65}_{-2.54}$	$7.88^{+1.47}_{-0.71}$	$13.84^{+6.73}_{-3.78}$	$54.03^{+1.69}_{-1.66}$	$1.18^{+0.20}_{-0.15}$	$0.28^{+0.16}_{-0.12}$	$0.00^{+0.00}_{-0.00}$	
NGC2976	79.44	11.82	19.95	56.75	1.62	0.36	0.00	0.79
	113.17	18.00	10.18	76.89	1.36	0.37	0.00	0.29
	$102.81^{+13.92}_{-21.15}$	$20.91^{+21.58}_{-8.70}$	$9.55^{+4.58}_{-3.99}$	$69.87^{+7.99}_{-10.31}$	$1.48^{+0.33}_{-0.28}$	$0.46^{+0.19}_{-0.25}$	$0.00^{+0.00}_{-0.00}$	
NGC2998	189.80	119.95	12.02	158.81	1.83	0.64	0.00	3.99
	202.55	184.01	3.95	175.02	1.47	0.74	0.00	3.70
	$168.11^{+16.47}_{-12.99}$	$58.49^{+71.71}_{-34.46}$	$8.69^{+13.08}_{-3.90}$	$159.82^{+12.71}_{-10.44}$	$1.59^{+0.13}_{-0.08}$	$0.65^{+0.15}_{-0.22}$	$0.00^{+0.00}_{-0.00}$	

Table A.1: Continued

NGC3109	68.89	16.16	1.82	42.94	0.44	0.72	0.00	0.27
	77.74	26.29	1.56	49.99	0.51	1.23	0.00	0.21
	$78.87^{+10.55}_{-9.46}$	$28.24^{+12.66}_{-9.79}$	$1.51^{+0.40}_{-0.24}$	$50.56^{+5.05}_{-5.06}$	$0.52^{+0.06}_{-0.04}$	$1.44^{+1.17}_{-0.97}$	$0.00^{+0.00}_{-0.00}$	
NGC3198	134.72	39.92	6.21	102.08	1.10	0.49	0.00	0.93
	135.97	24.37	6.42	103.86	0.79	0.37	0.00	0.74
	$136.66^{+4.99}_{-4.61}$	$23.87^{+14.90}_{-6.05}$	$6.56^{+0.99}_{-1.37}$	$104.06^{+4.78}_{-2.86}$	$0.81^{+0.03}_{-0.03}$	$0.38^{+0.17}_{-0.13}$	$0.00^{+0.00}_{-0.00}$	
NGC3521	228.02	100.34	59.34	159.34	1.87	0.44	0.00	0.68
	314.48	166.16	12.70	206.17	0.95	0.54	0.00	0.27
	$258.19^{+35.56}_{-72.68}$	$143.85^{+35.74}_{-81.18}$	$35.96^{+169.40}_{-17.90}$	$174.70^{+19.25}_{-30.39}$	$1.41^{+0.97}_{-0.31}$	$0.48^{+0.05}_{-0.27}$	$0.00^{+0.00}_{-0.00}$	
NGC3726	148.53	40.09	5.84	110.22	1.08	0.30	0.00	3.72
	169.62	144.06	1.40	129.81	0.98	0.48	0.00	2.19
	$149.74^{+27.73}_{-13.65}$	$68.32^{+62.93}_{-42.98}$	$1.99^{+1.62}_{-0.56}$	$120.52^{+10.56}_{-11.45}$	$0.85^{+0.09}_{-0.11}$	$0.38^{+0.08}_{-0.15}$	$0.00^{+0.00}_{-0.00}$	
NGC3741	52.82	13.18	2.55	32.60	0.52	1.00	0.00	1.09
	54.32	20.01	2.71	33.36	0.65	1.46	0.00	0.41
	$55.00^{+6.38}_{-4.88}$	$20.75^{+8.33}_{-5.67}$	$2.68^{+0.71}_{-0.52}$	$33.59^{+2.51}_{-2.09}$	$0.65^{+0.07}_{-0.06}$	$1.51^{+0.55}_{-0.49}$	$0.00^{+0.00}_{-0.00}$	
NGC3769	111.57	21.93	14.68	80.26	1.53	0.25	0.00	0.44
	111.81	18.60	9.25	83.74	1.37	0.20	0.00	0.40
	$112.23^{+6.38}_{-5.71}$	$21.77^{+16.40}_{-7.40}$	$8.65^{+3.55}_{-2.47}$	$85.17^{+4.72}_{-3.70}$	$1.44^{+0.19}_{-0.19}$	$0.24^{+0.13}_{-0.09}$	$0.00^{+0.00}_{-0.00}$	
NGC3877	145.00	19.56	12.40	106.58	1.18	0.20	0.00	2.69
	151.85	15.15	12.43	109.70	1.13	0.15	0.00	2.02
	$142.83^{+12.01}_{-12.73}$	$17.86^{+4.09}_{-2.41}$	$9.97^{+1.22}_{-1.58}$	$111.60^{+4.32}_{-3.59}$	$1.01^{+0.05}_{-0.06}$	$0.25^{+0.09}_{-0.07}$	$0.00^{+0.00}_{-0.00}$	
NGC3893	158.31	34.67	54.95	121.49	2.29	0.27	0.00	0.60
	161.90	31.10	33.78	126.23	2.02	0.22	0.00	0.30
	$166.89^{+35.07}_{-10.83}$	$43.59^{+61.83}_{-19.76}$	$26.10^{+19.34}_{-14.19}$	$129.69^{+16.12}_{-7.04}$	$1.95^{+0.22}_{-0.32}$	$0.30^{+0.18}_{-0.15}$	$0.00^{+0.00}_{-0.00}$	
NGC3917	127.48	20.10	5.41	87.31	0.80	0.25	0.00	1.16
	128.53	12.50	5.50	86.36	0.71	0.15	0.00	0.64
	$117.39^{+12.10}_{-13.32}$	$18.74^{+35.44}_{-5.02}$	$3.50^{+1.20}_{-1.79}$	$91.17^{+11.17}_{-4.44}$	$0.62^{+0.05}_{-0.06}$	$0.59^{+0.30}_{-0.29}$	$0.00^{+0.00}_{-0.00}$	
NGC3949	155.51	37.41	26.71	112.93	1.88	0.34	0.00	0.58
	132.21	14.62	39.46	100.01	2.10	0.10	0.00	0.26
	$161.96^{+53.52}_{-34.50}$	$57.43^{+49.94}_{-36.42}$	$11.30^{+16.99}_{-5.53}$	$118.60^{+25.48}_{-15.36}$	$1.79^{+0.38}_{-0.54}$	$0.36^{+0.11}_{-0.19}$	$0.00^{+0.00}_{-0.00}$	

Table A.1: Continued

NGC3953	173.19	36.76	19.95	141.92	1.60	0.36	0.00	0.61
	172.65	21.66	17.76	139.84	1.67	0.26	0.00	0.07
	$177.20^{+37.02}_{-16.06}$	$44.51^{+107.94}_{-20.45}$	$8.59^{+6.87}_{-5.07}$	$151.02^{+18.53}_{-9.29}$	$1.47^{+0.13}_{-0.11}$	$0.42^{+0.17}_{-0.16}$	$0.00^{+0.00}_{-0.00}$	
NGC3972	126.66	25.34	6.21	91.16	0.99	0.49	0.00	1.24
	117.65	12.73	7.94	82.95	0.95	0.24	0.00	0.80
	$121.44^{+38.95}_{-17.73}$	$30.65^{+51.01}_{-16.45}$	$4.27^{+2.85}_{-1.90}$	$92.22^{+18.62}_{-8.86}$	$0.92^{+0.06}_{-0.06}$	$0.64^{+0.26}_{-0.30}$	$0.00^{+0.00}_{-0.00}$	
NGC3992	201.85	65.63	9.26	172.84	1.23	0.64	0.00	0.64
	214.01	27.14	5.46	169.69	0.70	0.43	0.00	0.66
	$201.99^{+20.67}_{-19.81}$	$54.19^{+92.83}_{-22.95}$	$2.60^{+1.68}_{-1.17}$	$180.91^{+16.43}_{-9.26}$	$0.60^{+0.10}_{-0.10}$	$0.70^{+0.16}_{-0.22}$	$0.00^{+0.00}_{-0.00}$	
NGC4010	131.32	64.25	2.59	90.06	0.92	0.56	0.00	2.68
	119.88	15.03	4.68	81.67	0.73	0.11	0.00	1.34
	$128.14^{+31.00}_{-14.76}$	$34.26^{+40.51}_{-16.66}$	$2.85^{+1.52}_{-1.04}$	$91.75^{+16.07}_{-9.38}$	$0.79^{+0.09}_{-0.09}$	$0.37^{+0.21}_{-0.19}$	$0.00^{+0.00}_{-0.00}$	
NGC4013	159.70	47.38	20.57	121.46	1.85	0.36	0.36	1.60
	217.63	207.84	2.44	149.00	1.71	0.36	1.37	0.81
	$191.39^{+18.02}_{-21.46}$	$139.74^{+39.55}_{-55.64}$	$3.18^{+1.20}_{-0.58}$	$142.28^{+4.88}_{-7.02}$	$1.67^{+0.16}_{-0.22}$	$0.29^{+0.15}_{-0.12}$	$1.34^{+0.60}_{-0.63}$	
NGC4051	118.96	19.53	12.59	96.85	1.18	0.30	0.00	0.69
	112.83	11.55	12.83	98.82	1.37	0.33	0.00	0.57
	$127.71^{+29.75}_{-12.83}$	$30.92^{+59.63}_{-15.56}$	$6.58^{+4.45}_{-3.33}$	$110.64^{+13.91}_{-8.81}$	$1.00^{+0.21}_{-0.11}$	$0.37^{+0.11}_{-0.11}$	$0.00^{+0.00}_{-0.00}$	
NGC4085	151.60	27.51	8.58	103.48	1.19	0.23	0.00	2.76
	131.89	15.73	13.68	91.63	1.36	0.10	0.00	1.09
	$143.55^{+28.41}_{-20.99}$	$26.88^{+20.26}_{-9.44}$	$9.27^{+4.98}_{-3.16}$	$100.68^{+15.89}_{-11.29}$	$1.30^{+0.20}_{-0.17}$	$0.20^{+0.12}_{-0.08}$	$0.00^{+0.00}_{-0.00}$	
NGC4088	149.23	47.56	14.23	118.54	1.64	0.25	0.00	0.81
	144.18	16.09	10.23	113.23	1.05	0.15	0.00	0.50
	$146.82^{+34.32}_{-14.15}$	$43.60^{+84.67}_{-24.16}$	$4.92^{+3.58}_{-2.16}$	$123.75^{+14.47}_{-8.32}$	$1.05^{+0.25}_{-0.09}$	$0.26^{+0.07}_{-0.09}$	$0.00^{+0.00}_{-0.00}$	
NGC4100	153.98	39.05	23.62	120.87	1.86	0.40	0.00	1.57
	149.06	21.71	13.51	121.19	1.38	0.36	0.00	0.76
	$147.52^{+8.82}_{-9.19}$	$26.11^{+34.41}_{-6.95}$	$10.58^{+4.11}_{-4.67}$	$122.90^{+8.50}_{-3.31}$	$1.33^{+0.11}_{-0.07}$	$0.45^{+0.18}_{-0.13}$	$0.00^{+0.00}_{-0.00}$	
NGC4138	149.14	34.11	98.48	112.92	2.44	0.28	0.28	3.35
	145.78	69.66	31.10	123.38	2.60	0.59	0.12	1.24
	$149.83^{+27.34}_{-20.15}$	$60.39^{+51.63}_{-24.96}$	$41.15^{+107.59}_{-21.67}$	$123.07^{+8.07}_{-6.06}$	$2.57^{+0.38}_{-0.52}$	$0.36^{+0.22}_{-0.18}$	$0.43^{+0.55}_{-0.25}$	

Table A.1: Continued

NGC4157	166.13	39.68	21.54	127.03	1.81	0.25	0.25	0.60
	217.48	193.46	4.04	154.23	1.53	0.43	0.10	0.26
	$177.84^{+38.45}_{-15.59}$	$87.17^{+85.28}_{-52.40}$	$7.62^{+6.80}_{-3.05}$	$142.09^{+12.17}_{-11.14}$	$1.57^{+0.11}_{-0.12}$	$0.33^{+0.07}_{-0.13}$	$0.52^{+0.56}_{-0.31}$	
NGC4183	93.14	22.30	5.58	69.74	0.90	0.64	0.00	0.35
	92.87	66.34	1.21	90.51	0.68	1.36	0.00	0.44
	$88.64^{+7.88}_{-7.02}$	$18.49^{+29.72}_{-8.14}$	$2.83^{+1.88}_{-1.38}$	$77.27^{+9.85}_{-5.37}$	$0.67^{+0.04}_{-0.03}$	$0.97^{+0.30}_{-0.39}$	$0.00^{+0.00}_{-0.00}$	
NGC4214	106.14	17.81	15.14	70.24	1.13	1.21	0.00	0.96
	106.07	30.67	15.18	71.14	1.16	1.15	0.00	0.96
	$93.89^{+14.54}_{-17.05}$	$25.03^{+10.52}_{-11.70}$	$23.48^{+26.90}_{-9.32}$	$64.71^{+7.44}_{-8.19}$	$1.42^{+0.54}_{-0.30}$	$0.99^{+0.27}_{-0.37}$	$0.00^{+0.00}_{-0.00}$	
NGC4217	154.58	25.50	19.95	115.25	1.62	1.00	0.07	0.86
	166.44	37.12	16.34	127.18	1.68	0.61	0.10	0.85
	$182.36^{+39.57}_{-17.40}$	$77.24^{+67.03}_{-32.72}$	$9.03^{+5.58}_{-4.05}$	$137.41^{+15.89}_{-8.19}$	$1.54^{+0.13}_{-0.13}$	$1.14^{+0.44}_{-0.49}$	$0.13^{+0.04}_{-0.02}$	
NGC4559	107.30	30.04	5.84	78.82	1.09	0.36	0.00	0.32
	106.84	30.72	3.86	86.02	0.88	0.39	0.00	0.31
	$107.68^{+12.16}_{-5.49}$	$31.47^{+37.14}_{-15.80}$	$3.84^{+2.01}_{-1.39}$	$86.11^{+8.62}_{-6.52}$	$0.92^{+0.07}_{-0.07}$	$0.42^{+0.12}_{-0.17}$	$0.00^{+0.00}_{-0.00}$	
NGC5005	195.91	53.42	100.00	154.97	2.60	0.25	0.41	0.43
	352.23	181.33	28.13	236.99	1.28	0.50	0.49	0.06
	$305.59^{+46.72}_{-46.99}$	$145.02^{+86.92}_{-51.93}$	$78.18^{+123.51}_{-47.71}$	$210.68^{+24.36}_{-22.55}$	$1.57^{+0.37}_{-0.30}$	$0.39^{+0.13}_{-0.17}$	$0.45^{+0.12}_{-0.12}$	
NGC5033	200.95	67.82	57.54	146.86	2.20	0.36	0.39	14.22
	197.73	33.86	119.13	148.03	2.20	0.10	0.10	9.19
	$198.91^{+3.58}_{-3.37}$	$51.43^{+12.84}_{-7.50}$	$221.85^{+102.26}_{-67.03}$	$152.85^{+3.23}_{-2.62}$	$2.20^{+0.07}_{-0.10}$	$0.16^{+0.11}_{-0.05}$	$0.15^{+0.05}_{-0.03}$	
NGC5055	172.76	58.29	64.07	138.45	2.47	0.22	0.00	44.40
	174.33	26.64	47.67	134.34	1.97	0.11	0.00	11.55
	$167.71^{+4.64}_{-4.53}$	$43.06^{+25.33}_{-12.47}$	$50.30^{+14.73}_{-12.79}$	$139.19^{+4.84}_{-3.47}$	$1.98^{+0.13}_{-0.12}$	$0.22^{+0.08}_{-0.07}$	$0.00^{+0.00}_{-0.00}$	
NGC5371	154.58	25.50	16.09	144.62	1.15	0.38	0.00	9.02
	160.21	17.31	19.78	155.09	1.37	0.38	0.00	8.81
	$151.71^{+7.27}_{-4.44}$	$21.21^{+86.08}_{-3.10}$	$16.27^{+2.33}_{-12.36}$	$162.41^{+24.73}_{-3.65}$	$1.32^{+0.05}_{-0.31}$	$0.47^{+0.09}_{-0.05}$	$0.00^{+0.00}_{-0.00}$	
NGC5585	83.75	13.19	5.09	56.57	0.86	0.36	0.00	9.39
	95.47	34.21	2.94	67.75	0.78	0.59	0.00	5.09
	$89.31^{+11.28}_{-6.03}$	$24.01^{+15.00}_{-8.04}$	$3.53^{+1.05}_{-0.92}$	$64.29^{+5.68}_{-3.90}$	$0.77^{+0.05}_{-0.05}$	$0.49^{+0.11}_{-0.11}$	$0.00^{+0.00}_{-0.00}$	

Table A.1: Continued

NGC5907	183.88	37.36	12.02	147.11	1.25	0.42	0.00	5.82
	194.34	168.66	1.58	179.58	1.04	0.77	0.00	6.25
	$176.57^{+12.08}_{-12.49}$	$46.00^{+80.23}_{-20.43}$	$3.62^{+2.94}_{-1.79}$	$162.38^{+15.69}_{-8.66}$	$0.90^{+0.11}_{-0.08}$	$0.65^{+0.16}_{-0.20}$	$0.00^{+0.00}_{-0.00}$	
NGC5985	225.66	44.24	15.85	187.19	1.34	0.81	1.16	11.33
	264.71	38.63	26.44	190.84	1.81	0.10	0.95	1.34
	$246.81^{+14.68}_{-19.90}$	$42.22^{+12.10}_{-5.70}$	$21.74^{+4.81}_{-5.06}$	$193.67^{+4.81}_{-3.32}$	$1.71^{+0.11}_{-0.13}$	$0.38^{+0.25}_{-0.19}$	$1.42^{+0.63}_{-0.38}$	
NGC6015	139.51	46.23	16.09	108.83	1.74	0.61	0.00	11.43
	173.65	155.11	4.22	128.81	1.56	0.88	0.00	10.29
	$160.26^{+16.68}_{-20.22}$	$109.75^{+34.22}_{-52.11}$	$5.12^{+2.45}_{-0.88}$	$125.50^{+4.38}_{-7.07}$	$1.54^{+0.06}_{-0.09}$	$0.81^{+0.05}_{-0.10}$	$0.00^{+0.00}_{-0.00}$	
NGC6195	180.79	80.12	2.51	141.48	0.67	0.38	0.69	3.50
	309.53	317.14	10.33	212.69	1.30	0.23	0.70	1.94
	$250.13^{+47.41}_{-36.12}$	$170.28^{+87.99}_{-70.74}$	$17.80^{+12.82}_{-6.77}$	$195.65^{+14.90}_{-11.49}$	$1.58^{+0.20}_{-0.24}$	$0.22^{+0.10}_{-0.08}$	$0.59^{+0.08}_{-0.09}$	
NGC6503	109.01	26.00	56.67	81.60	2.18	0.34	0.00	2.30
	108.41	18.01	22.45	81.79	1.98	0.25	0.00	1.06
	$109.10^{+2.27}_{-2.13}$	$18.62^{+8.39}_{-5.01}$	$23.35^{+6.53}_{-4.97}$	$82.39^{+2.55}_{-1.95}$	$2.02^{+0.12}_{-0.11}$	$0.27^{+0.10}_{-0.08}$	$0.00^{+0.00}_{-0.00}$	
NGC6674	209.63	133.23	10.47	187.73	1.66	0.96	0.96	7.79
	238.32	222.88	30.16	207.85	1.94	0.75	2.35	2.45
	$221.93^{+11.62}_{-12.62}$	$95.22^{+71.63}_{-41.93}$	$58.28^{+316.31}_{-40.23}$	$196.00^{+8.71}_{-10.00}$	$2.19^{+0.28}_{-0.36}$	$0.53^{+0.27}_{-0.21}$	$0.92^{+0.88}_{-0.61}$	
NGC6946	136.89	35.77	20.89	111.28	1.79	0.38	0.38	3.25
	175.07	100.49	124.81	133.29	1.60	0.42	0.52	1.61
	$154.55^{+24.32}_{-8.41}$	$68.54^{+61.59}_{-30.13}$	$173.07^{+181.24}_{-94.80}$	$126.12^{+8.42}_{-6.16}$	$1.67^{+0.07}_{-0.05}$	$0.39^{+0.09}_{-0.12}$	$0.46^{+0.05}_{-0.05}$	
NGC7331	239.40	107.29	44.33	175.21	2.21	0.27	0.27	0.63
	257.96	172.91	12.98	189.80	1.80	0.33	0.19	0.51
	$238.25^{+36.39}_{-16.83}$	$116.95^{+85.49}_{-45.14}$	$21.42^{+14.95}_{-9.89}$	$181.91^{+13.39}_{-8.43}$	$1.97^{+0.21}_{-0.33}$	$0.24^{+0.09}_{-0.09}$	$0.50^{+0.44}_{-0.28}$	
NGC7814	210.88	53.59	8.19	145.21	1.29	0.95	0.54	1.90
	268.62	162.68	165.61	183.88	1.49	1.26	0.43	0.60
	$251.66^{+38.64}_{-19.83}$	$123.50^{+55.20}_{-37.53}$	$414.31^{+1267.93}_{-302.97}$	$175.93^{+17.91}_{-9.52}$	$1.61^{+0.24}_{-0.31}$	$0.79^{+0.53}_{-0.42}$	$0.38^{+0.11}_{-0.20}$	
PGC51017	14.77	2.60	9.70	8.83	1.29	0.06	0.00	3.01
	14.89	0.59	15.33	10.84	1.05	0.12	0.00	0.93
	$13.93^{+1.36}_{-0.66}$	$0.80^{+0.96}_{-0.19}$	$10.42^{+2.57}_{-5.09}$	$11.30^{+0.89}_{-0.83}$	$0.85^{+0.11}_{-0.11}$	$0.18^{+0.14}_{-0.06}$	$0.00^{+0.00}_{-0.00}$	

Table A.1: Continued

UGC00128	117.63	33.05	2.26	79.67	0.54	0.64	0.00	5.67
	116.55	87.69	1.04	92.52	0.72	2.04	0.00	6.05
	$115.88^{+4.61}_{-4.80}$	$51.16^{+24.20}_{-19.82}$	$1.42^{+0.44}_{-0.28}$	$87.05^{+4.84}_{-4.84}$	$0.66^{+0.07}_{-0.12}$	$1.47^{+0.53}_{-0.76}$	$0.00^{+0.00}_{-0.00}$	
UGC00731	64.73	9.48	4.04	41.36	0.65	1.00	0.00	1.31
	52.68	25.40	1.37	47.62	0.68	9.93	0.00	0.17
	$57.63^{+5.35}_{-4.29}$	$13.19^{+13.78}_{-5.90}$	$2.30^{+1.71}_{-0.94}$	$44.44^{+4.47}_{-3.14}$	$0.65^{+0.04}_{-0.06}$	$6.08^{+2.63}_{-3.71}$	$0.00^{+0.00}_{-0.00}$	
UGC01230	96.05	15.47	5.09	66.43	0.74	0.64	0.00	0.29
	104.96	10.23	4.82	68.22	0.66	0.11	0.00	0.20
	$91.88^{+10.70}_{-11.48}$	$15.61^{+18.76}_{-4.73}$	$3.35^{+1.60}_{-1.53}$	$72.20^{+6.81}_{-5.35}$	$0.72^{+0.08}_{-0.10}$	$1.14^{+0.92}_{-0.74}$	$0.00^{+0.00}_{-0.00}$	
UGC01281	55.59	11.96	2.75	35.59	0.61	0.64	0.00	0.21
	57.88	10.53	2.72	38.50	0.47	0.11	0.00	0.17
	$62.47^{+10.29}_{-8.31}$	$16.94^{+11.15}_{-6.46}$	$2.13^{+0.71}_{-0.47}$	$42.07^{+5.22}_{-4.72}$	$0.55^{+0.08}_{-0.06}$	$0.67^{+0.66}_{-0.44}$	$0.00^{+0.00}_{-0.00}$	
UGC02259	77.34	10.25	10.80	55.11	1.16	0.98	0.00	6.07
	72.83	5.92	9.38	54.68	1.04	1.03	0.00	4.23
	$70.37^{+12.23}_{-6.94}$	$15.91^{+26.06}_{-9.06}$	$4.23^{+3.82}_{-1.89}$	$62.09^{+7.43}_{-5.71}$	$1.00^{+0.06}_{-0.05}$	$2.17^{+0.61}_{-0.75}$	$0.00^{+0.00}_{-0.00}$	
UGC02487	285.69	64.85	10.63	231.08	1.25	0.71	0.96	6.98
	320.18	320.70	2.76	278.26	1.55	1.39	0.19	4.26
	$312.04^{+21.21}_{-18.51}$	$127.09^{+144.72}_{-61.46}$	$6.84^{+7.77}_{-3.16}$	$256.07^{+17.02}_{-11.88}$	$1.62^{+0.21}_{-0.22}$	$0.65^{+0.37}_{-0.38}$	$0.67^{+0.48}_{-0.38}$	
UGC02885	259.19	119.66	2.88	192.89	0.87	0.52	1.11	0.88
	297.16	225.11	19.18	228.32	1.37	0.49	0.97	1.02
	$284.22^{+25.03}_{-14.16}$	$166.10^{+105.93}_{-63.63}$	$28.75^{+29.92}_{-14.04}$	$220.68^{+13.21}_{-11.26}$	$1.47^{+0.19}_{-0.16}$	$0.41^{+0.17}_{-0.20}$	$0.91^{+0.13}_{-0.13}$	
UGC02916	140.97	43.94	4.43	113.60	0.78	1.00	0.50	12.78
	144.94	15.73	4781.21	143.60	2.37	1.23	0.10	8.89
	$143.11^{+16.16}_{-10.38}$	$27.81^{+57.66}_{-10.14}$	$73.52^{+183.88}_{-53.27}$	$146.38^{+17.62}_{-5.27}$	$2.23^{+0.22}_{-0.43}$	$1.15^{+0.34}_{-0.45}$	$0.32^{+0.12}_{-0.20}$	
UGC02953	255.96	129.11	36.31	199.43	2.31	0.53	0.53	9.43
	324.83	279.95	103.90	229.56	1.87	0.59	0.56	12.89
	$330.49^{+13.90}_{-14.85}$	$316.67^{+37.76}_{-48.14}$	$95.30^{+25.98}_{-19.27}$	$228.41^{+4.34}_{-4.28}$	$1.80^{+0.08}_{-0.08}$	$0.59^{+0.03}_{-0.04}$	$0.59^{+0.03}_{-0.03}$	
UGC03205	179.76	52.32	15.85	144.83	1.63	0.61	0.61	5.88
	196.31	31.72	123.02	150.24	2.25	0.11	0.24	1.08
	$194.32^{+4.70}_{-5.71}$	$36.52^{+7.56}_{-4.67}$	$111.13^{+22.28}_{-19.46}$	$152.71^{+2.64}_{-2.26}$	$2.15^{+0.09}_{-0.10}$	$0.19^{+0.09}_{-0.06}$	$0.35^{+0.12}_{-0.10}$	

Table A.1: Continued

UGC03546	178.92	45.52	35.21	134.67	2.10	0.34	0.34	1.88
	230.62	189.25	152.50	163.96	1.62	0.63	0.25	1.63
	$213.72^{+31.98}_{-13.31}$	$110.03^{+79.05}_{-36.08}$	$498.07^{+684.56}_{-324.78}$	$155.63^{+11.85}_{-6.24}$	$1.68^{+0.22}_{-0.28}$	$0.36^{+0.18}_{-0.16}$	$0.25^{+0.10}_{-0.10}$	
UGC03580	116.82	28.65	3.11	79.29	0.86	0.36	0.36	5.24
	125.58	60.33	4.41	90.41	1.06	0.57	0.13	2.10
	$121.15^{+9.33}_{-6.27}$	$45.50^{+19.52}_{-13.25}$	$6.55^{+2.83}_{-1.95}$	$87.65^{+4.32}_{-3.72}$	$1.05^{+0.06}_{-0.07}$	$0.42^{+0.10}_{-0.11}$	$0.23^{+0.05}_{-0.05}$	
UGC04278	89.10	20.96	2.59	58.45	0.63	0.74	0.00	0.80
	134.98	49.70	1.40	87.92	0.45	0.95	0.00	0.48
	$110.36^{+14.73}_{-20.38}$	$35.29^{+14.16}_{-14.50}$	$1.67^{+0.47}_{-0.27}$	$74.14^{+7.90}_{-11.25}$	$0.48^{+0.06}_{-0.05}$	$0.80^{+0.35}_{-0.32}$	$0.00^{+0.00}_{-0.00}$	
UGC04305	25.67	5.67	3.26	14.92	0.72	0.09	0.00	2.55
	22.45	1.91	6.13	16.90	0.71	0.28	0.00	1.82
	$25.18^{+1.36}_{-0.79}$	$2.08^{+1.16}_{-0.54}$	$7.13^{+2.53}_{-2.50}$	$17.92^{+0.81}_{-0.72}$	$0.79^{+0.12}_{-0.12}$	$0.16^{+0.09}_{-0.05}$	$0.00^{+0.00}_{-0.00}$	
UGC04325	77.35	9.72	18.20	57.88	1.45	1.00	0.00	2.68
	73.05	5.40	11.16	58.53	1.03	1.16	0.00	2.68
	$71.03^{+10.32}_{-5.40}$	$8.74^{+25.95}_{-2.49}$	$7.66^{+2.02}_{-4.59}$	$62.88^{+8.42}_{-3.28}$	$0.99^{+0.12}_{-0.08}$	$1.72^{+0.65}_{-0.53}$	$0.00^{+0.00}_{-0.00}$	
UGC04499	65.11	14.93	3.69	43.46	0.76	0.49	0.00	0.34
	63.75	8.91	3.61	45.74	0.60	0.31	0.00	0.26
	$64.99^{+9.88}_{-5.29}$	$13.58^{+19.17}_{-6.06}$	$2.81^{+1.49}_{-1.06}$	$48.58^{+7.26}_{-4.11}$	$0.66^{+0.10}_{-0.10}$	$0.60^{+0.41}_{-0.36}$	$0.00^{+0.00}_{-0.00}$	
UGC05005	91.58	43.02	1.15	55.65	0.45	0.42	0.00	0.28
	101.17	68.28	0.72	60.33	0.38	0.33	0.00	0.05
	$92.83^{+13.16}_{-10.66}$	$48.57^{+17.85}_{-17.45}$	$0.90^{+0.31}_{-0.17}$	$59.70^{+6.59}_{-5.92}$	$0.38^{+0.06}_{-0.05}$	$0.32^{+0.38}_{-0.17}$	$0.00^{+0.00}_{-0.00}$	
UGC05253	209.69	89.40	5.01	155.56	1.16	0.64	0.64	7.99
	240.52	118.96	460.62	183.03	1.87	0.38	0.46	8.74
	$247.39^{+14.28}_{-12.53}$	$200.92^{+37.91}_{-44.40}$	$320.05^{+133.69}_{-83.50}$	$185.99^{+4.57}_{-4.47}$	$1.76^{+0.09}_{-0.09}$	$0.58^{+0.07}_{-0.10}$	$0.54^{+0.03}_{-0.04}$	
UGC05716	66.30	13.84	4.37	45.05	0.88	1.17	0.00	15.88
	69.53	24.68	2.26	49.90	0.82	1.48	0.00	2.08
	$69.13^{+8.67}_{-4.57}$	$24.84^{+17.53}_{-11.53}$	$2.38^{+0.98}_{-0.58}$	$50.32^{+4.07}_{-3.95}$	$0.84^{+0.10}_{-0.11}$	$1.64^{+0.56}_{-0.71}$	$0.00^{+0.00}_{-0.00}$	
UGC05721	74.18	9.00	78.22	52.47	2.00	0.90	0.00	0.92
	73.74	5.95	53.39	52.93	1.96	0.46	0.00	0.48
	$74.82^{+3.27}_{-2.95}$	$7.53^{+2.57}_{-1.05}$	$48.75^{+12.98}_{-9.96}$	$54.40^{+2.06}_{-1.78}$	$1.88^{+0.13}_{-0.13}$	$0.66^{+0.26}_{-0.13}$	$0.00^{+0.00}_{-0.00}$	

Table A.1: Continued

UGC05986	110.35	18.18	7.36	76.00	1.10	0.56	0.00	7.18
	109.44	11.01	9.34	74.92	1.05	0.26	0.00	0.80
	$111.74^{+25.20}_{-7.66}$	$22.91^{+32.95}_{-10.25}$	$6.40^{+2.57}_{-2.80}$	$80.59^{+13.63}_{-5.49}$	$1.13^{+0.10}_{-0.09}$	$0.74^{+0.40}_{-0.35}$	$0.00^{+0.00}_{-0.00}$	
UGC06399	84.29	21.44	3.21	57.29	0.71	0.74	0.00	0.25
	82.14	8.83	4.40	54.32	0.63	0.13	0.00	0.03
	$80.67^{+19.46}_{-11.87}$	$20.11^{+26.75}_{-10.67}$	$2.46^{+1.79}_{-0.89}$	$60.75^{+9.77}_{-6.69}$	$0.69^{+0.06}_{-0.08}$	$1.03^{+0.55}_{-0.64}$	$0.00^{+0.00}_{-0.00}$	
UGC06446	75.73	9.94	8.07	51.96	1.03	1.00	0.00	0.72
	75.85	25.78	4.02	61.02	0.99	2.37	0.00	0.17
	$73.44^{+16.26}_{-6.56}$	$19.97^{+28.73}_{-11.57}$	$4.58^{+3.26}_{-1.79}$	$58.85^{+8.00}_{-5.97}$	$1.00^{+0.11}_{-0.11}$	$2.21^{+0.64}_{-0.90}$	$0.00^{+0.00}_{-0.00}$	
UGC06614	183.93	67.82	1.71	128.15	0.53	0.56	0.44	1.00
	209.82	120.85	5.29	148.35	1.40	0.13	0.45	0.20
	$206.11^{+25.23}_{-20.67}$	$135.39^{+54.49}_{-48.12}$	$4.19^{+2.08}_{-1.38}$	$150.51^{+9.42}_{-8.58}$	$1.30^{+0.23}_{-0.21}$	$0.31^{+0.27}_{-0.15}$	$0.43^{+0.09}_{-0.09}$	
UGC06628	32.62	7.93	2.71	18.98	0.64	0.09	0.00	0.62
	34.14	3.17	6.68	22.65	0.83	0.10	0.00	0.16
	$33.24^{+5.66}_{-2.88}$	$4.84^{+7.30}_{-2.43}$	$3.91^{+4.09}_{-2.06}$	$24.04^{+3.45}_{-2.72}$	$0.66^{+0.19}_{-0.08}$	$0.21^{+0.19}_{-0.09}$	$0.00^{+0.00}_{-0.00}$	
UGC06667	82.38	14.05	3.52	53.51	0.58	1.12	0.00	1.40
	72.63	7.08	4.04	51.50	0.54	2.65	0.00	0.14
	$68.90^{+10.70}_{-7.56}$	$8.31^{+5.57}_{-2.15}$	$3.32^{+0.94}_{-1.36}$	$52.85^{+5.42}_{-3.66}$	$0.48^{+0.07}_{-0.08}$	$4.35^{+2.50}_{-3.05}$	$0.00^{+0.00}_{-0.00}$	
UGC06786	205.29	43.62	16.85	148.82	1.64	0.58	0.58	3.08
	217.51	45.08	230.54	157.33	1.86	0.12	0.42	0.56
	$220.52^{+10.46}_{-6.33}$	$64.92^{+27.72}_{-14.42}$	$186.53^{+66.86}_{-64.50}$	$161.95^{+6.66}_{-4.18}$	$1.81^{+0.07}_{-0.09}$	$0.35^{+0.21}_{-0.16}$	$0.54^{+0.09}_{-0.08}$	
UGC06787	233.92	48.97	5.50	160.26	1.02	0.64	0.64	48.15
	355.69	283.96	55.07	230.85	1.06	1.60	0.52	19.07
	$306.03^{+29.61}_{-30.71}$	$191.27^{+43.55}_{-55.95}$	$228.20^{+384.64}_{-126.73}$	$207.86^{+13.87}_{-14.10}$	$1.30^{+0.20}_{-0.18}$	$1.10^{+0.20}_{-0.33}$	$0.53^{+0.03}_{-0.05}$	
UGC06818	89.57	24.95	1.42	55.87	0.40	0.16	0.00	1.04
	99.79	36.28	1.24	62.54	0.40	0.16	0.00	1.01
	$87.36^{+10.38}_{-14.90}$	$31.63^{+13.10}_{-11.20}$	$1.45^{+0.45}_{-0.26}$	$55.47^{+5.50}_{-7.66}$	$0.49^{+0.10}_{-0.07}$	$0.23^{+0.19}_{-0.10}$	$0.00^{+0.00}_{-0.00}$	
UGC06917	97.61	16.38	5.58	67.73	0.85	0.49	0.00	0.31
	94.64	10.69	5.27	67.61	0.84	0.39	0.00	0.20
	$97.13^{+22.25}_{-10.01}$	$21.02^{+41.46}_{-10.14}$	$3.28^{+1.93}_{-1.49}$	$74.19^{+13.43}_{-6.46}$	$0.84^{+0.10}_{-0.09}$	$0.80^{+0.34}_{-0.39}$	$0.00^{+0.00}_{-0.00}$	

Table A.1: Continued

UGC06923	73.15	9.47	6.92	49.03	0.94	0.25	0.00	0.72
	75.77	8.74	6.80	53.60	0.92	0.17	0.00	0.46
	$80.80^{+21.95}_{-13.62}$	$18.62^{+19.50}_{-10.26}$	$4.57^{+3.16}_{-1.50}$	$59.43^{+10.40}_{-7.31}$	$0.97^{+0.17}_{-0.15}$	$0.42^{+0.29}_{-0.22}$	$0.00^{+0.00}_{-0.00}$	
UGC06930	93.14	22.30	4.30	67.49	0.78	0.64	0.00	0.33
	92.28	10.36	4.55	66.56	0.75	0.41	0.00	0.20
	$89.01^{+9.49}_{-9.02}$	$16.50^{+28.03}_{-6.47}$	$2.94^{+1.80}_{-1.48}$	$71.13^{+9.88}_{-5.08}$	$0.76^{+0.09}_{-0.11}$	$0.80^{+0.39}_{-0.42}$	$0.00^{+0.00}_{-0.00}$	
UGC06973	217.19	47.22	54.95	143.80	1.03	0.20	0.41	9.69
	189.52	43.37	33.07	133.03	1.64	0.15	0.13	0.32
	$208.26^{+24.99}_{-23.52}$	$47.60^{+5.87}_{-5.86}$	$24.20^{+14.31}_{-7.49}$	$143.11^{+13.95}_{-12.58}$	$1.40^{+0.31}_{-0.23}$	$0.14^{+0.05}_{-0.03}$	$0.33^{+0.28}_{-0.17}$	
UGC06983	96.05	15.47	10.15	68.87	1.24	0.64	0.00	0.44
	96.06	12.30	6.17	70.59	1.05	0.60	0.00	0.42
	$97.17^{+8.88}_{-6.18}$	$16.92^{+26.07}_{-6.27}$	$4.93^{+2.00}_{-2.08}$	$73.51^{+9.33}_{-4.36}$	$1.07^{+0.14}_{-0.14}$	$0.85^{+0.48}_{-0.36}$	$0.00^{+0.00}_{-0.00}$	
UGC07125	53.06	14.65	2.55	32.90	0.60	0.16	0.00	0.64
	54.33	16.83	1.77	35.95	0.50	0.11	0.00	0.42
	$52.33^{+3.59}_{-3.36}$	$19.78^{+6.94}_{-6.34}$	$1.54^{+0.56}_{-0.28}$	$36.91^{+1.83}_{-1.61}$	$0.53^{+0.03}_{-0.02}$	$0.29^{+0.25}_{-0.14}$	$0.00^{+0.00}_{-0.00}$	
UGC07151	64.12	7.31	12.40	45.15	1.20	0.36	0.00	1.26
	59.49	5.21	9.44	46.44	1.07	0.52	0.00	0.88
	$60.80^{+13.79}_{-6.33}$	$12.94^{+22.25}_{-7.23}$	$4.84^{+3.75}_{-2.14}$	$52.56^{+7.36}_{-5.51}$	$1.03^{+0.05}_{-0.05}$	$0.87^{+0.26}_{-0.32}$	$0.00^{+0.00}_{-0.00}$	
UGC07261	68.40	16.66	10.80	51.18	1.44	0.85	0.00	0.74
	63.74	4.96	10.99	46.76	1.19	0.45	0.00	0.48
	$65.03^{+16.58}_{-8.14}$	$12.32^{+24.66}_{-6.43}$	$5.12^{+3.93}_{-2.39}$	$52.64^{+8.24}_{-5.23}$	$1.15^{+0.13}_{-0.14}$	$0.86^{+0.36}_{-0.37}$	$0.00^{+0.00}_{-0.00}$	
UGC07399	92.48	13.67	19.05	65.91	1.60	1.96	0.00	1.05
	92.02	11.03	19.13	66.82	1.49	1.22	0.00	0.51
	$99.50^{+22.91}_{-9.26}$	$17.26^{+15.86}_{-6.89}$	$13.87^{+6.98}_{-6.05}$	$72.09^{+12.75}_{-5.80}$	$1.35^{+0.20}_{-0.25}$	$1.79^{+0.81}_{-0.68}$	$0.00^{+0.00}_{-0.00}$	
UGC07524	71.75	20.21	2.75	46.30	0.58	0.64	0.00	0.29
	66.21	14.88	2.31	48.84	0.49	0.85	0.00	0.20
	$65.78^{+4.65}_{-5.19}$	$16.39^{+10.48}_{-4.58}$	$2.15^{+0.62}_{-0.61}$	$49.36^{+3.38}_{-2.29}$	$0.50^{+0.03}_{-0.04}$	$1.08^{+0.50}_{-0.52}$	$0.00^{+0.00}_{-0.00}$	
UGC07603	60.05	6.66	12.59	40.34	1.27	0.64	0.00	0.50
	59.73	4.76	13.41	40.55	1.21	0.24	0.00	0.12
	$62.98^{+11.24}_{-4.74}$	$8.34^{+8.66}_{-3.07}$	$10.07^{+3.56}_{-3.59}$	$43.91^{+6.70}_{-3.14}$	$1.19^{+0.13}_{-0.12}$	$0.63^{+0.45}_{-0.31}$	$0.00^{+0.00}_{-0.00}$	

Table A.1: Continued

UGC07690	48.85	5.14	48.60	36.49	2.05	0.42	0.00	0.35
	47.38	3.50	33.64	38.71	1.96	0.46	0.00	0.18
	$49.37^{+13.77}_{-5.91}$	$9.91^{+17.34}_{-5.80}$	$15.64^{+13.97}_{-7.27}$	$42.95^{+5.16}_{-3.55}$	$1.73^{+0.25}_{-0.31}$	$0.75^{+0.25}_{-0.25}$	$0.00^{+0.00}_{-0.00}$	
UGC08286	73.63	8.91	13.18	51.96	1.28	0.85	0.00	1.34
	74.35	6.20	9.97	52.78	1.03	0.67	0.00	1.68
	$74.49^{+18.69}_{-5.46}$	$15.35^{+36.85}_{-8.23}$	$5.40^{+3.63}_{-2.56}$	$58.35^{+9.46}_{-4.69}$	$1.05^{+0.09}_{-0.06}$	$1.72^{+0.60}_{-0.78}$	$0.00^{+0.00}_{-0.00}$	
UGC08490	72.31	11.49	29.74	52.99	1.84	1.10	0.00	0.21
	72.49	12.22	19.47	55.82	1.63	0.96	0.00	0.16
	$73.42^{+5.24}_{-2.55}$	$12.74^{+10.54}_{-4.74}$	$19.03^{+6.15}_{-5.51}$	$56.15^{+3.54}_{-2.27}$	$1.62^{+0.12}_{-0.12}$	$1.00^{+0.38}_{-0.33}$	$0.00^{+0.00}_{-0.00}$	
UGC08550	51.97	7.99	12.40	36.49	1.36	1.00	0.00	0.45
	58.25	17.28	5.06	42.59	1.25	1.44	0.00	0.36
	$56.16^{+15.16}_{-5.90}$	$14.95^{+17.98}_{-9.29}$	$5.54^{+4.40}_{-2.10}$	$41.49^{+6.22}_{-4.84}$	$1.21^{+0.14}_{-0.15}$	$1.36^{+0.46}_{-0.67}$	$0.00^{+0.00}_{-0.00}$	
UGC08699	162.57	48.57	22.56	122.97	1.91	0.61	0.61	2.38
	203.09	131.52	356.10	146.93	1.42	0.74	0.51	0.54
	$185.61^{+36.54}_{-12.79}$	$96.24^{+82.81}_{-42.66}$	$468.81^{+583.50}_{-317.78}$	$140.54^{+12.56}_{-7.10}$	$1.58^{+0.31}_{-0.26}$	$0.66^{+0.24}_{-0.33}$	$0.41^{+0.11}_{-0.19}$	
UGC09037	139.74	26.27	3.26	92.66	0.64	0.09	0.00	0.66
	136.25	21.02	3.02	97.90	0.63	0.10	0.00	0.60
	$137.53^{+10.54}_{-6.53}$	$31.32^{+28.54}_{-9.34}$	$2.38^{+0.75}_{-0.70}$	$103.09^{+9.43}_{-5.20}$	$0.68^{+0.07}_{-0.07}$	$0.17^{+0.09}_{-0.05}$	$0.00^{+0.00}_{-0.00}$	
UGC09133	205.74	63.14	19.95	171.26	1.76	0.53	0.53	8.09
	209.05	103.39	203.95	194.32	2.27	0.58	0.30	11.33
	$216.70^{+5.82}_{-5.22}$	$146.04^{+33.22}_{-27.43}$	$242.96^{+91.07}_{-64.13}$	$198.22^{+3.54}_{-3.56}$	$2.19^{+0.08}_{-0.07}$	$0.61^{+0.07}_{-0.08}$	$0.39^{+0.04}_{-0.05}$	
UGC09992	26.48	4.20	13.80	19.33	1.28	0.67	0.00	0.36
	23.58	1.37	8.85	19.09	0.79	0.67	0.00	0.04
	$27.84^{+6.08}_{-3.20}$	$4.26^{+6.15}_{-2.38}$	$4.25^{+4.56}_{-2.08}$	$22.72^{+4.21}_{-3.18}$	$0.78^{+0.12}_{-0.08}$	$0.52^{+0.53}_{-0.31}$	$0.00^{+0.00}_{-0.00}$	
UGC10310	61.44	10.84	6.31	43.27	0.90	0.64	0.00	0.11
	61.35	5.58	5.17	43.78	0.67	0.48	0.00	0.07
	$58.75^{+9.31}_{-6.28}$	$9.99^{+17.66}_{-4.47}$	$2.91^{+2.16}_{-1.49}$	$48.19^{+7.69}_{-4.93}$	$0.63^{+0.06}_{-0.05}$	$1.06^{+0.54}_{-0.59}$	$0.00^{+0.00}_{-0.00}$	
UGC11455	244.68	54.15	8.98	182.67	1.16	0.25	0.00	1.70
	247.88	35.05	8.56	180.32	1.01	0.15	0.00	1.40
	$241.28^{+11.80}_{-11.50}$	$49.44^{+66.45}_{-11.92}$	$6.78^{+1.58}_{-2.81}$	$186.62^{+14.79}_{-5.68}$	$0.99^{+0.07}_{-0.04}$	$0.26^{+0.15}_{-0.08}$	$0.00^{+0.00}_{-0.00}$	

Table A.1: Continued

UGC11914	276.49	68.51	16.85	191.90	1.60	0.53	0.99	2.02
	331.63	87.51	363.29	229.96	1.59	0.10	0.85	0.70
	$337.51^{+46.05}_{-37.08}$	$104.72^{+27.77}_{-12.28}$	$261.23^{+292.28}_{-154.72}$	$232.68^{+26.55}_{-21.08}$	$1.51^{+0.28}_{-0.28}$	$0.25^{+0.18}_{-0.11}$	$0.86^{+0.10}_{-0.20}$	
UGC12506	181.13	36.58	10.96	156.50	1.07	1.00	0.00	1.00
	195.24	23.37	6.71	159.72	0.89	0.76	0.00	0.96
	$180.42^{+15.65}_{-11.31}$	$31.92^{+74.65}_{-6.79}$	$4.54^{+1.28}_{-2.81}$	$166.21^{+20.51}_{-5.17}$	$0.79^{+0.06}_{-0.04}$	$1.10^{+0.34}_{-0.29}$	$0.00^{+0.00}_{-0.00}$	
UGC12632	61.32	13.73	3.80	41.19	0.70	0.83	0.00	0.08
	58.66	13.23	2.49	44.57	0.59	1.29	0.00	0.06
	$59.77^{+5.21}_{-5.94}$	$14.73^{+13.07}_{-5.73}$	$2.23^{+1.24}_{-0.82}$	$45.22^{+4.24}_{-2.85}$	$0.60^{+0.03}_{-0.05}$	$1.50^{+0.75}_{-0.97}$	$0.00^{+0.00}_{-0.00}$	
UGCA442	56.71	12.30	2.40	35.72	0.54	0.85	0.00	1.46
	58.53	18.42	2.19	40.51	0.67	1.52	0.00	0.90
	$60.84^{+10.87}_{-7.54}$	$21.81^{+14.69}_{-9.66}$	$2.01^{+0.81}_{-0.41}$	$41.82^{+4.14}_{-3.56}$	$0.69^{+0.10}_{-0.07}$	$1.85^{+1.58}_{-1.27}$	$0.00^{+0.00}_{-0.00}$	
UGCA444	37.30	5.74	4.23	23.20	0.71	1.00	0.00	0.62
	46.39	27.61	1.92	29.27	0.94	9.43	0.00	0.10
	$34.40^{+10.73}_{-5.85}$	$10.91^{+8.33}_{-5.19}$	$2.68^{+1.08}_{-0.51}$	$25.21^{+4.08}_{-2.71}$	$0.80^{+0.08}_{-0.08}$	$6.19^{+2.73}_{-3.40}$	$0.00^{+0.00}_{-0.00}$	

Table A.1: Continued

Appendix B

SIDM Modeling Parameters for Early-Type Galaxies

Re (1)	log$M_\star$ (2)	z (3)	$M_\star/M_{halo}$ (4)	δc_{200} (5)	σ/m (6)	$\sigma0$ (7)	$\rho0$ (8)	f_e3D (9)	$f_5$3D (10)	f_e (11)	f_5 (12)	logM_{DMe} (13)	logM_{DM5} (14)	$\delta\rho$(%) (15)	δM(%) (16)
4.82	11.52	0.56	0.015	0.0	0.8	304.00	2.50E+10	0.19	0.19	0.31	0.32	10.87	10.89	4.5	-4.6
4.82	11.52	0.56	0.015	-0.5	0.8	299.45	2.50E+10	0.17	0.17	0.28	0.29	10.82	10.84	4.9	-5.0
4.82	11.52	0.56	0.015	-1.5	0.8	291.00	3.00E+10	0.15	0.15	0.25	0.26	10.74	10.76	4.3	-4.8
8.92	11.45	0.75	0.015	0.0	0.8	270.00	5.00E+08	0.29	0.17	0.52	0.37	11.18	10.75	2.2	0.0
17.67	11.97	0.72	0.015	0.0	0.8	387.00	2.00E+08	0.40	0.12	0.63	0.32	11.90	10.94	-1.0	4.5
6.29	11.60	0.61	0.015	0.0	0.8	316.00	5.00E+09	0.18	0.15	0.35	0.30	11.02	10.87	4.1	-3.8
6.29	11.60	0.61	0.015	1.5	0.8	340.00	6.00E+09	0.30	0.26	0.48	0.43	11.26	11.11	1.6	2.0
4.27	11.53	0.65	0.015	0.0	0.8	310.00	1.50E+11	0.22	0.23	0.31	0.33	10.88	10.96	5.1	-5.0
7.90	11.54	0.88	0.015	0.0	0.8	292.00	1.00E+09	0.20	0.13	0.42	0.30	11.09	10.76	3.2	-3.8
8.59	11.81	0.24	0.015	0.0	0.8	385.00	7.00E+10	0.54	0.52	0.62	0.57	11.72	11.48	-4.9	4.0
8.59	11.81	0.24	0.015	-1.5	0.8	352.00	2.50E+11	0.42	0.42	0.51	0.46	11.52	11.29	-4.2	3.2
8.59	11.81	0.24	0.015	-2.0	0.8	343.00	2.50E+11	0.39	0.39	0.48	0.43	11.47	11.25	-4.8	3.5
6.44	11.73	0.49	0.015	0.0	0.8	350.00	1.00E+10	0.19	0.16	0.34	0.29	11.13	10.97	3.0	-4.4
6.44	11.73	0.49	0.015	-0.5	0.8	345.00	1.05E+10	0.18	0.15	0.32	0.27	11.09	10.93	4.6	-2.8
4.78	11.36	0.35	0.015	0.0	0.8	272.00	7.50E+09	0.18	0.19	0.34	0.35	10.77	10.80	4.5	-5.0
4.78	11.36	0.35	0.015	-1.5	0.8	258.50	1.00E+10	0.15	0.16	0.28	0.29	10.66	10.69	4.6	-3.9
9.21	11.71	0.67	0.015	0.0	0.8	327.50	2.00E+09	0.31	0.20	0.50	0.36	11.41	10.99	-3.9	2.1
3.21	11.24	0.68	0.015	0.0	0.8	255.00	4.50E+11	0.24	0.26	0.32	0.38	10.60	10.82	5.8	-5.4
6.11	11.52	0.27	0.015	0.0	0.8	301.00	6.50E+09	0.26	0.23	0.43	0.39	11.10	10.97	-0.6	-0.8
16.81	11.55	0.61	0.015	0.0	0.8	277.00	1.00E+08	0.55	0.19	0.74	0.45	11.71	10.79	-3.9	2.3
13.08	11.41	0.78	0.015	0.0	0.8	258.00	8.00E+07	0.39	0.14	0.65	0.39	11.38	10.63	4.6	-4.3
13.08	11.41	0.78	0.015	-1.0	0.8	246.20	8.00E+07	0.34	0.12	0.61	0.35	11.30	10.55	4.8	-4.6
11.78	12.10	0.46	0.015	0.0	0.8	467.00	8.00E+10	0.55	0.54	0.63	0.57	12.02	11.67	-4.9	4.9
7.86	11.76	0.48	0.015	0.0	0.8	351.50	5.00E+09	0.26	0.20	0.43	0.34	11.34	11.05	-0.8	0.7
3.86	11.26	0.40	0.015	0.0	0.8	255.00	5.00E+10	0.26	0.29	0.38	0.42	10.74	10.88	2.9	-0.7

Table B.1: ETG and SIDM parameters. The meaning of each column is listed as following: (1) Effective radius (2D). (2) Stellar Mass. (3) Redshift. (4) Ratio between stellar and halo mass. (5) Deviation of c_{200} from the mean value in units of 1σ. (6) Self-interacting cross section in units of cm^2/g. (7) SIDM velocity dispersion. (8) SIDM central density. (9) 3D SIDM fractions within the effective radii from (1). (10) 3D SIDM fractions within 5 kpc. (11) 2D SIDM fractions within the effective radii from (1). (12) 2D SIDM fractions within 5 kpc. (13) 2D SIDM mass within the effective radii from (1). (14) 2D SIDM mass within 5 kpc. (15) Percentage error of SIDM density at r_1. (16) Percentage error of SIDM mass at r_1.

Re (1)	log$M_\star$ (2)	z (3)	$M_\star/M_{halo}$ (4)	δc_{200} (5)	σ/m (6)	$\sigma 0$ (7)	$\rho 0$ (8)	f_e3D (9)	$f_5$3D (10)	f_e (11)	f_5 (12)	logM_{DMe} (13)	logM_{DM5} (14)	$\delta\rho$(%) (15)	δM(%) (16)
3.86	11.26	0.40	0.015	0.0	0.8	259.00	4.00E+11	0.35	0.36	0.43	0.47	10.84	10.96	2.6	-1.7
3.86	11.26	0.40	0.015	1.0	0.8	272.00	4.00E+11	0.41	0.42	0.49	0.53	10.94	11.06	3.7	-2.3
3.86	11.26	0.40	0.015	2.0	0.8	285.00	4.00E+11	0.46	0.48	0.54	0.58	11.03	11.15	4.6	-4.9
5.27	11.55	0.33	0.015	0.0	0.8	312.00	3.70E+10	0.29	0.29	0.41	0.40	11.10	11.07	-0.2	-0.7
4.35	11.60	0.72	0.015	1.0	0.8	342.00	1.00E+11	0.23	0.24	0.33	0.35	10.99	11.07	11.0	0.1
2.41	10.99	0.34	0.015	-1.5	0.8	212.00	1.00E+12	0.20	0.23	0.26	0.36	10.22	10.58	6.0	-6.2
2.41	10.99	0.34	0.015	-0.5	0.8	217.40	1.00E+12	0.23	0.26	0.29	0.40	10.30	10.66	7.4	-7.2
2.41	10.99	0.34	0.015	1.0	0.8	228.50	1.00E+12	0.29	0.34	0.36	0.48	10.44	10.80	9.6	-7.2
2.41	10.99	0.34	0.015	1.5	0.8	232.00	1.00E+12	0.31	0.36	0.38	0.50	10.48	10.84	9.1	-9.0
2.41	10.99	0.34	0.015	2.0	0.8	236.20	1.00E+12	0.33	0.38	0.41	0.53	10.52	10.88	9.4	-9.9
3.93	11.51	0.48	0.015	-2.0	0.8	305.50	4.00E+10	0.08	0.09	0.16	0.19	10.49	10.63	9.9	-8.5
3.04	11.28	0.32	0.015	-2.0	0.8	262.80	7.00E+10	0.09	0.11	0.16	0.23	10.26	10.56	9.7	-9.1
4.35	11.60	0.72	0.015	0.0	0.8	327.30	2.00E+11	0.21	0.21	0.29	0.30	10.90	10.97	6.2	-6.1
4.58	11.67	0.53	0.015	-1.5	0.8	338.00	6.00E+10	0.11	0.11	0.19	0.20	10.73	10.78	7.2	-9.3
3.47	11.28	0.55	0.015	-1.5	0.8	254.50	4.00E+10	0.11	0.13	0.20	0.26	10.37	10.60	7.2	-7.5
3.48	11.11	0.36	0.015	-1.5	0.8	217.00	4.00E+10	0.18	0.22	0.29	0.36	10.42	10.64	3.0	-2.2
3.48	11.11	0.36	0.015	-2.0	0.8	214.00	4.00E+10	0.17	0.19	0.27	0.33	10.37	10.59	2.2	-2.8
3.55	11.63	0.72	0.015	-1.5	0.8	346.00	2.00E+11	0.09	0.09	0.13	0.17	10.52	10.70	11.4	-11.2
3.55	11.63	0.72	0.015	-0.5	0.8	349.00	3.00E+11	0.11	0.12	0.17	0.20	10.63	10.80	12.7	-11.0
3.55	11.63	0.72	0.015	1.0	0.8	365.00	8.00E+11	0.19	0.20	0.26	0.30	10.87	11.03	22.2	-0.9
3.01	11.50	0.39	0.015	0.5	0.8	337.00	2.00E+11	0.11	0.13	0.18	0.25	10.54	10.84	25.7	-3.4
3.01	11.50	0.39	0.015	-0.5	0.8	328.00	1.00E+12	0.15	0.16	0.20	0.25	10.60	10.84	21.5	-3.6
3.45	11.36	0.57	0.015	-1.5	0.8	271.10	1.00E+11	0.13	0.14	0.20	0.25	10.46	10.67	8.0	-6.4
1.35	11.14	0.34	0.015	-2.0	0.8	304.00	5.00E+11	0.03	0.05	0.05	0.16	9.52	10.36	46.6	0.9

Table B.1: Continued